Technical University of Munich
TUM School of Life Sciences

Deciphering the lipidomic landscape of BAT mitochondria: Membrane lipid metabolism as regulator of UCP1 function

Sarah Stephanie Brunner

Vollständiger Abdruck der von der TUM School of Life Sciences der Technischen Universität München zur Erlangung einer

Doktorin der Naturwissenschaften (Dr. rer. nat.)

genehmigten Dissertation.

Vorsitz: Prof. Dr. Markus List

Prüfende der Dissertation:

1. Prof. Dr. Josef Ecker
2. Prof. Dr. Martin Klingenspor
3. Prof. Dr. Robert Ahrends

Die Dissertation wurde am 05.08.2024 bei der Technischen Universität München eingereicht und durch die TUM School of Life Sciences am 08.01.2025 angenommen.

LIST OF PUBLICATIONS AND CONFERENCE DISTRIBUTIONS

Publications

- Sarah Brunner*, Marcus Höring*, Gerhard Liebisch, Sabine Schweizer, Josef Scheiber, Piero Giansanti, Maria Hidrobo, Sven Hermeling, Josef Oeckl, Natalia Prudente de Mello, Fabiana Perocchi, Claudine Seeliger, Akim Strohmeyer, Martin Klingenspor, Johannes Plagge, Bernhard Küster, Ralph Burkhardt, Klaus-Peter Janssen, Josef Ecker. Mitochondrial lipidomes are tissue specific – a high phospholipid to cholesterol ratio relates to UCP1 activity.
  Published in Life Science Alliance 2024 – First Author

- Marcus Höring*, Sarah Brunner*, Josef Scheiber, Julius Honecker, Gerhard Liebisch, Claudine Seeliger, Laura Mengel, Melina Claussnitzer, Ralph Burkhardt, Hans Hauner, Josef Ecker. Sex-specific response of the human plasma lipidome to short-term cold exposure.
  Under revision in Biochimica et Biophysica Acta (Special Edition) 2024 – First Author

- Sarah Brunner, Klaus-Peter Janssen, Josef Ecker. Post-fast refeeding: rise of intestinal stemness and mutagen-induced cancer risk through polyamine metabolism.
  Published in Signal Transduction and Targeted Therapie 2024 - First Author

- Josef Ecker, Sarah Brunner, Klaus-Peter Janssen. Metabolic inflexibility of mitochondria: beneficial for the fitness of regenerating liver cells.
  Published in Signal Transduction and Targeted Therapie 2024 - Co-Author

- Josef Oeckl*, Petra Janovska, Katerina Adamcova, Kristina Bardova, Sarah Brunner, Sebastian Dieckmann, Josef Ecker, Tobias Fromme, Jiri Funda, Thomas Gantert, Piero Giansanti, Maria Hidrobo, Ondrej Kuda, Bernhard Kuster, Yongguo Li, Radek Pohl, Sabine Schmitt, Sabine Schweizer, Hans Zischka, Petr Zouhar, Jan Kopecky, Martin Klingenspor. Loss of UCP1 function augments recruitment of futile lipid cycling for thermogenesis in murine brown fat. **Published in Molecular Metabolism 2022 – Co-Author**

- Maria Hidrobo*, Marcus Höring*, Gerhard Liebisch, Sabine Schweizer, Sarah Brunner, Martin Klingenspor, Renate Schreiber, Rudolf Zechner, Ralph Burkhardt, Josef Ecker. Cold-induced phosphatidylethanolamine synthesis in liver and brown adipose tissue of mice.
  Under revision in Biochimica et Biophysica Acta (Special Edition) 2024 – Co-Author

- Johannes Plagge*, Maria Zimmermann-Kogadeeva*, Marcus Höring, Emma Slack, Jörg Heeren, Michael Zimmermann, Piero Giansanti, Marijana Basic, Anna Weiß, Claudine Seeliger, Andre Bleich, Sarah Brunner, Maria Hidrobo, Barbara Stecher, Olivia Coleman, Akim Strohmeyer, Martin Klingenspor, Bernhard Küster, Klaus-Peter Janssen, Dirk Haller, Ralph Burkhardt, Gerhard Liebisch, Josef Ecker. The gut microbiota reduces intestinal lipid absorption by induction of host phospholipase A1 activity in bile.
  Under revision in Gastroenterology 2024 – Co-Author

Conference Distributions

- International Conference of the Bioscience of Lipids 2021 (ICBL 2021)
  Utrecht, the Netherlands: Lipid Dynamics – From Molecular Species to Health and Disease
  Oral Presentation

- CPH BAT 2022 (Cphbat 2022)
  Copenhagen, Denmark: The Heterogeneity and Plasticity of Adipose Tissue
  Poster Presentation

- International Conference of the Bioscience of Lipids 2023 (ICBL 2023)
  Palma de Mallorca, Spain: Advances in Lipid Research - From Bench to Bedside
  Oral Presentation + Award for Best Oral Presentation

- Gordon Research Seminar 2024 (GRS 2024)
  Lucca, Italy: Toward Functional Lipidomics - Structure Elucidation, Quantification, Data Integration and Clinical Translation
  Oral Presentation

- Gordon Research Conference 2024 (GRC 2024)
  Lucca, Italy: Toward Functional Lipidomics - Structure Elucidation, Quantification, Data Integration and Clinical Translation
  Poster Presentation

- 47th European Lipoprotein Club Meeting 2024 (EAS-ELC 2024)
  Tutzing, Germany: Lipids, lipoproteins and lipid-associated diseases
  Oral Presentation

TABLE OF CONTENTS

LIST OF FIGURES

LIST OF SUPPLEMENTARY FIGURES

LIST OF TABLES

LIST OF SUPPLEMENTARY TABLES

LIST OF ABBREVIATIONS

^{18}F-FDG PET	^{18}Flurodeoxyglucose positron emission tomography
A.U.	Absorbance units
AC	Adenylyl cyclase
ACAT2	Acetyl-CoA acetyltransferase 2
ADCY5	Adenylate cyclase 5
ADIPOQ	Adiponectin
ADP	Adenosine diphosphate
Ago2	Argonaut RISC catalytic component 2
ALT	Alanine aminotransferase
AMPK	Adenosine monophosphate-activated protein kinase
AMV	Avian myeloblastosis virus
ANGPTL4	Angiopoietin like 4
Anti A	Antimycin A
ApoE	Apoliprotein E
Appl	Application
AST	Aspartate aminotransferase
AT	Adipose tissue
ATAD3A	ATPase family AAA domain containing 3A
ATGL	Adipose triglyceride lipase
ATP	Adenosine triphosphate
AUC	Area under the curve
BCA	Bicinchoninic acid assay
Bp	Base pair
BSA	Bovine serum albumin
C1P	Ceramide 1-phosphate
cAMP	Cyclic adenosine monophosphate
CCT	CTP: phosphocholine cytidylyltransferase
CD36	CD36 Molecule
cDNA	Complementary DNA
CDP	Cytidine diphosphate
CDS	CDP diacylglycerol synthase
CE	Cholesteryl ester
CEPT1	Choline/ethanolamine phosphotransferase 1
Cer	Ceramide
CGI-58	Comparative gene identification-58
cGMP	Cyclic guanosine monophosphate
CIDEA	Cell death inducing
CK	Choline kinase
CL	Cardiolipin
CLS	Cardiolipin synthase
cMito	Crude mitochondria
CMP	Cytidine monophosphate
CO_2	Carbon dioxide
COX7A1	Cytochrome C oxidase subunit 8A1
CPT	Choline phosphotransferase

CRE	Cyclization recombination
CT	Computer tomography
CTP	Cytidine triphosphate
CPT1B	Carnitine palmitoyl transferase 1B
DAG	Diacylglycerol
DB	Double bond
DDA	Data dependent acquisition
DGAT1/2	Diacylglycerol O-acyltransferase 1/2
DIO2	Iodothyronine deiodinase 2
DANN	Deoxyribonucleic acid
ECT	CTP: phosphoethanolamine cytidylyltransferase
EK	Ethanolamine kinase
ELISA	Enzyme-linked immunosorbent assay
ELOVL3/6	ELOVL fatty acid elongase 3/6
EPT	Ethanolamine phosphotransferase
ER	Endoplasmic reticulum
ER	Estrogen receptor
ERK	Extracellular signal-regulated kinase
ERMCS	Endoplasmic reticulum-mitochondria contact side
ESI-MS/MS	Electrospray ionization-tandem mass spectrometry
ETC	Electron transport chain
EtOH	Ethanol
eWAT	Epididymal white adipose tissue
FA	Fatty acid
FABP4	Fatty acid binding protein 4
FACL4	Acyl-CoA synthetase long chain family member 4
FADH	Flavine adenine dinucleotide
FC	Free cholesterol
FCCP	Carbonylcyanide-4(trifluoromethoxy)-phenylhydrazone
FDR	False discovery rate
FFA	Free fatty acid
FGF21	Fibroblast growth factor 21
FIA	Flow injection analysis
FTMS	Fourier transform mass spectrometry
G3P	Glycerol-3-phosphate
GATM	Glycine amidino transferase
GC	Guanosine cyclase
GDP	Guanosine diphosphate
Glut1/4	Solute carrier family 1/4
GPC	Glycerophosphocholine
GPL	Glycerophospholipid
GTT	Glucose tolerance test
H&E	Hematoxylin and eosin
HCL	Hydrochloric acid
HET	Heterogenous
HexCer	Hexosylceramide
HFD	High Fat Diet

HMG-CoA	3-hydroxy-3-methylglutaryl-coenzyme A
HMGCR	3-hydroxy-3-methylglutaryl-coenzyme A reductase
HR-MS	High resolution mass spectrometry
HSL	Hormone sensitive lipase
iBAT	Interscapular brown adipose tissue
IBM	Inner boundary membrane
IL-6	Interleukin 6
IMM	Inner mitochondrial membrane
IMS	Intermembrane space
i.p.	Intraperitoneal injection
IP3R	Inositol 1, 4, 5-triphosphate receptor
Iso	Isoproterenol
IT	Injection time
iWAT	Inguinal white adipose tissue
KD	Knockdown
kDA	Kilodalton
KO	Knockout
LCFA	Long chain fatty acid
LD	Lipid droplet
LPC	Lysophosphatidylcholine
LPCAT	Lysophosphatidylcholine acyltransferase
LPE	Lysophosphatidylethanolamine
LPEAT	Lyso phosphatidylethanolamine acyltransferase
LPL	Lipoprotein lipase
LPLAT	Lyso phospholipid acyltransferase
MAG	Monoacylglycerol
Mal	Malate
MAM	Mitochondria-associated membrane
MAP3K5	Mitogen-activated protein kinase kinase kinase 5
MAPK	Mitogen-activated protein kinase
Me-α/β-CD	Methyl- α/β-cyclodextrin
MGL	Monoglyceride lipase
mPBAC	Murine primary brown adipocytes
mPWAC	Murine primary white adipocytes
mRNA	Messenger ribonucleic acid
MSX	Multiplex acquisition
NADH	Nicotine amide adenine nucleotide
NAFL	Nonalcoholic fatty liver
NAFLD	Nonalcoholic fatty liver disease
NASH	Nonalcoholic steatohepatitis
NE	Norepinephrine
NST	Non-shivering thermogenesis
NTC	Non-targeting control
OCR	Oxygen consumption rate
OE	Overexpression
Oligo	Oligomycin
OMM	Outer mitochondrial membrane

OXPHOS	Oxidative phosphorylation
PA	Phosphatidic acid
PBS	Phosphate-buffered saline
PC	Phosphatidylcholine
PCR	Polymerase Chain Reaction
PE	Phosphatidylethanolamine
PE P	PE plasmalogen
PEMT	Phosphatidylethanolamine N-methyltransferase
PG	Phosphatidylglycerol
PGAM5	Mitochondrial serine/threonine protein phosphatase
PGC-1α	Peroxisome proliferator-activated receptor γ coactivator-1s
PI	Phosphatidylinositol
PISD	Phosphatidylserine decarboxylase
PK	Pyruvate kinase
PKA	Protein kinase A
PKG	Proteinkinase G
PLA	Phospholipase A
PLA2	Phospholipase A2
PLIN	Perilipin
pMito	Pure mitochondria
PPARγ	Proliferator-activated receptor γ
PS	Phosphatidylserine
PSS1/2	Phosphatidylserine synthase 1/2
PUFAS	Polyunsaturated fatty acids
Pyr	Pyruvate
qPCR	Quantitative polymerase chain reaction
QQQ	Triple quadrupole
RER	Respiratory exchange ratio
RF	Random forest
RIN	RNA integrity number
RIPA	Radioimmunoprecipitation assay
RISC	RNA-induced silencing complex
RNA	Ribonucleic acid
ROC	Receiver operator characteristics
RT	Room temperature
SCD1	Stearoyl-CoA desaturase
SERCA	Sarcoplasmic reticulum calcium ATPase
siRNA	Small interfering RNA
SL	Sphingolipid
SLN	Sarcolipin
SM	Sphingomyelin
SNS	Sympathetic nervous system
SPF	Specific pathogen free
SRE	Sterol regulatory element
SREBP	Sterol regulatory element-binding protein
StAR	Steroidogenic acute regulatory protein
STARD	StAR related lipid transfer domain containing

Suc	Succinate
SUCNR1	Succinate receptor 1
SUV	Small unilamellar vesicles
SVF	Stroma vascular fraction
T2DB	Diabetes mellitus type 2
TAG	Triacylglycerol
TAM	Tamoxifen
TBS-T	Tris Buffered Saline-Tween
TCA	Tricarboxylic acid cycle
tGFP	Turbo green fluorescent protein
TRL	Triglyceride-rich lipoprotein
TSPO	Translocator protein
UCP1	Uncoupling protein 1
UPs1p/UPs2p	PRELI domain containing 3B
USP35	Ubiquitin specific peptidase 35
VDAC	Voltage dependent anion channel
VLDL	Very low-density lipoprotein
WT	Wildtype
β-AR	Beta-adrenoreceptor

ABSTRACT

The composition of lipid species is conserved within sub-cellular compartments, although it is unclear whether organelle lipidomes differ between organs. Mitochondria present in brown adipose tissue (BAT) contain uncoupling protein 1 (UCP1), which enables them to convert chemical energy stored as triglycerides into heat, a process known as non-shivering thermogenesis. Therefore, we sought to determine whether UCP1 in BAT requires a distinct lipidomic environment within mitochondria that differs from those of other tissues, including white adipose tissue (WAT), muscle and liver. Lipidomic analyses of mitochondria revealed substantial differences in their glycerophospholipid (GPL) and free cholesterol (FC) contents. The GPL to FC ratio was 50-fold higher in BAT than WAT mitochondria. Their purity was confirmed following a proteomic comparison to ER and mitochondria-associated membrane (MAM). A lipid signature containing PC and FC, calculated from the lipidomic profiles, allowed differentiation of mitochondria from BAT of mice housed at different temperatures. To ascertain the functional relevance of specific mitochondrial lipid compositions, respiratory capacity, including UCP1 activity, was investigated. Elevating FC in isolated BAT mitochondria prevented UCP1 function, whereas increasing GPL boosted it. Similarly, overexpression of STARD3, which facilitates mitochondrial FC import, inhibited UCP1 function in primary brown adipocytes. Conversely, a knockdown promoted it.

As phosphatidylserine decarboxylase (PISD) decarboxylates PS to generate PE in mitochondria, it is evident that this enzyme essentially regulates mitochondrial GPL contents. In the subsequent step, we asked whether PISD can be related to adipose tissue browning and UCP1 function. Stable isotope labeling of cellular GPL metabolism revealed an increased PISD activity in brown compared to white adipocytes. Consequently, a mouse model having a tamoxifen-inducible PISD knockout in UCP1-expressing cells (iBcKO-PISD) was developed. Microplate-based respirometry analyses of brown adipocytes originating from iBcKO-PISD mice demonstrated an increased UCP1-mediated respiration upon β-adrenergic stimulation compared to adipocytes from wildtype animals. Further, their mitochondrial GPL/FC ratios were 2-fold higher. Most importantly, several pathologies observed in brown and beige adipose tissue as well as in liver of wildtype mice after high fat feeding, were alleviated or even absent in iBcKO-PISD animals after cold exposure. These included obesity-related parameters such as a higher fat mass, insulin and leptin resistance, and larger lipid droplets in brown/beige adipose tissue, as well as non-alcoholic fatty liver disease (NAFLD)-related measures such as elevated alanine aminotransferase (ALT) levels in plasma and immune cell infiltration in the liver.

In summary, our findings demonstrate that the lipidomic organization of mitochondria (GPL/FC) and the activity of PISD are critical for BAT function and for whole-body metabolism (e.g. for liver-BAT-communication). We propose that targeting the mitochondrial GPL/FC and/or PISD in BAT might be a promising strategy to promote UCP1 activity and metabolic health.

ZUSAMMENFASSUNG

Die Zusammensetzung von Lipidspezies ist innerhalb subzellulärer Kompartimente konserviert, jedoch ist bisher unklar, ob sich das Lipidom von Organellen zusätzlich zwischen verschiedenen Organen unterscheidet. Mitochondrien im braunen Fettgewebe (BAT) enthalten das Entkopplungsprotein 1 (UCP1), welches sie dazu befähigt, chemische Energie, die in Form von Triglyceriden gespeichert ist, in Wärme umzuwandeln (zitterfreie Thermogenese). Aus diesem Grund wurde in dieser Studie untersucht, ob die Funktion von UCP1 in BAT von einer spezifischen lipidomischen Zusammensetzung abhängt, die sich von der in anderen Geweben wie weißem Fettgewebe (WAT), Muskeln und Leber unterscheidet. Lipidomische Analysen der Mitochondrien ergaben erhebliche Unterschiede in ihrem Gehalt an Glycerophospholipiden (GPL) und freiem Cholesterin (FC). Das Verhältnis von GPL zu FC war in den Mitochondrien von BAT 50-mal höher als in denen von WAT. Ihre Reinheit wurde durch einen Vergleich des Proteoms mit ER und Mitochondrien-assoziierten Membranen (MAM) bestätigt. Eine aus den lipidomischen Profilen berechnete Lipidsignatur, die PC und FC enthielt, ermöglichte die Differenzierung von Mitochondrien aus BAT von Mäusen, die bei unterschiedlichen Temperaturen gehalten wurden. Um die funktionelle Bedeutung spezifischer mitochondrialer Lipidzusammensetzungen zu ermitteln, wurde die Atmungskapazität, einschließlich der UCP1-Aktivität, untersucht. Eine Erhöhung von Cholesterin in isolierten BAT-Mitochondrien hemmte die UCP1-Aktivität, während eine Erhöhung des GPL sie wiederum verstärkte. In ähnlicher Weise hemmte die Überexpression von STARD3, welches den mitochondrialen FC-Import ermöglicht, die UCP1-Funktion in primären braunen Adipozyten. Umgekehrt förderte ein Knockdown die UCP1 Aktivität.

Da die Phosphatidylserindecarboxylase (PISD) PS decarboxyliert, um PE in den Mitochondrien zu erzeugen, ist es offensichtlich, dass dieses Enzym den mitochondrialen GPL-Gehalt wesentlich reguliert. Daher stellten wir in einem weiteren Schritt die Frage, ob PISD mit der Bräunung des Fettgewebes und der Funktion von UCP1 in Verbindung gebracht werden kann. Die stabile Isotopenmarkierung des zellulären GPL-Stoffwechsels ergab eine erhöhte PISD-Aktivität in braunen im Vergleich zu weißen Adipozyten. Auf Grund dessen wurde ein Mausmodell mit einem Tamoxifen-induzierbaren PISD-Knockout in UCP1-exprimierenden Zellen (iBcKO-PISD) entwickelt. Mitochondriale Atmungsuntersuchungen in braunen Adipozyten von iBcKO-PISD-Mäusen zeigten eine erhöhte UCP1-vermittelte Atmung nach β-adrenerger Stimulation im Vergleich zu Adipozyten von Wildtyp-Tieren. Außerdem war ihr mitochondrialer GPL/FC-Ratio um das Zweifache gesteigert. Hervorzuheben ist, dass mehrere Pathologien, die im braunen und beigen Fettgewebe sowie in der Leber von Wildtyp-Mäusen nach einer fettreichen Fütterung beobachtet wurden, während diese bei iBcKO-PISD-Tieren nach einer Kälteexposition gemildert wurden oder sogar fehlten. Dazu gehörten mit Fettleibigkeit zusammenhängende Parameter, wie eine höhere Fettmasse, Insulin- und Leptin-Resistenz, größere Lipidtropfen im braunen/beigen Fettgewebe, sowie Messwerte, die mit der nicht-alkoholischen Fettlebererkrankung (NAFLD) zusammenhängen, zum Beispiel erhöhte Alanin-Aminotransferase (ALT)-Spiegel im Plasma und Immunzellinfiltration in der Leber.

Zusammenfassend zeigen unsere Ergebnisse, dass die lipidomische Organisation der Mitochondrien (GPL/FC) und die Aktivität von PISD für die Funktion von BAT und den Ganzkörperstoffwechsel (z.B. für die Leber-BAT-Kommunikation) entscheidend sind. Wir schlagen vor, dass die gezielte Beeinflussung des mitochondrialen GPL/FC und/oder der PISD-Aktivität in BAT eine vielversprechende Strategie zur Förderung der UCP1-Aktivität und der metabolischen Gesundheit sein könnte.

1 INTRODUCTION

1.1 THE METABOLIC SYNDROME AND OBESITY – A WORLDWIDE EPIDEMIC

A significant public health burden, linked to all-cause mortality, is given by the rapid increase in people suffering from metabolic syndrome. This includes a broad spectrum of metabolic abnormalities such as glucose intolerance, insulin resistance, hypertension, dyslipidemia, and central obesity *(Eckel et al. 2005)*. In particular, the prevalence of obesity is continuously rising, with more than 50% of the world's population being considered as being overweight or living with obesity. This is not limited to adults; as over 390 million adolescents and children (aged 5-19 years) are affected (*World Health Organization, 2022*). Overweight and obesity are characterized by a persistent positive energy balance, caused by genetic factors along with reduced energy expenditure (i.e. physical activity) and excessive energy intake from food *(Després und Lemieux 2006)*. To combat this global epidemic, novel therapeutic strategies for its prevention and treatment are crucial. The thesis presented here contributes to ongoing investigations in the field of lipid metabolism, providing valuable information for improving metabolic health.

1.2 THE MULTI-COLORED PICTURE OF THE ADIPOSE ORGAN – BROWN, BEIGE, AND WHITE ADIPOSE TISSUE

Historically, adipose tissue (AT) was not regarded as a metabolically active organ. Instead, it was considered to be merely an inert energy storage and connective tissue, with the primary function of insulating organs. After decades of research, it is evident that adipose tissue plays a pivotal role in energy homeostasis. It is an endocrine organ that utilizes glucose, and it releases and stores lipids *(Ottaviani et al. 2011)*. It is characterized by a highly unstructured and heterogeneous organization, comprising not only adipocytes but also a variety of other cell types, including pre-adipocytes and other precursor cells, stem cells, immune cells, vascular cells, mesothelial cells, and fibroblasts *(Emont et al. 2023; Schwalie et al. 2018; Cristancho und Lazar 2011)*. Each white adipocyte displays a single large lipid droplet (unilocular), which serves to store lipids in the form of triacylglycerol (TAG). The accumulation of lipids results in adipocyte hypertrophy and/or adipocyte hyperplasia, which ultimately leads to obesity *(Vishvanath und Gupta 2019)*. The adipose tissue depots of mammals are diverse, varying in composition, size, location, and function. In addition to numerous white adipose tissue (WAT) depots, primarily situated around blood vessels and organs within the abdominal cavity and subcutaneously, brown adipose tissue (BAT) represents another major adipose tissue depot *(Koenen et al. 2021)*. Until the late 2000s, it was believed that metabolically relevant BAT is not found in adult humans, but solely in infants and small rodents *(Cypess et al. 2009; Trayhurn 2022)*. The advent of technological innovations, such as computed tomography (CT) in conjunction with ^{18}fluoro-2-deoxyglucose positron emission tomography (18F-FDG-PET), has led to a paradigm shift in this field of study *(Cypess et al. 2009; van Marken Lichtenbelt et al. 2009; Virtanen et al. 2009)*. The area of BAT decreases with age, with approximately 4.3% of all AT depots in adult humans comprising BAT. It can be found in axillary, supraclavicular, cervical, mediastinal, paraspinal, and abdominal regions *(Leitner et al. 2017; Virtanen et al. 2009)*. Newborns as well as rodents possess an additional depot, interscapular BAT (iBAT) *(Lidell et al. 2013)*. In large contrast to white adipocytes, brown adipocytes display multilocular lipid droplets, higher vascularization and sympathetic innervation, and a large

number of mitochondria rich in cristae *(Koenen et al. 2021; Cinti 2012)*. Cristae serve to enlarge the inner mitochondrial membranes (IMM), which express the uncoupling protein 1 (UCP1) *(Klaus et al. 1991)*. Approximately two decades ago, Himms-Hagen and colleagues *(Himms-Hagen et al. 2000)* first described a third type of adipose tissue in rats, beige or bright ("brown in white") adipose tissue, which attracted considerable attention in research on human beige adipose tissue. It is a particular type of WAT which can recruit brown-like (beige) adipocytes in response to certain stimuli, including β3-adrenergic ligands, norepinephrine released upon cold exposure, peroxisome proliferator-activated receptor gamma (PPARγ) agonists, exercise, and cachexia. This process of adipocyte conversion is typically referred to as "browning". In a manner comparable to brown adipocytes, beige adipocytes display a multilocular morphology and have a higher level of mitochondria and UCP1 compared to white adipocytes *(Yao et al. 2017; Ikeda et al. 2018; Ikeda und Yamada 2020; Stanford et al. 2015; Petruzzelli et al. 2014)*.

In contrary to WAT, the size and activity of BAT depots have been linked to an improvement in metabolic health, particularly in insulin sensitivity and the prevention of obesity by affecting the glucose and lipid metabolism *(Stanford et al. 2013; Nishio et al. 2012)*. This suggests that brown adipose tissue may represent a novel therapeutic target to combat metabolic dysfunctions. As evidenced by numerous studies on mice (e.g. cold exposure), one potential therapeutic approach is the use of β-adrenergic agonists. This hypothesis can be extrapolated to humans. For instance, patients with phaeochromocytoma (a tumor of the adrenal medulla) display increased UCP1 expression due to an overactivity of the sympathetic nervous system and high levels of circulating catecholamines *(Lean et al. 1986; Ricquier et al. 1982; English et al. 1973; MELICOW 1957; Bouillaud et al. 1984)*. Unfortunately, the direct use of β-adrenergic agonists in humans has not yielded convincing results to this date. Clinical trials utilizing the β3-adrenergic agonist CL-316,243 demonstrated inauspicious pharmacokinetics and poor oral bioavailability (Arch 2008), while another β3-adrenergic agonist (L-796568) was unable to sustain an increase in energy expenditure in 12 obese subjects beyond 28 days *(Larsen et al. 2002; van Baak et al. 2002)*. Aldosterone antagonists have been proposed as a potential therapeutic target for obesity and hypertension. Mineralocorticoids have been shown to inhibit UCP1 expression, which in turn inhibits the conversion of white to beige adipose tissue and thermogenesis within BAT *(van Baak et al. 2002)*. Nadal-Casellas et al. revealed that progesterone treatment is positively correlated with BAT differentiation and mitochondriogenesis, as evidenced by increased gene expression of PPARγ *(Rodríguez-Cuenca et al. 2007)*. In contrast, testosterone decreased norepinephrine-induced expression of UCP1 in rodents, which was rescued by the androgen receptor antagonist flutamide *(Rodriguez et al. 2002)*. This indicates that sex hormones represent promising therapeutic targets, in line with Aaron Cypess' findings that females exhibit increased ^{18}F-FDG uptake activity using PET-CT scans, and a higher mass of brown adipose tissue compared to males *(Cypess et al. 2009)*. BAT is one of the most efficient tissues with respect to insulin-mediated glucose uptake and utilization, as evidenced by the elevation of GLUT4 expression *(Reddy et al. 2014)*. This finding has been corroborated by numerous authors who have demonstrated that metformin, a biguanide derivative used to treat type 2 diabetes mellitus (T2DM), increases BAT activity, thereby preventing weight gain *(Liang et al. 2016; Breining et al. 2018; Karise et al. 2019; Tokubuchi et al. 2017)*. It is noteworthy that Li et al. identified a correlation between BAT and diet, with the gut hormone secretin mediating a gut-BAT-Brain axis which promotes meal-induced thermogenesis and thereby, satiation *(Li et al. 2018)*. Despite of these findings, numerous studies have yielded conflicting results, suggesting a broad spectrum of possibilities for improving BAT activity. Consequently, there is a pressing need for further

research to elucidate the fundamental mechanism underlying the improvement of BAT thermogenesis and browning.

1.3 Oxidative phosphorylation in the light of UCP_1 uncoupling and non-shivering thermogenesis

A major function of mitochondria is the oxidative phosphorylation (OXPHOS). This process involves the transfer of electrons from electron donors to electron acceptors, such as oxygen, in a series of redox reactions. These reactions result in the liberation of energy, which is subsequently used to facilitate the transfer of protons across the mitochondrial inner membrane. OXPHOS consists of five distinct complexes: NADH-ubiquinone oxidoreductase (Complex I), succinate-ubiquinone oxidoreductase (Complex II), ubiquinol-cytochrome c oxidoreductase (Complex III), cytochrome c oxidase (Complex IV) and ATP-synthase (Complex V). The electron transport chain (ETC; Complex I-IV) facilitates the transfer of electrons from donors (NADH, $FADH_2$/succinate) derived from fatty acid (FA) oxidation and the tricarboxylic acid cycle (TCA) to oxygen, thereby generating a proton gradient in the intermembrane space. Eventually, Complex V dissipates the proton gradient by transporting protons back into the mitochondrial matrix, thereby phosphorylating adenosine diphosphate (ADP) to adenosine triphosphate (ATP) *(Xu et al. 2020)*.

In recent years, an increasing number of studies have indicated that BAT thermogenesis may be mediated by UCP1-independent pathways. A futile ATP-consuming fatty acid/triglyceride cycle that is independent of UCP1 has recently been discovered in knockout mice *(Oeckl et al. 2022)*. Furthermore, Ca^{2+}- and creatine-substrate-cycling have been proposed as alternative UCP1-independent pathways for thermogenesis in brown and beige fat. Creatine-substrate cycling has been described as an adaptive thermogenesis pathway, as evidenced by the observation that a reduction in creatin levels, for instance, through the selective deletion of creatine-synthase rate-limiting enzyme glycine amidino transferase (GATM), induced mild cold intolerance in murine beige AT *(Kazak et al. 2017)*. Ca^{2+}-cycling was discovered as UCP1 independent thermogenic mechanism in BAT through the activity of sarcolipin (SLN), which is a peptide-binding sarco-endoplasmic reticulum ATPase (SERCA). The surgical removal of iBAT in SLN knockout mice resulted in a reduction in their ability to tolerate cold temperatures. The maintenance of shivering thermogenesis in skeletal muscle indicates the existence of a non-shivering thermogenesis (NST) inducing ATP-turnover independent of ATPase activity via calcium cycling *(Bal et al. 2012)*. In beige adipocytes, the knockout of SERCA2 demonstrates the generation of heat via ATP-dependent Ca^{2+}- cycling in the absence of UCP1 *(Ikeda und Yamada 2020)*. Even though these considerations of UCP1-independent NST are valid, it is more commonly accepted that the primary function of brown and beige adipocytes is to protect mammals from hypothermia in a UCP1-dependent manner. This hypothesis is advocated by the observation that UCP1 knockout mice exposed to cold, develop hypothermia and are incapable in defending their body temperature *(Enerbäck et al. 1997)*.

The question remains as to how UCP1 mediates non-shivering thermogenesis in brown and beige adipocytes. UCP1 acts to uncouple ATP synthase from the electron transport chain, thereby generating energy in the form of heat instead of ATP *(Klaus et al. 1991)*. UCP1 is a 32 kDa sized protein that is localized to the inner mitochondrial membrane. It is widely accepted that UCP1 is competitively inhibited by purine nucleotides such as guanosine diphosphate (GDP) and fueled by free fatty acids

(FFA) released from adrenergic-induced lipid droplet lipolysis *(Ikeda und Yamada 2020; Hagen und Lowell 2000)*. β-adrenergic agonists, such as norepinephrine, induce lipid droplet lipolysis, making them highly relevant for UCP1 regulatory mechanisms. In humans, the predominant form of β-adrenoreceptors is β1 and β2 *(Riis-Vestergaard et al. 2020; Blondin et al. 2020)*, whereas in rodents it is β3 *(Zhao et al. 1994)*. The most prominent strategy to induce UCP1 activity is lipolysis, which is stimulated by the sympathetic nervous system (SNS) via cold exposure. Prior to adrenergic stimulation, the lipid droplet-associated protein 1 (PLIN1) serves to sequester the coactivator of adipose triglyceride lipase (ATGL), named the comparative gene identification-58 (CGI-58) *(Clark et al. 2020)*. Following the binding of adrenergic agonists to their respective G-protein coupled receptors, adenylate cyclase (AC) is activated. This results in an elevation of the concentration of cyclic adenosine monophosphate (cAMP), which in turn stimulates the protein kinase A (PKA). This kinase eventually phosphorylates PLIN1, resulting in the release of CGI-58, and subsequent binding to ATGL. Subsequently, ATGL catalyzes the hydrolysis of TAG to diacylglycerol (DAG). PKA further phosphorylates hormone sensitive lipase (HSL), resulting in its relocation to the lipid droplet surface. There, it interacts with PLIN1, inducing the degradation of DAG to monoacylglycerol (MAG) via the action of monoacylglycerol lipase (MGL). The in this pathway released FFA can fuel both, ß-oxidation (and thereby OXPHOS) as well as UCP1 *(Girousse und Langin 2012; Langin 2006; Lass et al. 2006; Arner und Langin 2014; Strålfors et al. 1984)*. Although the PKA cascade represents the primary mechanism of lipid droplet lipolysis, PLIN1 and HSL can also be phosphorylated by alternative protein kinases. Protein kinase G (PKG), which is activated by guanyl cyclase (GC), mediates the release of cyclic guanosine monophosphate (cGMP) upon the binding of atrial natriuretic peptides *(Carper et al. 2020)*, and ERK 1/2, which is functioning via the mitogen-activated protein kinase (MAPK) pathway in response to growth factors, mitogens and cytokine signaling *(Greenberg et al. 2001)*.

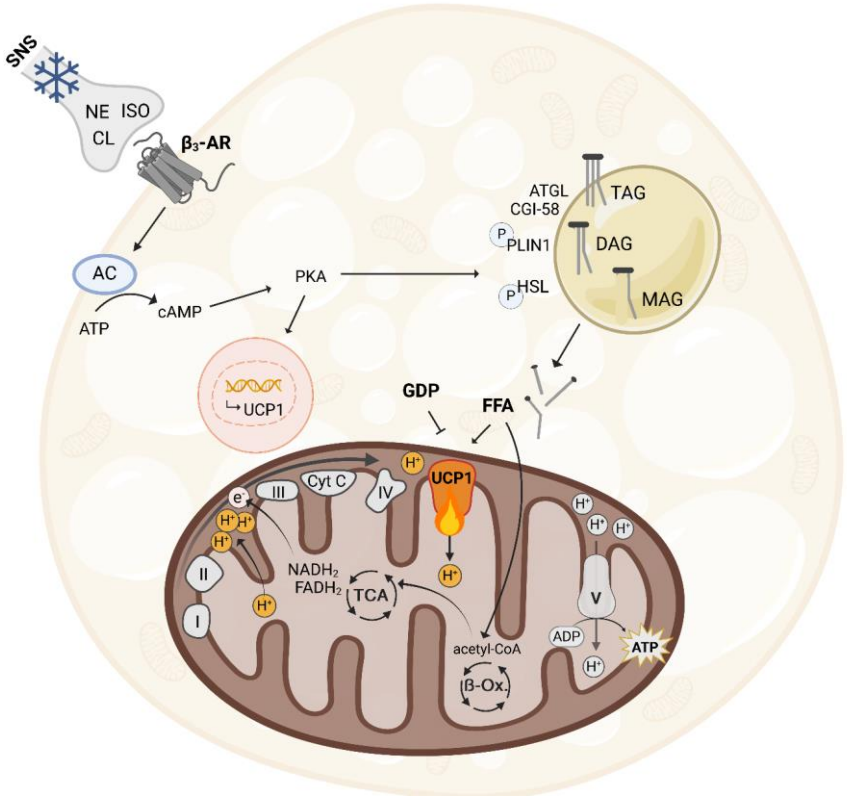

Figure 1: Schematic overview of UCP1 regulatory cascades upon β-adrenergic stimulation in brown and beige adipocytes. *After binding of β-adrenergic agonists released from the sympathetic nervous system (SNS), adenylyl cyclase (AC) is activated, which catalyses the generation of cAMP from ATP. cAMP, in turn, promotes the PKA-mediated transcriptional regulation of UCP1 expression as well as the phosphorylation of PLIN1 and hormone-sensitive lipase, eventually enabling ATGL and HSL-driven hydrolysis of TAG to DAG and MAG, respectively. Consequently, released FFAs are transported into mitochondria, where they either fuel β-oxidation, which ultimately promotes OXPHOS, or activate UCP1, which uncouples the electron transport chain from ATP synthesis, thereby generating heat. Modified from (Klingenspor et al. 2017; Kornmann et al. 2009; Bal et al. 2012; Adam 2016; Kornmann et al. 2009).*

Theories regarding the activation of UCP1 by lipolysis-released fatty acids include the following: (1) UCP1 operates as an OH^- uniporter, binding fatty acids allosterically *(Nicholls 2006)*. (2) Upon allosteric binding of FA, UCP1 functions as H^+ uniporter, transporting protons into the mitochondrial matrix *(Rial und González-Barroso 2001; Cannon und Nedergaard 2004; Shabalina et al. 2004)*. (3) UCP1 functions as a long chain fatty acid (LCFA; < 16 carbons)/H^+ symporter. LCFA establish hydrophobic interactions that prevent their dissociation from UCP1, thereby inducing a conformational change which turns UCP1 into a proton carrier into the mitochondrial matrix *(Fedorenko et al. 2012)*. (4) UCP1 protonates carboxylate groups delivered by direct fatty acid binding and carries them into the mitochondrial matrix (H^+-buffering model) *(Klingenberg und Huang 1999)*. (5) UCP1 facilitates the transport of deprotonated fatty acids from the matrix to the intermembrane space, thereby providing anions that can be protonated and flip-flop through lipid bilayers back into the matrix (fatty acid cycling model) *(Garlid et al. 1998)*.

Despite a considerable body of research investigating the induction of UCP1 via FFA released from lipid droplet lipolysis in BAT, the precise mechanism by which UCP1 is initiated remains unclear *(Cannon und Nedergaard 2017)*. For instance, Schreiber et al. and Shin et al. demonstrated that UCP1-mediated NST does not necessarily require intracellular lipid droplet lipolysis in BAT. This was evidenced by the observation that a conditional knockout of ATGL and/or CGI-58 in BAT did not impair cold-induced NST or the β3 -adrenergic thermogenic response in general *(Schreiber et al. 2017)*. The researchers revealed that circulating fatty acids originating from WAT lipid droplet lipolysis or diet can compensate for the loss of lipolysis in brown adipose tissue. In mice lacking CGI-58 it was found that the utilization of circulating substrates was increased, for example, through elevated expression of the glucose transporter GLUT1. Furthermore, these mice displayed a higher capacity for browning of white adipose tissue. Schreiber and colleagues propose that adequate cardiac function and the supply of circulating substrates are the primary causes of cold intolerance in mice with a whole-body ATGL knockout *(Schreiber et al. 2017; Shin et al. 2017; Schreiber et al. 2017)*. Moreover, it has been proposed that intracellular FA in brown adipose tissue may derive from alternative pathways to lipid droplet lipolysis, including the action of Ca^{2+}-independent phospholipase A2, as suggested by patch-clamp analysis on BAT mitoplasts *(Fedorenko et al. 2012)*. It is noteworthy that Nedergaard and Cannon speculate that not even circulating FA are required for NST, but that there is a hitherto unidentified direct activator of UCP1, which is released upon β-receptor activation *(Cannon und Nedergaard 2017)*.

This dissertation examines the mitochondrial membrane lipid composition as a potential and critical modulator of UCP1-mediated NST. This encompasses the ratio of glycerophospholipids (GPL) and free cholesterol (FC), as well as the role of phosphatidylserine decarboxylase (PISD) on modulating the GPL, specifically the levels of phosphatidylethanolamine (PE), within the mitochondria.

1.4 THE UNIQUE STRUCTURE OF MITOCHONDRIA AND THEIR MEMBRANES – NOT JUST THE POWERHOUSE OF THE CELL

In-depth investigation into mitochondria is of paramount importance, as mitochondrial dysfunction plays a significant role in the aetiology of several disorders, including metabolic and neurodegenerative diseases. Comparable to all biological membranes, mitochondrial membranes are built of a bilayer consisting of common membrane lipids with both a hydrophilic and a hydrophobic component, pierced with membrane proteins. Lipid bilayers are organized in a way that the polar component faces the aqueous phase, whereas the non-polar components interact with each other to form a hydrophobic interior, which serves as a barrier preventing the exchange of polar solutes and ions *(Kobayashi und Menon 2018; Singer und Nicolson 1972)*. Although membranes are spontaneously formed due to the self-association of hydrophobic moieties, which is entropically driven by water, the lipid composition of membranes is non-random and asymmetric. This is a prerequisite for cell physiology and autonomous function *(van Meer et al. 2008)*. For example, phosphatidylserine (PS) is situated within the inner leaflet of the plasma membrane to serve as a co-factor for membrane-bound enzymes, such as the Na^+/K^+-ATPase and protein kinase C (PKC). However, during apoptosis, PS is redistributed to the cell surface, functioning as a recognition signal for phagocytes *(Fadeel und Xue 2009; Fadok et al. 1998)*. Consequently, cells must invest a considerable amount of energy to maintain transbilayer lipid asymmetry *(Zwaal und Schroit 1997)*.

In addition to transmembrane lipid asymmetry, mitochondria present an inimitable structure, prompting the question of the underlying reason *(van Meer et al. 2008)*. Mitochondria are responsible for the generation of over 80% of cellular energy *(Nicolson et al. 2021)*. Nonetheless, the prevailing paradigm of mitochondria as solely a “powerhouse of the cell” is obsolete, as these organelles are involved in coordinating a multitude of cellular functions beyond ATP synthesis: Stem cell maintenance and differentiation *(Khacho et al. 2016)*, migration, metabolism (Giacomello et al. 2020), innate immune responses, inflammation *(Yasukawa et al. 2009)*, senescence (Herranz und Gil 2016; Chapman et al. 2019), as well as autophagy *(Gomes et al. 2011)* and eventually cell death *(Scorrano et al. 2002; Frank et al. 2001)*. Therefore, mitochondria orchestrate intricate cell signaling events, necessitating a perpetual reorganization of cellular mitochondrial networks through organelle fission/division, fusion, and ultrastructural membrane remodeling. These processes are collectively referred to as mitochondrial membrane dynamics *(Giacomello et al. 2020)*. The multiplicity of mitochondrial functions is enabled by its unique structure.

In contrast to other cellular organelles, mitochondria consist of two membranes surrounding the intermembrane space (IMS), the IMM and the outer mitochondrial membrane (OMM). These membranes display completely different tasks and compositions. The OMM provides membrane contact sites with other organelles, including lipid droplets, ER, peroxisomes, lysosomes, nuclei, the Golgi apparatus, melanosomes, endosomes, and plasma membranes *(Lackner 2019)*. As it is permeable for all molecules smaller than approximately 6,000 Dalton, the OMM functions as a diffusion barrier and is the part of the organelle that functions as platform for cell signaling processes *(Gellerich et al. 2000; Tait und Green 2012)*. In contrast, The IMM is further subdivided into two distinct compartments: Cristae and the inner boundary membrane (IBM). The cristae present invaginations of the IMM, which serves to magnify its surface area and host the bulk of ATP-synthase and respiratory chain complexes for oxidative phosphorylation. The surface area is directly proportional to the abundances of complex I-V and their proportion relative to the IMS, matrix and the overall size of mitochondria, thereby

determining OXPHOS efficiency *(Afzal et al. 2021)*. Cristae junctions are narrow clefts connecting cristae to the IBM to avoid the release of cristae contents into the IMS. The IBM mainly harbors channel transporters to shuttle ADP and ATP, small metabolites, and ions, between the mitochondrial matrix and the cytoplasm. The matrix is the innermost mitochondrial compartment, where processes such as DNA replication, protein biosynthesis and the TCA are located *(Giacomello et al. 2020)*.

The lipid composition of a biological membrane is organ-specific, conserved on the cellular and even on the subcellular/organelle level. Mitochondrial membranes are primarily composed of lipids belonging to the glycerophospholipid (GPL) category, although glycerolipids (GL), sphingolipids (SL), and sterols are also present. GPL is a collective term for phosphatidylcholine (PC), and its lyso- and ether-glycerophospholipid derivates, lysophosphatidylcholine (LPC) and PC plasmalogen (PC P), respectively. In addition to the aforementioned glycerophospholipids, phosphatidylethanolamine (PE) and its lyso- and ether-glycerophospholipids lysophosphatidylethanolamine (LPE) and PE plasmalogen (PE P), phosphatidylserine (PS), phosphatidylinositol (PI), phosphatidic acid (PA) and cardiolipin (CL) are also present. Glycerolipids include triacylglycerol (TAG) and diacylglycerol (DAG). Sphingolipids encompass sphingomyelin (SM), ceramide (Cer), and hexosylceramide (HexCer). The major sterols include free cholesterol (FC) and cholesteryl ester (CE) *(Casares et al. 2019)*. The principal lipid classes present in mitochondrial membranes are the GPLs PC and PE, whereas the portion of free cholesterol is relatively low. FC has a planar structure that intercalates between phospholipid chains, thereby promoting the transition from a fluid to a more solid gel phase, which is reflected in an increase in viscosity. Thus, the GPL/FC ratio represents a pivotal parameter for lipid packing density and fluidity of membranes. In organelles, this ratio typically ranges from 1.0 (~50% FC) in plasma membranes to 9.0 (~10% FC) in mitochondria *(van Meer et al. 2008; Ernst et al. 2016)*. The saturation of fatty acids esterified to the sn-1 and sn-2 position of GPLs affects the lipid packing density and fluidity of the membranes in which they are located. The greater the proportion of mono- and polyunsaturated fatty acids present in glycerophospholipids, the greater the membrane fluidity is (Ernst et al. 2016). The composition of cellular and mitochondrial lipids is not only essential for its functions, but also for maintaining health. For example, the inhibition of PC *de novo* synthesis (and with that its contents) in the liver has been linked to an impairment of very-low density lipoprotein (VLDL) secretion and fatty liver disease. Further, the mitochondrial PC/PE ratio affects mammalian energy production *(van der Veen et al. 2017)*.

The lipidome of murine brown, beige and white adipocytes exhibits substantial differences. Using direct infusion electrospray ionization coupled to tandem mass spectrometry (ESI-MS/MS), Schweizer et al. demonstrated striking differences between *ex vivo* differentiated primary brown and beige adipocytes to white adipocytes. White adipocytes composed the highest portion of PS, PE P, Cer and SM. Brown and beige adipocytes displayed more PE and PC with shorter fatty acyl chains, while white adipocytes comprised longer and more polyunsaturated fatty acids within the respective phospholipids. In accordance with the observed differences in mitochondrial mass, brown adipocytes exhibited the highest level in cardiolipin, followed by beige and subsequently white adipocytes. Of particular interest for our study, the analyzed lipidome resulted in higher GPL/FC ratios in brown and beige adipocytes compared to white adipocytes. Additionally, β-adrenergic stimulation of brown adipocytes resulted in elevated *de novo* synthesis of PC species (stable isotope labelling), while housing at different temperatures (4°C, 23°C, 30°C) demonstrated a correlation between the ceramide

composition and the degree of browning, indicating a potential link between the adipocyte lipidome and BAT activity *(Schweizer et al. 2019)*.

1.5 THE METABOLISM OF GLYCEROPHOSPHOLIPIDS AND FREE CHOLESTEROL

More than eight decades ago, the German scientists Konrad Emil Bloch and Feodor Lynen elucidated the intricate network of over 30 reactions involved in cholesterol biosynthesis, starting with acetyl coenzyme A (acetyl-CoA) *(Kennedy und Westheimer 1964)*. Most importantly, 3-hydroxy-3-methylglutaryl coenzyme A (HMG-CoA) is reduced to mevalonate via HMG-CoA reductase (HMGCR) as a rate-limiting step *(Duan et al. 2022)*. The synthesis of cholesterol is one of the most tightly regulated pathways in mammalian metabolism, with a feedback inhibitory loop initiated by FC itself. In brief, when cellular cholesterol levels are insufficient, sterol regulatory element binding protein (SREBP) is released from SREBP cleavage-activating protein (SCAP), an intracellular cholesterol sensor. In turn, SREBP binds to the sterol regulatory element (SRE) located in the promoter of HMGCR, thereby inducing the HMGCR transcription. Consequently, as this pathway is accelerating cholesterol biosynthesis, a reduction in SREBP is decelerating it *(Brown und Goldstein 2009)*.

The major glycerophospholipids PC and PE are *de novo* synthesized in the Kennedy pathway, which is localized in the endoplasmic reticulum. As depicted in **Figure 2**, choline kinase (CK) and ethanolamine kinase (EK) phosphorylate choline and ethanolamine, respectively, upon the utilization of ATP. Subsequently, pyrophosphate is released from phosphocholine and phosphoethanolamine through an exchange with the energy-rich molecule cytidine triphosphate (CTP), generating cytidine di-phosphocholine (CDP-choline) via CTP: phosphocholine cytidyltransferase (CCT) and cytidine di-phosphoethanolamine (CDP-ethanolamine) via CTP: phosphoethanolamine cytidyltransferase (ECT). Eventually, PC and PE are generated through the transfer of phosphocholine and phosphoethanolamine onto DAG (which is generated from PA dephosphorylation), releasing cytidine monophosphate (CMP). This is catalyzed by choline and ethanolamine transferases, DAG:CDP-choline choline phosphotransferase (CPT) and DAG:CDP-ethanolamine ethanolamine phosphotransferase (EPT), respectively *(Gibellini und Smith 2010)*. Additionally, PE can be converted into PC via methylation, which is enabled by phosphatidylethanolamine N-methyltransferase (PEMT). This reaction is predominantly known to occur in hepatocytes, accounting for approximately 30% of hepatic PC synthesis *(Vance 2014)*. PEMT was also identified to be expressed in adipocytes, initially described by Laura Cole and Dennis Vance for 3T3-L1 adipocytes *(Cole und Vance 2010)*, where it supports the biosynthesis and stabilization of lipid droplets *(Hörl et al. 2011)*. Notably, a global knockout of PEMT in mice caused a complete loss of UCP1 protein in brown adipose tissue, leading to cold intolerance in animals fed either chow or a high fat diet (HFD). As this was not observed in a conditional knockout of PEMT in UCP1-expressing cells, it is likely that UCP1 suppression in BAT is induced upon inter-organ communication with tissues not expressing UCP1 *(Johnson et al. 2020)*. Phosphatidylserine can be synthesized through a head group exchange with either PC or PE. This is catalyzed by phosphatidylserine synthase 1 (PSS1; PC) and phosphatidylserine synthase 2 (PSS2; PE), which are mainly located in the ER and mitochondria-associated membranes (MAM) *(Arikketh et al. 2008)*. Within mitochondria, PS is decarboxylated to PE via phosphatidylserine decarboxylase activity (PISD) *(Zborowski et al. 1983; Percy et al. 1983; Vance und Tasseva 2013)*. In the CDP-DAG pathway, CDP-DAG is generated from PA via CDP-DAG synthase (CDS) activity and serves as a substrate for the synthesis of PI and PG. PG, in turn, serves as a substrate for cardiolipin synthesis, utilizing cardiolipin synthase

(CLS) *(Jennings und Epand 2020)*. Furthermore, the so-called Land's cycle mediates glycerophospholipid turnover. Phospholipase activity (PLA_1, PLA_2) catalyzes the enzymatic deacylation of PE and PC at the sn-2 position, resulting in the formation of lysophospholipids (LPE and LPC). Conversely, they can be reacylated by lysophospholipid acyltransferases (LPLAT), including LPCAT and LPEAT *(Ståhl et al. 2008; D'Arrigo und Servi 2010)*.

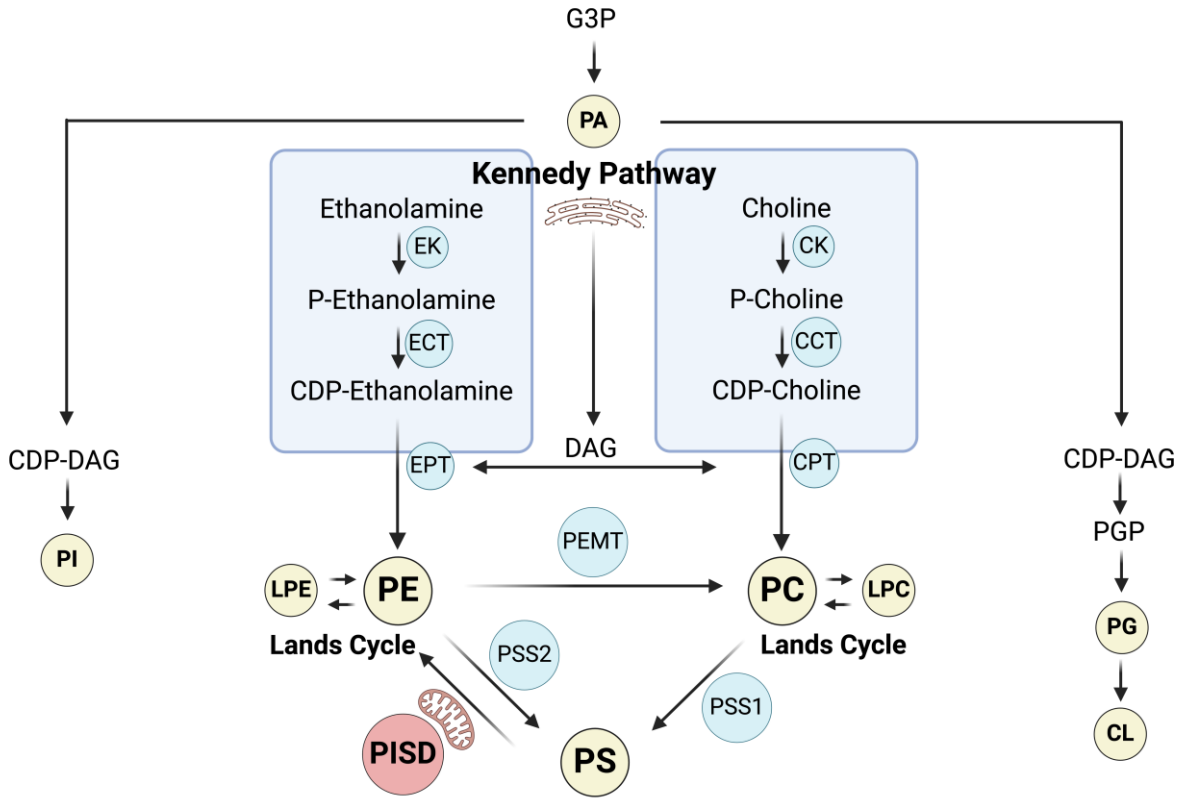

Figure 2: Schematic overview of phospholipid synthesis pathways in mammalian cells.

1.6 THE CURRENT UNDERSTANDING OF THE COMPLEXITY IN MITOCHONDRIAL LIPID TRAFFICKING

To facilitate mitochondrial functions such as an efficient distribution of mitochondria-deriving metabolites, the mitochondrial structure is constantly reshaped during fission and fusion events *(Chan 2012)*. This highly dynamic behavior necessitates continuous membrane remodeling to maintain a distinct distribution of proteins and lipids in the mitochondrial outer and inner membranes. Although mitochondrial proteostasis is well understood *(Baker et al. 2011)*, there are significant knowledge gaps regarding the maintenance of the lipid complement, given the vast and diverse repertoire of mitochondrial lipids. The major portion of lipids is synthesized within the endoplasmic reticulum, necessitating extensive lipid exchange between the ER and OMM as well as between OMM and the IMM *(Tatsuta et al. 2014; Yang et al. 2021)*. Due to the hydrophobic characteristics of the majority of phospholipids, spontaneous diffusion across aqueous phases is not sufficient to meet the demands of mitochondrial dynamics. Hence, more sophisticated transportation mechanisms, such as vesicle transport cascades, close membrane contacts, lipid transfer proteins, tethering complexes, or the direct reduction in hydrophobicity (i.e. the addition of hydrophilic moieties, removal/exchange of acyl chains), are required *(Tatsuta et al. 2014)*.

Membrane contact sides are of particular interest as they are assumed to substantially facilitate the lipid exchange between mitochondria and other organelles. The most prominent junction between mitochondria and endoplasmic reticula is the mitochondria-associated membrane (MAM), which has a thickness of approximately 10-50 nm. MAM is part of the ER network and in direct proximity to the OMM, mainly to maintain lipid and Ca^{2+} homeostasis *(Vance 1990; Flis und Daum 2013; Giacomello und Pellegrini 2016; Kornmann 2013; Szymański et al. 2017)*.

Cardiolipin represents an exception in mitochondrial lipid trafficking, as it is known as mitochondria-specific phospholipid that is exclusively synthesized on the matrix side of mitochondrial inner membranes, with phosphatidylglycerol (PG) serving as a substrate. Consequently, no extra-mitochondrial lipid exchange mechanism is known to be required. Nevertheless, cardiolipin is externalized from the IMM to the mitochondrial surface (via elusive mechanisms) due to its protein sorting function and its role as an “eat-me” signal for mitophagy *(Chu et al. 2013; Gebert et al. 2009; Zinser et al. 1991)*.

Mitochondrial PE synthesis via PISD represents the main source for mitochondrial PE. Nonetheless, mitochondrial PE can also originate from other (unknown) pathways and organelles, as evidenced by studies on HeLa-, CHO-K1- and MCA-RH 7777 (“McArdle”) cells using heavy isotope-labelled ethanolamine *(Bleijerveld et al. 2007; Kainu et al. 2013)*. It appears that PE generated in the CDP-ethanolamine pathway is limited in its access into mitochondria and is therefore unable to fully compensate for the lack of IMM-originating PE. However, exogenous LPE and LPE that has been acylated to PE in mitochondria-associated membranes (MAM) can be efficiently imported into mitochondria by so far unknown mechanisms and can therefore restore mitochondrial PE deficiencies *(Vance 2015; Riekhof und Voelker 2006; Joshi et al. 2012; Birner et al. 2001; Bürgermeister et al. 2004)*. PE synthesized by PISD activity can be exported from mitochondria, as it displays the major supplier of phosphatidylethanolamine to other organelles *(Voelker 1984)*. The underlying mechanism remains poorly understood. However, a study in yeast suggested that PE export is regulated by Ups1p and Ups2p, which are located in the intermembrane space rather than simple diffusion, and further, that Ups1p is required for the activity of the phosphatidylserine decarboxylase (Psd1p) *(Tamura et al. 2012)*. Interestingly, mitochondrial PE export heavily relies on environmental changes as it is regulated by ER stress *(Kannan et al. 2016)*.

The majority of PS synthase (PSS1 and PSS2) is localized to mitochondria-associated membranes. In the event that the donor membrane comprises a significant portion of PS, the import of PS into mitochondria is elevated. Mammalian cells labelled with [3H]-serine display a greater abundance of hydrophilic PE species containing [3H]-labels than their hydrophobic counterparts. This indicates that phosphatidylserine diffuses spontaneously into mitochondria *(Heikinheimo und Somerharju 1998; Vance 2015)*. This is further supported by a study which reported that the inhibition of phosphatidylserine decarboxylase with hydroxylamine causes the accumulation of PS in MAM compartments. However, it is not clear whether this accumulation is solely due to a reduced import of PS into mitochondria or whether the diffusion is bidirectional, with PS also transported back into MAM *(Shiao et al. 1995)*.

Given that PC and PI cannot be synthesized within mitochondria, it follows that they must be imported entirely from other organelles. During the import process, both phospholipids can be observed within mitochondrial contact sites. However, the detailed mechanisms involved remain poorly understood

(Lampl et al. 1994). The steroidogenic acute regulatory protein (StAR)- related lipid transfer domain proteins STARD2 and STARD7 were identified as intracellular phospholipid binding proteins that can particularly mediate the transport of PC between the cytosol and mitochondrial outer membranes (in both directions) *(Dolis et al. 1996; Horibata et al. 2016; Yang et al. 2017)*.

Similarly to PC, mitochondrial cholesterol import is mainly regulated by protein members of the StAR-family. In particular, in the IMM of steroidogenic cells, cholesterol levels are very low, which enables the regulation of steroidogenesis depending on the rate of cholesterol import as a rate-limiting step. The StAR- family comprises 15 proteins with diverse functions and lipid binding characteristics. Of these, STARD1, STARD3, STARD4, and to some extent also STARD5 and STARD6 are known to bind sterols. STARD1 is primarily responsible for importing cholesterol into mitochondria from the endoplasmic reticulum/MAM contact sites. In contrast, STARD3 is mainly involved in the transfer from late endosomes, while STARD4 (as well as STARD1) mediates the import from cytosol. It is postulated that StAR proteins function as multiprotein complexes in cooperation with the ATPase family AAA domain-containing protein 3 (ATAD3), the translocator protein (TSPO) and the voltage-dependent anion channel (VDAC) *(Elustondo et al. 2017)*.

1.7 Phosphatidylserine decarboxylase – A key enzyme in mitochondrial phospholipid metabolism

Phosphatidylserine decarboxylase (PISD) is an integral membrane protein in the mammalian IMM, with a size of 46,672 Da/409 amino acids (according to typical databases such as UniProt and Gene Cards). It catalyzes the decarboxylation of phosphatidylserine to phosphatidylethanolamine *(Voelker 1997)* (**Figure 2**). To date, PISD is believed to be the primary source of mitochondrial PE, as other underlying mechanisms of mitochondrial PE synthesis or transport mechanisms from other organelles to mitochondria (after *de novo* synthesis by PTDSS1/2 in ER/MAM) remain poorly understood. The enzyme is a heterodimer consisting of a membrane-spanning element, an autocatalytic proteolysis site generating pyruvoyl-containing α- subunits and a large membrane-associated β- subunit, in addition to a mitochondrion-targeting signal that is canonical and amino-terminal cleaved. The pyruvoyl group functions as a proton acceptor, eventually facilitating the removal of the carboxyl group of PS *(Sam et al. 2021; Li und Dowhan 1988; Kuge et al. 1991; Chacinska et al. 2009; Clancey et al. 1993; Trotter et al. 1993)*.

The whole-body knockout of PISD in mice results in embryonic lethality between days 8 and 10 of the development, alongside with extensive mitochondrial misshape and fragmentation. This shows that the PISD pathway in mitochondria is essential for normal development *(Steenbergen et al. 2005; Fujimoto et al. 1988)*. In humans, PISD is considered a novel mitochondrial disease gene, as fibroblasts of patients with variants in the PISD gene display enlarged lysosomes, fragmented mitochondrial networks, and a decrease in maximal oxygen consumption. This can cause the development of diseases such as skeletal dysplasia, white matter changes and the vision disorder cataracts *(Zhao et al. 2019)*.

Despite the fact that PISD is commonly known as an enzyme that is uniquely expressed in mitochondria, it was recently discovered that PISD is also present in other organelles. For instance, PISD can localize to lipid droplets through alternative splicing of its pre-mRNA (PISD-LD). It is noteworthy that the targeting of PISD is subject to regulation by nutritional state. RNAi-mediated

inhibition of PISD and PISD-LD results in a suppression of TAG storage in cells when grown in high lipid conditions *(Kumar et al. 2021)*. In yeast, mitochondrial targeting was observed to be preferred when grown on glucose, whereas elevated ER targeting was observed when grown on fermentable carbon sources. This suggests that there is a reduced mitochondrial targeting of PISD when cell growth requires cellular respiration *(Friedman et al. 2018)*.

PISD might not only be involved in lipid metabolism but also in the (negative) regulation of energy consumption in brown adipose tissue. As demonstrated in a brown adipocyte knockout mouse line, PGAM5, which is a mitochondria-resident phosphatase, suppresses the expression of UCP1 and CL-316,243 (β3-adrenergic agonist)-mediated respiration. This results in a reduced accumulation of lipids in iBAT and even in high fat diet resistance. Most importantly, these effects not only necessitate the phosphatase activity of PGAM5, but also its intramembrane cleavage, which is regulated by PISD *(Sugawara et al. 2020)*.

1.8 BAT AND ITS ROLE IN WHOLE-BODY METABOLISM – BAT-LIVER CROSSTALK

In the last years, several scientists have proposed a negative correlation between brown adipose tissue activity and non-alcoholic fatty liver disease (NAFLD), which is mediated through liver-(brown) adipose tissue crosstalk *(Wang et al. 2014; Ahmed et al. 2021; Liu et al. 2013; Giles et al. 2017; Shen et al. 2019)*. As illustrated in **Figure 3**, NAFLD is defined as a cluster of conditions in which lipids accumulate in hepatocytes, frequently occurring in conjunction with other metabolic conditions such as obesity, dyslipidemia, insulin resistance or hypertension. A new terminology has recently been proposed to more accurately reflect the underlying origins of the disease. This new terminology better reflects the bidirectional interplay between (extrahepatic) metabolic alterations and fatty liver, independently from the consumption of alcohol and other reasons of liver disease. From this point forward, non-alcoholic fatty liver disease (NAFLD) will be referred to as metabolic-associated fatty liver disease (MAFLD) *(Pipitone et al. 2023)*. It encompasses a spectrum of pathologies, including simple steatosis (non-alcoholic fatty liver; NAFL), non-alcoholic steatohepatitis (NASH), which includes inflammation, and can progress to fibrosis, cirrhosis and even cancer, particularly hepatocellular carcinoma (HCC) *(Pouwels et al. 2022)*. UCP1 KO mice exhibit elevated plasma levels of ALT and AST, markers of liver damage, as well as a higher liver weight, which can be attributed to hepatocyte hypertrophy, fibrosis, and an elevated immune cell load *(Mills et al. 2021)*.

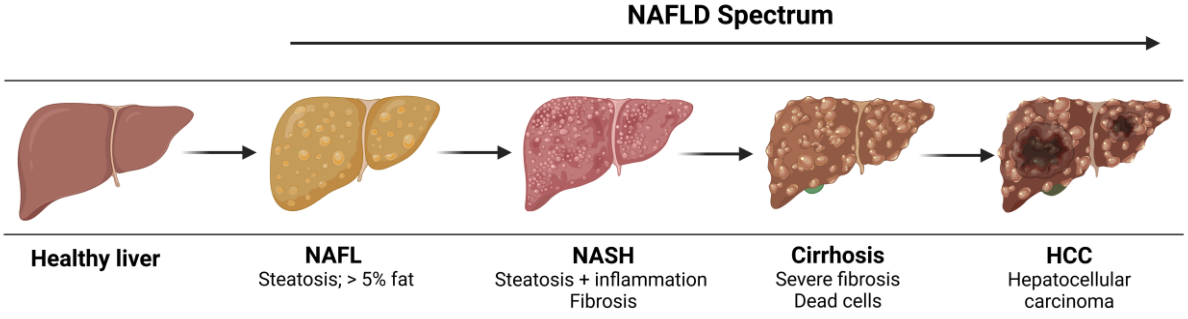

Figure 3: The progression of lipid accumulation, inflammation, and fibrosis within the non-alcoholic fatty liver disease (NAFLD) spectrum.

The potential for BAT activity to improve liver dysfunction is currently under investigation. Nevertheless, a plethora of hypotheses have already been proposed in the literature: Following the activation of BAT (e.g. via cold exposure), UCP1 is not only fueled by FFA derived from local lipid droplet lipolysis and circulating FFA originating from white adipose tissue lipolysis, but also by glucose-mediated *de novo* lipogenesis and triglyceride-rich lipoproteins (TRL) generated in the liver. As the thermogenic activity of brown adipose tissue is not restricted to local fuel sources but elevates the consumption of fatty acids and glucose from plasma/other tissues, BAT is meanwhile attributed a role in whole-body metabolism. For example, the clearance of plasma TAG by brown adipose tissue, particularly of very-low density lipoprotein (VLDL) remnants generated in the liver, is enabled by fatty acid translocase (CD36) and lipoprotein lipase (LPL) *(Bartelt et al. 2011; Berbée et al. 2015; Yang und Stanford 2022)*. LPL is regulated/inhibited via angiopoietin-like 4 (ANGPTL4), which is secreted, among other tissues, from the liver and adipose tissue. The abundance of ANGPTL4 is dependent on the nutritional state, with an increase observed following fasting and a decrease following feeding. This is mediated by the action of nuclear receptor PPARγ (adipose tissue) and the glucocorticoid receptor (liver). The deletion of ANGPTL4 in BAT has been demonstrated to elevate the catabolism of VLDL and subsequently increase fatty acid uptake, thereby improving thermogenesis *(Kersten et al. 2000; Singh et al. 2018)*. A study in which BAT from male donor mice was transplanted into the visceral cavity of sex- and age-matched recipient mice demonstrated increased insulin sensitivity and glucose tolerance. The findings are consistent with the observation of a reduction in body and fat mass, as well as a full recovery of high fat diet induced insulin resistance. The transplantation of BAT additionally demonstrated a reduction in insulin, leptin, and cholesterol levels in the plasma, indicating an improved metabolic profile. Using labelled [3H]2-deoxyglucose in combination with either 20% glucose or saline, confirmed a connection of improved glucose homeostasis with a high glucose uptake in endogenous BAT and visceral WAT and heart, but not skeletal muscle, exerted by endocrine and/or paracrine effects such as increases in circulating norepinephrine and BAT-derived FGF21 and interleukin 6 (IL-6) levels (“batokines”) *(Stanford et al. 2013)*. The neurotransmitter norepinephrine, BAT-derived fibroblast growth factor FGF21 and interleukin 6 (IL-6) can increase GLUT1 (insulin-independent) and GLUT4 (insulin-dependent) expression and/or activity in brown and white adipose tissue. This explains the elevated glucose clearance observed in these tissues, as GLUT proteins act as glucose uniporters on plasma membranes *(Ge et al. 2011; Rotter et al. 2003; Ebeling et al. 1998; Shimizu et al. 1996; Bartelt et al. 2011)*. A substantial body of research indicates that the effects of batokines are mediated by a bi-directional communication with other tissues, particularly the liver. For example, FGF21 secretion from the liver increases glucose uptake in brown adipose tissue and browning of WAT, while IL-6 secretion from BAT enhances hepatic gluconeogenesis *(Emanuelli et al. 2014; Qing et al. 2020)*. Another intriguing endocrine pathway that connects UCP1 function in BAT and liver inflammation is the UCP1-succinate-SUCNR1 axis. Mice lacking UCP1 exhibit elevated levels of extracellular succinate in the liver, which binds to the succinate receptor 1 (SUCNR1) localized in stellate cells and macrophages, thereby inducing inflammation. In contrast, increasing the mass of brown and beige adipocytes (and thus UCP1) antagonizes this receptor ligation by highly sequestering succinate from the circulation, thereby fueling thermogenesis as succinate is a TCA cycle intermediate *(Mills et al. 2018; Mills et al. 2021)*.

1.9 OBJECTIVES OF THIS THESIS

The lipid species composition is conserved on the cellular and sub-cellular level, but to this date it is unclear whether organelle lipidomes differ between various tissues. Previous investigations on the cellular lipidome of brown, beige and white adipocytes revealed substantial differences in common membrane lipids *(Schweizer et al. 2019)*.

We asked whether this has a functional relevance for brown and beige adipose tissue. The main objective of this work was to study the mitochondrial lipid composition, particularly glycerophospholipids and free cholesterol, of brown adipose tissue, and elucidate its impact on UCP1 activity, both *in vitro* and *in vivo*. This included:

1. Investigations on the impact of experimentally altered GPL/FC ratios in brown adipocytes, brown adipose tissue, and thereof isolated mitochondria on UCP1 activity.
2. Generation of a tamoxifen-inducible conditional knockout mouse model of phosphatidylserine decarboxylase (PISD) in UCP1 expressing cells to modulate the mitochondrial lipid composition in an *in vivo* approach and characterization of PISD's physiological and pathophysiological relevance as well as its impact on UCP1 activity.

2 MATERIALS AND METHODS

2.1 ANIMALS

2.1.1 MOUSE HOUSING AND ETHICAL STATEMENT

All mouse experiments were performed according to the relevant ethical guidelines (German Animal Welfare Act). Breeding and experimental use of mice used for this study were approved by the local institution in charge (General Administration of the Free State of Bavaria, approval numbers: 55.2-1-54-2531-99-13-2015, 55.2-1-54-2532-17-2015, 55.2-1-54-2532-34-2016 and ROB-55.2-2532.Vet_02-19-193; Cantonal Ethics Committee of the Veterinary Office of the Canton of Zurich, approval number: ZH047/18).

All mice were bred either at the specific pathogen-free facility of the Technical University of Munich (ZIEL - Institute for Food & Health), or in the specific pathogen-free facility of the Federal Institute of Technology Zurich (EPIC/ETH Phenomics Centre). If not stated otherwise, mice were housed under controlled housing conditions in ventilated cages. In Freising (TUM), controlled conditions were defined as: Group-housing, 55% relative humidity, 23°C ambient temperature, 12h/12h light/dark cycle (light phase: 6 a.m. - 6 p.m.). In Zurich (ETH) controlled conditions were defined as: Group-housing, 40% relative humidity, 22°C ambient temperature, 12h/12h reversed light/dark cycle (light phase: 6 p.m. - 6 a.m. or 7 p.m. – 7 a.m.; winter/summertime, respectively). Mice had *ad libitum* access to water and food (either to chow, control, or high fat diet; see **Supplementary Table 2** for specific dietary composition). The health status of mice was controlled according to the FELASA guidelines, and they were regularly checked for pathogens.

For experiments analyzing PISD activity, the iBcKO-PISD mouse line was bred on a C57BL/6N genetic background. For *in vivo* experiments the conditional knockout in UCP1-expressing cells was induced using oral gavages of 2 mg/mouse 4-hydroxy-tamoxifen in sunflower oil on three consecutive days at the age of ten weeks. For long term housing (three months HFD), tamoxifen was refreshed using another oral gavage per month. For *ex vivo* experiments, the conditional knockout was induced at day four of adipocyte differentiation by treating cells with 2 µM 4-hydroxy-tamoxifen for 48 hours. In both cases, wildtype controls received the same tamoxifen treatment. For all other experiments wildtype mice of the 129SV/S6 background and homozygous UCP1 KO mice of the 129S1/SvImJ background were used.

2.1.2 GENERATION OF A CONDITIONAL KNOCKOUT MOUSE LINE

The iBcKO-PISD mouse line was generated at the Translational Nutrition Laboratory (ETH Zurich) in cooperation with Dr. Lucia Balazova. Briefly, the commercially available vector $PISD^{tm1a(EUCOMM)Wtsi}$ was injected into blastocytes collected from pregnant wildtype mice. Subsequently, embryos were implanted into female surrogates of the C57BL/6N strain to yield chimeric offspring. LoxP positive mice were crossed with a Flp -/- mouse line to eliminate the Flippase, LacZ and Neo cassette of the vector. Thereof resulting mice heterozygous for PISD were bred to generate mice homozygous for the conditional knockout of PISD (PISD fl/fl). Eventually, their offspring was bred with heterozygous $UCP1^{CreER}$ (Cre +/-) mice (obtained from Prof. Dr. Christian Wolfrum), expressing the tamoxifen-

inducible recombinase in UCP1-expressing cells to generate a BAT specific knockout *(Rosenwald et al. 2013)*.

2.1.3 GENOTYPING OF IBCKO-PISD MICE

To stabilize DNA integrity, murine ear punches were stored in nucleic acid preservation buffer until genomic DNA isolation. The tissue was digested by incubation at 1,000 rpm and 55°C for two hours within lysis buffer enriched in protein kinase K (**Table 1**).

Table 1: *Ear lysis buffer for digestion and DNA precipitation of ear punches of iBcKO-PISD and WT mice.*

Compound	Company	Cat. No.	Concentration
Protein kinase K	Thermo Fisher Scientific	EO0491	0.1 mg/mL
EDTA	Sigma-Aldrich/Merck	E9884	5 mM
Tris	Sigma-Aldrich/Merck	648310	100 mM
NaCL	Sigma-Aldrich/Merck	S7653	200 mM
SDS	Sigma-Aldrich/Merck	L3771	0.2%

Cell debris and hair were removed after centrifugation at maximum speed for 15 minutes (RT) and DNA was precipitated using isoproterenol (1:1) and the same centrifugation settings. The resulting pellet was resuspended in 750 µL 70% ethanol and the centrifugation was repeated. The supernatant was discarded, and remnants were allowed to evaporate for approximately 30 minutes at room temperature, followed by 10 minutes at 37°C. The DNA was resuspended in RNAse free H_2O, the concentration was measured using a NanoDrop™ 2000 spectrophotometer (Thermo Fisher Scientific) and stored at -20°C, if not directly processed. Mice homozygous for PISD were PCR genotyped using respective primer pairs (Eurofins Genomics Germany) and protocols shown in **Table 2** and **Table 3** (LacZ, LoxP, Neo, Flippase, PISD WT/het/hom).

Table 2: *Primers and probes for genotyping of iBcKO-PISD and wildtype mice.*

	Forward sequence	Reverse sequence
LacZ	GTTGCAGTGCACGGCAGATACACTTGCTGA	GCCACTGGTGTGGGCCATAATTCAATTCGC
Neo	GGGATCTCATGCTGGAGTTCTTCG	GAAGATGAGGACCTGGTGCAA
LoxP	GAGATGGCGCAACGCAATTA	CGTAGGTGGCTGGAGCTAAG
Flippase	CACCACCTAAGGTGCTTGTTC	CTGCTTCTTCCGATGATTCG
PISD	GCAGGGTGATGTAGATCTGGG	GAAGATGAGGACCTGGTGCAA
ApoE	TCACCAGTCATTTCTGCCTTTG	CACGTGGGCTCCAGCATT
ApoE probe	AT550-CCAATGGTCGGGCACTGCTCAA-BHQ2	
Cre	GTGAAACAGCATTGCTGTCACTT	GCGGTCTGGCAGTAAAAACTATC
Cre probe	FAM-AAACATGCTTCATCGTCGGTCCGG-BHQ1	

The final genotype of iBcKO-PISD (Cre +) and wildtype (Cre -) mice was assessed using a TaqMan (ThermoFisher, 4440040) based multiplex real-time quantitative PCR (qPCR) assay. Samples were labeled with fluorescent probes (ApoE as internal standard and Cre) and detected at 465-510 nm and 533-580 nm, respectively. Probes, Primers (Eurofins Genomics Germany) and protocols are shown in **Table 2** and **Table 3**.

Table 3: *PCR protocols for genotyping of LacZ, LoxP, Flippase, Neo, PISD and qPCR protocol for genotyping of ApoE and Cre.*

LacZ (PCR)	**Duration**	**Temperature**	**Cycles**
Initial denaturation	1 minute	94°C	1
Denaturation	20 seconds	94°C	35
Elongation	3 minutes	68°C	
Hold	∞	16°C	1
LoxP/Flippase (PCR)	**Duration**	**Temperature**	**Cycles**
Initial denaturation	10 minutes	95°C	1
Denaturation	10 seconds	95°C	35
Annealing	30 seconds	53°C	
Elongation	20 seconds	72°C	
Final Extension	3 minutes	72°C	1
Hold	∞	16°C	
Neo (PCR)	**Duration**	**Temperature**	**Cycles**
Initial denaturation	10 minutes	95°C	1
Denaturation	10 seconds	97°C	35
Annealing	15 seconds	58°C	
Elongation	20 seconds	72°C	
Final Extension	3 minutes	72°C	1
Hold	∞	16°C	
PISD (PCR)	**Duration**	**Temperature**	**Cycles**
Initial denaturation	10 minutes	95°C	1
Denaturation	10 seconds	97°C	35
Annealing	25 seconds	61°C	
Elongation	30 seconds	72°C	
Final Extension	3 minutes	72°C	1
Hold	∞	16°C	
ApoE/Cre (qPCR)	**Duration**	**Temperature**	**Cycles**
Initial denaturation	2 minutes	50°C	1
	10 minutes	95°C	
Denaturation	15 seconds	95°C	40
Annealing	1 minute	60°C	

2.2 TISSUE DISSECTION, PLASMA COLLECTION AND STORAGE

All animals were euthanized using CO_2 asphyxiation (iBAT) or cervical dislocation (eWAT, iWAT, liver, muscle). For *ex vivo* experiments, mice of both sexes were euthanized at the age of four to six weeks (pre-adipocyte isolation) or eight to ten weeks (tissue and mitochondria isolation). For *in* vivo experiments, male mice were euthanized at the age of 12-13 weeks (chow diet) or 24-26 weeks (HFD). In the case of CO_2 asphyxiation, the death of animals was confirmed via a firm paw pinch reflex test as well as an incision of the diaphragm. Before dissection of liver, it was perfused using 0.9% saline and a 26 G Sterican® cannula (B. Braun SE). To avoid contamination with hair, mice were wetted with ethanol and the required organs were dissected. To avoid contamination with remnants other than the desired tissue (e.g. blood), tissue was thoroughly washed in cold or pre-warmed PBS +++ (**Table 6**). Tissue which was not directly used after dissection was snap frozen and stored at -80°C until further

processing. Tissue for isolation of mitochondria which were not used for respiratory analysis was snap frozen in liquid nitrogen and stored temporarily at -80°C completely covered with storage buffer (20% DMSO, 0.21 M mannitol, 0.07 M sucrose; pH 7.5). Directly before isolation of mitochondria, tissue was defrosted as quickly as possible in pre-warmed (45°C) thawing buffer (0.25 M sucrose, 0.01 M Tris-HCL, 0.4% essential fatty acid-free BSA; pH 7.5) in a 1:4 ratio. Tissue which was used for pre-adipocyte isolation or the isolation of mitochondria for respiratory analysis was minced in very small pieces, to allow for an efficient release of pre-adipocytes/adipocytes, and stored in pre-warmed PBS +++ (**Table 6**) or ice-cold STE + 2% essential fatty acid-free BSA (**Table 17**), respectively, until further processing. Blood was drawn by cardiac puncture using a 24 G Sterican® cannula (B. Braun SE, 4657675). For Plasma collection, blood was transferred into EDTA tubes (Sarstedt, 20.1341) and centrifuged for ten minutes at 1,500xg and 4°C. The supernatant was transferred into microtubes, snap frozen in liquid nitrogen and stored at -80°C until further processing.

2.3 ALT ASSAY

The ALT assay was conducted according to the manufacturer's instructions (Sigma-Aldrich/Merck; MAKO52). After preparation of the plate, the ALT activity was captured using a coupled enzyme assay resulting in a calorimetric (570 nm)/fluorometric product (λex= 535 nm/ λem= 587 nm), which is proportional to the generated pyruvate concentration. An initial measurement was conducted using an Infinite® M200 multi-detection microplate reader (Tecan) at room temperature, followed by measurements at 37°C every five minutes over a time course of 60 minutes.

2.4 LEPTIN ELISA

The Leptin ELISA was conducted according to the manufacturer's instructions (R&D Systems; DuoSet™ Ancillary Reagent Kit 3; DY009B). Plasma was diluted in a 1:4 ratio per well of a flat transparent plate (Costar). After plate preparation and assay procedure, the optical density was determined using an Infinite® M200 multi-detection microplate reader (Tecan), set to 450 nm, with a wavelength correction set to 570 nm to adjust for optical imperfections in the plate.

2.5 HISTOLOGY

Dissected tissue (liver, eWAT, iWAT, iBAT) in embedding cassettes was fixated in 4% formaldehyde (VWR, 97131000) at room temperature for 48-72 hours. Next, cassettes were submerged with 70% ethanol for dehydration. After more than 24 hours, dehydration was continued using different xylene and ethanol concentrations in an automatic tissue processor (Leica TP1020, Leica Biosystems), eventually completed with submerging the tissue in paraffin (**Table 4**). The tissue was fully embedded in paraffin blocks using an embedding machine (Leica EC1150C, Leica Biosystems). A rotary microtome (Leica RM2255, Leica Biosystems) was used to cut the samples in 0.5 µm sections, which were subsequently transferred into a pre-warmed water bath (42°C) to straighten the slices and facilitate the following transfer onto Superfrost® microscope glass slides (VWR, 631-0708). On the next day, the slides were placed in an incubator for 30 minutes at 60°C to melt off the paraffin. The tissue sections were stained using an automatic Multi-Stainer (Leica ST5020, Leica Biosystems) according to a typical Hematoxylin & Eosin staining protocol (**Table 4**). Eventually, the samples were mounted with mounting

medium and coverslips (VWR, 631.0973), dried overnight, and stored at room temperature until imaging. For imaging, the digital M8 microscope and scanner (PreciPoint) and the ViewPoint Software (PreciPoint) were used at a 20x magnification. Adapted from Galarraga et al., the lipid droplet area and number was quantified using the Fiji/ImageJ plugin Adiposoft *(Galarraga et al. 2012)*.

Table 4: *Dehydration and H&E staining protocols for adipose tissue and liver sections.*

Device	Purpose	Reagent	Time (minutes)
Automatic tissue processor (Leica TP1020)	Dehydration	70% EtOH	60
		70% EtOH	60
		80% EtOH	60
		96% EtOH	60
		96% EtOH	60
		100% EtOH	60
		100% EtOH	60
		100% EtOH	60
		100% Xylene	60
		100% Xylene	60
	Paraffin submerging	100% Paraffin	60
		100% Paraffin	60
Automatic multi-stainer (Leica ST5020)	Deparaffinization + rehydration	Xylene	3
		Xylene	3
		100% EtOH	2
		96% EtOH	2
		70% EtOH	1
	Haematoxylin & Eosin staining	dH_2O	1
		Haematoxylin	4
		dH_2O	2
		Eosin	2
		70% EtOH	1
		96% EtOH	1
		100% EtOH	1
		100% EtOH	1.5
		Xylene/EtOH	1.5
		Xylene	1
		Xylene	2

2.6 Isolation of mature adipocytes from brown adipose tissue

Mature brown adipocytes were isolated of tissue homogenates pooled from two to three female mice. Therefore, tissue was minced in small pieces and incubated in 5 mL pre-warmed collagenase buffer (1 mg/mL collagenase; see **Table 5**) at 37°C on a rocker (120 rpm) for 60 minutes. The tissue was vigorously shaken every 15 minutes. Homogenates were diluted with DMEM (1:1; 10% FBS, 1% P/S) and centrifuged at 1,000 rpm for ten minutes. Adipocytes floating at the top were carefully collected using a G 18 cannula (B. Braun SE) and resuspended in 8 mL ice-cold PBS. Subsequently, homogenates

were filtered and washed twice through a 100 µm nylon mesh with fresh PBS. Cells were again centrifuged at 1,000 rpm for 10 minutes, collected in microfuge tubes and incubated in Trizol (1:4) for five minutes at room temperature (storage at -80°C until RNA isolation).

Table 5: *Composition of collagenase buffer for isolation of mature brown adipocytes.*

Compound	Company	Cat. No.	Concentration
Collagenase	Sigma-Aldrich/Merck	C1-22	1 mg/mL
$NaHCO_3$	Carl Roth	6885.1	25 mM
KH_2PO_4	Carl Roth	3904.1	12 mM
$MgSO_4$	Sigma-Aldrich/Merck	M3409	1.2 mM
KCL	Sigma-Aldrich/Merck	P3911	4.8 mM
NaCL	Sigma-Aldrich/Merck	6404	120 mM
$CaCL_2$ * 2 H_2O	Carl Roth	5239.1	1.4 mM
Glucose	Carl Roth	6780.1	5 mM
BSA Fraction V	Carl Roth	8076.3	2.5%
Penicillin/Streptomycin	Biochrome	A2212	1:100
ddH_2O	-	-	-

2.7 CELL CULTURE

2.7.1 ISOLATION OF MURINE PRIMARY BROWN AND BEIGE PRE-ADIPOCYTES

To isolate adipocyte precursor cells for *ex vivo* cultivation, minced iBAT and iWAT was placed in pre-warmed isolation medium containing 0.1% collagenase to ensure proper digestion (**Table 6**). By using 1 mL cut-end tips, the tissue was transferred into 15 mL canonical tubes, filled up to a final volume of 8 mL. The following tissue digestion was conducted in a WiseCube® shaker (WITEG Labortechnik GmbH; 37°C, 120 rpm, one hour). Canonical tubes were placed horizontally and rigorously shaken every 15 minutes. Next, a 250 µM pore-sized nylon mesh was used to filter cell suspensions to fresh tubes, residues of the cell suspension remaining in the tube were rinsed with 6-7 mL wash buffer (**Table 6**) and combined with previous cell suspension through another nylon-mash. Cell suspensions were centrifuged (250xg, five minutes) at room temperature (RT). To release remaining pre-adipocytes from the fat layer on top of the tube, it was shaken and centrifuged again under the same conditions. Mature adipocytes and buffer (supernatant + upper fat layer) were discarded, whereas the stroma vascular fraction (SVF) containing pre-adipocytes (pellet) was transferred under a sterile laminar flow hood to continue under aseptic conditions. Cells were re-suspended and incubated in 1 mL pre-warmed blood-cell lysis buffer for five minutes (**Table 6**). After re-suspending the cell lysates to a final volume of 10 mL wash buffer, they were centrifuged (500xg, five min, RT) and supernatants were aspirated. The pellet was re-suspended with 3-4 mL of culture medium (**Table 6**) and filtered through a 40 µM cell strainer (BD Biosciences, 352340). Cell suspensions were combined with the appropriate volume of culture medium and plated onto respective cell culture dishes (10 cm dishes, 6-, 12-, 24- well plates or SeahorseXF96 microplates). In the case of 129Sv mice, pre-adipocytes of 2-3 (iBAT) or 1-2 (iWAT) mice were equally seeded onto cell culture plates, whereas pre-adipocytes originating of BL6/N mice were pooled of 4-5 mice (iBAT) and 2-3 mice (iWAT). Adipocytes were kept in an incubator at 37°C and 5% CO_2.

Table 6: *Composition of buffers, media and solutions used for primary adipocyte isolation and differentiation.*

Compound	Company	Cat. No.	Concentration
PBS +++			
PBS	Sigma-Aldrich/Merck	D8662	-
Amphotericin B	Biochrome	A2612	500 ng/mL
Gentamycin	Sigma-Aldrich/Merck	G1272	40 µg/mL
Penicillin/Streptomycin	Sigma-Aldrich/Merk	P0781	40 µg/mL
Isolation medium			
HBSS	Gibco	14025	-
BSA fraction V	Carl Roth	8076.3	3.5%
Glucose	Carl Roth	6780.1	0.55 mM
Amphotericin B	Biochrome	A2612	500 ng/mL
Gentamycin	Sigma-Aldrich/Merck	G1272	40 µg/mL
Penicillin/Streptomycin	Sigma-Aldrich/Merck	P0781	40 µg/mL
Collagenase Type I	Sigma-Aldrich/Merck	C1-22	0.1% (w/v)
Wash medium			
HBSS	Gibco	14025	-
BSA fraction V	Carl Roth	8076.3	3.5%
Amphotericin B	Biochrome	A2612	500 ng/mL
Gentamycin	Sigma-Aldrich/Merck	G1272	40 µg/mL
Penicillin/Streptomycin	Sigma-Aldrich/Merck	P0781	40 µg/mL
Red blood cell lysis buffer			
ddH_2O	-	-	-
EDTA	Carl Roth	8043	0.1 mM
NH_4CL	Carl Roth	P726	154 mM
K_2PO_4	Carl Roth	T875	10 mM
Cultivation medium			
DMEM high glucose	Sigma-Aldrich/Merck	D5796	-
FBS	Sigma-Aldrich/Merck	S0615	20% (v/v)
Amphotericin B	Biochrome	A2612	500 ng/mL
Gentamycin	Sigma-Aldrich/Merck	G1272	40 µg/mL
Penicillin/Streptomycin	Sigma-Aldrich/Merck	P0781	40 µg/mL
Induction medium			
DMEM high glucose	Sigma-Aldrich/Merck	D5796	-
FBS	Sigma-Aldrich/Merck	S0615	10% (v/v)
Gentamycin	Sigma-Aldrich/Merck	G1272	40 µg/mL
Penicillin/Streptomycin	Sigma-Aldrich/Merck	P0781	40 µg/mL
Rosiglitazone	Biomol	Cay71740	1 µM
Insulin	Sigma-Aldrich/Merck	I9278	850 nM
T3	Sigma-Aldrich/Merck	T2752	1 nM
Indomethacin	Sigma-Aldrich/Merck	I7378	125 µM
Dexamethasone	Sigma-Aldrich/Merck	D4902	1 µM
IBMX	Sigma-Aldrich/Merck	I5879	500 µM

Differentiation medium			
DMEM high glucose	Sigma-Aldrich/Merck	D5796	-
FBS	Sigma-Aldrich/Merck	S0615	10% (v/v)
Gentamycin	Sigma-Aldrich/Merck	G1272	40 µg/mL
Penicillin/Streptomycin	Sigma-Aldrich/Merck	P0781	40 µg/mL
Rosiglitazone	Biomol	Cay71740	1 µM
Insulin	Sigma-Aldrich/Merck	I9278	850 nM
T3	Sigma-Aldrich/Merck	T2752	1 nM

2.7.2 CULTIVATION, INDUCTION, AND DIFFERENTIATION OF PRIMARY MURINE BROWN AND BEIGE PRE-ADIPOCYTES

24 hours after isolation of adipocyte precursor cells, cells were washed twice with pre-warmed PBS and the medium was changed to fresh cultivation medium (**Table 6**) which was replaced every other day. When cells reached ~90% confluency (approximately after 4 days) they were induced for 48 hours with induction medium (**Table 6**). Afterwards, cells were washed once with pre-warmed PBS and medium was changed to differentiation medium (**Table 6**) for another 7-8 days. After full differentiation, mature adipocytes were harvested according to their further use or analyzed using micro-plate based respirometry. As depicted in **Figure 4** primary brown and beige adipocytes were modulated in mitochondrial GPL/FC ratios by various approaches: A) Lentivirus-mediated overexpression of STARD3; B) Tamoxifen-induced conditional knockout of PISD in UCP1-expressing cells; C) siRNA-mediated gene silencing of STARD3 and PISD.

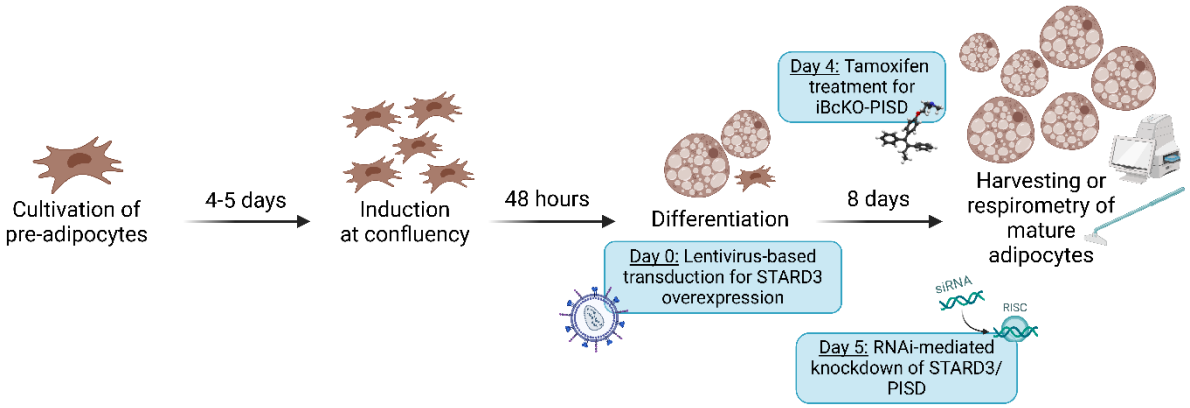

Figure 4: Timeline of cultivation, induction, and differentiation of pre-adipocytes, as well as approaches to modulate mitochondrial GPL/FC ratio.

2.7.3 LENTIVIRUS-BASED OVEREXPRESSION OF STARD3

2.7.3.1 STARD3 AMPLIFICATION AND PURIFICATION

cDNA was synthesized according to the manufacturer's instructions (Tetro™ cDNA synthesis kit: Meridian Bioscience, BIO-65042). The prepared master mix (**Table 7**) was incubated with high-quality BAT mRNA originating from 129SV/S6 mice for 40 minutes at 45°C and the reverse transcriptase was inactivated via incubation at 85°C for five minutes.

Table 7: *Master mix composition for cDNA synthesis with the Tetro™ cDNA synthesis kit.*

Compound	Company	Cat. Nr.	Concentration
DEPC H_2O	-	-	-
5x RT Buffer	Meridian Bioscience	BIO-65042	1x
Tetro reverse transcriptase	Meridian Bioscience	BIO-65042	20 U/µL
RiboSafe RNase inhibitor	Meridian Bioscience	BIO-65042	0.5 U/µL
10 mM dNTP mix	Meridian Bioscience	BIO-65042	0.5 mM
Primer oligo $(dT)_{18}$	Meridian Bioscience	BIO-65042	0.4 µM
mRNA	-	-	4 µg

From the generated cDNA library, genes were PCR-amplified using the Phusion High Fidelity PCR Kit (NEB, E0553S) and primers comprising restriction sides on the 5'-end (BamHI) and 3'-end (NotI). To enable a more efficient digestion, six spacers (nonsense nucleotides) were additionally attached to the 5'-end (spacer yellow, restriction sides orange; **Table 8**).

Table 8: *Primer composition for STARD3 digestion and primer amplification.*

Primer	Company	Forward sequence (BamHI)	Reverse sequence (NotI)
STARD3	Eurofins	5'-TAAGCAGGATCC- -ATGAGCAAGCGACCTGGTGATCT-3'	5'-TGCTTAGCGGCCGC- -TCAAGCTCGGGCCCCCAGCT-3'

Table 9: *Master mix composition for PCR amplification using the Phusion High Fidelity PCR Kit.*

Primer	Company	Concentration
DMSO	Sigma-Aldrich/Merck	3%
5x Phusion HF buffer	NEB	1x
Phusion HF DNA-Polymerase	NEB	1 U
10 mM dNTPs	NEB	200 µM
Forward primer (10 µM)	NEB	0.5 µM
Reverse primer (10 µM)	NEB	0.5 µM
RNAse-free H_2O	Sigma-Aldrich/Merck	-
cDNA	-	< 250 ng

The amplification was conducted using the in **Table 9** and **Table 10** shown master mix and PCR protocol. To exclude off-target amplicons, not fully synthesized amplicons, and residues of reactants, targeted DNA fragments were isolated. Therefore, the PCR products were separated conducting agarose gel electrophoresis (1.5% agarose in TAE buffer) at 90 V and STARD3 bands were excised from the gel under minimal UV light exposure. The gel slices were purified using the Wizard SV Gel and PCR cleanup system (Promega, A9282), according to the manufacturer's instructions.

Table 10: *PCR protocol for STARD3 amplification.*

STARD3	Duration	Temperature	Cycles
Initial Denaturation	30 seconds	98°C	1x
Denaturation	10 seconds	98°C	
Annealing	25 seconds	59.4°C	35x
Elongation	35 seconds	72°C	
Final extension	10 minutes	72°C	1x
Hold	∞	4°C	1x

2.7.3.2 DIGESTION AND LIGATION

To synthesize the respective overexpression vectors, the STARD3 inserts as well as the pCDH-PGK backbone (Addgene, plasmid #72268) were digested. Therefore, they were incubated at 37°C for 30-60 minutes with BamHI-HF (NEB, R3136S) and Not1-HF (NEB, R3189S) restriction enzymes simultaneously, producing sticky ends. The enzymes were separated from digested fragments using agarose gel electrophoresis (1.5% gel for STARD3, 0.8% gel for pCDH-PGK) at 90 V and bands were excised from the gel and purified as described above (see **Figure 5**).

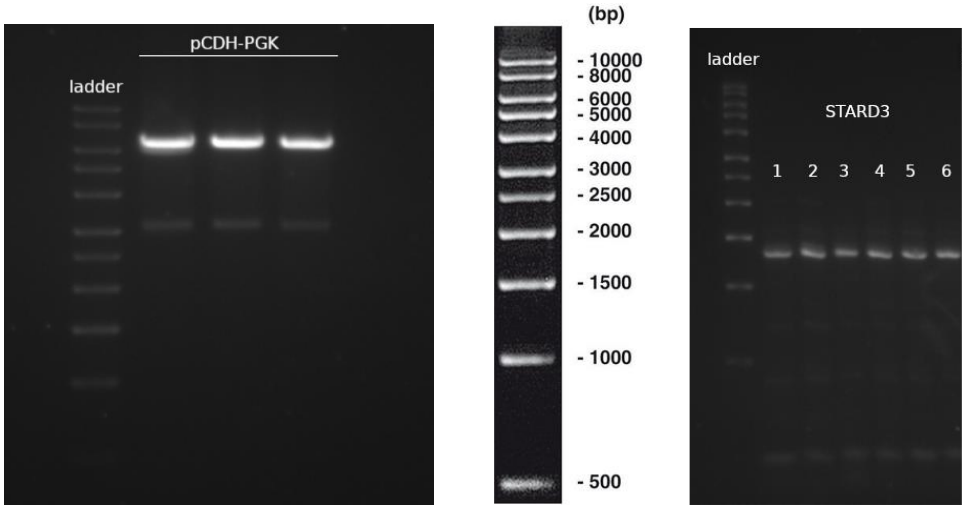

Figure 5: Agarose gel electrophoresis of STARD3 (1.37 kbp) and pCDH-PGK (6.39 kbp) amplicons based on Tetro™ cDNA as matrix after digestion with restriction enzymes. *The second band of pCDH-PGK (approximately half of the length) visualizes undigested backbone.*

Eventually, the backbone vector was ligated with STARD3 fragments in a 1:3 ratio through incubation (16-22 hours, 16°C) and heat inactivation (10 minutes, 65°C), using a T4 ligase (NEB). Digestion and ligation were conducted according to the instructions of NEB.

2.7.3.3 TRANSFORMATION, BACTERIAL CULTURE, MINI/MIDI PREP

The composition of media and solutions used for transformation, plasmid amplification, and purification is listed in **Table 11**. For high efficiency, 1-5 ng plasmid or 1-5 µL ligation product were mixed and incubated for 30 minutes with on ice thawed stable competent *E. coli* (NEB, C3040H) for transformation. This was followed by heat shock (30 seconds at 42°C) and incubation on ice (five minutes). After dilution in SOC-medium, the mix was incubated for 60 minutes at 30°C and 300 rpm.

Table 11: *Composition of media used for transformation, bacterial culture, and plasmid amplification.*

Compound	Company	Cat. No.	Concentration
LB-Medium			
ddH_2O	-	-	-
Yeast extract	Carl Roth	2363.2	0.5%
Tryptone	Carl Roth	8952.2	1%
NaCL	Sigma-Aldrich/Merck	6404	0.5 mM

LB-Medium + Ampicillin			
LB-medium	See above	See above	1x
Ampicillin	Sigma-Aldrich/Merck	A1593	100 µM
SOC-Medium			
Yeast extract	Carl Roth	2363.2	0.5%
KCL	Sigma-Aldrich/Merck	P3911	2.5 mM
NaCL	Sigma-Aldrich/Merck	6404	10 mM
Tryptone	Carl Roth	8952.2	2%
$MgSO_4$	Sigma-Aldrich/Merck	M3409	10 mM
$MgCL_2$	Sigma-Aldrich/Merck	M3409	10 mM
Glucose	Carl Roth	6780.1	20 mM

Pre-heated LB/ampicillin-agar plates were used as breeding ground for the next 24 hours at 30°C (until colonies were visible). Not only pCDH-PGK-STARD3 plasmids, but also pCDH-PGK-tGFP plasmids as well as non- digested and digested empty pCDH-PGK vectors were transformed as controls. To isolate the plasmids from bacterial colonies, up to six colonies were picked under flame, mixed with ampicillin enriched LB-medium, and incubated in a WiseCube® shaker (WITEG Labortechnik) overnight at 30°C and 220 rpm with loosely attached lids. After 14-20 hours, the PureYield™ Plasmid Miniprep System was used for plasmid purification, according to the manufacturer's instructions. Plasmids were amplified in bacterial culture and purified with the Nucleobond® Xtra Midi Plus Kit (Macherey Nagel, 740412), according to the manufacturer's instructions. Plasmid concentrations were measured using the NanoDrop® and stored at -20 °C until further use.

Table 12: *Primer pairs for sequencing of STARD3 and pCDH-PGK vectors.*

Primer	Company	Forward sequence	Reverse sequence
STARD3 (middle of ORF)	Eurofins	5'-ATGAGCAAGCGACCTGGTGATCT-3'	5'-TCAAGCTCGGGCCCCCAGCT-3'
STARD3 (end of ORF)	Eurofins	5'-CACTGGTGTCCAGTGCATTC-3'	5'-CTGGGCAGCAAGATACCATC-3'
pCDH-PGK	Eurofins	5'-TACAGTGCAGGGGAAAGAATAG-3'	5'-CCACGTTGCCTGACAAC-3'

The successful incorporation of STARD3 inserts into the pCDH-PGK backbone was verified by sending them for sequencing (Eurofins) using the primers shown in **Table 12**. Once the plasmids were synthesized, they were used to produce lentivirus particles for the transduction of murine primary brown adipocytes.

2.7.3.4 LENTIVIRUS PRODUCTION AND INFECTION OF PRIMARY BROWN ADIPOCYTES

All required media is listed in **Table 13**. HEK293T cells were thawed and cultivated seven days before transfection (maximal until passage 20) in HEK cultivation medium which was changed every 24 hours. To ensure a rapid cell replication, cells were divided at least twice before downstream procedure, each division after reaching 80% but before reaching full confluency. 24 hours prior to transfection, 4.23 x 10^6 cells were seeded per poly-D-lysin (Sigma-Aldrich/Merck, P7280) coated well of a 6-well plate. 22 hours later, the medium was changed once more. HEK293T-cells were $CaCL_2$- based co-transfected at 50% confluency with a second-generation packaging psPAX.2 plasmid (addgene, plasmid #12260, see **Supplementary Figure 13**), an envelope pMD2.G plasmid (addgene, plasmid #12259, see

Supplementary Figure 12), and either pCDH-PGK-STARD3, pCDH-PGK (negative control; empty vector), or pCDH-PGK-tGFP (positive control) in a 3:1:4 ratio. Therefore, $CaCl_2$ medium, as well as HEPES buffered saline (**Table 13**) were used. To enable continuous production of lentivirus, the medium was collected and replaced with fresh cultivation medium after 24 hours. Cultivation of primary brown adipocytes was conducted on a schedule to overlap day 0 of differentiation with this time point of lentivirus production in HEK293T- cell medium. The lentivirus containing medium was enriched with T3, insulin and rosiglitazone, and filtered through a 0.45 µM polyether-sulfone membrane before transducing adipocytes using 8 g/L polybrene to increase transduction efficiency. 24 hours later, the medium was replaced with the second batch of lentivirus containing medium. After a total of 48 hours, lentivirus-medium was replaced with normal differentiation medium every other day until day eight of differentiation. Eventually, mature adipocytes were harvested according to their further use or analyzed using microplate-based respirometry.

Table 13: *Composition of buffers and media required for transduction.*

Compound	Company	Cat. No.	Concentration
$CaCL_2$ medium			
Sterile ddH_2O	-	-	-
$CaCL_2$	Carl Roth	5239.1	2.5 mM
HEPES buffered H_2O			
Sterile ddH_2O	-	-	-
HEPES	Sigma-Aldrich/Merck	H4034	50 mM
HEPES buffered saline			
Sterile ddH_2O	-	-	-
HEPES	Sigma-Aldrich/Merck	H4034	50 mM
Na_2HPO_4	Sigma-Aldrich/Merck	S9390	1.5 mM
NaCL	Sigma-Aldrich/Merck	6404	280 mM
HEK cultivation medium			
DMEM high glucose	Sigma-Aldrich/Merck	D5796	-
Penicillin/Streptomycin	Biochrome	A2212	1:500
FBS	Sigma-Aldrich/Merck	S0615	10%
Transduction medium			
HEK cultivation medium + virus	See above	See above	See above
Polybrene	Sigma-Aldrich/Merck	TR-1003	8 µg/mL
T3	Sigma-Aldrich/Merck	T2752	1 nM
Insulin	Sigma-Aldrich/Merck	I9278	850 nM
Rosiglitazone	Biomol	Cay71740	1 µM

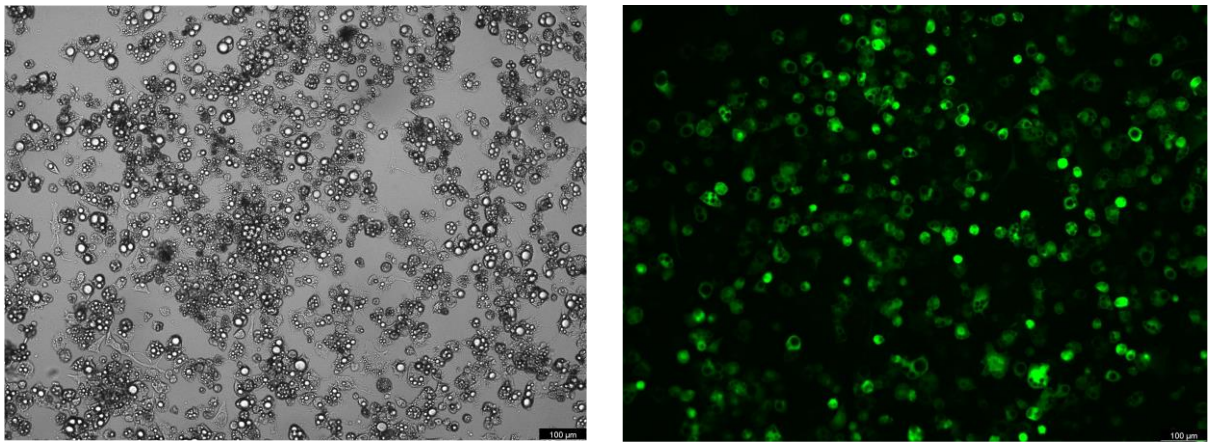

Figure 6: Microscopic pictures (five days post transduction) of successfully pCDH-PGK-tGFP transduced primary brown adipocytes. *The left picture captures fluorescence through the DIC channel and the right picture through the GFP channel using a LAS X microscope (Leica) at 527 nm emission.*

2.7.4 SIRNA-MEDIATED GENE SILENCING OF STARD3 AND PISD

To silence the gene expression of STARD3 and PISD, the method of transient gene knockdown via dicer-substrate small interfering RNA (DsiRNA) was chosen (see **Figure 7**). This method is based on RNA interference (RNAi), which downregulates the expression of specific genes post transcriptionally by using double-stranded RNA (dsRNA). These strands must be homologues to the target genes *(Laganà et al. 2015)*. Previously, it was reported that long dsRNA (> 30 bp) can silence genes in organisms such as D. melanogaster or C. elegans. However, the use of longer exogenous dsRNA should be avoided because it triggers a nonspecific interferon response in mammalian systems, leading to a global repression of mRNA translation by degrading mRNA in an unspecific manner *(Hannon und Rossi 2004; Pham et al. 2004; Dykxhoorn et al. 2003)*. Additionally, it was published that artificial DsiRNA with the length of 25-30 nucleotides might be up to 100-fold more efficient in RNAi compared to conventional 21- mer small interference RNA (siRNA) *(Kim et al. 2005)*. Thus, synthetic DsiRNA with a length of 27 bp was used in this work. These dsRNA molecules are processed into shorter siRNA fragments (~21 nucleotides) with 5'-phosphate- and 2-nucleotide-3'- overhangs by a RNase-III-type endonuclease (Dicer). Both overhangs are important for the following complex assembly: The in this process generated siRNA is incorporated into the RNA induced silencing complex (RISC). By unwinding siRNA duplexes, one strand (passenger strand) is discarded, whereas the other strand (guide strand) associates with the argonaut protein (Ago2) of the RISC complex. Finally, the target mRNA, which is complementary to the guide siRNA strand, will be identified and silenced. This is achieved by Ago2 acting as ribonuclease, which cleaves the target mRNA under direction of the guide strand. This leads to inhibited mRNA translation and subsequently, transient silencing of the selected gene *(Meister und Tuschl 2004; Sontheimer 2005)*.

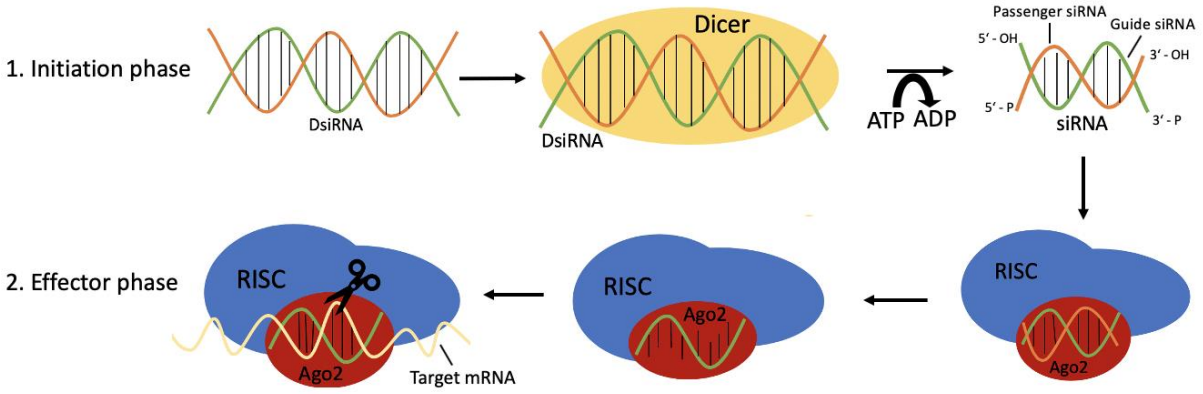

***Figure 7: Initiation and effector phase of RNAi in mammalian cells**. In the first phase, a dicer cleaves DsiRNA (27 bp) in an ATP-depended manner into smaller siRNA duplexes (21 bp). In the second phase, the assembly of the RISC complex takes place and siRNA duplexes get unwound. The siRNA guide strand remains bound to the Ago2 protein and subsequently the RISC complex recognizes the target mRNA by base pairing between siRNA guide strand and complementary target mRNA sequence. Finally, the RISC complex cleaves the target mRNA by its endoribonuclease activity, thereby inhibiting mRNA translation and silencing respective protein expression. Figure modified from (Sontheimer, 2005).*

Adipocytes were reverse transfected on day five of the differentiation with the transfection mix shown in **Table 14**.

***Table 14:** Composition of transfection mix used for siRNA-mediated gene silencing.*

Compound	Company	Cat. No.	Concentration
Lipofectamine RNAiMAX	Thermo Fisher Scientific	I9278	2.5 µL/mL
siRNA	IDT	-	50 nM
OptiMEM	Gibco	31985047	16.61%
Cell suspension/well	-	-	83.04%

The mix was incubated (20 min, RT) and distributed on respective cell culture plates (6-, 12-, 24-well plates or SeahorseXF96- microplates). During the incubation time, primary brown/beige adipocytes were washed twice with pre-warmed PBS. Cells were detached using pre-warmed trypsin (Sigma-Aldrich/Merck, T3924) enriched with collagenase (0.5 mg/mL) and incubated for five to ten minutes (37°C, 5% CO_2). The trypsinization was stopped with antibiotic free differentiation medium and cell clumps were carefully separated. Cell suspensions were transferred into 15 mL canonical tubes and centrifuged (five min, 250xg, RT). Next, cell pellets were re-suspended in antibiotic free medium, equally distributed on the respective cell culture plate containing transfection mix, kept under the hood for 60 minutes to enable an even distribution of the cells, and subsequently, cells were differentiated (37°C, 5% CO_2) for three more days. After the first 24 hours, the medium was changed to a differentiation medium containing antibiotics. After the differentiation was completed, cells were harvested for further processing or analyzed using microplate-based respirometry. This practical procedure was modified from Isidor et al. *(Isidor et al. 2016)*. The used DsiRNAs are shown in **Table 15**.

Table 15: *Sequences of DsiRNA obtained from IDT DNA used for transfections.*

siRNA	Forward sequence 5'-3'	Reverse sequence 3'-5'
NTC	CGUUAAUCGCGUAUACGCGUAT	AUACGCGUAUUAUACGCGAUUAACGAC
STARD3	GGAUCAUCGAGCUAAAUACCAACAC	GACCUAGUAGCUCGAUUUAUGGUUGUG
PISD	AAAUCUGUGCCAACGCGUUUGCUGT	ACAGCAAACGCGUUGGCACAGAUUUU

2.7.5 HARVESTING OF PRIMARY BROWN AND BEIGE ADIPOCYTES

For RNA isolation, RLT lysis buffer (RNeasy® Mini Kit, Qiagen) enriched with 1% β-mercaptoethanol was added to PBS- washed cells. For lipid profile analysis, 0.2% SDS (five min incubation before 1:1 dilution to 0.1% SDS) was pipetted on PBS- washed cells. For proteomics, ice-cold PBS was added on PBS-washed cells. In all cases, cells were harvested by carefully scraping cell lysates from the plate using a cell scrapper. For RNA isolation and lipidomics, cell lysates were homogenized and stored at -80°C for at least 24 hours prior further processing. For proteomics, cell lysates were centrifuged (4°C, 14,000 rpm, 2.5 min) and the pellet was stored at -80°C. For protein isolation (immunoblotting), cells were thoroughly washed with ice-cold PBS. Fluid was fully aspirated and dry cell plates were stored at -80°C until further processing (> 24 hours). For isolation of mitochondria from brown adipocytes, cells were washed twice with pre-warmed PBS and detached using trypsin + collagenase as described in **section 2.7.4**. All harvesting steps were performed on ice. Relevant media and buffers can be found in **Table 16**.

Table 16: *Composition of solutions used for adipocyte harvesting.*

Compound	Company	Cat. Nr.	Concentration
RNA			
β-mercaptoethanol	Sigma-Aldrich/Merck	M3148	1%
RLT Buffer	Qiagen	74106	-
Lipidomics			
ddH_2O	-	-	-
10% SDS solution	Sigma-Aldrich/Merck	L3771	0.2%

2.8 PROCESSING OF TISSUE AND CELLS

2.8.1 ISOLATION OF MITOCHONDRIA

All mitochondrial isolations were conducted on ice and/or in a 4°C cold-room to avoid the activation of phospholipases and proteases. For lipidomic analyses, the mitochondrial pellet was resuspended in 100 µL 0.1% SDS and stored at -80°C. For proteomic analyses, the pellet was stored without any liquid at -80°C. For respiratory analyses, which was directly conducted after mitochondrial isolation and protein concentration measurement (Biuret assay), the pellet was resuspended in 100-150 µL STE + 0.4% BSA. For Western Blot analyses, the pellet was resuspended in 50 µL of RIPA buffer (+1% triton). All buffers are listed in **Table 17** and **Table 21**.

Table 17: *Composition of buffers and media used for mitochondria isolation. All buffers adjusted to pH 7.4.*

Compound	Company	Cat. No.	Concentration
Percoll medium			
Mannitol	Sigma-Aldrich/Merck	M4125	225 mM
HEPES	Sigma-Aldrich/Merck	H4034	25 mM
EGTA	Carl Roth	3054.2	1 mM
Percoll	Sigma-Aldrich/Merck	P4937	30%
MRB solution			
Mannitol	Sigma-Aldrich/Merck	M4125	250 mM
HEPES	Sigma-Aldrich/Merck	H4034	5 mM
iB_{iBAT-1}			
Mannitol	Sigma-Aldrich/Merck	M4125	225 mM
Sucrose	Sigma-Aldrich/Merck	84097	75 mM
Tris-HCL	Sigma-Aldrich/Merck	T3253	30 mM
iB_{iBAT-2}			
iB_{iBAT-1}	See above	See above	See above
BSA, essentially FA-free	Sigma-Aldrich/Merck	A3803	0.5%
EGTA	Carl Roth	3054.2	0.5 mM
iB_{iBAT-3}			
iB_{iBAT-1}	See above	See above	See above
BSA, essentially FA-free	Sigma-Aldrich/Merck	A3803	0.5%
STE buffer			
Sucrose	Sigma-Aldrich/Merck	84097	250 mM
Tris	Sigma-Aldrich/Merck	T3253	5 mM
EGTA	Carl Roth	3054.2	2 mM
BSA, essentially FA-free	Sigma-Aldrich/Merck	A3803	0.1%, 0.4%, 2%, 4%
Preparation buffer			
KCL	Sigma-Aldrich/Merck	P3911	0.1 M
Tris-HCL	Sigma-Aldrich/Merck	T3253	0.05 M
EGTA	Carl Roth	3054.2	2 mM
Digestion $buffer_{WAT}$			
HBSS	Gibco	14025	-
Collagenase Type I	Sigma-Aldrich/Merck	C1-22	1 g/L
BSA, Fraction V	Carl Roth	8076.3	40 g/L
Digestion $buffer_{Muscle}$			
KCL	Sigma-Aldrich/Merck	P3911	0.1 M
Tris-HCL	Sigma-Aldrich/Merck	T3253	0.05 M
ATP	Sigma-Aldrich/Merck	A6419	1 mM
BSA, essentially FA-free	Sigma-Aldrich/Merck	A3803	0.5%
Protease Type VIII	Sigma-Aldrich/Merck	P5380	245.7 U/100 mL
EGTA	Carl Roth	3054.2	2 mM
$MgCL_2$	Sigma-Aldrich/Merck	M8266	5 mM

2.8.1.1 ISOLATION AND PURIFICATION OF MITOCHONDRIA, ER AND MAM FROM IBAT AND LIVER

To isolate and purify mitochondrial, ER and MAM fractions, a protocol describing density gradient centrifugation was adapted from Wieckowski et al. *(Wieckowski et al. 2009)*. For BAT mitochondria, the tissue of 13-15 mice was used, whereas for liver five mice were required. After thawing iBAT and

liver as described in **section 2.2**, it was directly transferred into ice-cold IB_{iBAT-2}. Afterwards, it was washed four times in ice-cold IB_{iBAT-1} to remove blood and other residues. The tissue was minced with scissors and washed once again with ice-cold IB_{iBAT-2}. Tissue pieces and fresh ice-cold IB_{iBAT-2} (1:4) were transferred to a precooled 5 mL loose fitting glass/Teflon Potter Elvehjem homogenizer. Per homogenization process, less than 1 g of tissue was homogenized with a pre-cooled pestle (15-25 strokes). To protect the mitochondrial integrity, the homogenization was conducted at low force and speed as well as with fluid movements. Homogenates were combined in a 30 mL polypropylene centrifugation tube and centrifuged (five minutes, 740xg, 4°C). The pellet with unbroken cells and nuclei was discarded, whereas the supernatant was centrifuged twice more with the same settings. The supernatant was centrifuged again (9,000xg, 4°C, ten minutes), resulting in a cytosolic fraction (supernatant) which was stored on ice for later sub-fractionation. The pellet was transferred to a 15 mL loose fitting glass/Teflon Potter Elvehjem homogenizer by using 1 mL cut-end tips, a soft paintbrush, and a small volume of ice-cold IB_{iBAT-3}. Then, it was resuspended in two runs with 10 mL of IB_{iBAT-3} each (2-3 strokes). The suspension was centrifuged (4°C, 10,000xg, 20 minutes) and the resulting pellet was gently resuspended with 20 mL of ice-cold IB_{iBAT-1} as described above. The centrifugation was repeated with the same settings for ten minutes. The obtained mitochondrial pellet was resuspended in 3 mL of ice-cold MRB with a 5 mL loose fitting glass/Teflon Potter Elvehjem homogenizer (as described above).

The resulting homogenate was pipetted into a 17 mL open-top thin wall ultra-clear ultracentrifuge tube (Beckman Coulter). Afterwards, suspension was under-layered with 8 mL of Percoll medium and over-layered with 4-5 mL of MRB solution using long needles and syringes. The tube had to be filled up to 4-5 mm below the top to avoid damage during centrifugation. The tube was weighted and balanced with MRB solution before they were centrifuged in a Sorvall Discovery 90 Ultracentrifuge/Sorvall SureSpin 630 swinging bucket rotor (4°C, 28,500 rpm, 37 minutes). The MAM- fraction (diffuse white band on top of the tube) was collected with a 1 mL cut-end tip, whereas the pure mitochondrial fraction (dense band at the bottom of the tube) was collected with a 100 µL cut-end tip. Both were diluted in MRB buffer (1:10) and centrifuged (6,300xg, 4°C) for either ten min (MAM) or 20 min (pure mitochondria). The mitochondrial pellet was resuspended in 20 mL of MRB buffer as previously described using a 15 mL loose fitting glass/Teflon Potter Elvehjem homogenizer. Another centrifugation step (6,300xg, 4°C, ten minutes) followed and the pellet was resuspended with an Elvehjem homogenizer in a small volume of MRB (1.5 mL). The final (pure) mitochondrial pellet was obtained after centrifugation using the same settings. The supernatant of the MAM fraction was transferred into a new ultracentrifugation tube. The temporarily for ER isolation stored cytosolic fraction was centrifuged (4°C, 20,000xg, 30 minutes) and the supernatant was pipetted into another ultracentrifuge tube. Both ultracentrifuge tubes were centrifuged (30,000 rpm, 4°C, three hours) and supernatants were gently aspirated using a long cannula. A schematic description of the organelle fractionation is depicted in **Figure 8**.

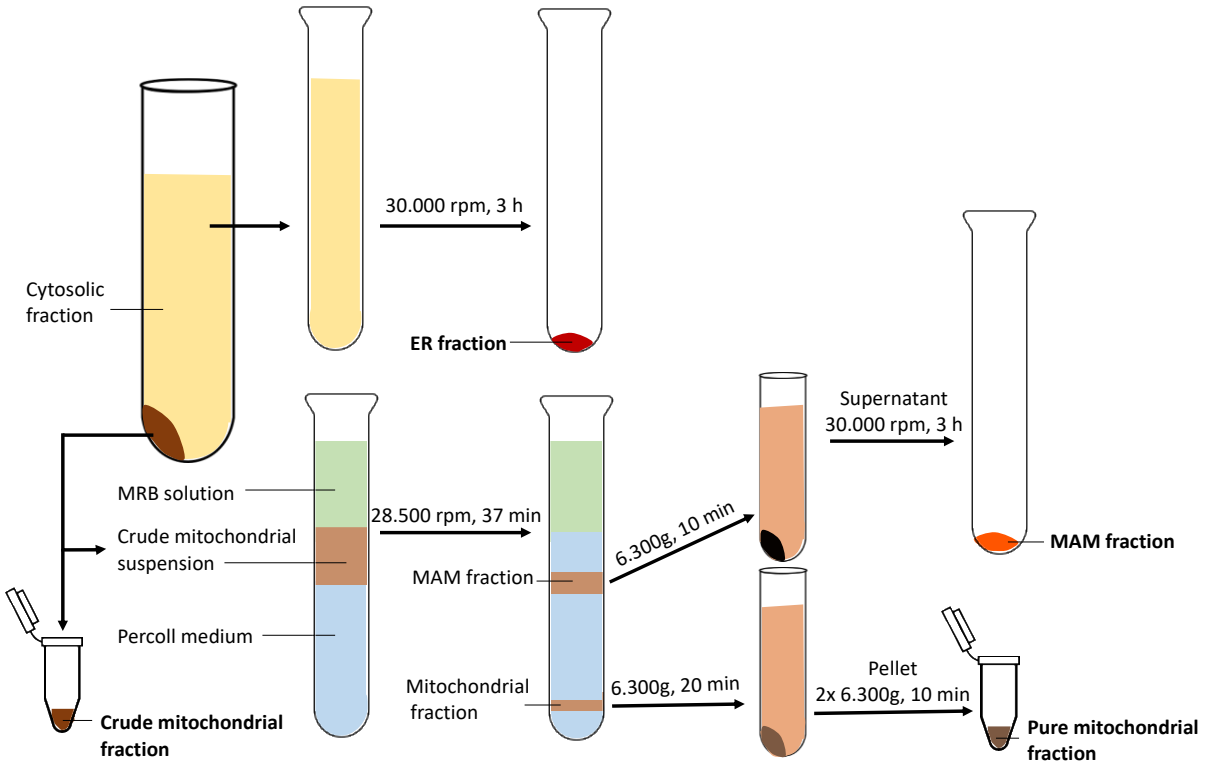

Figure 8: Protocol used for purification of mitochondria, ER and MAM from iBAT and liver. *Schematic depiction of the fractionation of crude mitochondrial and cytosolic fraction into ER, MAM and pure mitochondria.*

2.8.1.2 ISOLATION OF CRUDE MITOCHONDRIA FROM IBAT

Dissected brown adipose tissue of three to five mice was pooled and directly rinsed with ice-cold STE + 2% fatty acid-free BSA. Within the same (but fresh) buffer, tissue was minced in small pieces and transferred to a pre-cooled 5 mL loose fitting glass/Teflon Potter Elvehjem homogenizer. To protect the mitochondrial integrity, the homogenization was conducted at low force and speed as well as with fluid movements in two to four strokes. Homogenate was filtered through a 250 µm nylon gaze into a pre-cooled 30 mL polypropylene centrifugation tube and the process was repeated with remaining tissue pieces on the potter wall. The suspensions were combined and centrifuged for ten minutes at 8,500xg and 4°C. The supernatant was discarded, and the pellet was carefully resuspended in small volume of ice-cold STE + 2% BSA, using a fine brush, cut-end tips, and 1.5 mL tubes. The homogenate was transferred into a new round bottom tube filled up to 30 mL without carrying over erythrocytes and fat. After centrifugation (800xg, ten minutes, 4°C), the supernatant was transferred in fresh tubes and centrifuged at 10,000xg and 4°C. The pellet was resuspended in STE + 0.4% essential fatty acid-free BSA as described above, and the last centrifugation step was repeated.

2.8.1.3 ISOLATION OF CRUDE MITOCHONDRIA FROM LIVER

Mitochondria isolation from liver of one to two mice was conducted using the same protocol as described above with following variations: The tissue was homogenized with five to seven strokes and not filtered through nylon gaze, STE buffer did contain 0.1% fatty acid-free BSA. The centrifugation steps (each at 4°C) were set at three minutes and 1,000xg, followed by two times ten minutes at 11,600xg.

2.8.1.4 ISOLATION OF CRUDE MITOCHONDRIA FROM WAT

White adipose tissue (eWAT and iWAT) of ten mice was minced and digested in HBSS containing 1 g/L collagenase and BSA Fraction V (Digestion buffer$_{WAT}$) at 120 rpm and 37°C for 45-60 minutes. The tissue of two to three mice was digested in portions in 15 mL canonical tubes filled with 8 mL digestion buffer and combined in 50 mL tubes at the end of digestion. Next, it was filtered through a 250 µm nylon mesh and centrifuged in STE + 4% essential fatty acid-free BSA (500xg, two minutes, RT). The upper fat layer was transferred into 15 mL loose fitting glass/Teflon Potter Elvehjem homogenizer and combined with mature adipocytes resulting from three repetitions of the upper centrifugation step. The homogenate resulting from three strokes was transferred to pre-cooled 30 mL round bottom tubes and centrifuged at 800xg (mitochondria in supernatant) and subsequently at 10,000xg (mitochondria in pellet), both with two repetitions at 4°C for ten minutes.

2.8.1.5 ISOLATION OF CRUDE MITOCHONDRIA FROM MUSCLE

The skeletal muscle (musculus biceps femoris) of five mice was weighted. It was washed 3x and minced in ice-cold preparation buffer. Afterwards it was transferred to Digestion buffer$_{Muscle}$ (40 mL/4-5 g tissue) and stirred on ice for three minutes. The tissue was homogenized using a Polytron homogenizer for 3x3 seconds at 18,000 turns (fat and connective tissue was removed in between). The homogenate was stirred on ice for six more minutes and eventually centrifuged at 4°C and 490xg for ten minutes. The supernatant was filtered through nylon gaze and centrifuged at 10,400xg and 4°C for ten minutes. The pellet was resuspended in preparation buffer and centrifugation was repeated. Subsequently, mitochondria were pelleted at 4°C and 3,800xg for ten minutes.

2.8.1.6 ISOLATION OF MITOCHONDRIA FROM PRIMARY BROWN ADIPOCYTES

Mitochondria were isolated from primary brown adipocytes using a commercially available mitochondria isolation kit (Miltenyi Biotech, 130-096-946) according to manufacturer's instructions. Briefly, cells were harvested using trypsin enriched with collagenase as described in **section 2.2** and washed three times with ice-cold PBS (300xg, ten minutes, 4°C). Next, cell pellets were carefully and slowly lysed using a G18 cannula (max. 14 strokes). After magnetic labeling with mouse Anti-TOM22 Microbeads for 60 minutes and enrichment using a LS Column in the magnetic field of a QuadroMACS separator, mitochondria were pelleted and washed with both, STE + 2% and 0.4% essentially FA-free BSA (13,000xg, two minutes, 4°C). Per mitochondrial sample, cells from BAT of three mice were pooled.

2.8.1.7 PREPARATION OF SMALL UNILAMELLAR VESICLES AND FUSION WITH IBAT MITOCHONDRIA

Small unilamellar donor vesicles were generated according to the principles described by Kainu and colleges *(Kainu et al. 2010)* and Suresh and London *(Suresh und London 2022)*. Briefly, palmitoyl-oleoyl-phosphatidylcholine (POPC, Avanti Polar Lipids, 850457P), palmitoyl-oleoyl-phosphatidic acid (POPA, Avanti Polar Lipids, 840857P) and free cholesterol (FC, Sigma-Aldrich, C3045) were mixed in varying ratios (0% FC, 95% POPC, 5% POPA; 20% FC, 75% POPC, 5% POPA; 40% FC, 55% POPC, 5% POPA and 60% FC, 35% POPC, 5% POPA) in chloroform/methanol (9:1) with a total lipid concentration of 0.5 mM. The solvent was evaporated using a nitrogen stream leaving a thin lipid film on Pyrex® tube walls. After PBS was added, donor vesicles were generated using sonication and vortex intervals of 6x5 min and 7x1 min, respectively. Undispersed lipids and probe particles were removed (3,000xg, five minutes). For fusion with mitochondria, donor vesicle solutions were incubated with 10 mM methyl-

α-cyclodextrin (AraChem Cyclodextrin-shop) for 60 minutes at 63°C and 300 rpm, and subsequently, with 0.5-0.8 mg of isolated BAT mitochondria for 60 minutes at 4°C. Next, mitochondria-vesicle solutions were centrifuged and washed at 10,000xg and 4°C for ten minutes. Control mitochondria were treated as those incubated with donor vesicles. Mitochondrial pellets were either resuspended in 0.1% SDS for lipidomic analyses or in mitochondrial respiration buffer for respiratory analyses. For mitoplast preparation, mitochondrial pellets were incubated with digitonin (100 µg mitochondrial protein with 100 µl of 1.2 mg/mL digitonin) for 25 minutes on ice. Digitonin was removed after a final ten minute centrifugation step of 10,000xg at 4°C.

2.8.2 RNA ISOLATION OF ADIPOSE TISSUE AND ADIPOCYTES

2.8.2.1 ADIPOSE TISSUE

RNA from tissue was isolated using phenol/chloroform (Trizol, Thermo Fisher Scientific, 15596018; chloroform, Sigma-Aldrich/Merck, 34854) extraction and the SV total RNA Isolation system (Promega, Z3101). Briefly, frozen tissue covered with Trizol was homogenized using an Ultra-Turrax® (IKA), incubated for five minutes at room temperature, and centrifuged at 2,500xg and 4°C for five minutes. The supernatant was collected and shaken after adding 200 µL chloroform. After three minutes incubation at room temperature, phases were separated at 12,000xg (15 minutes, 4°C). The clear upper phase was collected and further processed as recommended by Promega's instructions.

2.8.2.2 ADIPOCYTES

RNA from cells was isolated using the RNeasy® Mini Kit (Qiagen, 74106). This technology combines the speed of micro spin technology with selective binding properties of a silica-based membrane. Therefore, cells were harvested as described in **section 2.2**. Lysates were defrosted on ice, pipetted onto a QIAshredder® spin column and centrifuged (two min, 14,000 rpm, RT). The flow-through was transferred into a new 1.5 mL tube and mixed with 70% Ethanol (1:1). Up to 700 µL of this mixture was pipetted onto a RNeasy® spin column in a 2 mL collection tube. The flow-through, which was generated during centrifugation (15 seconds, 8,000xg, RT), was discarded. This was repeated with the same column if the lysate exceeded 700 µL. The centrifugation was rerun twice with 700 µL RW1 buffer and 500 µL of RPE buffer, respectively, and the flow-through was discarded. The centrifugation was repeated after adding 500 µL of RPE buffer. Eventually, the RNeasy® spin column within the emptied collection tube was filled again with 500 µL of RPE buffer, centrifuged (two min, 8,000xg, RT) and placed in a new 2 mL collection tube. Next, the dry column was centrifuged (one min, 10,000xg, RT) to eliminate buffer residues. Afterwards, the spin column was transferred into a new 1.5 mL tube and a final centrifugation step (8,000xg, RT, one min) followed, after pipetting 30 µL of ultra- pure RNase-free water onto the spin column. The RNA eluate was stored at -80°C.

2.8.3 CDNA SYNTHESIS, PRIMER DESIGN AND REAL-TIME QUANTITATIVE PCR

RNA concentration was measured using a NanoDrop™ 2000 spectrophotometer (Thermo Fisher Scientific). To ensure sufficient purity of the isolated RNA, the 260/280 ratio (protein/phenol contamination) as well as the 260/230 ratio (ethanol contamination) was controlled. To confirm a high quality of RNA, RNA integrity was assessed using a Bioanalyzer RNA 6000 Nanochip® according to the manufacturer's instructions (Agilent Technologies). RNA was only used if RNA integrity numbers (RIN) exceeded seven.

As template for real-time quantitative polymerase chain reaction (qPCR), complementary deoxyribonucleic acid (cDNA) was reverse transcribed from RNA using the reverse transcriptase Avian Myeloblastosis Virus (AMV). Therefore, 0.1-1.0 µg of RNA (defrosted on ice) was mixed with RNAse-free water to a final volume of 10.4 mL. The master mix with reagents from a reverse transcription system (Promega, A3500) was prepared according to **Table 18**, of which 9.6 µL were added to each RNA dilution. RNA was reverse transcribed (one hour, 45°C) and subsequently, AMV-reverse transcriptase was inhibited (five min, 95°C). The synthesized cDNA was diluted using RNase-free water (5 ng/µL) and stored at -20°C.

Table 18: *Master mix composition for cDNA synthesis (Promega; A3500).*

Compound	Company	Cat. No.	Concentration
RNA	-	-	100 ng - 1 µg
AMV reverse transcriptase	Promega	M5108	15 u
10x reaction buffer	Promega	A356A	1x
RNAsin®	Promega	N251A	40 u
$MgCL_2$	Promega	A351H	5 mM
dNTP mix	Promega	C114B	1 mM
Random primers	Promega	C118B	0.5 µg

Gene expression levels were assessed applying real-time quantitative PCR (qPCR). cDNA and master mix, consisting of SyGreen Mix Lo-Rox (Nippon Genetics, PB20.11) and 0.25 µM forward/reverse primer, were combined in 384-well FrameStar® PCR plates (2 µL cDNA + 8 µL master mix/well). Finally, the plate was centrifuged (1,500 rpm, 30 seconds) and measured using a LightCycler 480® (Roche LifeScience, protocol see **Table 19**). The mRNA expression levels were normalized to 18S, ß-actin or TBP and quantified using the $2^{-\Delta\Delta CT}$ method *(Livak und Schmittgen 2001; Langmann et al. 2006)*.

Table 19: *Protocol for real-time qPCR.*

	Duration	Temperature	Cycles
Initial denaturation	7 minutes	95°C	1
Denaturation	10 seconds	95°C	
Annealing	15 seconds	60°C	45
Extension	15 seconds	72°C	
Melting Curve	3 minutes	60-95°C	1

For primer sequence design, respective *mus musculus* transcripts were obtained from ENSEMBL (http://www.ensembl.org). The primer flanked between two exons located in the upper part of the respective gene and base pairs (bp) were controlled for possible mutations. The sequences were designed with primer lengths between 18-25 bp, GC contents between 40-70% and melting temperatures (Tm) between 58-65°C. Primer quality was reviewed via OligoCalc (http://biotools.nubic.northwestern.edu) and the amplicon length (70-150 bp) as well as primer specificity was checked via *in-silico* PCR using the USCS genome browser (http://genome.ucsc.edu). All primers are listed in **Table 20**.

Table 20: *Primer sequences used for real time qPCR.*

Primers for qPCR	Forward sequence 5'-3'	Reverse sequence 5'-3'
Housekeeper genes		
TBD	GAAGCTGCGGTACAATTCCAG	CCCCTTGTACCCTTCACCAAT
18S	GGCCCTGTAATTGGAATGAGTC	CCAAGATCCAACTACGAGCTT
ß-Actin	CTCTGGCTCCTAGCACCATGAAGA	GTAAAACGCAGCTCAGTAACAGTCCG
UCP1	GGCCTCTACGACTCAGTCCA	TAAGCCGGCTGAGATCTTGT
STARD3	CACCTTCTGCCTCTTCGTCACC	AACACTGGCATCCGGAAGAA
STARD7	AGAATCCAGGAGGAGGAGTT	CTTTGGTTCGGGAGGGTAAT
PISD	CCTCTTCAGGCAGGTGTCAGA	CCAGTGACTAGCAAGTTTGGG
FABP4	GATGGTGACAAGCTGGTGGT	TTTATTTAATCAACATAACCATATCCA
DIO2	GATGCTCCCAATTCCAGTGT	TGAACCAAAGTTGACCACCA
ATGL	GGAAATTGGGTGACCATCTG	AAGGCCACATTGGTGCAG
HSL	CTTCTCCCTCTCGTCTGCTG	GCCTAGTGCCTTCTGGTCTG
DGAT1	GGAATATCCCCGTGCACAA	CATTTGCTGCTGCCATGTC
DGAT2	CCGCAAAGGCTTTGTGAA	GGAATAAGTGGGAACCAGATCAG
HMGCR1	ATGCCTTGTGATTGGAGTTGG	TGGACGACCCTCACGGCTTTC
PPARγ	GAAGGATGCAAGGGTTTTTTCC	GGCACTTCTGAAACCGACAGT
CIDEA	TGCTCTTCTGTATCGCCCAGT	GCCGTGTTAAGGAATCTGCTG
CPT1B	GGCACCTCTGGGAGTTTGTCCT	TGCTCGGGAATGTCCCAC
ELOVL3	AGGAGTACTGGGTAAGCTCAT	GCAAGCTGAAGCTCTTCC
ELOVL6	CAGGAAAACTGGAAGAAGTCTTTCC	CTGAAGACGGCAAGAGTCAGC
ADIPOQ	GAAAGGAGATGCAGGTCTTCTTGG	ACATAAGCGGCTTCTCCAGGC
FAS	ATGAAGCTGGGCATGCTCAG	CCGGCATTCAGAATCGTGGC
SREBP2	GACGTTCAGCACCGCTCC	AGGCTTTGCACTTGAGGCTG
ACAT2	GCAGAGGGCCAAGGTGGCT	TGCACCCACACTGGCTTGTCG
HMGCS	GTCTCCTTGCTTTGCTCGTT	TCCAGCATCTACACCATCGT
MVK	ATATCCCTGGAGTGTGAGCG	CCACTGTGGCTTGCTCTAGA
PMVK	TGGATGCGAGCACCTACAAGG	TCACAGCCCCATAGGCCTCC
MVD	CTCAGCCGCAGGCTATGC	AGACTGCGGCACGCACTG
GGPS1	CACAGGCATTTAATCACTGGCTG	CTGGGAAACCACGTCGGAGC
IDI1	GGAGAGGATTGAAGTACAGCTCT	CAATAAGAATACACATCTCCGCTAG
FDFT1	CCGACAAGTGCTGGAGGACTT	TGGCAGATGTCATCGATCACTG
SQLE	CCGGAAGTGATCATCGTGGGAT	GACTCATGATGAATCGGCCATGG
LSS	GGCAGAGATGGACTTATTATCAAGC	TCAGCCTGCAGCTTGGCAT
SC5DL	GGCCTGCACCACAGACTGGT	CTCTGAAGGAAGCCGTCCACA
DHCR7	GGCCATGCTAGTCTGGCAGA	ACCTGGCAGAAATCTGTGGCAG
LDLR	CTAGCGATGCATTTTCCGTC	GTCATCGCCCTGCTCCTT
CYP51A1	CCAATTCCATTCCTTGGCCATGC	CTTCTTCTGCATTCAGGTCTTCG
STARD1	TTGGGCATACTCAACAACCA	GAAACACCTTGCCCACATCT
STARD4	AAGCTCAAGGAGTTATGGATGACG	TCTTCATAGCCCACAGTATAGGAGA
STARD5	GTACCGAGGAGAAGGGATTCT	GAACCTCCACGCCCTCAGCTG
TSPO	GGAACAACCAGCGACTGC	GTACAAAGTAGGCTCCCATGAA
VDAC1	CTTGCTCGTGGACTGAAGCT	CACAGCCGAGGTTGATGTGCT
ATAD3a	ACCGCCAGACCATCTTGGAGT	TTTGTCCCAGTCTGTCACAAATGCA
Cox7a1	GCCGACAATGACCTCCCAGTA	TGTTTGTCCAAGTCCTCCAA
PEMT	GGTTACATGGACCCCACAGA	AGTTCTCTGCTCCCATCTCG
Adcy5	CAACGCCAAGCAGGAGGATA	GCGAAGAGCTCATTGAGGGT
PSS1	CTTCATGCATCTCCTGCCCAATTTT	TTGAAGCTTGCCCAGTGGTAAG
PSS2	GAGATCTACGACTTCATGGATG	CCTGCTGGCCCAGCTTCCT

SCD1	TGCCTCTTCGGGATTTTCTACTAC	TGGAACGCCATGGTGTTGGC
SREBP-1c	ATGGATTGCACATTTGAAGACATG	AGAGGAGGCCAGAGAAGCAG
SREBP-2c	GACGTTCAGCACCGCTCC	AGGCTTTGCACTTGAGGCTG
PGAM5	GAACTACATCCACCGAGCTGA	GGGAAACTGCAACGCTCTAC

2.8.4 PROTEIN ISOLATION AND BCA ANALYSIS

Frozen cell plates were kept on ice and adipocytes were slowly defrosted in RIPA buffer (+ 0.1% phosphatase and 0.1% protease inhibitor). Cells were detached with cell scrappers and transferred in 1.5 mL tubes. The cell suspensions were shaken at maximum speed and 4°C for 15 minutes on a VXR basic Vibrax® (IKA) and subsequently centrifuged at 16,000xg and 4°C for another 15 minutes. The middle phase (protein) was collected in fresh tubes and stored at -80°C. The protein concentration was assessed conducting a bicinchoninic acid assay (BCA) according to the manufacturer's instructions (Pierce BCA protein assay; Thermo Fisher Scientific; 23225). Protein lysate dilutions (1:10) and a BSA standard curve (0 µg/mL, 125 µg/mL, 250 µg/mL, 500 µg/mL, 1000 µg/mL, 1500 µg/mL, and 2000 µg/mL) were mixed with assay reagents and incubated at 37°C for 30 minutes. The absorbance was determined using an Infinite® M200 multi-detection plate reader (Tecan) at 562 nm. All used compounds and buffers are listed in **Table 21**.

Table 21: *Composition of buffers and solutions used for protein isolation and immunoblotting.*

Compound	Company	Cat. No.	Concentration
RIPA buffer			
ddH_2O	-	-	-
NaCL	Sigma-Aldrich/Merck	6404	150 mM
Tris-HCL	Sigma-Aldrich/Merck	T3253	50 mM
Na-deoxycholate	Sigma-Aldrich/Merck	D6750	0.25%
Nonidet-P40	Fluka	74385	1%
EDTA	Sigma-Aldrich/Merck	P7626	1 mM
Protease Inhibitor	Sigma-Aldrich/Merck	P8340	0.1%
Phosphatase Inhibitor	Sigma-Aldrich/Merck	P5726	0.1%
1x running buffer			
ddH_2O	-	-	-
NuPAGE™ MES SDS-Running Buffer (20x)	Thermo Fisher Scientific	NP0002	1x
1x transfer buffer			
ddH_2O	-	-	-
Methanol	Sigma-Aldrich/Merck	322415	10%
NuPAGE™ Transfer Buffer (20x)	Thermo Fisher Scientific	NP0006	1x
10x TBS			
ddH_2O	-	-	-
NaCL	Sigma-Aldrich/Merck	6404	1500 mM
Tris Base	Sigma-Aldrich/Merck	T1503	200 mM
1x TBS-T			
ddH_2O	-	-	-
Tween-20	Sigma-Aldrich/Merck	P1379	0.1%
10x TBS	See above	See above	1x
Blocking buffer			

TBS-T	See above	See above	1x
Milk powder	Carl Roth	T-145.2	5%
Sample buffer			
ddH_2O	-	-	-
NuPAGE™ Reducing Agent (10x)	Thermo Fisher Scientific	NP0009	10%
NuPAGE™ LDS Sample Buffer (4x)	Thermo Fisher Scientific	NP0007	25%
Protein isolate	-	-	40 µg

2.8.5 IMMUNOBLOTTING

2.8.5.1 SDS-PAGE GEL ELECTROPHORESIS AND SEMI-DRY BLOTTING

For immunoblotting, a Minigel-Tank and Blot-Modul system was used (Thermo Fisher Scientific, NW2000). Proteins were separated in pre-cast gradient Bis-Tris gels (NuPAGE™ 4-12%; Thermo Fisher Scientific, NP0321) according to the manufacturer's recommendations. For 40 µg of protein per lane and 3 µg leader (PageRuler Plus prestainend; Thermo Fisher Scientific, 26619), the gel electrophoresis run at 150 V for 60 minutes. The gel containing separated proteins was assembled between pre-soaked filter papers (Thermo Fisher Scientific, 84784) and sponges according to the manufacturer's instructions and, eventually, transferred onto a nitrocellulose membrane 0.45 (Thermo Fisher Scientific, 88018) at 10 V for 60 minutes. All used compounds and buffers are listed in **Table 21**.

2.8.5.2 BLOCKING, INCUBATION WITH PRIMARY/SECONDARY ANTIBODIES, AND DETECTION

Nitrocellulose membranes were blocked with 5% milk powder diluted in TBS-T for two hours (or overnight) on a shaker at 4°C. Between blocking and the first antibody incubation, as well as between incubations with different antibodies, the membrane was washed for 30-40 minutes conducting TBS-T changes every five minutes. Primary antibodies were incubated for two hours or overnight at 4°C, whereas secondary antibodies were incubated for 1.5 hours at room temperature. All employed antibodies and dilutions are listed in **Table 22**. Sapphire Biomolecular Imager (Azure Biosystems) and Image Studio™ Lite v.5.2. were utilized for antibody detection, analysis, and quantification.

Table 22: *Primary and secondary antibodies used for immunoblotting.*

Antibodies for Western Blot	Concentration	Company	Cat. No.
Loading control			
HSP90	1:1.000	Cell Signalling	4877S
Primary Antibodies			
Cytochrome C	1:500	Santa Cruz	Sc-13156
FACL4	1:200	Abcam	Ab155282
VDAC1	1:500	Abcam	Ab15895
PISD	1:250	Sigma-Aldrich/Merck	HPA031091
Na^+/K^+-ATPase	1:500	Santa Cruz	sc-21712
Tubulin	1:500	Santa Cruz	sc-58884
Perilipin	1:250	Millipore	AB 10200
IP3R	1:100	Santa Cruz	sc-377518
UCP1	1:1.000	Abcam	Ab23841

Secondary Antibodies			
Donkey anti-Mouse IgG 680RD	1:20.000	Licor	926-68072
Goat anti-Rabbit IgG 680RD	1:20.000	Licor	926-68071
Goat anti-Mouse IgG 800CW	1:15.000	Licor	926-32210
Goat anti-Rabbit IgG 800CW	1:20.000	Licor	926-32211

2.8.6 LIPIDOMICS

Lipid profile analysis was conducted at the University Hospital Regensburg in collaboration with Gerhard Liebisch and Marcus Höring (Institute of Clinical Chemistry and Laboratory Medicine). Lipid species were annotated according to the proposal for shorthand notation of lipid structures that are derived from mass spectrometry *(Liebisch et al. 2020)*. Measurements were taken from distinct samples.

2.8.6.1 INTERNAL STANDARDS

The following non-naturally occurring lipid species were applied as internal standards: CE 17:0, CE 22:0, CL 14:0/14:0/14:0/14:0, Cer 18:1;O2/14:0, Cer 18:1;O2/17:0, DG 14:0/14:0/0:0, DG 20:0/20:0/0:0, [D7]FC, HexCer 18:1;O2/12:0, HexCer 18:1;O2/17:0, LPC 13:0/0:0, LPC 19:0/0:0, LPE 13:0/0:0, PC 14:0/14:0, PC 22:0/22:0, PE 14:0/14:0, PE 20:0/20:0, PI 17:0/17:0, PS 14:0/14:0, PS 20:0/20:0, SM 18:1;O2/12:0, TG 17:0/17:0/17:0, and TG 19:0/19:0/19:0.

2.8.6.2 TISSUE HOMOGENIZATION

Tissue was homogenized using a Precellys® 24 tissue homogenizer from Bertin Instruments (Berlin, Germany). Therefore, an amount of approximately 25-75 mg was added to a Precellys cup (Sarstedt, 72.694) containing ceramic beads (VWR, 432-0356) (V= 2 mL). H_2O/MeOH = 1/1 (v/v) was added to suspend the samples at a concentration of 0.05 mg/µL. The homogenizer (FastPrep®, Fisher Scientific) was operated at 5,000 rpm, two cycles of 15 seconds run time, and a 60 second break interval between both cycles.

2.8.6.3 LIPID EXTRACTION

Samples were spiked with internal standards prior to lipid extraction (solvent of standards was removed by vacuum centrifugation). Mitochondria containing approximately 100 µg of protein were extracted according to the protocol described by Bligh and Dyer *(BLIGH und DYER 1959)* with a total chloroform volume of 2 mL. A volume of 0.8 mL (for FIA-MS/MS), 0.5 mL (for FIA-FTMS) and 0.3 mL (for FIA-FTMS, CL determination) of the separated chloroform phase was transferred by a pipetting robot (Tecan Genesis RSP 150, Männedorf, Switzerland) and vacuum dried. The residues were dissolved in 0.8 mL methanol/chloroform (3:1, v/v) with 7.5 mM ammonium acetate, 1.2 mL chloroform/methanol/2-propanol (1:2:4 v/v/v) with 7.5 mM ammonium formate, or 0.5 mL methanol/chloroform (5:1, v/v) with 0.005% methylamine, respectively. For analysis of adipose tissue and adipocytes, tissue homogenates containing a wet weight of 2 mg and cell homogenates containing 100 µg protein were extracted instead. A total chloroform volume of 1.6 mL was vacuum dried, dissolved in 1.6 mL methanol/chloroform (3:1, v/v) with 7.5 mM ammonium acetate and analyzed by FIA-MS/MS.

2.8.6.4 LIPID ANALYSIS BY MASS SPECTROMETRY

The analysis of lipids was performed by direct flow injection analysis (FIA), using either a triple quadrupole mass spectrometer (QQQ; FIA-MS/MS) or a hybrid quadrupole-Orbitrap high-resolution mass spectrometer (FIA-FTMS). Both instruments were equipped with a heated electrospray ionization source. FIA-MS/MS (QQQ) was performed in positive ion mode using the analytical setup and strategy described previously *(Liebisch et al. 2004)*. For the FIA-MS/MS analyses a fragment ion of *m/z* 184 was used for PC and *m/z* 193 for choline labeled PC[D_9]. The following neutral losses were applied: PE, 141; PE[D_4], 145; PG, 189; PI, 277 and PS, 185. PE-based plasmalogens (PE P) were analyzed according to the principles described by Berry and colleagues *(Zemski Berry und Murphy 2004)*. Sphingosine-based Cer were analyzed using a fragment ion of *m/z* 264. Correction for isotopic overlap of lipid species was performed for all lipid classes. A detailed description of the FIA-FTMS method was published recently *(Höring et al. 2021)*. TG, DG, and CE were recorded in positive ion mode as $[M+NH_4]^+$ in *m/z* range 500–1,000 and a target resolution of 140,000 (at *m/z* 200). CE species were corrected for their species-specific response *(Höring et al. 2019)*. PC, ether PC (PC O), and SM were analyzed as $[M+HCOO]^-$ in negative ion mode in *m/z* range 520–960 at the same resolution setting. Multiplexed acquisition (MSX) was applied for the $[M+NH_4]^+$ of FC and the corresponding internal standard [D_7]FC *(Höring et al. 2019)*. CL were determined as deprotonated adducts in negative ion mode in *m/z* range 1,200–1,600 from the extract dissolved in methanol/chloroform (5:1, v/v) with 0.005% methylamine. Quantification was achieved by multiplication of the spiked-in IS amount with the analyte-to-IS intensity ratio.

2.8.6.5 STATISTICAL ANALYSIS OF LIPIDOMIC DATA

Lipidomic data were analyzed as described previously *(Kindt et al. 2018)*. Generated data were exported to Excel 2016 and further analyzed by self-programmed Macros. If measured in different batches, lipid species concentrations were quotient normalized *(Dieterle et al. 2006)*. For generation of volcano plots, all data were log2 transformed to ensure that they were normally distributed. Lipid species were excluded if they were undetectable in more than 50% of the samples per group. A standard two-sided, unpaired t-test assuming unequal variances was used to test for significantly different abundances in the conditions. The Benjamini–Hochberg method to calculate the false discovery rate (FDR) was used to account for multiple testing ($p_{adj} < 0.01$). Fold changes were calculated as the difference between mean of the log-transferred values in iBAT and liver or eWAT or iWAT or muscle.

2.8.7 PROTEOMICS

Proteomics was conducted in cooperation with Bernhard Küster (TUM, Chair of Proteomics and Bioanalytica) and Piero Giansanti (MRI, Bavarian Center for Biomolecular Mass Spectrometry).

2.8.7.1 LYSIS, PROTEIN DIGESTION AND PEPTIDE FRACTIONATION

Isolated organelles were resuspended in lysis buffer consisting of 8 M urea in 50 mM Tris-HCl pH 8 and containing EDTA-free protease inhibitors cocktail (Roche). Lysis was performed by sonication in a Bioruptor Pico (Diagenode) using a ten cycles program (30 s ON, 30 s OFF), and lysate were subsequently cleared by centrifugation for ten minutes at 20,000xg and 4°C. Protein was reduced with 10 mM DTT at 37°C for 40 minutes on a thermoshaker at 700 rpm and alkylated with 55 mM chloroacetamide at RT for 30 minutes in the dark. Tryptic digestion was performed overnight at 37°C

with sequencing grade modified trypsin (Promega, 1:50 enzyme-to-substrate ratio) after 4-fold dilution with 50 mM Tris-HCl, pH 8. Digests were acidified by addition of formic acid (FA) to 1% (v/v) and desalted using Sep-Pak C18 cartridges (Waters). Desalted peptides were resuspended in 10 mM ammonium acetate, pH 4.7, and subjected to peptide fractionation via trimodal mixed mode chromatography on a Dionex Ultra 3000 HPLC system operating an Acclaim Trinity P1 3 µM 2.1×150 mm column (Thermo Fisher), as previously described *(Yu et al. 2017)*. A total of 32 fractions were collected, vacuum-dried in a SpeedVac (UniEquip) and stored at -20°C until LC-MS/MS analysis.

2.8.7.2 PROTEOMIC MEASUREMENT OF MITOCHONDRIA AND CELLULAR HOMOGENATES

Mitochondrial samples were analyzed on a micro-flow LC-MS/MS system using a modified Vanquish pump coupled to an Orbitrap Fusion Lumos mass spectrometer (both Thermo Fisher). Chromatographic separation was performed via direct sample injection onto the head of a 15 cm Acclaim PepMap 100 C18 column (2 µm particle size, 1 mm ID, Thermo Fisher) at a flow rate of 50 µL/min *(Bian et al. 2020)*. Solvent A was 0.1% FA + 3% DMSO in water, and solvent B was 0.1% FA + 3% DMSO in ACN. Samples were separated with a linear gradient of 3% to 28% B in 15 min. Total analysis time was 17 minutes. The Fusion Lumos was operated in positive ion mode, using an electrospray voltage of 3.5 kV, capillary temperature of 325°C and vaporizer temperature of 125°C. The flow rates of sheath gas, aux gas and sweep gas were set to 32, 5, and 0, respectively. The Fusion Lumos was operated in a data-dependent acquisition (DDA) to automatically switch between MS and MS/MS. Survey full-scan MS spectra were recorded in the orbitrap at a resolution of 60,000 at m/z 200 and an AGC target value of 4E5 with a maximum injection time (IT) of 50 ms. The MS1 mass range was set to 360-1300. The isolation width was set to 0.4 m/z, and the first mass was fixed at 100 m/z. The normalized collision energy was set to 32%. Peptide match was set to 'preferred', and isotope exclusion was enabled. MS2 spectra for peptide identification were recorded in the ion trap in rapid scan mode with a top speed approach using a 0.6-s duration (isolation window 0.4 m/z, AGC target value of 1e4, maxIT of 10 ms). MS1 and MS2 spectra were acquired in profile and centroid mode, respectively. The dynamic exclusion value was set to 12 s. Measurements were taken from distinct samples.

For cell homogenates, first TMT 10-plex labelling according to Zecha et al. *(Zecha et al. 2019)* was applied. Therefore, samples were resuspended in 20 µL HEPES (50 mM, pH 8.5) and mixed for one hour at 25°C with 5 µL TMT reagent stock solution (11.6 mM) in 100% anhydrous ACN. Samples were quenched by using 2 µL 5% hydroxylamine, pooled, and acidified by using 20 µL of 10% FA. Before further processing, the pooled samples were vacuum dried, desalted and stored at -80°C. The dried peptides were resuspended in ammonium acetate (10 mM, pH 4.7) and fractionated by trimodal mixed mode chromatography on an Acclaim Trinity P1 2.1 x 150 mm, 3 µm column (Thermo Fisher) *(Yu et al. 2017)*. The measurements were conducted using Nano flow LC-ESI-MS, carried out in a Dionex Ultimate 3000 UHPLC+ system coupled to a Fusion Lumos Tribrid mass spectrometer (Thermo Fisher Scientific). The peptides were transferred to a trap column (75 µm x 2 cm, packed in-house with 5 µm Reprosil C18 resin, Dr. Maisch). After a washing step with 0.1% FA (ten minutes, flow rate 5 µL/min), the peptides were put in an analytical column (75 µm x 45 cm, packed in-house with 3 µm Reprosil C18 resin, Dr. Maisch) for 50 minutes (flow rate 300 nL/min) and chromatographically separated in a linear gradient (ranging from 8%-34% solvent B: 0.1% FA, 5% DMSO in ACN in solvent A: 0.1% FA in 5% DMSO). The MS3-based TMT method employed an initial MS2 spectrum for peptide identification recorded in the ion trap in rapid scan mode with a top speed approach utilizing a 2-second duration (isolation window 0.7 m/z, AGC target value 1E4, maxIT of 35 mn). The fragmentation setting was CID,

with a NCE of 35% and an activation Q of 0.25. Subsequently, an additional MS3 spectrum for TMT quantification was obtained for each peptide precursor in the Orbitrap at 50,000 resolutions (AGC of 5E4 charges, maxIT of 86 ms). The precursor was fragmented in a manner analogous to that employed for the MS2 analysis. Thereafter, the ten most intense peptide fragments were selected in a synchronous manner, and further fragmentation was achieved via HCD, utilizing a NCE of 55%. The dynamic exclusion period was set to 90 seconds.

2.8.7.3 DATA PROCESSING AND BIOINFORMATIC ANALYSIS

Raw data files were processed with MaxQuant (version 1.6.10.43) using default parameters *(Cox und Mann 2008)*. Spectra were searched against the UniProtKB database (Mus musculus, UP000000589, 55,431 entries downloaded on 12.2019). Enzyme specificity was set to trypsin and up to two missed cleavages were allowed. Cysteine carbamidomethylation was set as a fixed modification while Ntem-acetylation of protein and oxidation of methionine were selected as variable modifications. Precursor tolerance was set to 5 ppm, and fragment ion tolerance to 20 ppm. Results were adjusted to 1% false discovery rate at protein, peptide levels. Identifications were filtered to remove contaminants and decoy hits using in Perseus (v. 1.6.1.1) *(Tyanova et al. 2016)*, before any subsequent analysis. The mass spectrometry proteomics data have been deposited in the ProteomeXchange Consortium *(Vizcaíno et al. 2013)* via the PRIDE partner repository with the dataset identifier PXD028128 (https://www.ebi.ac.uk/pride/archive/login - username: reviewer_pxd028128@ebi.ac.uk, password: bxO95E4L).

2.8.7.4 HIERARCHICAL CLUSTERING OF PROTEOMIC DATA

Proteomics data (Log_{10}(signal intensities)) were hierarchically clustered using a distance matrix based on Euclidean distance and complete linkage in KNIME 4.3.2. Analytics Platform (https://www.knime.com).

2.9 RESPIRATORY ANALYSIS OF PRIMARY BROWN/BEIGE ADIPOCYTES AND MITOCHONDRIA

All utilized buffers for microplate-based respirometry are listed in **Table 23** and for high-resolution respirometry in **Table 24**.

Table 23: *Composition of buffers used for microplate-based respirometry.*

Compound	Company	Cat. No.	Concentration
Respiration buffer adipocytes, pH 7.4			
DMEM Base	Sigma-Aldrich/Merck	D5030	-
Glutamax	Life Technologies	35050-061	2 mM
Glucose	Carl Roth	X997.1	25 mM
NaCl	Carl Roth	3957.1	31 mM
Fatty acid-free BSA	Sigma-Aldrich/Merck	A3803	2%
ddH_2O	-	-	-
Respiration buffer mitochondria, pH 7.2			
Sucrose	Sigma-Aldrich/Merck	84097	125 mM
K^+-TES	Carl Roth	9137.1	20 mM
$MgCL_2$	Sigma-Aldrich/Merck	M3409	2 mM
EDTA	Sigma-Aldrich/Merck	E9884	1 mM
KH_2PO_4	Carl Roth	3904.1	4 mM
Pyruvate	Sigma-Aldrich/Merck	COM448637111	10 mM
Malate	Sigma-Aldrich/Merck	M9138	2 mM
Fatty acid-free BSA	Sigma-Aldrich/Merck	A3803	0.4%
ddH_2O	-	-	-

Table 24: *Composition of buffer used for high-resolution respirometry.*

Compound	Company	Cat. No.	Concentration
Respiration buffer BAT cMito (KHE), pH 7.2			
KCL	Sigma-Aldrich/Merck	P3911	50 mM
TES	Carl Roth	9137.1	5 mM
$MgCL_2$	Sigma-Aldrich/Merck	M3409	2 mM
KH_2PO_4	Carl Roth	3904.1	4 mM
EGTA	Carl Roth	3054.2	1 mM
Fatty acid-free BSA	Sigma-Aldrich/Merck	A3803	0.4%
ddH_2O	-	-	-

2.9.1 RESPIRATORY FUNCTION AND UCP1 ACTIVITY ANALYSES IN INTACT ADIPOCYTES USING MICROPLATE-BASED RESPIROMETRY

Mitochondrial bioenergetics in primary cells were assayed using microplate-based respirometry as previously published *(Schweizer et al. 2019; Oeckl et al. 2020)*. After seeding pre-adipocytes equally onto 96-well seahorse plates, cells were differentiated as described before and exposed to respective treatments (e.g. lentiviral overexpression). On the experimental day, the cells were washed twice with respiration medium. The adipocytes were kept in respiration medium supplemented with 2% essentially fatty-acid free BSA for 60 minutes in a 37°C incubator w/o CO_2. One to two days before conducting the experiment, injection cartridges were hydrated with calibrant at 37°C in a non-CO_2 incubator. One hour before the measurement, the calibrant was replaced with fresh calibrant. After loading the cartridge with substrates and inhibitors required for the respiratory analysis, it was calibrated/equilibrated at 37°C using an XF96 or XF96 Pro Extracellular Flux Analyzer (Agilent Technology). Subsequently, the cells were loaded into the same analyzer and the basal oxygen consumption rate (OCR) was assessed. Afterwards, ATP-linked respiration (5 µM oligomycin; Sigma-Aldrich/Merck), UCP1-mediated uncoupled respiration (0.5 µM isoproterenol; Sigma-Aldrich/Merck) and maximal oxidative capacity (7 µM FCCP; Sigma-Aldrich/Merck) were assessed. To distinguish

mitochondrial oxygen consumption from non-mitochondrial oxygen consumption, 5 µM antimycin A (Sigma-Aldrich/Merck) was injected at the end of the measurement. A scheme and description of the protocol is illustrated in **Table 25** and **Figure 9**. To compare UCP1 activity between different groups, data obtained from the XF96 Analyzer were normalized to the end point of ATP-linked respiration (oligomycin), whereas data obtained from the XF96 Pro analyzer were normalized to the cell number determined using a BioTek Cytation 1 cell reader (Agilent Technologies). For cell counting, cells were subjected to a brightfield scan directly before recording the OCR, and to a fluorescent scan after the measurement by enriching antimycin injections with Hoechst dye (nuclei staining). Data analysis was conducted using Wave or Wave Pro Software (Agilent Technologies).

Table 25: *Protocol for microplate-based respirometry assay for brown and beige adipocytes.*

Protocol	Time (min)	Loop/ Compound	Company	Cat. No.	Concentration
Calibration					
Equilibration	15				
Mixture	4	4x			
Measure	2				
Injection Port A		**Oligomycin**	Merck	O4876	5 µM
Mixture	4	4x			
Measure	2				
Injection Port B		**Isoproterenol**	Merck	I6505	0.5 µM
Mixture	4	4x			
Measure	2				
Injection Port C		**FCCP**	Merck	C2920	7.5 µM
Mixture	4	3x			
Measure	2				
Injection Port D		**Anti A + Hoechst**	Merck	A8674, H3570	5 + 8 µM
Mixture	4	4x			
Measure	2				

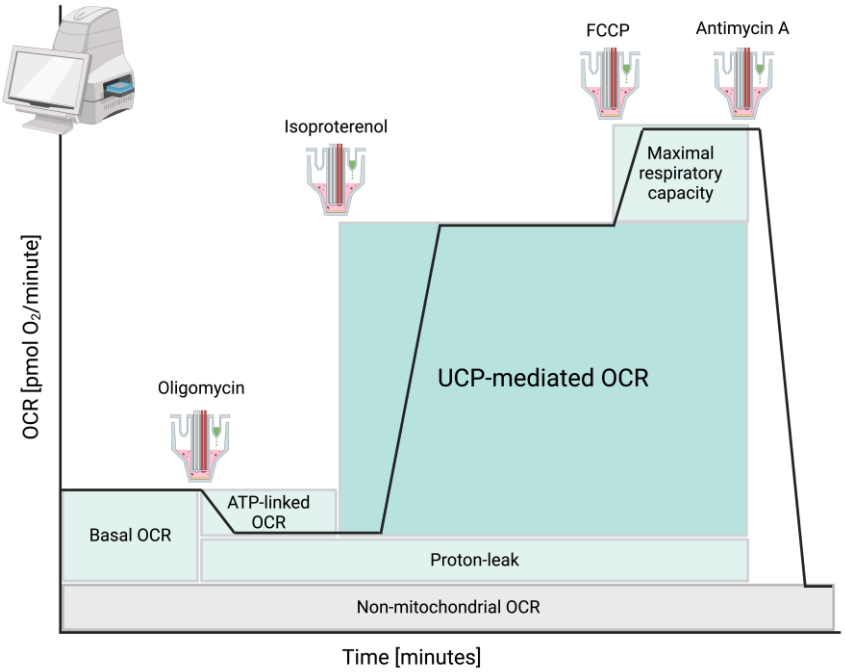

Figure 9: Schematic illustration of microplate-based respirometry assay on primary brown adipocytes.

2.9.2 RESPIRATORY FUNCTION AND UCP_1 ACTIVITY ANALYSIS IN BAT MITOCHONDRIA

Mitochondrial bioenergetics was assayed using microplate-based respirometry as previously published *(Sustarsic et al. 2018)*. The OCR of mitochondria was measured at 37°C using an XFe96 Extracellular Flux Analyzer (Agilent Technologies). Mitochondrial pellets were resuspended in respiration buffer containing 0.4% essentially fatty acid-free BSA and equally seeded into a pre-cooled 96-well Seahorse plate (4 µg mitochondrial protein/well, protein concentration was determined using the Biuret assay). Mitochondria were pelleted at 2,000xg for 20 minutes at 4°C using a swing bucket centrifuge with fast acceleration and slow break settings. The OCR was measured using two assays. Assay I: After two basal measurements, ATP-linked respiration (injection of 5 µM oligomycin) was assessed and general respiration was fueled using glycerol-3-phosphate (G3P) (injection of 5 mM G3P). Assay II: After three basal measurements, general respiration was fueled using glycerol-3-phosphate (G3P) (injection of 5 mM G3P). In both assays, UCP1 activity was calculated by subtraction of O_2 consumed after 3 mM injection (Assay I: OCRs at 42.7 and 48.6 min; Assay II: OCRs at 36.7, 42.6 and 48.5 min) from O_2 consumed directly before injection (Assay I: OCR at 42.6 min; Assay II: OCR at 36.6 min). For analysis of non-mitochondrial O_2-consumption, in both assays, the electron flow was blocked using a complex-III inhibitor (injection of 5 µM anti A) at the end of each measurement. To analyze maximal respiratory capacity, mitochondrial pellets were resuspended in the identical respiration buffer, seeded into a 96-well Seahorse plate, and pelleted as for the UCP1 activity measurements described above. General respiration was fueled by injection of 5 mM G3P, UCP1 inhibited with 3 mM and maximal respiration was induced with 7.5 µM FCCP (Assay III). Schemes and descriptions of the assays are illustrated in **Table 26, 27**, **28** and **Figure 10**, **11**, **12**. Data were normalized to the OCR determined before G3P injections, which may lead to negative OCRs after injection with Anti A for certain conditions.

Table 26: *Protocol for assay I of microplate-based respirometry for BAT mitochondria.*

Protocol	Time (min)	Loop/ Compound	Company	Cat. No.	Concentration
Calibration					
Equilibration	15				
Mixture	4	2x			
Measure	2				
Injection Port A		**Oligomycin**	Merck	O4876	5 µM
Mixture	4	2x			
Measure	2				
Injection Port B		**G3P**	Merck	G7886	5 mM
Mixture	4	3x			
Measure	2				
Injection Port C		**GDP**	Merck	G7127	3 mM
Mixture	4	2x			
Measure	2				
Injection Port D		**Antimycin A**	Merck	A8674	5 µM
Mixture	4	3x			
Measure	2				

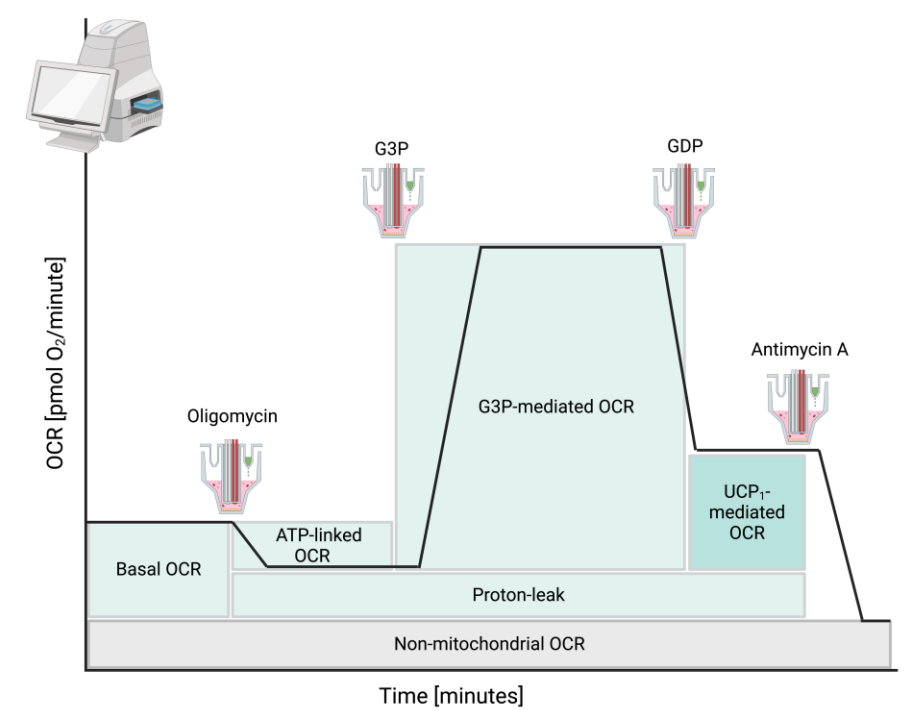

Figure 10: Schematic illustration of microplate-based respirometry assay of BAT mitochondria (assay I).

Table 27: *Protocol for assay II of microplate-based respirometry for BAT mitochondria.*

Protocol	Time (min)	Loop/ Compound	Company	Cat. No.	Concentration
Calibration					
Equilibration	15				
Mixture	4	3x			
Measure	2				
Injection Port A		**G3P**	Merck	G7886	5 mM
Mixture	4	3x			
Measure	2				
Injection Port B		**GDP**	Merck	G7127	3 mM
Mixture	4	2x			
Measure	2				
Injection Port C		**Anti A**	Merck	A8674	5 µM
Mixture	4	3x			
Measure	2				

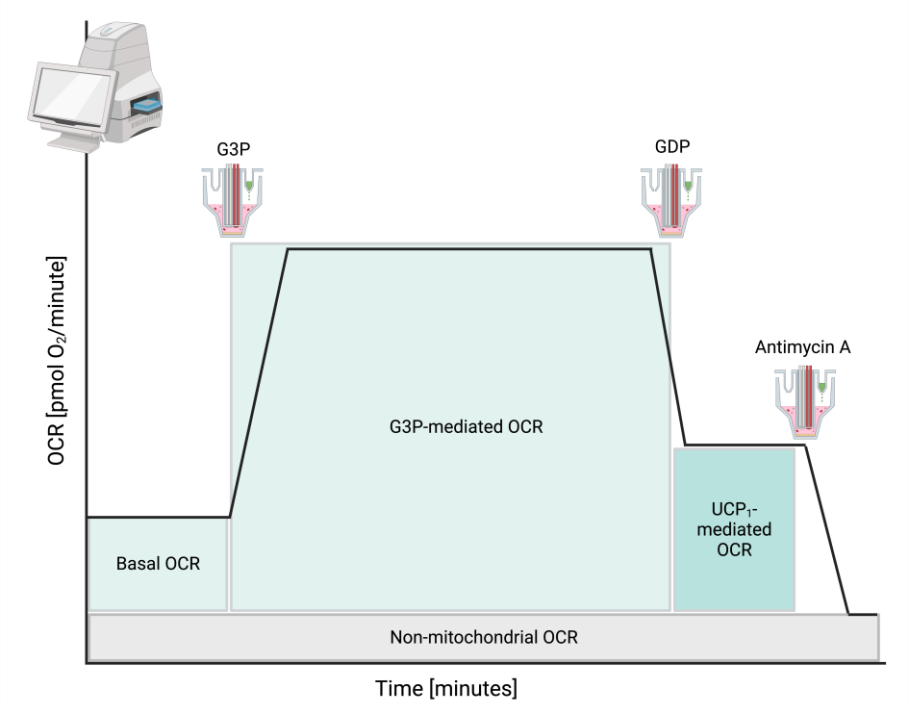

Figure 11: Schematic illustration of microplate-based respirometry assay of BAT mitochondria (assay II).

Table 28: *Protocol for assay III of microplate-based respirometry for BAT mitochondria.*

Protocol	Time (min)	Loop/ Compound	Company	Cat. No.	Concentration
Calibration					
Equilibration	15				
Mixture	4	2x			
Measure	2				
Injection Port A		**G3P**	Merck	G7886	5 mM
Mixture	4	3x			
Measure	2				
Injection Port B		**GDP**	Merck	G7127	3 mM
Mixture	4	2x			
Measure	2				
Injection Port C		**FCCP**	Merck	C2920	7.5 µM
Mixture	4	2x			
Measure	2				
Injection Port D		**Antimycin A**	Merck	A8674	5 µM
Mixture	4	3x			
Measure	2				

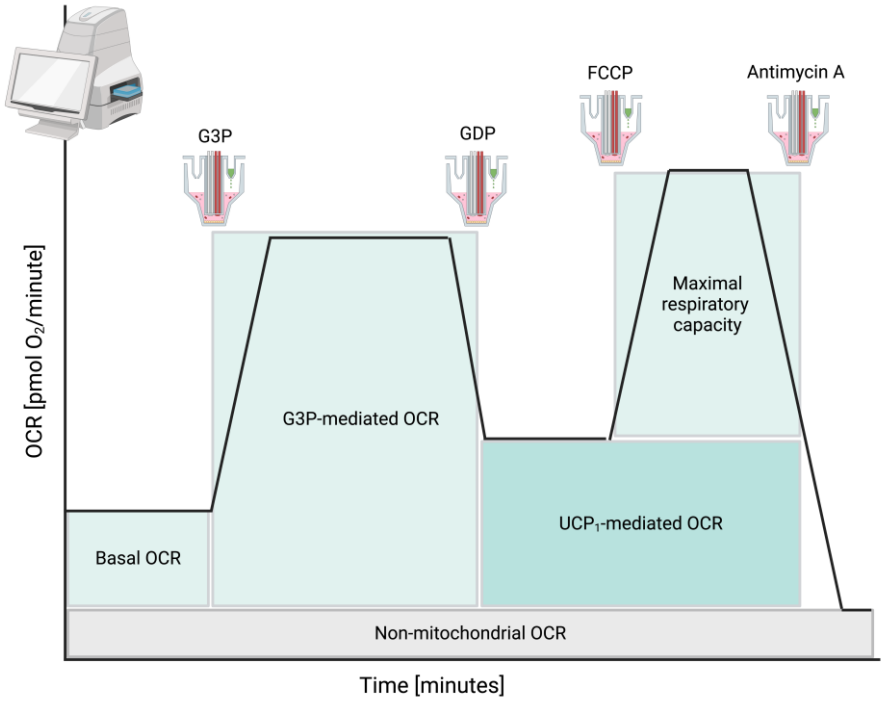

Figure 12: Schematic illustration of microplate-based respirometry assay of BAT mitochondria (assay III).

2.9.3 Respiratory function and UCP1 activity analysis in BAT mitochondria, as well as mitochondria isolated of primary brown adipocytes using high-resolution respirometry

Respiratory measurements of isolated mitochondria were conducted with the Oroboros O2K respirometer (Oroboros Instruments). Chambers were air saturated with 2 mL of 37°C pre-heated respiration buffer. To avoid O_2 dependent artifacts, the respiration buffer was continuously stirred, and oxygen concentration was kept above 50 µM. After mitochondrial isolation, 0.1 mg/mL mitochondria were transferred into O2K chambers. Protein concentration was determined using the Biuret assay. When basal oxygen consumption was stable, the following compounds were applied sequentially: iBAT mitochondria: 5 mM pyruvate (Pyr), 2 mM malate (Mal, C I substrates); 5 mM glycerol-3-phosphate (G3P); 2.5 mM guanosine diphosphate (GDP) as UCP1 inhibitor; 1 µM FCCP to induce maximal respiratory capacity. mPBAC mitochondria: 5 mM pyruvate (Pyr), 2 mM malate (Mal, C I substrates); 5 mM glycerol-3-phosphate (G3P); BSA coupled to palmitate (to induce UCP1 activity; palmitate and BSA were complexed in 14:62 ratio of 10% BSA and 200 mM palmitate stocks at 37°C and 400 rpm); 2.5 mM guanosine diphosphate (GDP) as UCP1 inhibitor. In both cases, non-mitochondrial oxygen consumption was subtracted from mitochondrial oxygen consumption by blocking the electron flow with 2.5 µM C III inhibitor antimycin A (Anti A) at the end of each measurement. The measured OCRs are given related to mitochondrial protein.

2.10 Classification and prediction model

The prediction model was built with KNIME 4.3.2. Analytics Platform (https://www.knime.com). We applied random forest (RF, a supervised decision tree learning procedure, to identify the most predictive lipid species indicating the sample origin. Only lipid species from GPL and FC detected in all

applied tissues were considered, including 94 species. We used data obtained from the experiments shown in **Figure 18-21** for model training (BAT, n= 6; liver, n= 3; eWAT, n= 3; muscle, n= 3; ∑ n= 15) and verification (liver, n= 11; BAT, n= 7; eWAT n= 6; ∑ n= 24). For feature selection and model learning, training data were 90% portioned and drawn randomly, the information gain ratio was used as tree split criterion and the number of decision trees to be learned was set to 100 using a static random seed. Application data were obtained from a new experiment comprising mitochondrial samples from mice housed at 4°C, 23°C and 30°C (BAT, iWAT and eWAT; 4°C, 23°C, 30°C; n= 3/condition; ∑ n= 27). Classification probabilities indicate the individual prediction confidences for each tissue class (BAT, eWAT, liver, muscle).

2.11 Analysis of body composition, calorimetry and glucose tolerance

The body composition of iBcKO-PISD and wildtype mice (body weight, lean mass, fat mass) was assessed after six hours of fasting, either two weeks after first tamoxifen induction at the age of 12 weeks or at the age of 24 weeks when mice received 12 weeks HFD and cold exposure. This was conducted using the magnetic resonance imaging system EchoMRI 130 and the respective EchoMRI 14 software (Echo Medical Systems). Indirect calorimetry, locomotor activity, food and water intake of mice were determined at the age of 12 weeks before and during cold exposure, using the PhenoMaster system (TSE systems). To assess the glucose tolerance of mice, they were fasted for six hours at the age of 13 or 25 weeks, weighed, and blood was drawn by tail vein puncture. To determine fasting and non-fasted glucose concentrations, a glucometer (ACCU-CHEK Aviva, Roche) was used. The glucose levels were analyzed before, as well as 15, 30, 60 and 120 minutes after receiving i.p. injections of D-Glucose (1 mg/g body weight).

2.12 Statistical analysis, data presentation and graphical illustrations

Illustrations were created with Microsoft PowerPoint 16.84 or Biorender.com, figures and statistical analysis were generated and conducted using GraphPad Prism 10.1.2, OriginPro 2021 and Microsoft Excel 16.84. The data is presented as mean +SD/SEM or ±SD/SEM if not stated otherwise. Equal/unequal variance was tested using the Levene's test. All statistical tests were two-tailed. To test for significance between multiple groups, one-way Anova with post-hoc Tukey-HDS-test was performed, if not stated otherwise. To test for significance between two groups, the unpaired t-test was applied for normal distributed samples with equal variances. If variances were unequal, Welch's t-test was performed. For volcano plots, $\log_2$ transformed fold changes were tested using Welch's t-test and FDR corrected using the Benjamini-Hochberg technique (FDR 1% or FDR 5%). For all tests, the respective p-values are stated in the figure legends (usually below 0.05).

3 RESULTS

3.1 MITOCHONDRIAL LIPID COMPOSITION AND ITS ROLE FOR BROWN ADIPOSE TISSUE FUNCTION

A previous lipid profile analysis of primary *ex-vivo* differentiated white, beige, and brown adipocytes revealed significant differences in the distribution of cardiolipins, sterols, glycerolipids, as well as common membrane lipids such as PC, PE, PE P, PS, PI, LPC, SM, Cer, and HexCer between white and brown adipocytes *(Schweizer et al. 2019)*. To date, the lipidome of white, beige, and brown adipose tissue has not been investigated at the subcellular/organelle level. However, it is well established that white and brown adipocytes possess an unequal magnitude of mitochondria with markedly dissimilar functions *(Rosenwald und Wolfrum 2014)*. This study aims to determine whether mitochondrial lipidomes differ between different tissues and whether this has an impact on mitochondrial function.

3.1.1 MITOCHONDRIA OF MURINE BAT AND LIVER ISOLATED BY DIFFERENTIAL CENTRIFUGATION ARE HIGHLY ENRICHED AND CONTAIN NEGLIGIBLE FRACTIONS OF ER AND MAM

ER and mitochondria are connected via junctions termed mitochondria-associated membranes (MAM), rendering them potential co-isolates of mitochondria *(Kornmann et al. 2009; Kornmann 2013)*. Previous isolation protocols based on density gradient centrifugation occurred to yield purer mitochondrial fractions compared to differential centrifugation-based protocols. Yet, to use mitochondria for both descriptive and functional analyses, including respiratory analyses, it is inevitable to employ a less time-consuming and practical protocol for the isolation of intact and respiring mitochondria using differential centrifugation. It should also not be neglected that this technique is preferable from an ethical standpoint, as it requires fewer animals to obtain enriched mitochondrial fractions from iBAT compared to density gradient centrifugation (5 mice per sample vs. 15 mice per sample). We have refined existing differential centrifugation protocols specifically for BAT mitochondria and compared their (referred to as cMito) full proteomes and lipidomes to those of more pure mitochondrial fractions (pMito) as well as ER- and MAM-fractions, all separated by density gradient centrifugation. A total of 7,149 proteins were identified, with the highest number observed in the ER fraction of liver. This was followed by the MAM and cMito portion of liver, the MAM, ER, and cMito fraction of iBAT, and finally, the lowest numbers in pMito of liver and iBAT (**Figure 13** A, B; **Figure 14** A-D; **Figure 15** A-D). 77% (iBAT) and 91% (liver) of the proteins detected in MAM were identical to those found in cMito; while 81% (iBAT) and 89% (liver) of the ER proteins were identical to those found in cMito (**Figure 13** A, B).

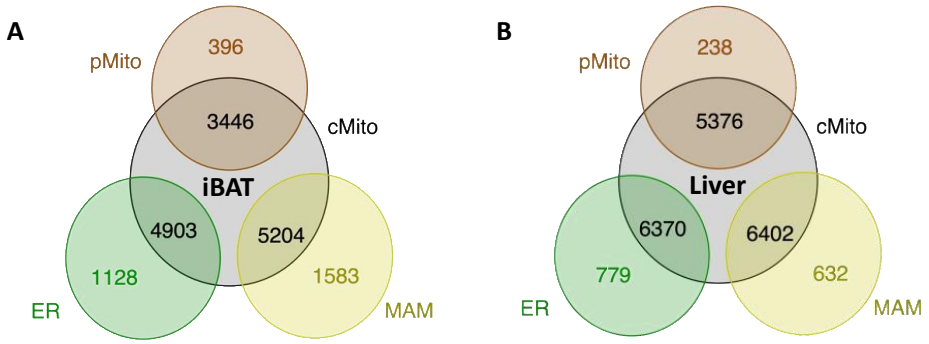

Figure 13: Distribution of protein numbers detected in cMito, pMito, ER and MAM of iBAT and liver mitochondria. *(A) Venn diagram of iBAT proteins detected in cMito and pMito or ER or MAM. (B) Venn diagram of liver proteins detected in cMito and pMito or ER or MAM. Proteomic data was obtained from ER, MAM, cMito and pMito samples prepared from pooled iBAT of 5-15 mice or liver of 5 mice.*

As illustrated in the rank order profiles, exemplary proteins relevant for BAT function and for this study are expressed at comparable levels between the cMito and pMito fractions (**Figure 14** A-B). Of the 1,000 most abundant ER proteins (**Figure 14** I-J; **Figure 15** I-J), 247 (BAT) and 114 (liver) were not detected or detected at low levels in the cMito fraction. Similarly, of the 1,000 most abundant MAM proteins (**Figure 14** G-H; **Figure 15** G-H), 246 (BAT) and 21 (liver) were not detected or detected at low levels in the cMito fraction. This suggests that the cMito fraction is only marginally contaminated with these organelles. These included several proteins specifically localized in the ER or MAM (**Figure 14** G, I; **Figure 15** G, I; ER: purple dots, MAM: orange dots) like stearoyl-CoA Desaturase (SCD1) and mitogen activated protein kinase kinase kinase (MAP3K5) *(Man et al. 2006; Nishitoh et al. 2002; Xiang et al. 2017)*. The cMito fraction constituted a greater proportion of proteins than the pMito fraction, indicating that the pMito fraction was purified to a greater extent than the cMito fraction (**Figure 14** B; **Figure 15** B). The distribution of expression levels of the 1,000 most abundant proteins (after classification into not expressed [NE], low, medium, and high) exhibited greater similarity between cMito and pMito than with ER or MAM (**Figure 14** E, F; **Figure 15** E, F). With a correlation coefficient of $R^2 > 0.76$, the signal intensities of uniquely occurring proteins exhibited a high degree of correlation between the cMito and pMito isolates (**Figure 14** K; **Figure 15** K). Finally, hierarchical cluster analysis of the proteome obtained from the different organelle fractions revealed a high degree of comparability between the cMito and pMito proteins, followed by MAM, while the distribution of ER proteins was found to be most different to that of mitochondrial fractions (**Figure 14** L; **Figure 15** L). This was further illustrated in a heat map diagram showing the abundancies of the top 100 pMito proteins, in pMito, cMito, MAM, and ER preparations (**Figure 14** M; **Figure 15** M).

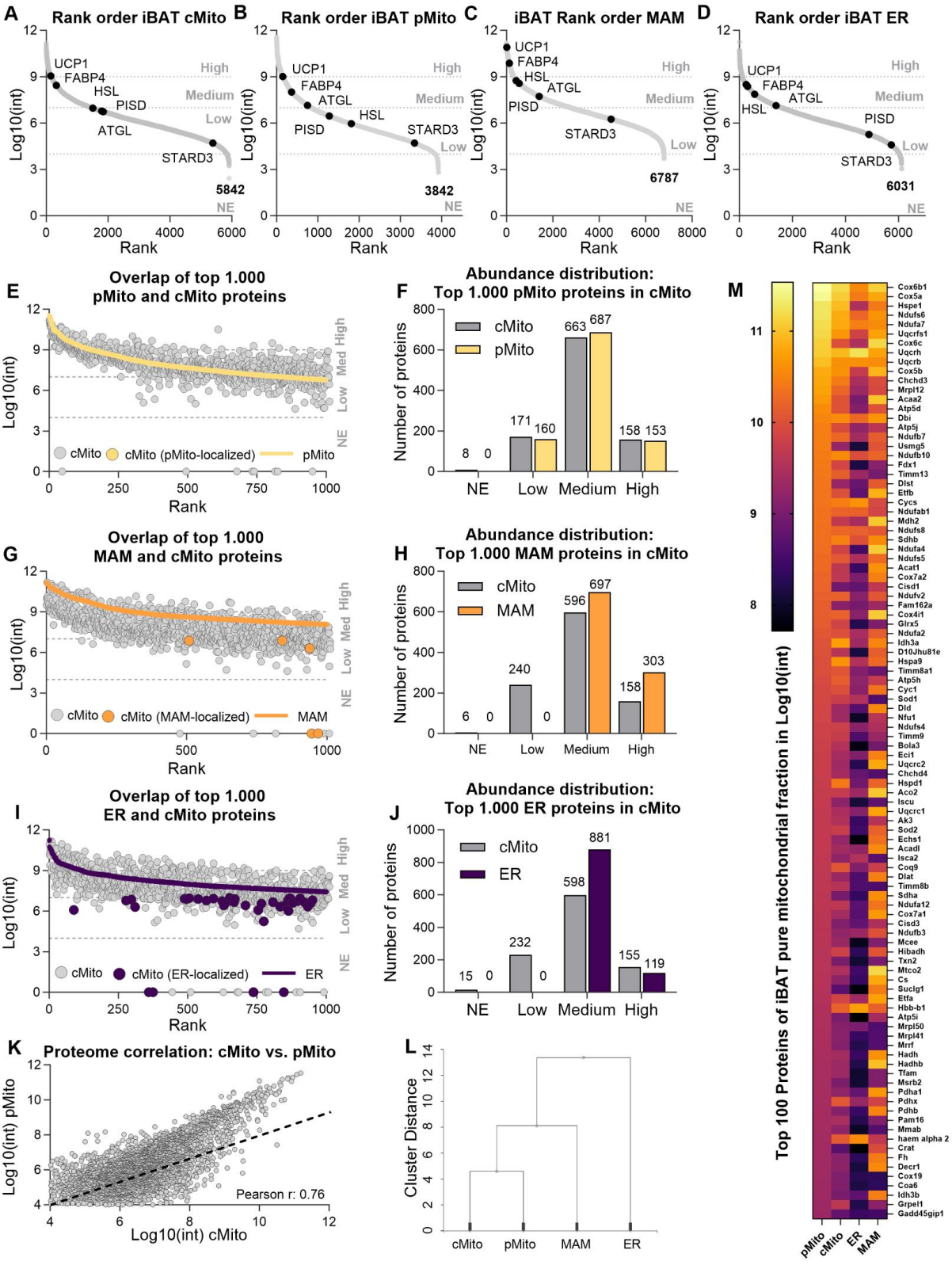
A
Rank order iBAT cMito
B
Rank order iBAT pMito
C
iBAT Rank order MAM
D
Rank order iBAT ER
Log10(int)
Rank
UCP1
FABP4
HSL
PISD
ATGL
STARD3
High
Medium
Low
NE
5842
3842
6787
6031
E
Overlap of top 1.000
pMito and cMito proteins
cMito
cMito (pMito-localized)
pMito
F
Abundance distribution:
Top 1.000 pMito proteins in cMito
Number of proteins
8 0 171 160 663 687 158 153
NE Low Medium High
G
Overlap of top 1.000
MAM and cMito proteins
cMito (MAM-localized)
MAM
H
Abundance distribution:
Top 1.000 MAM proteins in cMito
6 0 240 0 596 697 158 303
I
Overlap of top 1.000
ER and cMito proteins
cMito (ER-localized)
ER
J
Abundance distribution:
Top 1.000 ER proteins in cMito
15 0 232 0 598 881 155 119
K
Proteome correlation: cMito vs. pMito
Log10(int) pMito
Log10(int) cMito
Pearson r: 0.76
L
Cluster Distance
cMito pMito MAM ER
M
Top 100 Proteins of iBAT pure mitochondrial fraction in Log10(int)
Cox6b1
Cox5a
Hspe1
Ndufs6
Ndufa7
Uqcrfs1
Cox6c
Uqcrh
Uqcrb
Cox5b
Chchd3
Mrpl12
Acaa2
Atp5d
Dbi
Atp5j
Ndufb7
Usmg5
Ndufb10
Fdx1
Timm13
Dlst
Etfb
Cycs
Ndufab1
Mdh2
Ndufs8
Sdhb
Ndufa4
Ndufs5
Acat1
Cox7a2
Cisd1
Ndufv2
Fam162a
Cox4i1
Glrx5
Ndufa2
Idh3a
D10Jhu81e
Hspa9
Timm8a1
Atp5h
Cyc1
Sod1
Dld
Nfu1
Ndufs4
Timm9
Bola3
Eci1
Uqcrc2
Chchd4
Hspd1
Aco2
Iscu
Uqcrc1
Ak3
Sod2
Echs1
Acadl
Isca2
Coq9
Dlat
Timm8b
Sdha
Ndufa12
Cox7a1
Cisd3
Ndufb3
Mcee
Hibadh
Txn2
Mtco2
Cs
Suclg1
Etfa
Hbb-b1
Atp5i
Mrpl50
Mrpl41
Mrrf
Hadh
Hadhb
Tfam
Msrb2
Pdha1
Pdhx
Pdhb
Pam16
Mmab
haem alpha 2
Crat
Fh
Decr1
Cox19
Coa6
Idh3b
Grpel1
Gadd45gip1
pMito cMito ER MAM

Figure 14: BAT mitochondria isolated by differential centrifugation are highly enriched and contain negligible fractions of ER and MAM*. (A) Rank order of proteins after a full proteome analysis for cMito-, (B) pMito-, (C) MAM-, and (D) ER-fractions. Proteins relevant for this work are highlighted as examples. (E) Comparison of signal intensities in the top 1,000 ranked pMito, (G) MAM and (I) ER proteins with cMito; Grey dots indicate cMito proteins, yellow dots pMito-localized, orange dots MAM-localized and purple dots ER-localized proteins; identified with PubMed, UniProt or the Gene Ontology Resource. (F) Distribution of the top 1,000 ranked proteins according to their signal intensities in pMito, (H) MAM and (J) ER in comparison to cMito after classification into not expressed (NE; log10(int) <4), low (log10(int) 4-6), medium (log10(int) 7-9) and high (log10(int) >9) expressed proteins. (K) Correlation of signal intensities from all proteins detected in pMito and cMito. (L) Hierarchical cluster analysis of the 1,000 most abundant pMito proteins compared to cMito, ER and MAM. (M) Heatmap of top 100 ranked pMito proteins after hierarchical cluster analysis. All proteomic data were obtained from ER, MAM, cMito and pMito samples prepared from pooled BAT of 15 mice. R indicates Pearson's correlation coefficient*

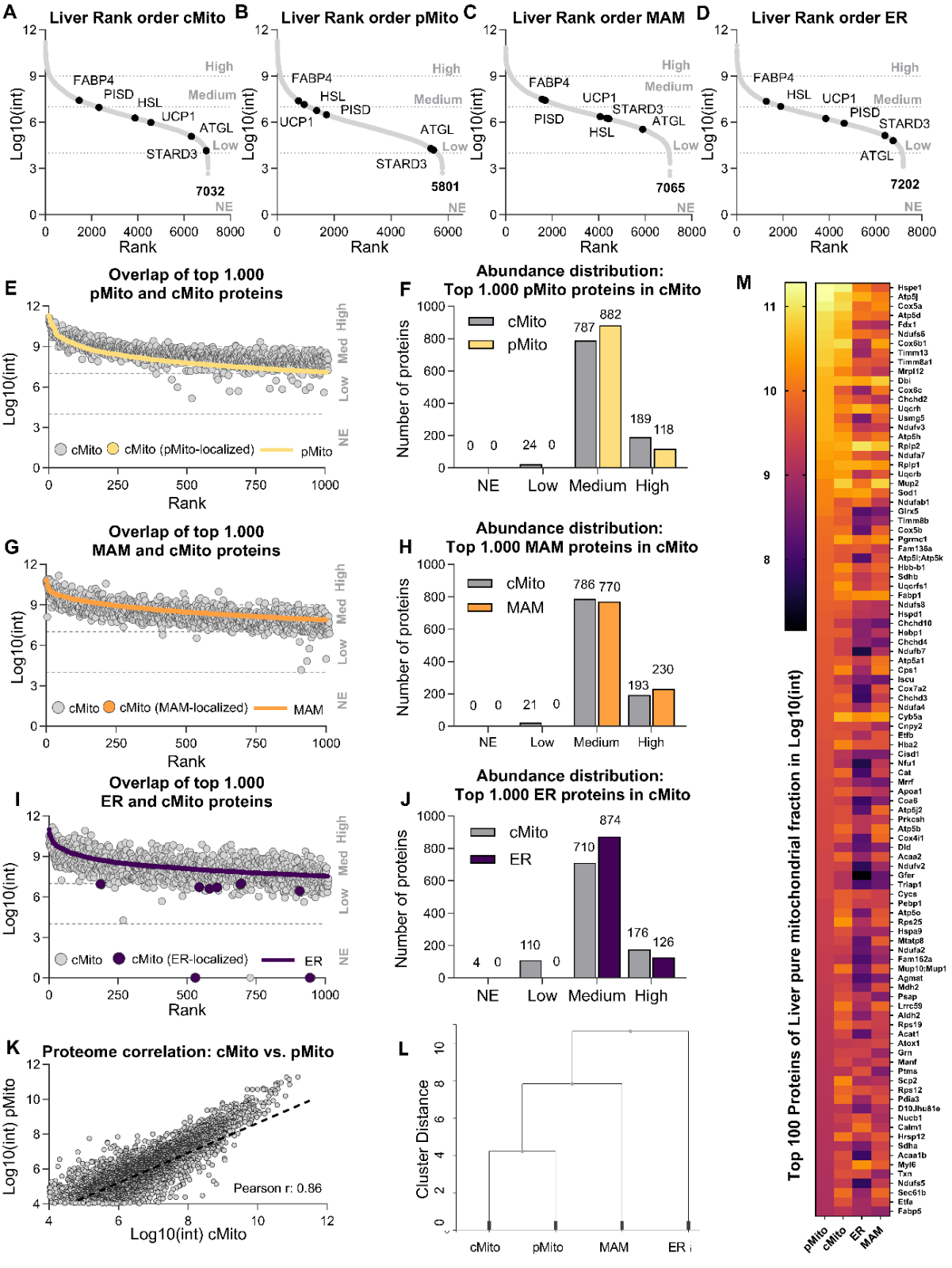
A
Liver Rank order cMito
B
Liver Rank order pMito
C
Liver Rank order MAM
D
Liver Rank order ER
Log10(int)
Rank
High
Medium
Low
NE
FABP4
PISD
HSL
UCP1
ATGL
STARD3
7032
5801
7065
7202
E
Overlap of top 1.000
pMito and cMito proteins
cMito
cMito (pMito-localized)
pMito
F
Abundance distribution:
Top 1.000 pMito proteins in cMito
Number of proteins
0 0 24 0 787 882 189 118
NE Low Medium High
G
Overlap of top 1.000
MAM and cMito proteins
cMito (MAM-localized)
MAM
H
Abundance distribution:
Top 1.000 MAM proteins in cMito
0 0 21 0 786 770 193 230
I
Overlap of top 1.000
ER and cMito proteins
cMito (ER-localized)
ER
J
Abundance distribution:
Top 1.000 ER proteins in cMito
4 0 110 0 710 874 176 126
K
Proteome correlation: cMito vs. pMito
Log10(int) pMito
Log10(int) cMito
Pearson r: 0.86
L
Cluster Distance
cMito
pMito
MAM
ER
M
Top 100 Proteins of Liver pure mitochondrial fraction in Log10(int)
pMito
cMito
ER
MAM

Figure 15: Liver mitochondria isolated by differential centrifugation are highly enriched and contain negligible fractions of ER and MAM*. (A) Rank order of proteins after a full proteome analysis for cMito-, (B) pMito-, (C) MAM-, and (D) ER-fractions. Proteins relevant for this work are highlighted as examples. (E) Comparison of signal intensities in the top 1,000 ranked pMito, (G) MAM and (I) ER proteins with cMito; Grey dots indicate cMito proteins, yellow dots pMito-localized, orange dots MAM-localized and purple dots ER-localized proteins; identified with PubMed, UniProt or the Gene Ontology Resource. (F) Distribution of the top 1,000 ranked proteins according to their signal intensities in pMito, (H) MAM and (J) ER in comparison to cMito after classification into not expressed (NE; log10(int) <4), low (log10(int) 4-6), medium (log10(int) 7-9) and high (log10(int) >9) expressed proteins. (K) Correlation of signal intensities from all proteins detected in pMito and cMito. (L) Hierarchical cluster analysis of the 1,000 most abundant pMito proteins compared to cMito, ER and MAM. (M) Heatmap of top 100 ranked pMito proteins after hierarchical cluster analysis. All proteomic data were obtained from ER, MAM, cMito and pMito samples prepared from pooled liver of 5 mice. R indicates Pearson's correlation coefficient.*

This work specifically focuses on the comparison of mitochondrial fractions of different adipose tissue depots. Therefore, it was investigated whether potential contaminations of the cMito occur in comparable levels between various adipose tissue depots. Western Blot analysis was conducted on several marker proteins, including cytochrome C (mitochondria), IP3R and calreticulin (ER), FACL4 (MAM), Na^+-K^+ -ATPase (plasma membrane), as well as tubulin (cytosol), in adipose tissue depots and thereof isolated cMito fractions. This revealed that mitochondria isolated from either iBAT, iWAT, or eWAT were all strongly enriched in the mitochondrial marker protein cytochrome C (**Figure 16** A) and further, were contaminated with respective organelles to a similar extent. The levels of ER marker proteins in all tissue samples decreased by >80% (IP3R) and >90% (calreticulin) following cMito isolation (**Figure 16** B, C). The MAM marker protein (FACL4) was reduced by over 98% in cMito isolates, while the cytosol marker tubulin was reduced by about 80% (**Figure 16** D, F). These results indicate that the cMito isolates of iBAT, iWAT, and eWAT exhibited very low and comparable contaminations with ER, MAM, and cytosol. The Na^+-K^+-ATPase was reduced by approximately 50% in brown adipose tissue mitochondria, while white adipose tissue mitochondria showed an approximately 65% lower abundance of the plasma membrane marker (**Figure 16** E). This may indicate a slight increase in the contamination of iBAT cMito samples with lipids that are specifically enriched in the plasma membrane, such as sterols.

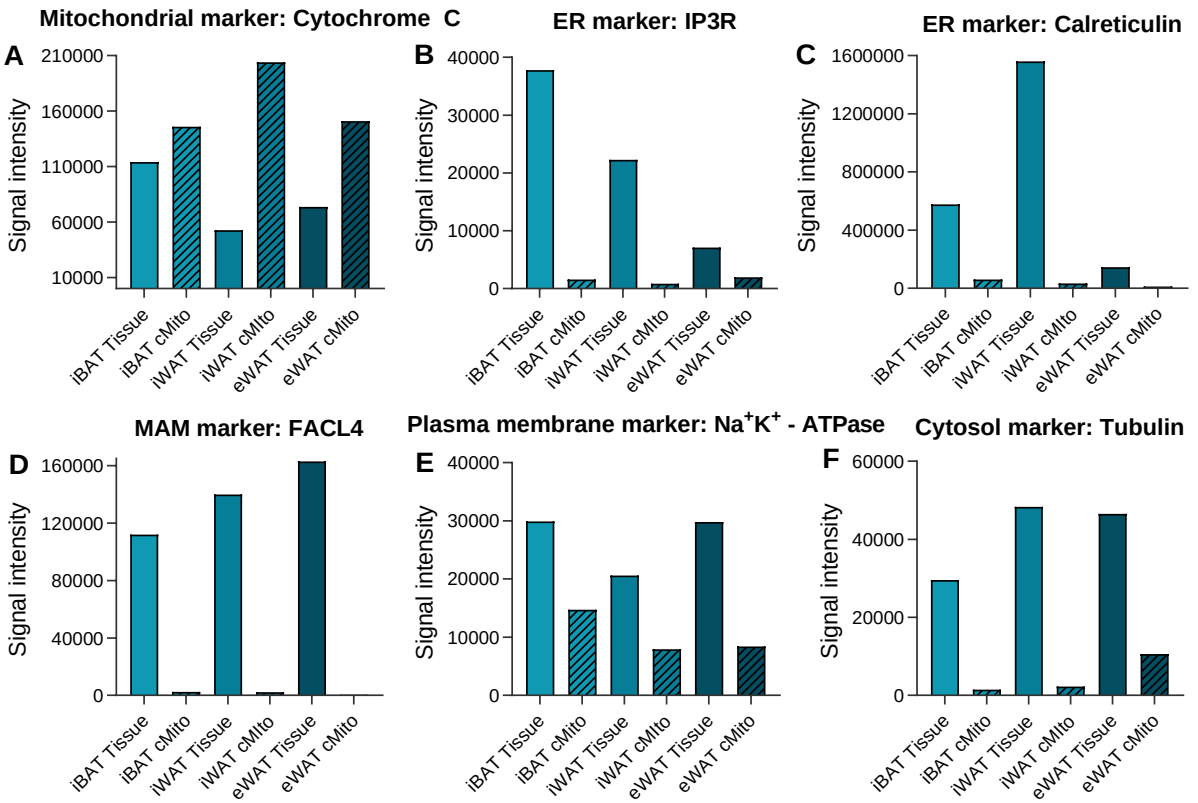

Figure 16: Western Blot analysis revealing that potential organelle contaminations in cMito fractions are comparable between different adipose tissue depots. *(A) Quantified signal intensities of mitochondrial marker protein cytochrome C, (B-C) ER marker proteins IP3R and calreticulin, (D) MAM marker FACL4, (E) plasma membrane marker Na^+-K^+-ATPase and (F) cytosol marker tubulin in iBAT, iWAT and eWAT as well as thereof isolated mitochondria. Each mitochondrial sample was isolated from tissue of n= 5 (BAT) or n= 10 (WAT) mice. Signal intensities of protein were determined using the Image Studio™ Light quantification software after background correction.*

To ascertain whether the lipid composition of pMito is comparable to that of cMito isolates, a comprehensive and quantitative lipidomic analysis was performed using high-resolution mass spectrometry (HR-MS) and tandem mass spectrometry (QQQ). This analysis encompassed glycerophospholipids (GPL) (which included: PC, phosphatidylcholine; PE, phosphatidylethanolamine; PE P, PE-based plasmalogens; PI, phosphatidylinositol; PS, phosphatidylserine; CL, cardiolipin), sphingolipids (SL) (which included: SM, sphingomyelin; Cer, ceramide; Hex-Cer, hexosylceramide), glycerolipids (GL) (which included: DG, diglycerides; TG, triglycerides), and sterols (ST) (which included: FC, free cholesterol; CE, cholesteryl ester). A correlation of all quantified lipid species, in total 275, revealed a highly comparable lipidomic composition between the pMito and cMito fractions (**Figure 17** A, B). This was demonstrated by a Pearson R^2 value of >0.97 and a Spearman rho value of >0.83).

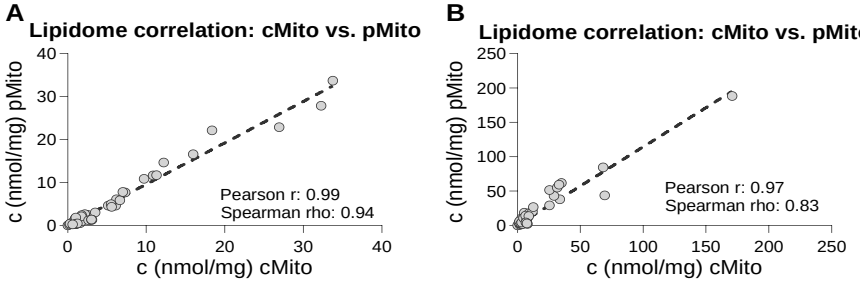

Figure 17: Lipidomic analysis of iBAT and liver mitochondria showing a high correlation between lipid species in cMito and pMito fractions. *(A) iBAT lipidome correlation between lipid species quantified in pMito (isolated from pooled iBAT of n= 15 mice) and cMito (isolated from pooled iBAT of n= 5 mice), (B) Liver lipidome correlation between lipid species quantified in pMito (isolated from pooled liver of n= 5 mice) and cMito (isolated from pooled liver of n= 2 mice). Shown are means of n= 7 preparations after a lipidomic analysis. R indicates Pearson's, rho indicates Spearman's correlation coefficients.*

3.1.2 MITOCHONDRIAL LIPIDOMES, PARTICULARLY THEIR PHOSPHATIDYLCHOLINE, PHOSPHATIDYLETHANOLAMINE AND FREE CHOLESTEROL CONTENTS ARE TISSUE SPECIFIC

Next, it was investigated whether the mitochondrial lipid profile of brown adipose tissue has a unique composition or is comparable to mitochondria isolated from other tissues, including iWAT, eWAT, liver and muscle. To reinforce the following findings of this study, a comparison was conducted between iBAT and liver mitochondria using the same sample set utilized for the pMito-cMito correlation shown in **Figure 17**. Additionally, a second iBAT mitochondria sample set was employed to assess its characteristics in comparison to those of the other tissue preparations.

Total lipid contents (related to protein) were increased 2-fold in iBAT mitochondria compared to iWAT (**Figure 18** C), 1.5-fold (**Figure 19** C) compared to eWAT, 1.7-fold (**Figure 21** C) compared to muscle, and decreased by 58% compared to liver mitochondria (**Figure 20** C). In all tissues, the largest part of total lipids were GPLs. Most strikingly, iBAT mitochondria consisted of 90%-96% of GPL (**Figure 18**-**Figure 21** C). It is noteworthy that mitochondria from all tissues possessed significantly higher contents of sterols, especially free cholesterol, in comparison to iBAT cMito (**Figure 18**-**Figure 21** A, E). In iWAT, FC levels were 4.3-fold elevated compared to iBAT mitochondria, eWAT revealed a 6.7-fold increase, and in liver and muscle mitochondria, FC was 10-fold and almost 2-fold higher, respectively. Given that mitochondria isolated from BAT expressed higher levels of Na^+-K^+-ATPase compared to the other adipose tissue depots (**Figure 16** E), it can be concluded that this finding is not a consequence of potential contamination with cholesterol-rich plasma membranes. For a more comprehensive comparison of the typical GPL/FC and FC composition in various organelles, please refer to **Supplementary Table 1**.

In iWAT mitochondria, 17 GPL species exhibited significant differences when compared to iBAT cMito (**Figure 18** B). Among the identified GPL species, PC, PE, and PI levels were found to be higher in iBAT, with increases of 70%, 84%, and 53%, respectively. In contrast, PS levels were found to be approximately three times higher in iWAT cMito. The sphingolipids SM (7.8-fold) and Cer (4.7-fold) were found to be increased in iWAT compared to iBAT mitochondria (**Figure 18** A, E). This led to a portion of 5.6% SL, 32.4% sterols, and 62% GPL of total iWAT lipids, as well as 0.5% SL, 3.7% sterols and 95.8% GPL in total lipids of iBAT mitochondria (**Figure 18** C). In comparison to iWAT mitochondria, the GPL portion of total iBAT cMito lipids exhibited a greater proportion of lipids with tri-, tetra-, and penta-unsaturated acyl chains (including PC 36:3, PC 36:4, PC 38:4, PC 38:5, PC O 36:5, PE 36:3, PE 36:4, PE 38:5, PI 36:3, PI 38:4), and less with highly unsaturated (>5 DB) acyl chains (including PS 40:6, PS 40:7) (**Figure 18** D, F; **Supplementary Figure 1**).

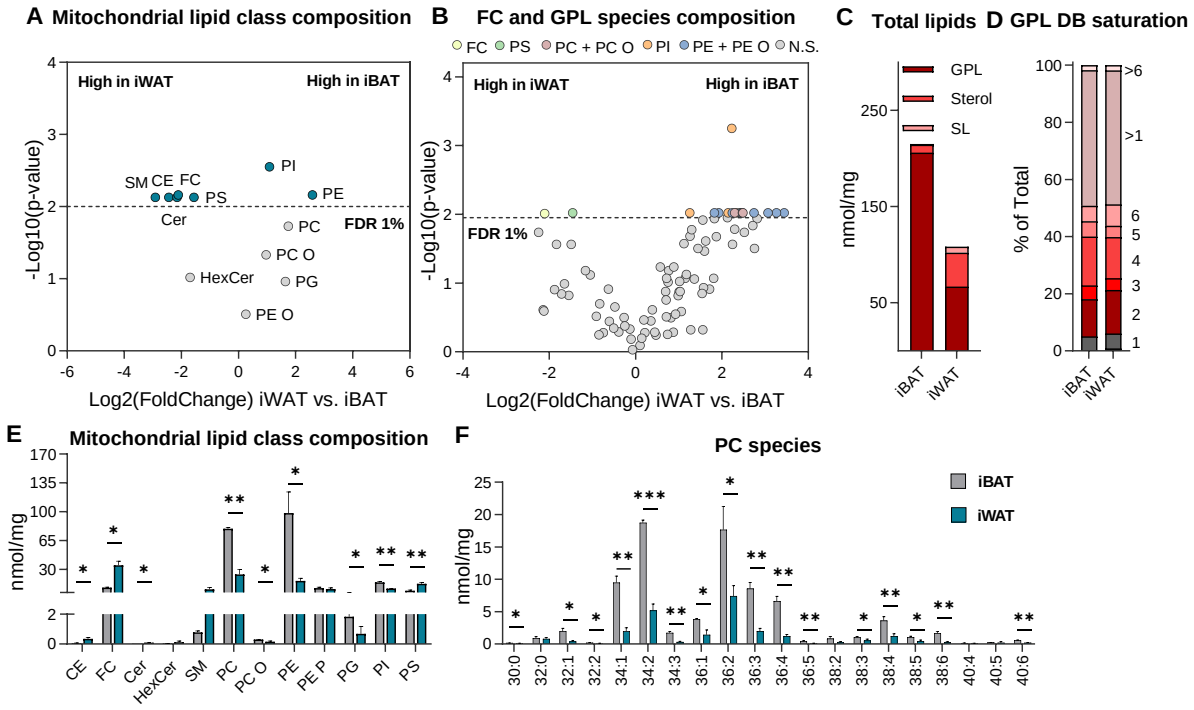

Figure 18: The mitochondrial lipidome including GPL and FC of iBAT mitochondria significantly differs to iWAT. *(A) Lipid class composition of mitochondria isolated from iBAT (n= 3) vs. iWAT (n= 3), shown as volcano plots presenting significant differences (-Log$_{10}$(q-value)) of Log$_2$(FoldChange) in lipid classes. Turquoise dots indicate lipid species significantly decreased in iBAT (left) or significantly increased in iBAT (right) after FDR correction (Welch's test + Benjamini-Hochberg) at p< 0.01. (B) GPL species and FC composition of mitochondria from iBAT (n= 3) vs. iWAT (n= 3); Volcano plots show significant differences (-Log$_{10}$(q-value)) of Log$_2$(FoldChange) in GPL species and FC. Each coloured dot represents a specific lipid species significantly decreased in iBAT (left) or significantly increased in iBAT (right) after FDR correction at p< 0.01, with the colour indicating to which lipid class it belongs. (C) Stacked bar plots show total lipid levels and distribution into SL, Sterols, and GPL (means), and (D) distribution of saturation in GPL as number of double bonds (means). (E) Lipid class composition and (F) PC species composition of mitochondria from iBAT (n= 3) vs. iWAT (n= 3); Bar plots show means +SD; *p< 0.05, **p< 0.01 and ***p< 0.001 indicate significant differences relative to iBAT, determined using a two-sided student's t-test with Welch's correction. Each mitochondrial sample was isolated from tissue pooled of n= 5-10 mice.*

A comparison of eWAT mitochondria with iBAT cMito revealed that 22 GPL species significantly exhibited differences (**Figure 19** B). Among the identified differences, PC, PE, and PG were found to be present in higher levels in iBAT, with increases of 3-fold, 5.7-fold and 4.5-fold, respectively. In contrast, PS exhibited a 4.6-fold increase in eWAT cMito. The sphingolipids SM (87%) and Cer (84%) were found to be elevated in eWAT compared to iBAT mitochondria (**Figure 19** A, E). This translated to a portion of 7.6% SL, 37.9% sterols and 54.5% GPL of total eWAT lipids, as well as 0.5% SL, 3.7% sterols, and 95.8% GPL in total lipids of iBAT mitochondria (**Figure 19** C). Similarly to iWAT, the GPL portion in total lipids of eWAT mitochondria consists of less lipids with tri-, tetra-, and penta-unsaturated acyl chains compared to iBAT (including PC 36:3, PC 36:4, PC 38:4, PC 38:5, PC O 36:5, PE 36:3, PE 36:4, PE 38:4, PE 38:5, PI 36:3, PI 38:4), and more with highly unsaturated (>5 DB) acyl chains (including PS 40:5, PS 40:6, PS 40:7) (**Figure 19** D, F; **Supplementary Figure 2**).

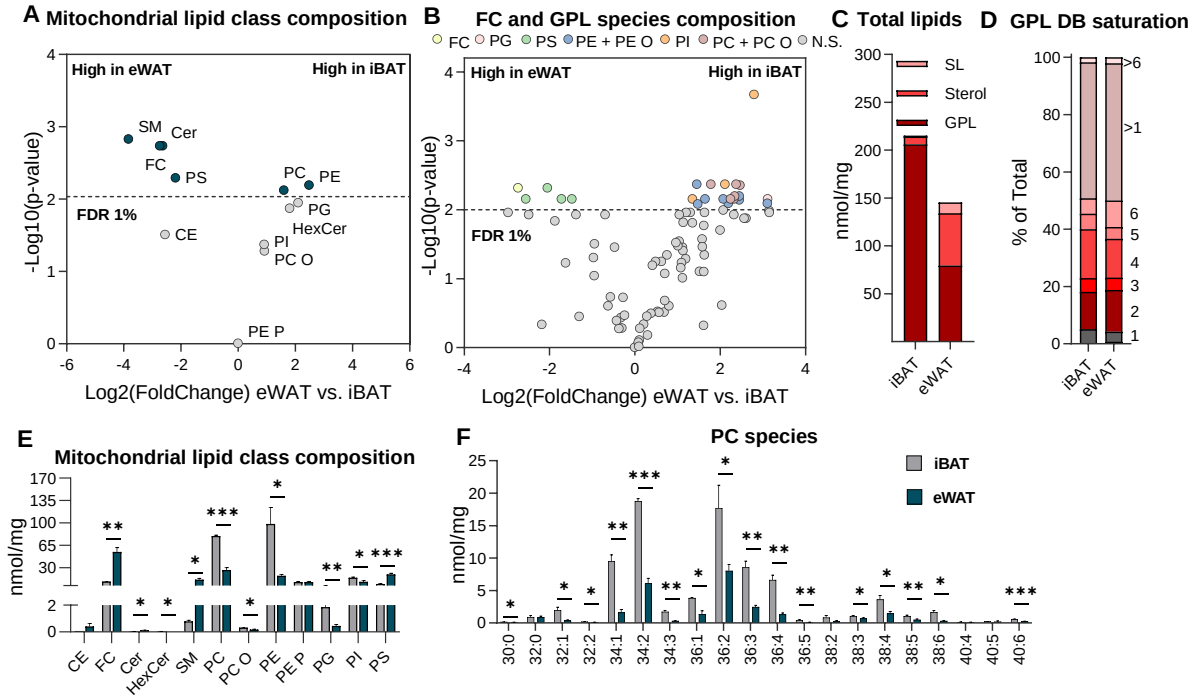

Figure 19: The mitochondrial lipidome including GPL and FC of iBAT mitochondria significantly differs to eWAT. *(A) Lipid class composition of mitochondria isolated from iBAT (n= 3) vs. eWAT (n= 3), shown as volcano plots presenting significant differences (-Log$_{10}$(q-value)) of Log$_2$(FoldChange) in lipid classes. Blue dots indicate lipid species significantly decreased in iBAT (left) or significantly increased in iBAT (right) after FDR correction (Welch's test + Benjamini-Hochberg) at p< 0.01. (B) GPL species and FC composition of mitochondria from iBAT (n= 3) vs. eWAT (n= 3); Volcano plots show significant differences (-Log$_{10}$(q-value)) of Log$_2$(FoldChange) in GPL species and FC. Each colored dot represents a specific lipid species significantly decreased in iBAT (left) or significantly increased in iBAT (right) after FDR correction at p< 0.01, with the color indicating to which lipid class it belongs. (C) Stacked bar plots show total lipid levels and distribution into SL, Sterols, and GPL (means), and (D) distribution of saturation in GPL as number of double bonds (means). (E) Lipid class composition and (F) PC species composition of mitochondria from iBAT (n= 3) vs. eWAT (n= 3); Bar plots show means +SD, *p< 0.05, **p< 0.01 and ***p< 0.001 indicate significant differences relative to iBAT, determined using a two-sided student's t-test with Welch's correction. Each mitochondrial sample was isolated from tissue pooled of n= 5-10 mice.*

In liver mitochondria, PC was found to be more than 2-fold more abundant compared to iBAT. This contrasts with mitochondria isolated from WAT depots, in which GPL levels, i.e. PC and PE, were significantly lower concentrated in iBAT. Moreover, PI and PS levels increased by approximately 90% in liver samples (**Figure 20** A, E). In total, 39 GPL species were significantly different between the two groups (**Figure 20** B). The sphingolipids SM, Cer, and Hex-Cer exhibited higher levels in liver cMito, with fold changes of 5.3-14.3 (**Figure 20** A, E). This resulted in a portion of 2.6% SL, 2.5% GL, 9.9% sterols, and 85% GPL of liver total lipids, as well as 0.8% SL, 2.3% sterols, 7.1% GL, and 89.8% GPL in total lipids of iBAT mitochondria (**Figure 20** C). The GPL fraction of iBAT mitochondria comprised more lipids with mono-, di-, and tri-saturated acyl chains (including PC 32:2, PC O 34:3, PE 32:1, PE 34:3, PG 34:2, PS 36:2) and less with highly unsaturated (>3 DB) acyl chains (including PC 36:4, PC 38:4, PC 38:5, PC 38:6, PE 38:6, PE 40:6, PI 38:4, PI 38:5, PS 38:4, PS 40:5, PS 40:6) compared to liver mitochondria (**Figure 20** D, F; **Supplementary Figure 4**; **Supplementary Figure 5**).

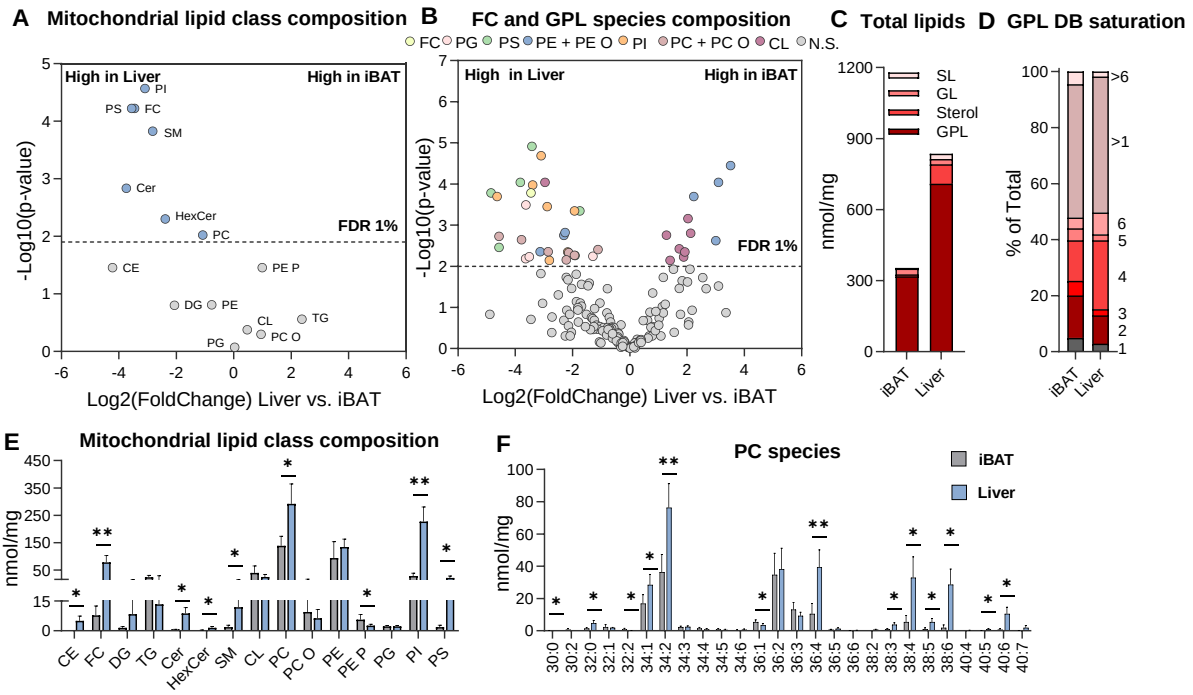

Figure 20: The mitochondrial lipidome including GPL and FC of iBAT mitochondria significantly differs to liver. *(A) Lipid class composition of mitochondria isolated from iBAT (n= 7) vs. liver (n= 4), shown as volcano plots presenting significant differences (-Log$_{10}$(q-value)) of Log$_2$(FoldChange) in lipid classes. Light blue dots indicate lipid species significantly decreased in iBAT (left) or significantly increased in iBAT (right) after FDR correction (Welch's test + Benjamini-Hochberg) at p< 0.01. (B) GPL species and FC composition of mitochondria from iBAT (n= 7) vs. liver (n= 4); Volcano plots show significant differences (-Log$_{10}$(q-value)) of Log$_2$(FoldChange) in GPL species and FC. Each colored dot represents a specific lipid species significantly decreased in iBAT (left) or significantly increased in iBAT (right) after FDR correction at p< 0.01, with the color indicating to which lipid class it belongs. (C) Stacked bar plots show total lipid levels and distribution into SL, Sterols, GL, and GPL (means), and (D) distribution of saturation in GPL as number of double bonds (means). (E) Lipid class composition and (F) PC species composition of mitochondria from iBAT (n= 7) vs. liver (n= 4); Bar plots show means +SD, *p< 0.05 and **p< 0.01 indicate significant differences relative to iBAT, determined using a two-sided student's t-test with Welch's correction. Each mitochondrial sample was isolated from tissue pooled of n= 2-5 mice.*

In muscle mitochondria, 41 GPL species were significantly different to iBAT cMito (**Figure 21** B). Among those, PC (40%), PE (70%) and PG (50%) were found in elevated portions in iBAT, while a 2.7-fold increase in PS and 2-fold increase in PC O was found in cMito isolated from muscle. The sphingolipids SM (3.5-fold), Cer (12.3-fold) and Hex-Cer (2.8-fold) were accelerated in muscle compared to iBAT mitochondria (**Figure 21** A, E). This translated to a portion of 2.3% SL, 10.9% sterols and 86.8% GPL of total muscle lipids, as well as 0.5% SL, 3.7% sterols, and 95.8% GPL in total lipids of iBAT mitochondria (**Figure 21** C). Mitochondria isolated from muscle harbor more GPL with highly unsaturated acyl chains (> 5) (including PC 38:6, PC 40:6, PE 40:6, PE P 16:0/22:6, PE P 18:0/22:6, PE P 18:1/22:6, PI 40:6, PS 40:6) and less with di-, and tri-unsaturated acyl chains (including PC 34:2, PC 36:2, PC 36:3, PE 34:2, PE 36:2, PE 36:3, PE P 16:0/18:2, PG 34:2, PI 36:2, PI 36:3, PS 36:2) compared to iBAT mitochondria (**Figure 21** D, F; **Supplementary Figure 3**).

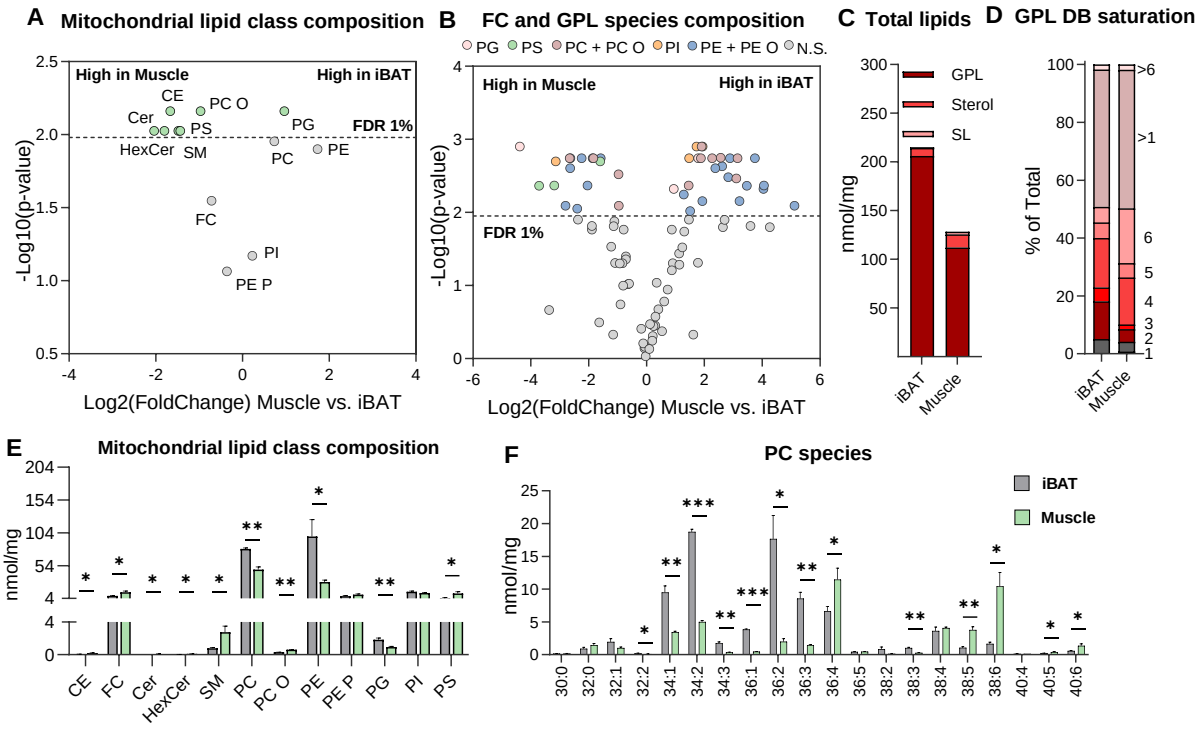

Figure 21: The mitochondrial lipidome including GPL and FC of iBAT mitochondria significantly differs to muscle. *(A) Lipid class composition of mitochondria isolated from iBAT (n= 3) vs. muscle (n= 3), shown as volcano plots presenting significant differences (-Log$_{10}$(q-value)) of Log$_2$(FoldChange) in lipid classes. Green dots indicate lipid species significantly decreased in iBAT (left) or significantly increased in iBAT (right) after FDR correction (Welch's test + Benjamini-Hochberg) at p< 0.01. (B) GPL species and FC composition of mitochondria from iBAT (n= 3) vs. muscle (n= 3); Volcano plots show significant differences (-Log$_{10}$(q-value)) of Log$_2$(FoldChange) in GPL species and FC. Each colored dot represents a specific lipid species significantly decreased in iBAT (left) or significantly increased in iBAT (right) after FDR correction at p< 0.01, with the color indicating to which lipid class it belongs. (C) Stacked bar plots show total lipid levels and distribution into SL, Sterols and GPL (means), and (D) Distribution of saturation in GPL as number of double bonds (means). (E) Lipid class composition and (F) PC species composition of mitochondria from iBAT (n= 3) vs. muscle (n= 3); Bar plots show means +SD, *p< 0.05, **p< 0.01 and ***p< 0.001 indicate significant differences relative to iBAT, determined using a two-sided student's t-test with Welch's correction. Each mitochondrial sample was isolated from tissue pooled of n= 5 mice.*

Taken together, the lipidomic composition of mitochondria isolated from various tissues demonstrated notable differences. Those purified from liver and white adipose tissue displayed significantly higher amounts of FC, whereas the total amount of major GPL species such as PC and PE was reduced in white adipose tissue and muscle samples compared to iBAT mitochondrial isolates. This resulted in the following ratios of GPL/FC, PC/FC, and PE/FC: a 35-fold lower GPL/FC ratio in eWAT mitochondria, 27-fold lower in iWAT, 6-fold lower in muscle, and 5.6-fold lower in liver mitochondria compared to iBAT cMito. The PC/FC ratios were reduced by 52-fold, 35-fold, 7-fold, and 6.4-fold in eWAT, iWAT, muscle, and liver, respectively. Mitochondria isolated from brown adipose tissue showed 58-fold, 40.4-fold, 8.5-fold, and 9.8-fold increases in PE/FC ratios compared to eWAT, iWAT, muscle and liver, respectively (**Figure 22**).

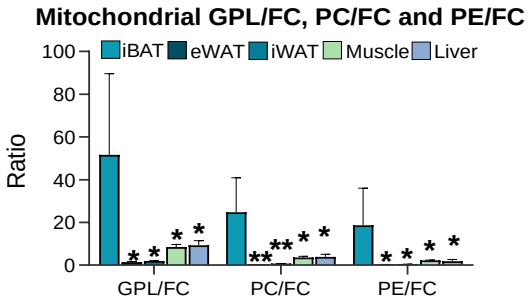

Figure 22: Mitochondrial lipid ratios in iBAT are significantly different to WAT, liver, and muscle. GPL/FC, PC/FC and PE/FC ratios calculated from all analysed mitochondrial samples of iBAT (n= 10), liver (n= 4), muscle (n= 3), iWAT (n= 3) and eWAT (n= 3); GPL included PC, PC O, PE, PE P, PS, PI, PG; Shown are means +SD, *p<0.05 and **p<0.01 indicate significant differences to iBAT, determined using a two-sided student's t-test with Welch's correction. Each mitochondrial sample was isolated from tissue pooled of n=2-10 mice.

3.1.3 Differences in the GPL composition between fat depots are related to adipose tissue browning

To test whether differences in the mitochondrial lipidome, as indicated by GPL/FC, of iBAT, iWAT, and eWAT can be related to the browning capacity of the respective adipose tissue depot, mice were housed at 4°C, 23°C or 30°C for seven days to either promote or antagonize adipose tissue browning. This resulted in decreasing concentrations of the glycerophospholipids PC, PE, PG and PI with increasing housing temperatures in brown adipose tissue mitochondria (**Figure 23** A). In inguinal white adipose tissue, which is, after cold exposure, composed of beige adipocytes exhibiting a phenotype and function intermediate between white and brown adipocytes *(Rosenwald et al. 2013; Wu et al. 2012)*, PE also decreased with rising temperatures, although to a lesser extent than observed in iBAT mitochondria (**Figure 23** B). In mitochondria isolated from eWAT, consisting only of white adipocytes, no differences were observed between the different temperatures (**Figure 23** C). As iWAT contains beige adipocytes, its capacity for browning, i.e. UCP1 activity, is lower as it is in iBAT but higher than that of eWAT. This suggests a relation between mitochondrial GPL composition and the browning capacity of adipose tissue.

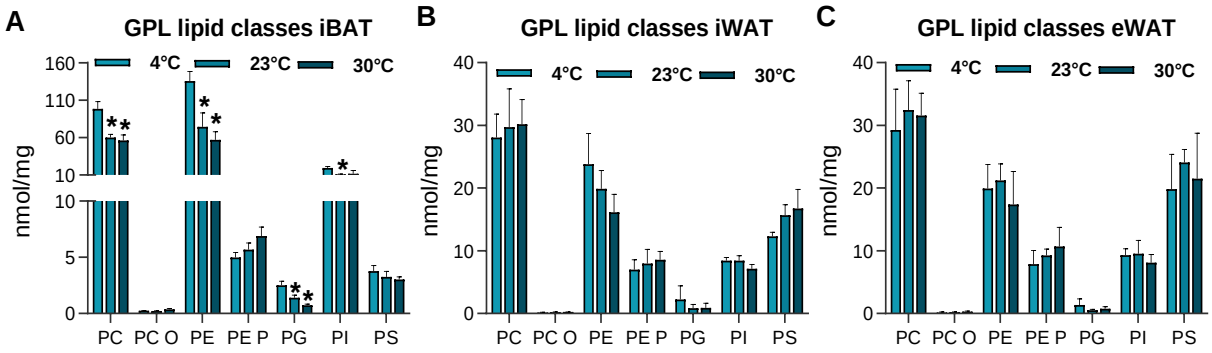

Figure 23: GPL lipid classes in iBAT, but not in WAT mitochondria, are dependent on the housing temperature of mice. GPL composition of (A) iBAT, (B) iWAT and (C) eWAT mitochondria isolated from mice housed at 4°C, 23°C or 30°C. Shown are means +SD of n= 3 per group, *p<0.01 indicates significant differences to 4°C determined using a two-sided student's t-test with Welch's correction. Each mitochondrial sample was isolated from tissue pooled of n= 5-10 mice.

3.1.4 INCREASED GPL/FC RATIO IN BAT MITOCHONDRIA DERIVES FROM INCREASED GPL *DE NOVO* SYNTHESIS

We proceeded to inquire as to whether the observed elevation in GPL/FC ratios in iBAT mitochondria was a consequence of GPL *de novo* synthesis or from cholesterol biosynthesis. Cholesterol biosynthesis was investigated by measuring the mRNA expression levels of genes involved in the HMGCR pathway. There was no systemic difference in enzyme expression levels between different adipose tissue depots. A few genes demonstrated increased expression levels in iBAT compared to WAT (e.g. SREBP2). However, the upregulation of genes involved in an increase in FC biosynthesis does certainly not explain the increased GPL/FC ratios (**Figure 24** A).

The total GPL portion of iBAT mitochondria was primarily composed of PC and PE. Thus, it was tested whether brown adipose tissue has a distinctive *de novo* synthesis rate in these major GPL classes. As illustrated in **Figure 24** D, a stable isotope labelling strategy (Kennedy pathway; see introduction **Figure 2**) was employed to compare PC and PE *de novo* synthesis capabilities in the three adipose tissue depots. Mice were intraperitoneally injected with stable isotope-labeled choline[D_9] and ethanolamine[D_4]. After two hours, it was quantified how much of these lipids were incorporated into the respective GPL in the adipose tissue depots. This revealed elevated synthesis capacities for both phospholipid classes in brown adipose tissue compared to iWAT (decrease: PC[D_9], 5-fold; PE[D_4], 3-fold) and eWAT (decrease: PC[D_9], 5.5-fold; PE[D_4], 7.7-fold) depots (**Figure 24** B, C). PC[D_4], which originates from PEMT activity, could not be detected.

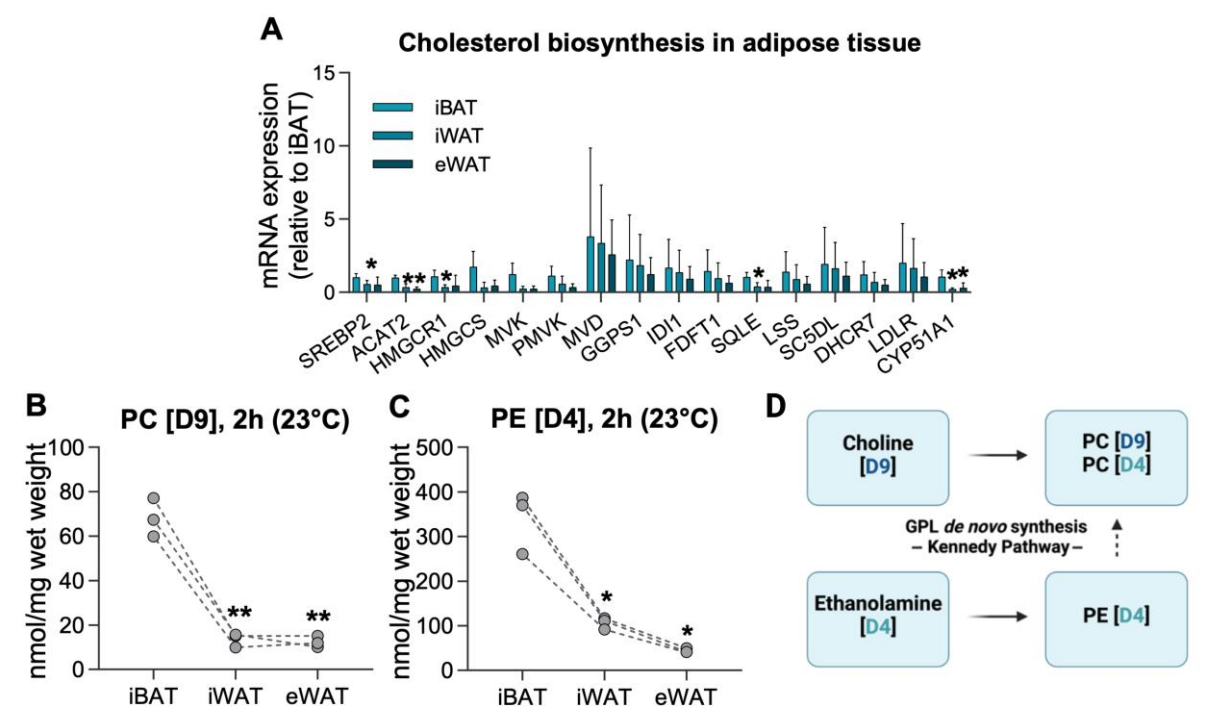

Figure 24: Increased GPL/FC ratios in iBAT mitochondria derive from increased GPL de novo synthesis. *(A) mRNA expression of genes involved in cholesterol biosynthesis in iBAT (n= 8), iWAT (n= 7) and eWAT (n= 8) from mice housed at room temperature. (B) PC[D_9], and (C) PE[D_4] levels detected 2 hours after intraperitoneal injection of choline[D_9] and ethanolamine[D_4] in iBAT, iWAT and eWAT of n= 3 mice housed at 23°C. Associated samples originating from the identical mouse are linked by dashed lines. (D) Scheme of applied labelling strategy to quantify de novo PC and PE synthesis in mouse tissue. Shown are means +SD; *p<0.05 and **p<0.01 indicate significant differences relative to iBAT determined with two-sided student's t-test with Welch's correction.*

3.1.5 A BAT SPECIFIC LIPID SPECIES SIGNATURE COMPRISING PC 38:2 AND FC AS WELL AS THE GPL/FC RATIO CAN BE RELATED TO ADIPOSE TISSUE BROWNING

To validate these results, we applied machine learning to develop a BAT-specific lipid signature that could be used to predict the tissue origin of unknown mitochondrial samples. Random Forest (RF)-based models were employed to accurately classify observations (i.e. lipid species) into categories (i.e. tissue origin of mitochondrial samples). RF is a supervised decision tree learning algorithm that can handle large numbers of variables with small sample sizes without overfitting *(Biau 2010)*

The RF model was able to classify samples based on 94 lipid species, including GPL species (PC, PC O, PE, PE P, PG, PI, PS) and FC, obtained from subsets of liver, muscle, iBAT, and eWAT samples, as input for variable reduction and selection. The lipid species that most effectively classified our samples were: (1) PC 38:2, (2) FC, and (3) PE P-16:0/22:6. The top 10 lipid species are depicted in (**Table 29**).

Table 29: *Top 10 ranked lipid species most effectively classifying samples after RF analysis of the training dataset.*

Rank	**1**	**2**	**3**	**4**	**5**	**6**	**7**	**8**	**9**	**10**
Lipid species	PC 38:2	FC	PE P 16:0/22:6	PE P 18:0/22:6	PS 38:3	PE 40:7	PC 34:2	PE 34:2	PE P 16:0/20:4	PG 32:1

Next, two models were trained that differed in using either the top three (A) or top two (B) lipid species for sample classification. Both models effectively classified our samples from the training set with high sensitivity and specificities (Receiver operator characteristic (ROC) – area under the curve (AUC): (A) 0.932, (B) 0.927). The models also performed well on an independent sample set consisting of iBAT, WAT, and liver samples for verification (**Figure 25** A, B, E, F). Both models performed similarly, with the model containing two variables achieving a slightly higher verification ROC-AUC (0.856 vs. 0.809). All three sample types (BAT, eWAT, liver; muscle data were not available for verification) were clearly classified, although classification probabilities were higher for iBAT and eWAT mitochondrial preparations than for liver (**Figure 25** C, G).

As illustrated in **Figure 23**, the GPL profile was found to be related to the browning capacity of iBAT mitochondria. Therefore, both random forest models were tested on mitochondria originating from iBAT, iWAT, and eWAT of mice housed at 4°C, 23°C, or 30°C for seven days to either promote or antagonize adipose tissue browning. iWAT's browning capacity is lower than it is in iBAT, but higher than it is in eWAT. According to both models, the prediction probabilities of analyzed iBAT samples decreased at 30°C, while the prediction probabilities for WAT decreased at 4°C (**Figure 25** D, H). As mitochondria purified from iWAT were not included in the training sample set, it was not possible to accurately predict their origin. They were classified as originating from liver (Model B, 2 lipid species), or either liver or eWAT (Model A, 3 lipid species) depending on the housing temperature. As the temperatures rose from 4°C to 30°C, the probability of iWAT being classified as eWAT increased, whereas the probability of iBAT being classified as such decreased, respectively.

These analyses further validate the notion that distinct types of mitochondria exhibit notable disparities in their PC and FC contents. Additionally, the findings indicate a relation to browning capacity and that GPL and FC are sufficient to predict the tissue origin of mitochondrial preparations from eWAT and iBAT (**Figure 25** D, H).

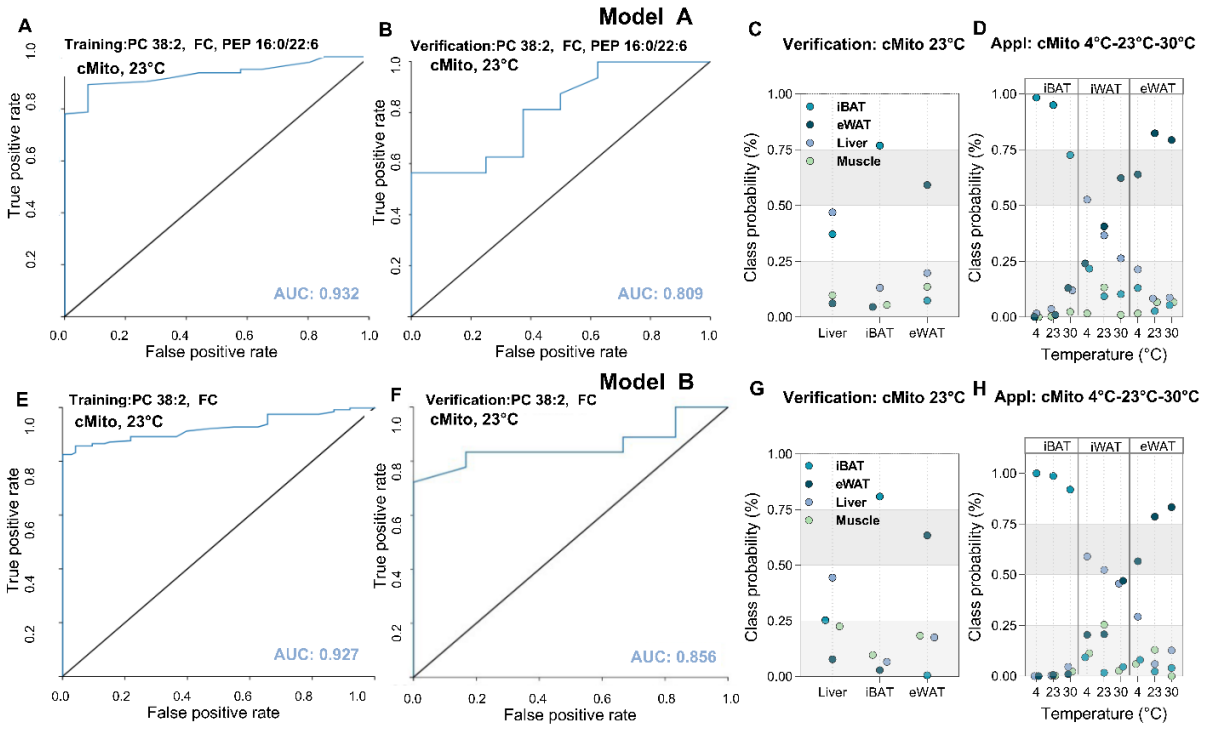

Figure 25: PC 38:2, PEP 16:0/22:6 and FC can predict mitochondrial tissue origin and can be related to adipose tissue browning. (A-D) Model A based on Random Forest (RF) containing 3 lipid species (PC 38:2, FC, PE P 16:0/22:6) and (E-H) Model B with 2 lipid species (PC 38:2, FC). ROC curves with (A, E) training (iBAT, n= 6; liver, n= 3; eWAT, n= 3; muscle, n= 3) and (B, F) verification (liver, n= 11; iBAT, n= 7; eWAT n= 6; muscle was not tested) sample sets; (C, G) Classification probabilities, which indicate the individual prediction confidences for iBAT, eWAT, liver and muscle, tested on the verification sample set. A score of 1 equals to 100% confidence; (D, H) Classification probabilities of both models tested on a new set of mitochondria isolated from eWAT, iWAT and iBAT of mice housed at 4°C, 23°C and 30°C of n= 3 per condition. Shown are means. iWAT was not part of the training sample set and hence, cannot be predicted as such. Each mitochondrial preparation was isolated from tissue pooled of n= 5-10 mice.

Independent of the housing temperature, the same mitochondrial sample set showed dramatically different FC levels between all three adipose tissue depots (**Figure 26** A, B). The abundance of PC 38:2 as well as the total GPL content was approximately 3-fold (4°C), 2-fold (23°C), and 1.2-fold (GPL, 30°C; unchanged for PC 38:2) elevated in BAT mitochondria compared to WAT mitochondria (**Figure 26** C, G), demonstrating a clear correlation with decreasing housing temperatures in iBAT but not in WAT mitochondria (**Figure 26** D, H). The concentrations of PE P 16:0/22:6 (included only in model A) negatively correlated with adipose tissue browning capacity, independent of the housing temperature (**Figure 26** E, F). The GPL/FC ratio was significantly elevated in iBAT mitochondria compared to WAT mitochondria at all housing temperatures (4°C 25-fold, 23°C 20-fold, 30°C 15-fold) (**Figure 26** I).

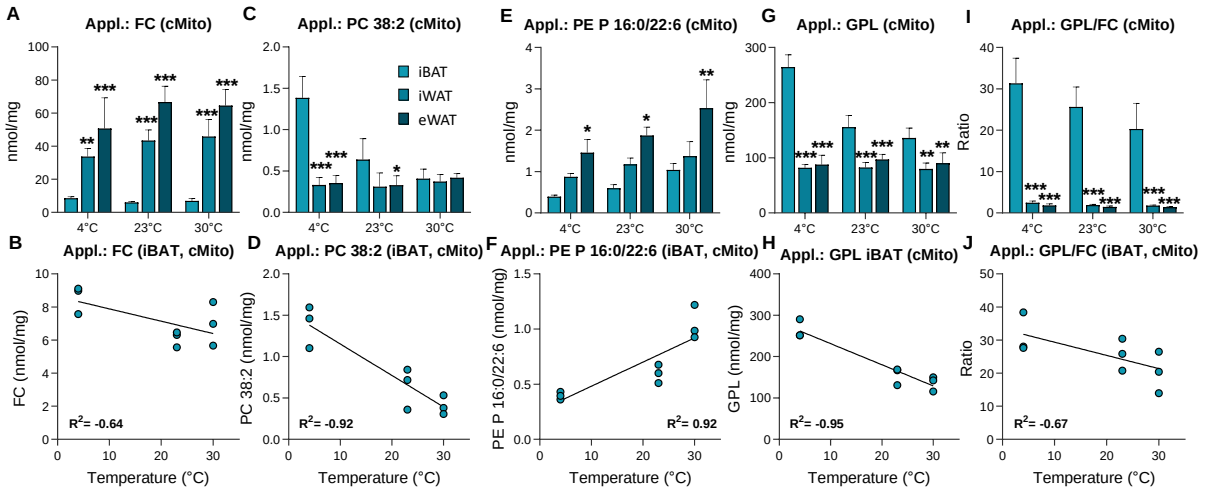

Figure 26: GPL, FC and the GPL/FC ratio can be related to adipose tissue browning. *(A) FC, (C) PC 38:2, (E) PE P 16:0/22:6, (G) GPL and (I) GPL/FC ratio in cMito isolated of iBAT, iWAT and eWAT of mice housed at room temperature. Correlation of (B) FC, (D) PC 38:2, (F) PE P 16:0/22:6, (H) GPL and (J) GPL/FC ratio of cMito originating from iBAT with housing temperatures (4°C-23°C-30°C). Samples were identical to those used in* ***Figure 25*** *D and H. R^2 indicates Pearson's correlation coefficient. Shown are means of n= 3 +SD; *p<0.05, **p<0.01 and ***p<0.001 indicate significant differences relative to iBAT of respective temperatures, determined using a two-sided student's t-test with Welch's correction.*

3.1.6 UCP_1 ACTIVITY IN BAT MITOCHONDRIA DEPENDS ON THE GPL/FC RATIO

The extremely low levels of FC and high levels of GPL observed in brown adipose tissue mitochondria and their association with browning suggest a causal role in thermogenic function, including UCP1-mediated respiration. To investigate this hypothesis, a series of experiments was performed using brown adipose tissue, primary brown adipocytes, and thereof isolated mitochondria originating from UCP1 WT and UCP1 KO mice.

3.1.6.1 LOADING BAT MITOCHONDRIA WITH BSA-FC-COMPLEX DECREASES UCP_1 ACTIVITY

Mitochondria isolated from iBAT were incubated with cholesterol coupled to BSA (0.2 mg cholesterol coupled to BSA/mg mitochondrial protein). Oxygen consumption was measured using high resolution respirometry. Following the measurement of basal respiration, G3P was injected to fuel general respiration and UCP1, and subsequently GDP was injected to estimate UCP1 activity. GDP competitively binds UCP1, thereby interrupting the interaction with respective activators, such as free fatty acids. This resulted in a markedly reduced GPL/FC ratio, approaching 1.0, comparable to that previously observed in white adipose tissue mitochondria (**Figure 27** C; **Figure 22**). Further, UCP1 activity was strongly diminished (by ~80%; as calculated from the difference between G3P- and GDP-mediated respiration) (**Figure 27** A-B), hinting towards a potential correlation between BAT function and the GPL/FC ratio. It should be noted that this experimental approach does not clearly proof the possibility that the cholesterol-mediated inhibition of respiratory capacity on iBAT mitochondria is solely mediated through UCP1 activity, given that basal respiration is already inhibited to a high extent (before GDP-mediated UCP1 inhibition). It may be possible that insufficient saturation of BSA with cholesterol was achieved, allowing free BSA to adhere to mitochondria and thereby interact with hydrophobic species presented by those.

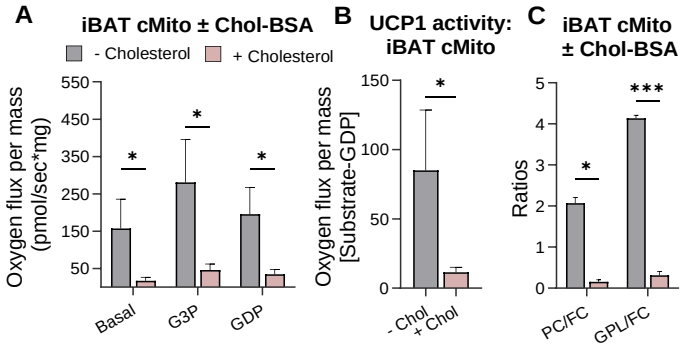

Figure 27: Decreasing mitochondrial GPL/FC via BSA-coupled-cholesterol decreases UCP1 activity in iBAT mitochondria. *(A) High resolution respirometry of iBAT mitochondria treated with 0.2 mg cholesterol coupled to BSA/mg mitochondrial protein. G3P was injected as OXPHOS and UCP1 substrate, GDP to inhibit UCP1; (B) UCP1 activity was calculated by subtracting the GDP-mediated oxygen flux from G3P-mediated respiration; (C) PC/FC and GPL/FC ratios. Shown are means +SD of n= 4 (A, B) and n= 2 (C), *p<0.05, **p<0.01 and ***p<0.001 indicate significant differences to control mitochondria (treated with BSA), determined using a two-sided student's t-test with Welch's correction. Each mitochondrial sample was isolated from tissue pooled of n= 5 mice.*

3.1.6.2 ME-β-CD INCREASES UCP$_1$ ACTIVITY IN MITOCHONDRIA AND PRIMARY BROWN ADIPOCYTES OF WT, BUT NOT UCP$_1$ KO MICE

Methyl-β-cyclodextrins (me-β-CD) are molecules that can be used to either load or remove cholesterol from natural and artificial membranes. This is achieved by exploiting their structure, which comprises a hydrophobic cavity surrounded by a polar surface *(Sanchez et al. 2011)*. Therefore, the identical high-resolution respirometry-based assay, as performed in **Figure 27**, was employed, resulting in a slight increase in UCP1-mediated respiration in isolated iBAT mitochondria treated with 1 µM me-β-CD (**Figure 28** A-B).

Additionally, murine primary brown adipocytes (mPBAC) were treated with me-β-CD before respiratory analyses, which was conducted using microplate-based respirometry. The following assay was employed: After the measurement of basal respiration, oligomycin was administered in order to inhibit CV of the electron transport chain, thereby allowing for the estimation of proton leak-linked respiration. Subsequently, cells were treated with isoproterenol, which induces β_3-adrenergic-mediated lipolysis, thereby releasing FFA that fuel UCP1. FCCP was injected to measure maximal respiratory capacity, and antimycin A was administered to inhibit CIII, thereby inhibiting OXPHOS. To ensure that alterations in cholesterol levels reached the mitochondrial level, not only primary brown adipocytes were used for respiratory analysis, but also thereof isolated mitochondria, which were obtained using a commercially available antibody-based isolation technique. For the isolated mPBAC mitochondria, high-resolution based respirometry was applied. In contrast to mitochondria isolated from tissue, mitochondria isolated from primary brown adipocytes exhibited minimal responsiveness to any substrates (neither pyruvate, malate, succinate, nor G3P). Consequently, UCP1 was additionally fueled by the injection of a previously prepared BSA-palmitate-complex (10:1). This resulted in a significant increase in UCP1 activity in both cells (1.5-fold) and thereof isolated mitochondria (3.5-fold) following incubation with 10 µM me-β-CD. This effect was not observed in primary brown adipocytes isolated from UCP1 knockout mice, indicating that mitochondrial cholesterol concentrations have a specific effect on UCP1 activity (**Figure 28** C-F).

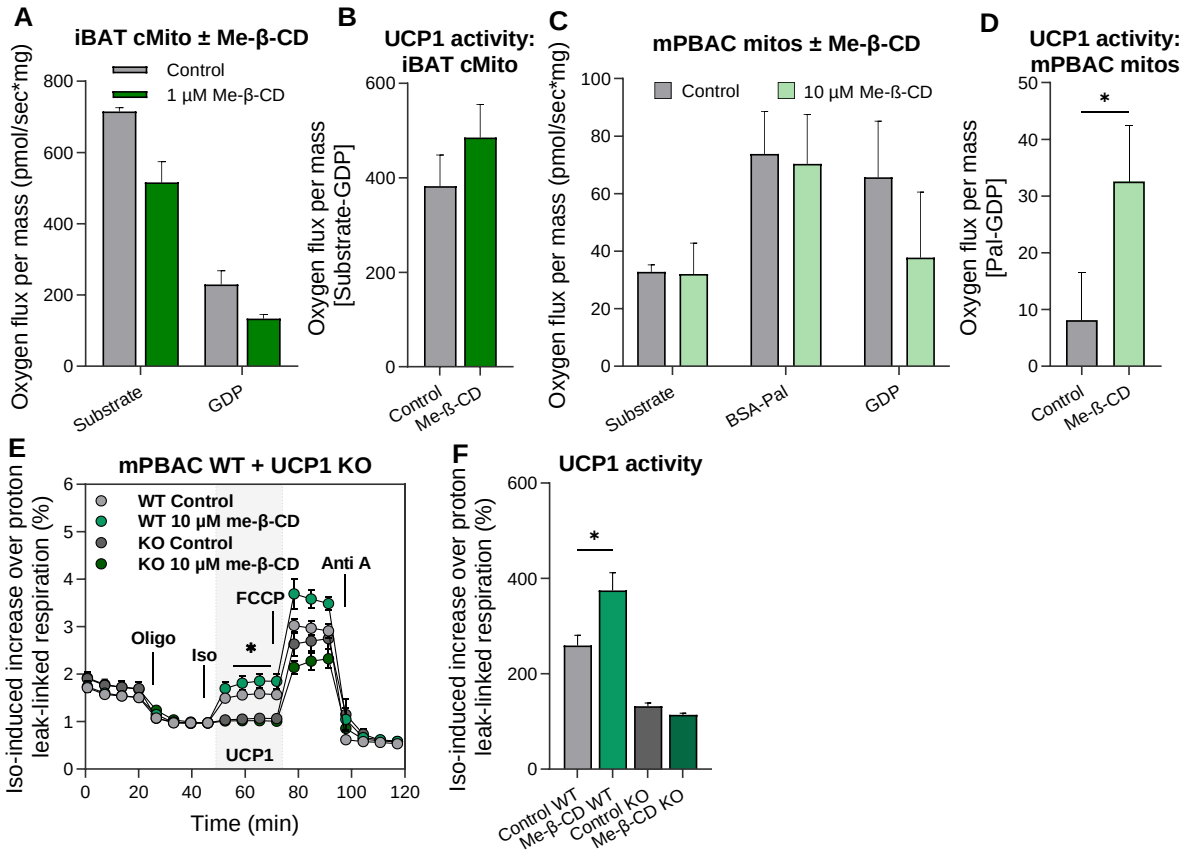

Figure 28: Me-ß-CD treatment of mPBAC and thereof isolated mitochondria as well as of iBAT increases UCP1 activity in WT, but not in UCP1 KO mice. *(A) High resolution respirometry of iBAT mitochondria treated with 1 µM me-ß-CD. G3P was injected as OXPHOS and UCP1 substrate, GDP to inhibit UCP1; (B) UCP1 activity was calculated by subtracting the GDP-mediated oxygen flux from G3P-mediated respiration. (C) High resolution respirometry of mPBAC mitochondria treated with 10 µM me-ß-CD. G3P was injected as OXPHOS and UCP1 substrate, UCP1 was additionally induced by injection of palmitate coupled to BSA (1:10), GDP was injected to inhibit UCP1; (D) UCP1 activity was calculated by subtracting the GDP-mediated oxygen flux from palmitate-mediated respiration. (E) Microplate-based respirometry was applied on primary brown adipocytes of WT and UCP1 KO mice which were previously treated with 10 µM me-ß-CD. Measurement of basal respiration, proton leak-linked respiration (oligomycin; CV inhibitor), UCP1-mediated respiration (isoproterenol; β-adrenergic agonist), maximal respiratory capacity (FCCP; uncoupling reagent) and non-mitochondrial respiration (antimycin A; CIII inhibitor). (F) UCP1 activity was calculated as isoproterenol-induced increase of oxygen consumption over proton leak-linked respiration. Shown are means +SD of n= 2 (A, B), n= 3 (C, D) and means ±SEM of n= 5 (E, F), *p<0.05 indicates significant differences to control mitochondria, determined using a two-sided student's t-test.*

To enrich mitochondria with FC, primary brown adipocytes and thereof isolated mitochondria were incubated with me-β-CD coupled to cholesterol (5 µM). The used me-β-CD-cholesterol complex was commercially obtained as "water-soluble-cholesterol" (Sigma-Aldrich/Merck) in a fully saturated state, ensuring that me-β-CD cannot bind any other lipids and solely loads mitochondria with cholesterol. This resulted in a mildly reduced GPL/FC ratio (**Figure 29** E). As anticipated, UCP1 activity levels declined by approximately 2-fold in both mPBAC and thereof isolated mitochondria, assayed using the same setups as shown in **Figure 28** (**Figure 29** A-D). To validate that this effect is observed specifically due to UCP1 activity and not due to the inhibition of general respiration, the respiratory capacity of mPBAC isolated from UCP1 KO mice was measured. This analysis did not reveal a difference in UCP1 activity

between control and me-β-CD-cholesterol-treated cells, further strengthening the previous results (**Figure 29** A-B).

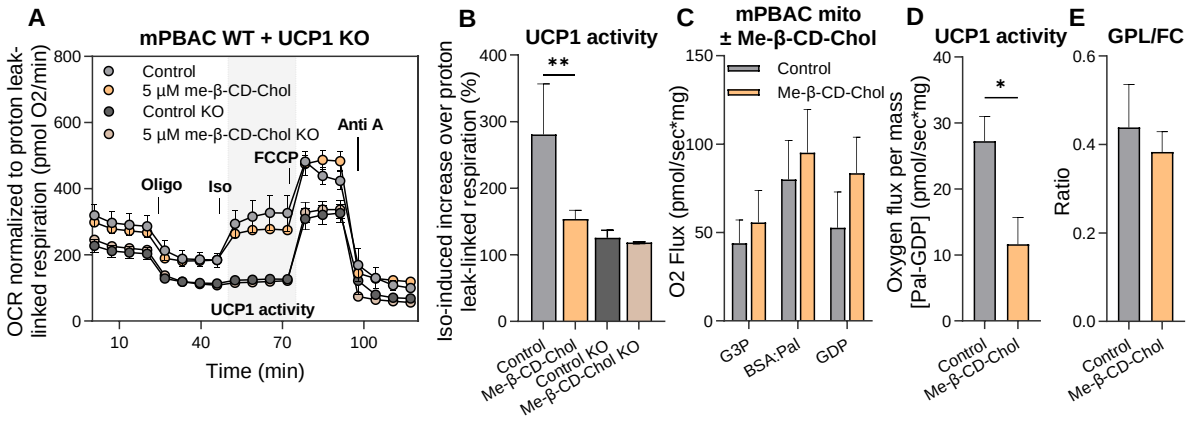

Figure 29: Increasing FC in mPBAC and thereof isolated mitochondria by incubation with a saturated me-ß-CD-cholesterol-complex decreases UCP1 activity in WT mice, but not in UCP1 KO mice. *(A) Microplate-based respirometry was applied on primary brown adipocytes differentiated from pre-adipocytes originating of iBAT of WT and UCP1 KO mice. The cells were previously treated with 5 µM me-ß-CD coupled to cholesterol. Measurement of basal respiration, proton leak-linked respiration (oligomycin; CV inhibitor), UCP1-mediated respiration (isoproterenol; β-adrenergic agonist), maximal respiratory capacity (FCCP; uncoupling reagent) and non-mitochondrial respiration (antimycin A; CIII inhibitor). (B) UCP1 activity was calculated as isoproterenol-induced increase of oxygen consumption over proton leak-linked respiration. (C) High resolution respirometry of mPBAC mitochondria treated with 5 µM me-ß-CD coupled to cholesterol. G3P was injected as OXPHOS and UCP1 substrate, palmitate-BSA complex (1:10) to additionally induce UCP1 activity, and GDP to inhibit UCP1; (D) UCP1 activity was calculated by subtracting the GDP-mediated oxygen flux from palmitate-mediated respiration. (E) GPL/FC ratio of mitochondria isolated from mPBAC treated with 5 µM me-ß-CD coupled to cholesterol. Shown are means ±SEM of n= 7 WT and n= 5 UCP1 KO (A, B) and means +SD of n= 4 (C-E); *p<0.05 and **p<0.01 indicate significant differences to control mitochondria, determined using a two-sided student's t-test with Welch's correction.*

Taken together, modulating GPL/FC ratios using me-β-CD impacts UCP1 activity. Nevertheless, it should be noted, that the use of me-β-CD to extract FC from membranes is controversially discussed in the literature, as it also removes phospholipids at high concentrations. It is not clear at which concentration me-β-CD can specifically remove FC from lipid domains with different packing densities *(Sanchez et al. 2011)*. In this work, a range of concentrations between 1 and 50 µM me-β-CD were tested. The concentrations depicted in **Figure 28** and **Figure 29** appear to be within an optimal range, as higher concentrations resulted in a reversal of the effects on UCP1 activity (not shown), potentially suggesting an impact on other phospholipids.

3.1.6.3 UCP$_1$ FUNCTION DEPENDS ON STARD3-MEDIATED CHOLESTEROL IMPORT INTO MITOCHONDRIA OF PRIMARY BROWN ADIPOCYTES

To exclude the possibility that the impact on UCP1 activity through me-β-CD is not specifically due to alterations in FC levels, an alternative experimental approach was selected to alter GPL/FC ratios in primary brown adipocyte mitochondria. The GPL/FC ratio in mitochondria was modified by altering the

level of mitochondrial lipid transporters. To identify suitable candidates, potential cholesterol transport proteins were evaluated in terms of their mRNA expression levels in adipose tissue depots as well as in their protein abundance in primary brown adipocytes. All tested transporters were detected in adipose tissue on the mRNA level, with the highest expression in STARD1, which is known to be the main mitochondrial cholesterol transporter *(Voilquin et al. 2019)*. However, STARD1 was not identified in a full proteome analysis of primary brown adipocytes (**Figure 30** A, B). Consequently, it was excluded as a potential candidate. For the same reason, the mitochondrial cholesterol transporter TSPO was excluded as a candidate. Additionally, TSPO displayed minimal mRNA expression in brown adipose tissue, which was not consistent across the various adipose tissue types (**Figure 30** A, B). VDAC1 was excluded as it acts in cooperation with TSPO to transport cholesterol *(Shoshan-Barmatz et al. 2019)*. STARD4 and STARD5 were excluded as they are primarily known for cholesterol transport into ER compartments *(Voilquin et al. 2019)*. Ultimately, STARD3 was selected as mitochondrial cholesterol transporter *(Balboa et al. 2017; Elustondo et al. 2017; Horibata und Sugimoto 2010)* due to its abundance in the brown adipocyte proteome and comparable gene expression levels between adipose tissue depots (**Figure 30** A, B). To ensure that isoproterenol utilized for the induction of UCP1 activity does not influence STARD3 expression levels, the proteome of brown adipocytes incubated with and without isoproterenol (0.5 µM, 30 min) was analyzed. STARD3 protein was neither upregulated nor downregulated following incubation with the β-adrenergic agonist (**Figure 30** C).

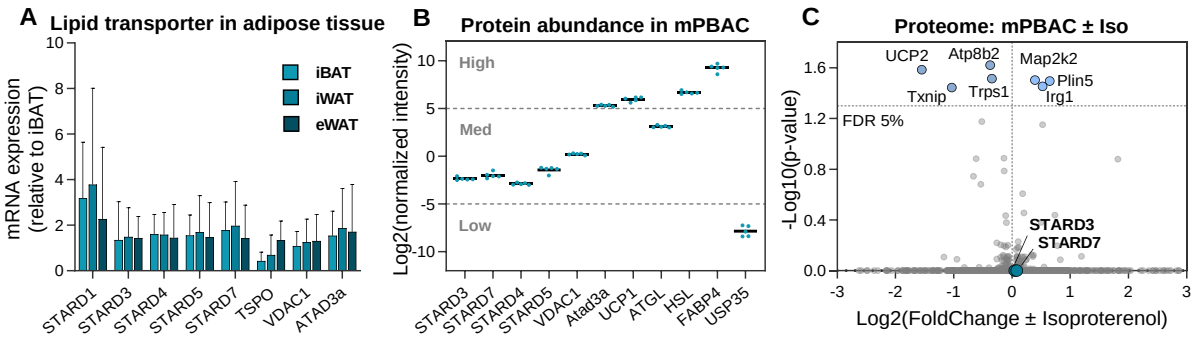

Figure 30: Mitochondrial lipid transporter STARD3 is expressed in white and brown adipose tissue and primary brown adipocytes on mRNA and protein level. *(A) mRNA expression of lipid transporter in iBAT, iWAT and eWAT. Shown are means +SD of n= 8 (iBAT, eWAT) and n= 7 (iWAT); no significant differences relative to iBAT were determined using a two-sided student's t-test with Welch's correction. (B) Lipid transporter identified in full proteomic dataset generated using LC-HR-MS/MS of primary brown adipocytes. (C) Volcano plot presenting significant differences (-Log$_{10}$(q-value)) of Log$_2$(FoldChange) of proteins identified in primary brown adipocytes, previously treated with 0.5 µM isoproterenol for 30 minutes. Blue dots indicate proteins significantly decreased (left) or increased (right) in mPBAC after Benjamini-Hochberg FDR correction at p<0.05. Turquois dot represents STARD3 (no significant change). Proteomic data from n= 5 samples per group, each pooled from primary brown adipocytes originating of n= 3 mice.*

To address the question of whether modulating the STARD3 expression in primary brown adipocytes alters mitochondrial GPL/FC ratios and, most importantly, whether it affects UCP1 function, lentivirus-based overexpression as well as siRNA-mediated gene silencing were employed. For microplate-based respirometry, a similar assay compared to the one depicted in **Figure 29** was used:

Measurement of [1] basal respiration; [2] basal uncoupled respiration after blocking ATP synthase with oligomycin; [3] induction of UCP1 by addition of isoproterenol (ISO) as β-adrenergic agonist; [4] assessment of the maximal respiratory capacity by using carbonyl cyanide 4-(trifluoromethoxy) phenylhydrazone (FCCP) as uncoupling agent; and [5] non-mitochondrial O2 consumption applying antimycin A (Anti A). UCP1 activity was calculated by subtraction of the OCR determined at [2] (basal uncoupled respiration, Oligo) from the OCR at [3] (UCP1 induction, ISO).

As already demonstrated in **Figure 30**, STARD3 is expressed at significant but not differential levels in white and brown adipose tissue of mice (**Figure 31** A). Lentivirus-based overexpression of STARD3 resulted in an approximately 350-fold increase in mRNA expression levels, whereas the knockdown led to a 2.5-fold decrease (**Figure 31** E, H). This resulted in a significant increase in mitochondrial FC and a 30% reduction in the GPL/FC ratio in the overexpression cells (**Figure 31** N, O). In contrast, cells with STARD3 knockdown exhibited decreased FC levels and a 1.2-fold elevated GPL/FC ratio (**Figure 31** K, L). Most importantly, UCP1 activity levels were also affected. With higher FC levels, UCP1 activity decreased by more than 2-fold (**Figure 31** I), while with lower FC levels, UCP1 activity increased by 55% (**Figure 31** F). To confirm that STARD3-mediated FC transport is specifically linked to UCP1-mediated uncoupled respiration, siRNA-mediated knockdown was also conducted in primary brown adipocytes derived from UCP1 KO animals. This resulted in a reduction of approximately 50% in STARD3 mRNA levels, while UCP1 activity remained unaltered (**Figure 31** B-C).

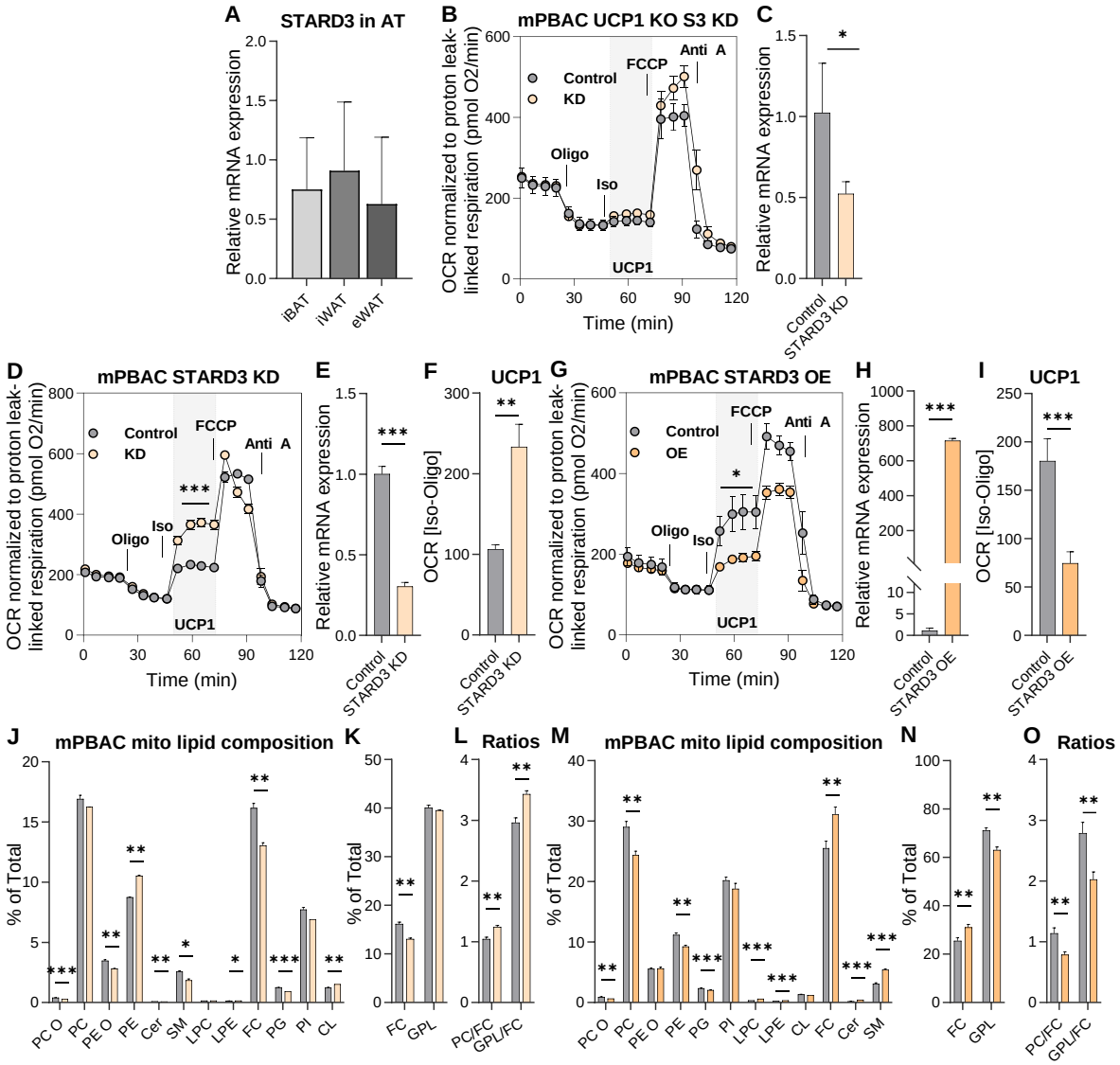

Figure 31: UCP1 function depends on STARD3-mediated mitochondrial cholesterol import in mPBAC of WT mice, but not of UCP1 KO mice. *(A) Relative mRNA expression of STARD3 in iBAT (n= 8), iWAT (n= 7) and eWAT (n= 8). (B, D, G) Microplate-based respirometry in primary brown adipocytes originating from (B) UCP1 KO mice (n= 5-6) and (D) wildtype mice (n= 10-12) which were previously treated with either non-targeting control or siRNA against STARD3 or (G) wildtype mice (n= 19) which were previously treated with lentivirus-based overexpression vectors of STARD3; The oxygen consumption rate (OCR) was measured at basal conditions, at proton leak-linked respiration (oligomycin; CV inhibition), UCP1-mediated respiration (isoproterenol; β-adrenergic agonist), maximal respiratory capacity (FCCP; uncoupling reagent) and after inhibition of the electron transport chain (antimycin A; CIII inhibitor). (C, E, H) STARD3 mRNA expression after siRNA mediated knockdown in UCP1 KO cells (n= 3) (C), wildtype cells (n= 3) (E) or wildtype cells after lentivirus-based overexpression (n= 3) (H). (F, I) UCP1 activity was calculated via subtraction of the OCR after oligomycin injection from OCR measured after isoproterenol treatment. (J-L) Lipid class composition (n= 3) (J), FC and GPL composition (n= 3) (K), as well as PC/FC and GPL/FC composition (n= 3) (L) in mitochondria of cells having the siRNA-mediated knockdown. (M-O) Lipid class composition (n= 3) (M), FC and GPL composition (n= 3) (N), as well as PC/FC and GPL/FC composition (n= 3) (O) in mitochondria of cells having the lentivirus-based overexpression. Shown are means ±SEM (B, D, G) and means +SD (bar plots); *p<0.05, **p<0.01 and ***p<0.001 indicate significate differences relative to controls, determined using two-sided t-tests with Welch's correction.*

3.1.6.4 UCP$_1$ FUNCTION IN BAT MITOCHONDRIA IS ALTERED AFTER FUSION WITH SMALL UNILAMELLAR VESICLES CONTAINING GPL AND FC

To study whether the GPL/FC ratio of intact mitochondria purified from iBAT of WT mice controls UCP1 activity in a concentration-dependent manner, mitochondria were incubated with small unilamellar vesicles (SUV) containing varying compositions of FC and GPL. The following compositions were used in the presence of methyl-α-cyclodextrin (me-α-CD): 95% PC, 5% phosphatidic acid (PA); 75% PC, 5% PA, 20% FC; 55% PC, 5% PA, 40% FC; and 35% PC, 5% PA, 60% FC). The addition of PA was not solely intended to alter the GPL/FC ratio; it was also designed to reduce the size of donor vesicles through its conical shape and small headgroups, thereby accelerating their fusion with mitochondria *(Clark et al. 2020; Hauser und Gains 1982)*. As illustrated in **Figure 32**, SUVs exhibit hydrophilic properties on their outer shell, which is exposed to the mitochondria. In contrast, their inner core is hydrophobic. Me-α-CD is used as a lipid carrier, facilitating the fusion of GPL- and FC-containing vesicles with lipid bilayers. Me-α-CD was used instead of me-β-CD (**Figure 28** and **Figure 29**), as it cannot bind free cholesterol and is therefore solely transporting FC incorporated in the vesicle without changing cholesterol that was already integrated in mitochondrial membranes beforehand *(Li et al. 2016)*.

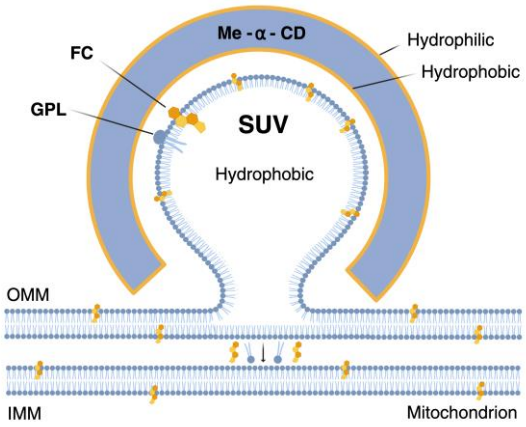

Figure 32: Scheme illustrating the fusion of SUV containing varying compositions of GPL and FC with the mitochondrial outer membrane, facilitated by methyl-alpha-cyclodextrin.

The mitochondrial bioenergetics profile was measured using microplate-based respirometry. Since mitochondrial membranes do not express adrenergic receptors, the use of isoproterenol would not be effective and the assay was modified as follows: [1] Measurement of basal respiration; [2] inhibition of ATP synthase by oligomycin (oligo) to distinguish oxygen consumption used for ATP synthesis (coupled respiration) from the basal proton leak (basal uncoupled respiration); [3] fueling general respiration and UCP1 with glycerol-3-phosphate (G3P); [4] inhibition of UCP1-mediated respiration with guanosine diphosphate (GDP); and eventually [5] blocking complex III of the electron transport chain with antimycin A (anti A) to inhibit mitochondrial respiration and leave only non-mitochondrial oxygen consumption. UCP1 activity was calculated by subtraction of the O_2 consumption rates (OCR) at [4] (UCP1 inhibition, GDP) from the OCR at [3] (UCP1 fueling, G3P).

Donor vesicles comprising only GPL increased the PC/FC ratio 8.1-fold and the GPL/FC ratio 3.5-fold (**Figure 33** F). The ratios were gradually decreased following the addition 20-60% FC to the SUVs, leading to an increase in mitochondrial FC levels and a reduction in PE and, especially, PC portions

(**Figure 33** E-F). To ascertain whether the SUVs' lipids had reached the inner mitochondrial membranes where UCP1 is located, the lipidome of mitoplasts, which had been treated with vesicles prior to the detachment of the outer mitochondrial membrane, was investigated. This revealed similar results (**Supplementary Figure 6**). Most strikingly, the UCP1 activity of mitochondria loaded with GPL-only vesicles was 1.7-fold higher compared to untreated mitochondria, which was stepwise reduced with an increase in FC loading, matching to the lipidomic data (**Figure 33** A, D). The FC and GPL contents added to the donor vesicles (**Figure 33** G-H) as well as the ones measured in mitochondria using mass spectrometry after treatment with SUVs (**Figure 33** I-J) highly correlated with UCP1 activity, with an R^2 value of approximately 0.95. To ensure that the alterations in oxygen consumption were specifically induced through UCP1 activity, mitochondria originating from UCP1 KO mice were studied. Mitochondria were either directly analyzed (referred to as "UCP1 KO") or mixed with wildtype mitochondria in a ratio of 1:1 (referred to as "WT/UCP1 KO 1:1"). While in mixed WT-UCP1 KO mitochondria, UCP1 activity was approximately half as high as in WT mitochondria, in UCP1 KO mitochondria, UCP1 function was almost absent (**Figure 33** B-D). As visible in the respiratory blots (**Figure 33** A-C), oxygen consumption dropped after G3P injection at each timepoint, suggesting that mitochondria rapidly consume all available oxygen in the plates. To ensure that the observed reduction in UCP1 activity was not the biased result of mitochondrial oxygen consumption (independent of lipid alterations), the oxygen consumption of WT and UCP1 KO mitochondria (both untreated) was analyzed for the three timepoints after G3P injection (25-31-37 minutes) as well as after GDP injection at 43 minutes. This revealed that the timepoints preceding the GDP injection could be related by linear regression, while the OCR following the GDP injection exhibited a pronounced decline (due to the inhibition of UCP1 activity) (**Supplementary Figure 6**). In contrast, linear regression analysis revealed that all timepoints in UCP1 KO mitochondria could be related, indicating that GDP had no effect on G3P-induced oxygen consumption (**Supplementary Figure 6**).

The choice of substrates and the sequence of their application can impact respiratory analyses in BAT mitochondria, including UCP1 activity, as demonstrated by the Nedergaard & Cannon group *(Shabalina et al. 2010)*. To ascertain whether the inhibition of ATPase prior to the injection of G3P might have biased the findings, the UCP1 activity of WT mitochondria incubated with selected vesicles was analyzed in the absence of oligomycin (**Supplementary Figure 6**). In accordance with our previous results, donor vesicles containing solely GPL elevated UCP1 activity, while addition of 20% FC lowered it (**Supplementary Figure 6**). To test whether GPL/FC also affects maximal respiratory capacity of mitochondria, the respiration was measured after injecting GDP (to inhibit UCP1) and carbonyl cyanide 4-(trifluoromethoxy) phenylhydrazone (FCCP) as an uncoupling reagent using both, high-resolution and microplate-based respirometry. The application of both methodologies did not reveal any discernible discrepancies in the maximal respiratory capacity of mitochondria that had been incubated with or without donor vesicles containing varying GPL and FC contents (**Supplementary Figure 6**).

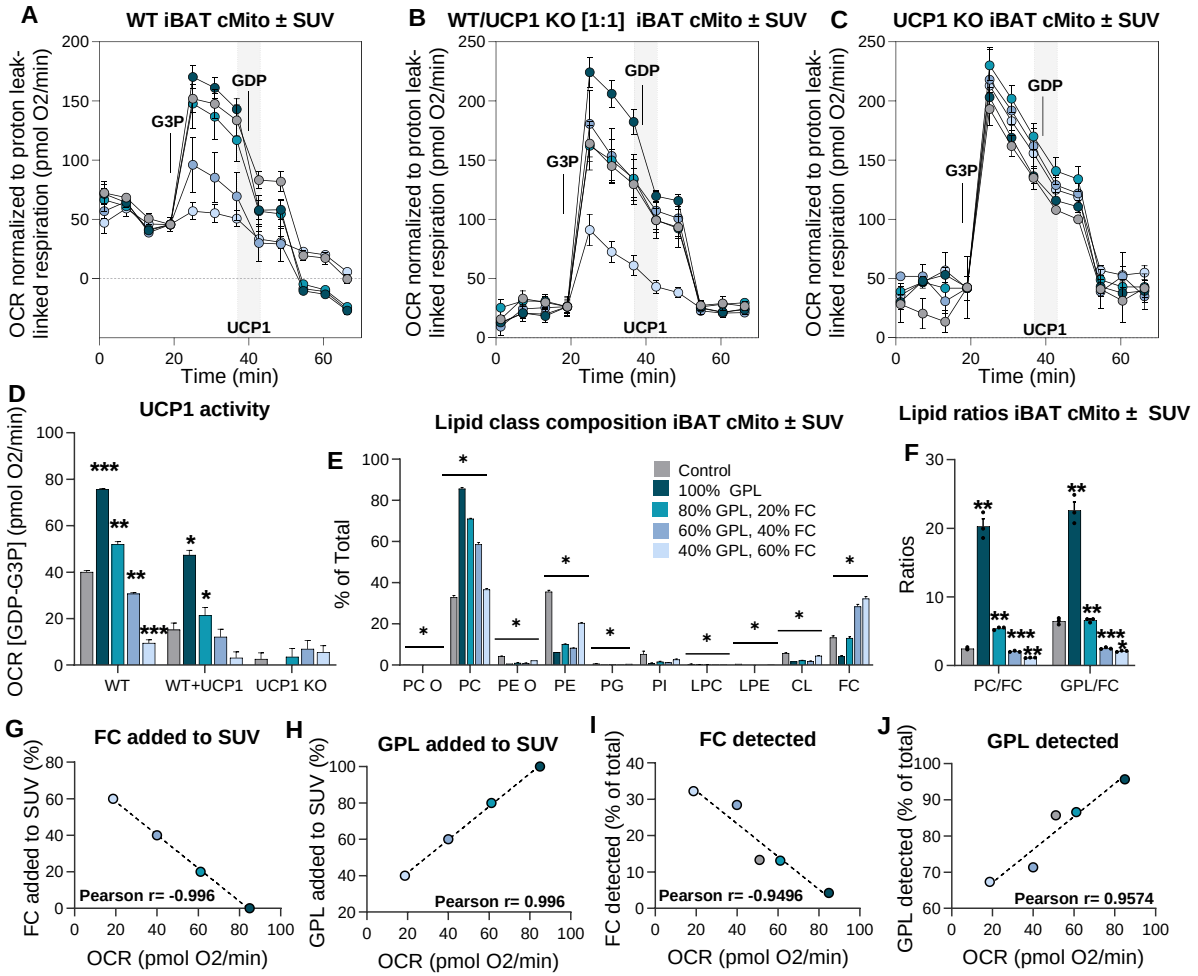

Figure 33: UCP1 function in iBAT mitochondria depends on their GPL/FC ratio when modulated with SUVs consisting of varying lipid compositions. *(A-C) Microplate-based respirometry applied to profile UCP1 activity in mitochondria isolated from iBAT of mice housed at 23°C. The oxygen consumption rate (OCR) was measured at basal conditions, after injections of oligomycin (to inhibit CV, equals basal leak respiration), G3P (to fuel ETC and UCP1 activity), GDP (to inhibit UCP1 activity) and antimycin A (to block electron transport chain, equals non-mitochondrial respiration). Mitochondrial bioenergetics of (A) iBAT WT (n= 8-16), (B) mixed WT-UCP1 KO (1:1) (n= 8-14), and (C) UCP1 KO mitochondria (n= 6-14) loaded with small unilamellar vesicles (SUV) containing varying ratios in GPL (PC, PA) and FC. Shown are data normalized to the OCR determined before G3P injection (19.0 min). (D) UCP1 activity calculated by subtraction of the OCR after GDP-mediated respiration from G3P-induced respiration determined in A-C. (E) Lipid class composition, (F) PC/FC and GPL/FC of iBAT mitochondria that were untreated or loaded with SUVs containing varying ratios in GPL (POPC, POPA) and FC (n= 3). Measured with mass spectrometry. Shown are means ±SEM (A-C) and +SD (bar blots); *p<0.05, **p<0.01, and ***p<0.001 indicate a significant difference for the comparisons control vs. 100% GPL, 100% GPL vs. 80% GPL + 20% FC, 80% GPL + 20% FC vs. 60% GPL + 40% FC and 60% GPL + 40% FC vs. 40% GPL + 60% FC; determined using a two-sided Student's t-test with Welch's correction. (G-H) Correlation of UCP1 activity with contents of FC (G) or GPL (H) added to SUV. (I-J) Correlation of UCP1 activity with contents of FC (I) or GPL (J) measured with mass spectrometry in iBAT mitochondria incubated with donor vesicles. R indicates Pearson's correlation coefficient. Each mitochondrial sample was isolated from tissue pooled of n= 5 mice.*

3.1.6.5 THE DIETARY FAT CONTENT IMPACTS MITOCHONDRIAL GPL/FC AND UCP$_1$ FUNCTION IN BAT MITOCHONDRIA OF MICE

It was previously published that feeding a high fat diet to mice can cause an adaptive induction of norepinephrine-induced UCP1-dependent thermogenesis while attenuating their body weight and thereby the risk for obesity. This is particularly evident in 129Sv/Ev Tac mice, which exhibit a markedly higher capacity for UCP1-mediated uncoupled respiration than other mouse strains *(Feldmann et al. 2009; Luijten et al. 2019)*. To investigate whether this observation might be attributed to alterations in the GPL/FC ratio, mice were fed a HFD for two weeks (**Supplementary Table 2**). The oxygen consumption of iBAT mitochondria originating from these mice was analyzed using the same high-resolution respirometry assay previously described in **Figure 27**. Consistent with the literature, this revealed that feeding 129Sv/Ev Tac mice a diet enriched in fat (without additional cholesterol) does not impact body weight (**Figure 34** A). However, it does increase UCP1-mediated activity almost 2-fold (**Figure 34** B-C). Notably, the levels of GPL, specifically PE and with that the GPL/FC ratio, was increased in the HFD fed mice compared to those receiving control diet (**Figure 34** D-E). This implies that a diet-induced increase in mitochondrial GPL/FC ratios may result in enhanced UCP1 activity and energy expenditure, thereby contributing to resistance to weight gain.

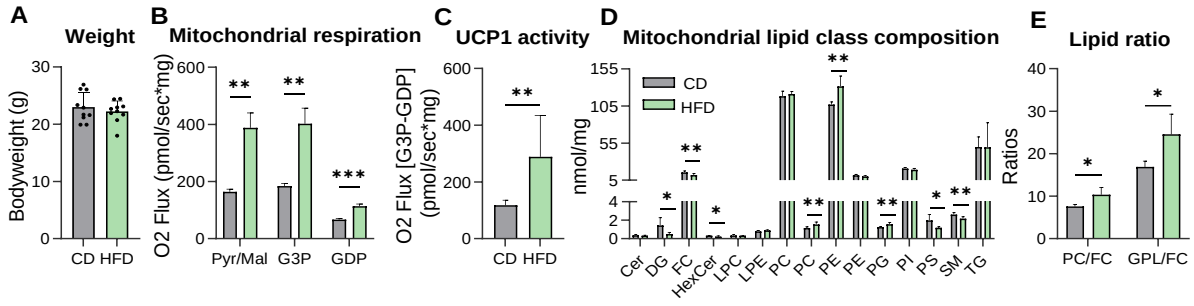

Figure 34: High fat diet increases GPL/FC ratios and UCP1 activity while attenuating body weight. *Mice received either control diet or HFD for 14 days at the age of 10 weeks. (A) Bodyweight of mice (n= 10), (B) High resolution respirometry to profile UCP1 activity in mitochondria isolated from iBAT. OCR flux was measured after injections of substrates for electron transport chain and UCP1 (pyruvate, malate, G3P) and GDP to inhibit UCP1 activity (n= 8). (C) UCP1 activity calculated by subtraction of the O2-flux after GDP treatment from respiration after injection of G3P determined in B (n= 8). (D) Lipid class composition (n= 5-6), as well as (E) PC/FC and GPL/FC of mitochondria isolated from iBAT. Shown are means +SD; *p<0.05, **p<0.01, and ***p<0.001 indicate a significant difference to control diet determined using a two-sided Student's t-test with Welch's correction. Each mitochondrial sample was isolated from tissue pooled of n= 5 mice.*

Taken together, the results of **section 3.1.6** clearly demonstrate a link between GPL/FC ratios in brown adipose tissue mitochondria and UCP1 activity.

3.2 THE ROLE OF PISD FOR BROWN ADIPOSE TISSUE FUNCTION AND UCP$_1$ ACTIVITY

3.2.1 PISD CAN BE RELATED WITH UCP$_1$ ACTIVITY IN BROWN ADIPOSE TISSUE

To provide further and *in vivo* evidence for the findings presented in **3.1**, we asked whether PISD activity, which regulates the mitochondrial PE contents, is critical for UCP1 activity. PE is a major GPL

in BAT mitochondria (**Figure 18**-**Figure 21**), where it can be generated from PS after decarboxylation by PISD activity. Further, PE/FC ratios were almost 60-fold higher in BAT mitochondria compared to WAT mitochondria and could be related to adipose tissue browning (**Figure 22**, **Figure 23**). To date, PISD is believed to be the primary source of mitochondrial PE, as other underlying mechanisms of mitochondrial PE synthesis or transport mechanisms from other organelles to mitochondria (after *de novo* synthesis by PTDSS1/2 in ER/MAM) remain poorly understood. PE levels are significantly elevated in BAT cMito compared to eWAT (**Figure 19**), and in iBAT and iWAT cMito isolated from mice housed at 4°C compared to those from mice housed at 23°C and 30°C (**Figure 23**).

The lipidomic data presented in **Figure 18**-**Figure 21** (mitochondria isolated from iBAT, iWAT, eWAT, liver, and muscle) and **Figure 23** (mitochondria isolated from iBAT, iWAT, and eWAT of mice housed at 4°C, 23°C, and 30°C) were utilized to calculate PE/PS ratios, which can be considered as a measure for PISD activity (**Figure 35**). Of note, this revealed a 33-fold and almost 50-fold lower ratio in iWAT and eWAT compared to mitochondria isolated from iBAT of mice housed at room temperature, respectively. The PE/PS ratios in liver and muscle mitochondria were strongly reduced, although not to the same extent as observed in white adipose tissue mitochondria (**Figure 35** B). Furthermore, the PS fraction declined with the housing temperature (30°C-23°C-4°C) in iWAT and, especially, iBAT mitochondria, thereby increasing PE/PS. This was not observed in mitochondria isolated from white adipose tissue (**Figure 35** A). These results indicate a correlation between mitochondrial PE/PS ratios, i.e. PISD activity, with adipose tissue browning.

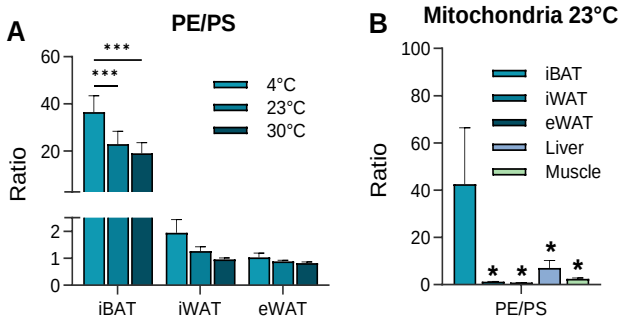

Figure 35: PE/PS of mitochondria isolated from iWAT, eWAT, muscle, and liver significantly differ compared to iBAT mitochondria and depend on the housing temperature of mice (4°C, 23°C, and 30°C). *(A) PE/PS ratio calculated from lipidomic data shown in* ***Figure 23*** *of mitochondria isolated from iBAT, iWAT, and eWAT originating from mice housed at 4°C, 23°C, or 30°C. (B) PE/PS ratios calculated from lipidomic data shown in* ***Figure 18***-***Figure 21*** *of mitochondria isolated from iBAT, iWAT, eWAT, muscle, and liver originating from mice housed at 23°C. Shown are means +SD of (A) n= 3 and (B) and n= 7 (iBAT), n= 3 (iWAT, eWAT, muscle) as well as n= 4 (liver); *p<0.05 and ***p<0.001 indicate significant differences to either (A) 4°C or (B) iBAT, determined with a two-tailed student's t-test with Welch's correction. Each mitochondrial sample was isolated from tissue pooled of n= 5-10 mice.*

A comprehensive proteomic analysis of primary brown adipocytes differentiated from pre-adipocytes isolated of brown adipose tissue revealed notable PISD expression levels, comparable to those of DGAT1 and ATGL. Following incubation with the β-adrenergic agonist isoproterenol (0.5 µM) for 30 minutes (*in vitro*), no significant change in PISD protein expression was observed (**Figure 36** A-B). The analysis of PISD mRNA expression in BAT revealed comparable levels to those of UCP1. In BAT of mice that received oral gavages of the β-adrenergic agonist CL-316,243 within 2 consecutive days (0.1

mg/kg/day), the mRNA expression of PISD was found to be more than 2-fold upregulated (UCP1: ~ 4-fold) (**Figure 36** C).

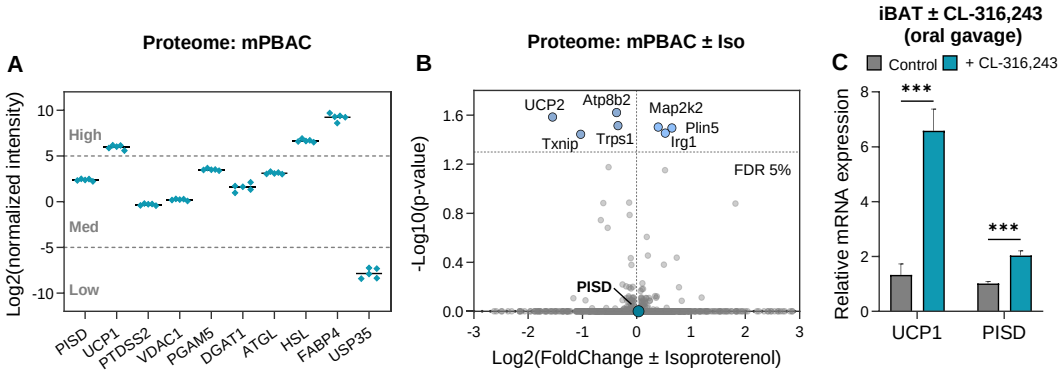

Figure 36: PISD is expressed in brown adipose tissue and thereof isolated adipocytes which is further induced after treatment with CL-316,243. *(A) Estimation of protein expression after a full proteome analysis of murine primary brown adipocytes via LC-HR-MS/MS. Shown is the Log_2 normalized signal intensity of several proteins relevant for adipose tissue. (B) Volcano plot of primary brown adipocytes previously incubated with 0.5 µM isoproterenol for 30 minutes over untreated cells. Shown are significant differences ($-Log_{10}$(q-value)) of Log_2 Fold changes of protein expression. Blue dots indicate significant differences after isoproterenol treatment (left: downregulation, right: upregulation), grey and turquoise dots (PISD) indicate non-significant differences. Significant differences were determined using a student's t-test with Welch's and FDR correction using the Benjamini-Hochberg method (p<0.05); n= 5 of cells each pooled from 3 mice. (C) mRNA expression of UCP1 and PISD in brown adipose tissue of mice with and without oral gavages of CL-316,243. Shown are means +SD of n= 7; ***p<0.001 indicates a significant difference determined using a two-sided Student's t-test with Welch's correction.*

Next, the stable isotope labelling strategy described below (**Figure 37**) was applied to further study cellular PISD activity as well as PC and PE metabolism.

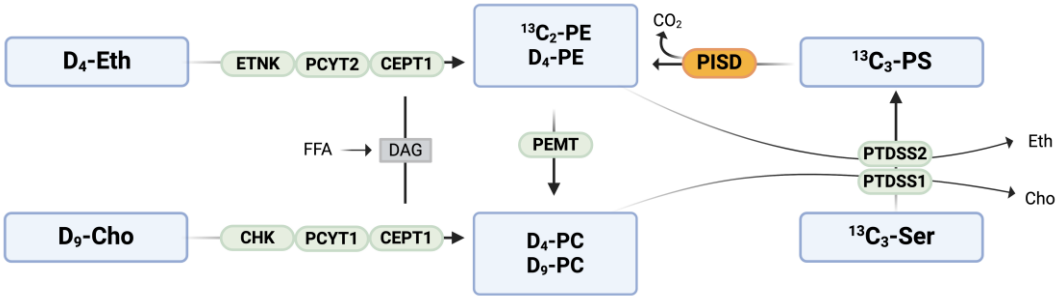

Figure 37: Schematic description of isotope labelling strategy applied to analyze the de novo synthesis rate of PC, PE and PS (Kennedy pathway) as well as PE from PS decarboxylation (PISD).

Therefore, primary brown, beige, and white adipocytes were supplied with stable-isotope labeled D_9-choline, D_4-ethanolamine, as well as $^{13}C_3$-serine for two and six hours to analyze the PE and PC *de novo* synthesis (Kennedy pathway), as well as the activity of PISD via ESI-MS/MS. After two hours, all types of adipocytes exhibited comparable levels of *de novo* PC and PE synthesis (**Figure 38** A-B; top panel). In contrast, the PS *de novo* synthesis and PE generation via PISD were elevated in brown and beige adipocytes relative to white adipocytes (**Figure 38** C-D; top panel). When adipocytes were treated with

the β-adrenergic agonist isoproterenol, the activity of PISD was reduced in beige and brown adipocytes, but not in white adipocytes, especially after six hours of stable isotope incubation (**Figure 38** B, D, F; bottom panel). The *de novo* synthesis of PC and PE was not affected (**Figure 40** A, C, E; bottom panel).

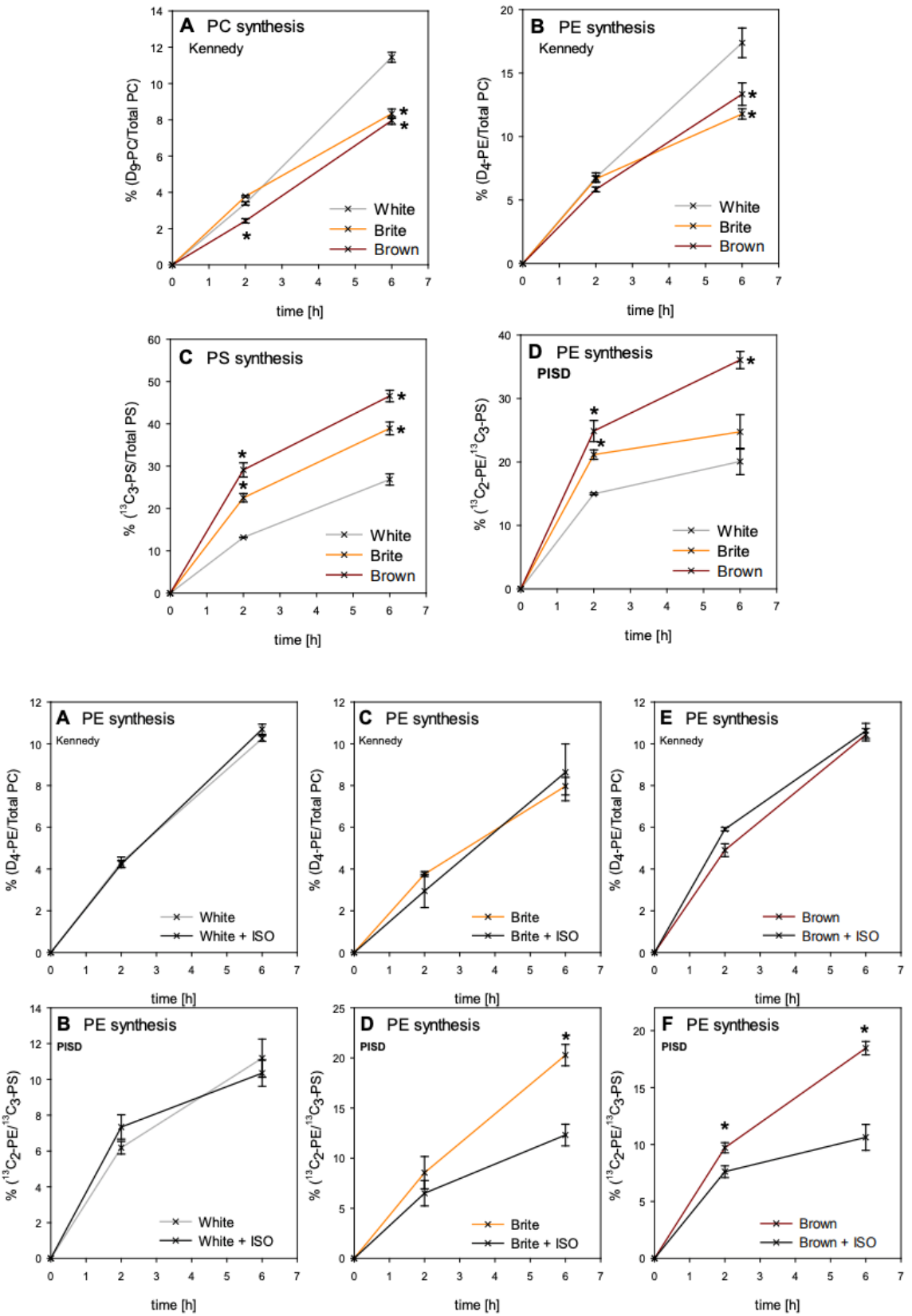

Figure 38: PISD activity in brown and beige adipose tissue differs from white adipose tissue and is reduced upon isoproterenol treatment. *Top panel: Cells were incubated with D_9-choline, D_4-ethanolamine, and $^{13}C_3$-serine (50 µg/mL) for either two or six hours. Labelled and non-labelled lipids were quantified using ESI-MS/MS. (A) PC, (B) PE and (C) PS de novo synthesis via Kennedy pathway; (D) PE synthesis via PISD activity of primary white, beige, and brown adipocytes differentiated from pre-adipocytes of eWAT, iWAT and iBAT of 129 Sv/Ev Tac mice. Bottom panel: Cells were incubated with D_9-choline, D_4-ethanolamine, and $^{13}C_3$-serine (50 µg/mL) for either two or six hours. Additionally, cells were treated with β-adrenergic agonist isoproterenol (0.5 µM) or ethanol as control for 30 minutes. Labeled and non-labeled lipids were quantified using ESI-MS/MS. PE synthesis via Kennedy pathway or PISD activity in (A-B) white, (C-D) beige and (E-F) brown adipocytes differentiated from primary pre-adipocytes of eWAT, iWAT and iBAT originating of 129 Sv/Ev Tac mice. Shown are means +SD of n= 3 per group. *p<0.01 indicates a significant difference to white adipocytes (top) or to ethanol control (bottom) determined using an independent Student's t-test.*

In conclusion, these data suggest a critical link between adipose tissue browning, UCP1 activity, and PISD. Consequently, we proceeded to delve deeper into the relevance of PISD for brown adipose tissue function by generating a conditional knockout mouse model, in which PISD was absent in UCP1-expressing cells.

3.2.2 Generation of a transgenic mouse strain for a tamoxifen-inducible conditional knockout of PISD in UCP_1-expressing cells (iBcKO-PISD)

A transgenic PISD knockout model in BL/6N mice was generated in collaboration with Christian Wolfrum and Lucia Balazova from the ETH Zürich. A global knockout of PISD in mice lead to embryonic lethality *(Steenbergen et al. 2005)*. Therefore, we chose to conditionally induce PISD KO in UCP1-expressing cells, i.e. brown and beige adipocytes, through the administration of tamoxifen. The mouse strain will be referred to as iBcKO-PISD in this work. To generate the mouse line, the commercially available vector $PISD^{tm1a(EUCOMM)Wtsi}$ was injected into blastocytes collected from pregnant mice. Subsequently, embryos were implanted into female surrogates of the C57BL/6N strain to yield chimeric offspring (**Figure 39**).

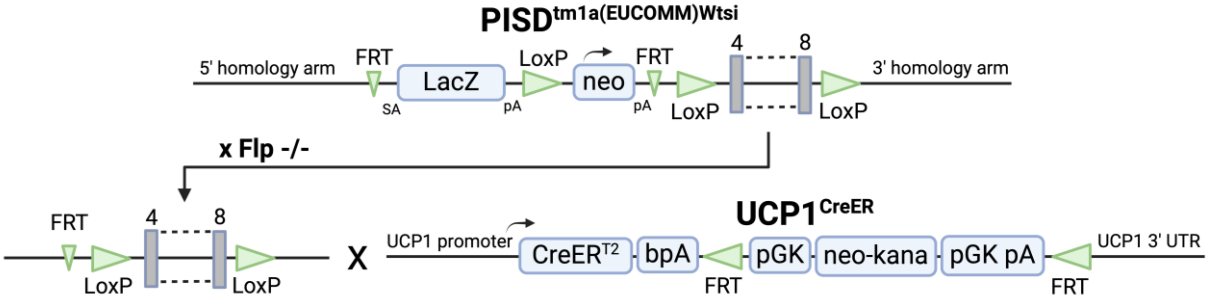

Figure 39: Scheme of targeting vector and generation strategy of iBcKO-PISD mouse line. *Targeted locus on PISD gene. Exons are depicted as grey boxes, vertical triangles as FRT sites and horizontal triangles as LoxP sites. Targeting vector was crossed with Flippase deleter mouse line to eliminate LacZ/Neo cassette. Subsequently, mice were bred with the $UCP1^{CreER}$ strain to enable the expression of a tamoxifen-inducible Cre recombinase in UCP1-expressing cells.*

To ascertain whether the injected vector had been incorporated into the genome of mice, a polymerase chain reaction (PCR) test was conducted to detect LacZ expression. When mice expressed LacZ, they were bred with a Flippase-deleter mouse line (Flp -/-) to eliminate the Flippase, LacZ, and Neo-cassette from the genome. Only mice that exhibited the LoxP sequence were further mated and eventually screened for the PISD genotype. This involved the use of a primer specific for PISD (within the respective exon) and another primer for the LoxP sequence. This procedure yielded three genotypes: Wildtype mice (PISD +/+), heterozygous mice (PISD fl/+), and homozygous mice (PISD fl/fl). Male and female PISD fl/fl mice were crossed to ensure that only animals homozygous for the inducible PISD cKO sequence were retained. Subsequently, their offspring was bred with heterozygous UCP1^{CreER} (Cre +/-) mice, which express the tamoxifen-inducible recombinase in UCP1-expressing cells, to generate a BAT-specific knockout *(Rosenwald et al. 2013)*. As parental animals of experimental cohorts, PISD fl/fl UCP1^{CreER} +/-, as well as PISD fl/fl UCP1^{CreER} +/+ mice were bred to yield both, wildtype controls and iBcKO-PISD mice (**Figure 40**).

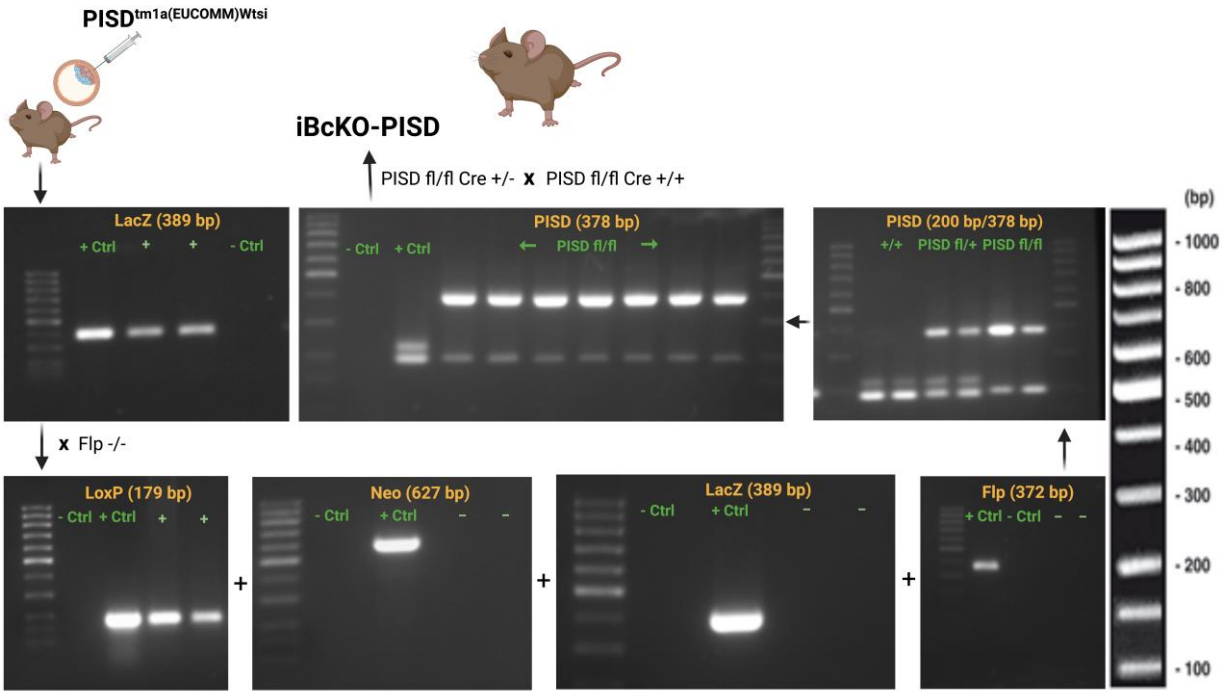

Figure 40: PCR genotyping process during the generation of a transgenic mouse strain from commercially acquired PISD$^{tm1a(EUCOMM)Wtsi}$ vector to iBcKO-PISD mice. *LacZ PCR confirming successful incorporation of PISD$^{tm1a(EUCOMM)Wtsi}$ vector in offspring of foster C57BL/6N mice after implantation of injected blastocysts. After crossing with Flp -/- mice, elimination of LacZ/Neo cassette displayed via respective PCRs. Mice which were PCR positive for LoxP and negative for Flippase at the same time were PCR-tested for PISD. Homozygous mice (fl/fl at 378 bp) were crossed, and subsequently bred with UCP1^{CreER} mice. Respective primer pairs are shown in the methods section.*

Mice of experimental cohorts were genotyped for CRE presence/absence using a multiplex TaqMan qPCR. Therefore, isolated genomic DNA was labeled with fluorescent probes targeting CRE and ApoE,

serving as internal standard. Fluorescence was measured at 465-510 nm (CRE) and 533-580 nm (ApoE). As illustrated in **Figure 41**, ApoE was detected in all samples, except for negative controls (H_2O). Conversely, CRE was detected exclusively in iBcKO-PISD samples, in addition to the positive controls.

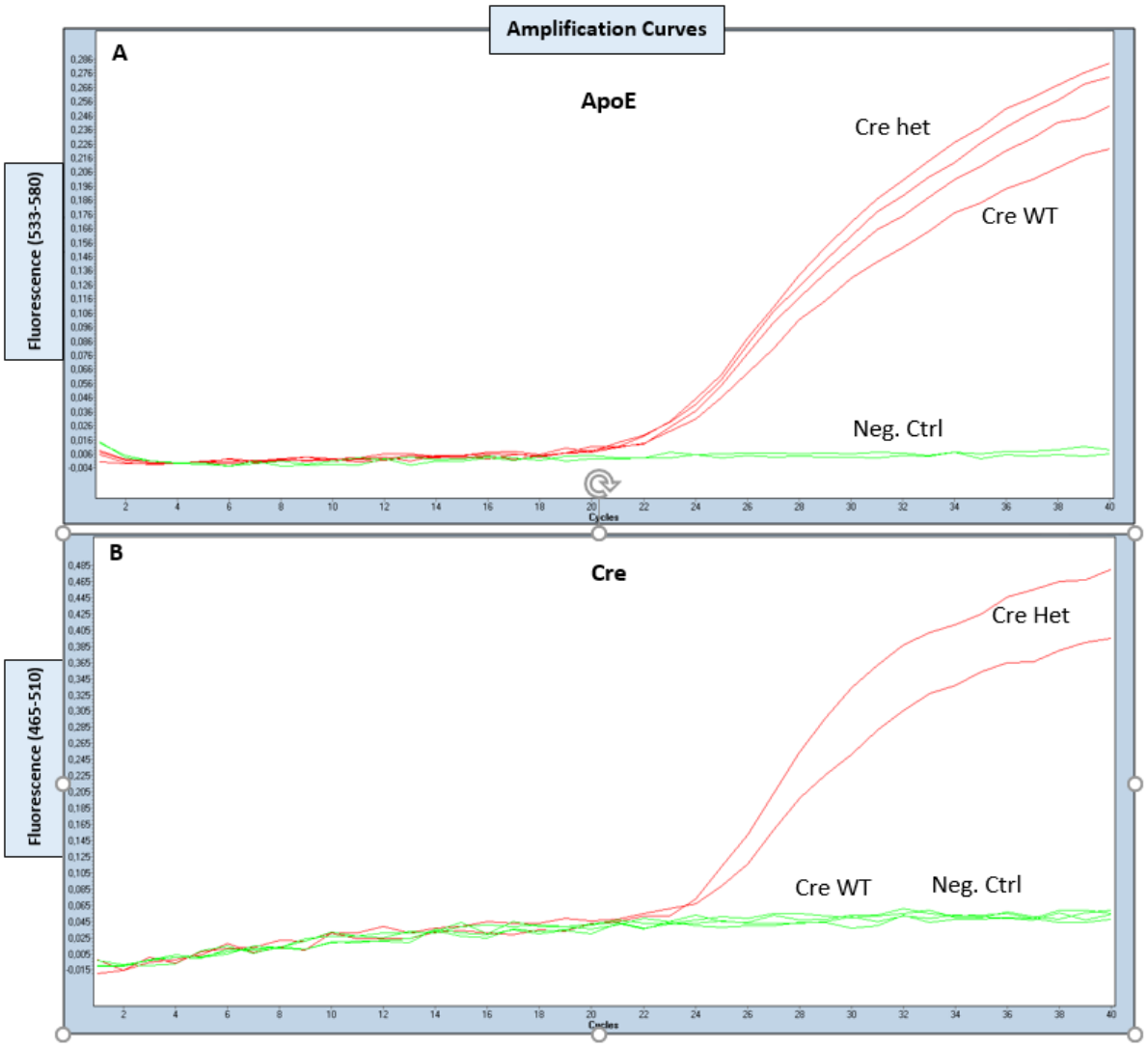

Figure 41: Fluorescence detection of ApoE (533-580 nm) and Cre (465-510 nm) in murine genomic DNA samples using multiplex TaqMan qPCR. *(A) Detection of ApoE as internal standard in CRE positive sample (iBcKO-PISD) and CRE negative sample (Wildtype), as well as negative control (H2O); (B) Detection of CRE in CRE positive sample (iBcKO-PISD) and CRE negative sample (Wildtype), as well as negative control (H2O). Amplification curves in green display samples not expressing ApoE (A) or Cre recombinase (B), amplification curves in red demonstrate samples expressing ApoE (A) or Cre recombinase (B). All samples were analysed in duplicates.*

3.2.3 KNOCKOUT EFFICIENCY OF PISD IN BROWN AND BEIGE ADIPOSE TISSUE

To induce the conditional knockout for *in vivo* analysis, mice (iBcKO-PISD and WT) were administered 2 mg/mouse tamoxifen for three consecutive days at ten weeks of age. When mice were fed a high fat diet (HFD) and were therefore not euthanized before they reached six months of age, an additional

oral gavage of tamoxifen (2 mg/mouse) was administered once per month. To induce a knockout in mature adipocytes differentiated from primary pre-adipocytes isolated from BAT (iBcKO-PISD and WT), 2 µM tamoxifen was added to the culture medium for 48 hours four days after they were fully differentiated.

In iBcKO-PISD mice treated with tamoxifen for three consecutive days, the mRNA expression of PISD in brown adipose tissue was significantly reduced by approximately 70% (**Figure 42** A). The mRNA expression of PISD in mature brown adipocytes isolated from iBcKO-PISD iBAT of mice previously receiving oral gavages of tamoxifen was comparable, although there were relatively strong variations between the mice (**Figure 42** B). Primary brown and beige adipocytes of iBcKO-PISD mice, which were induced with tamoxifen in cell culture, displayed a 2.5-fold and 1.5-fold lower expression, respectively (**Figure 42** C, E). The protein abundance of PISD in primary brown and beige adipocytes was analyzed using Western Blot, which revealed a significant reduction of PISD by about 50% in mPBAC, but no difference in protein expression within beige adipocytes (**Figure 42** D, F).

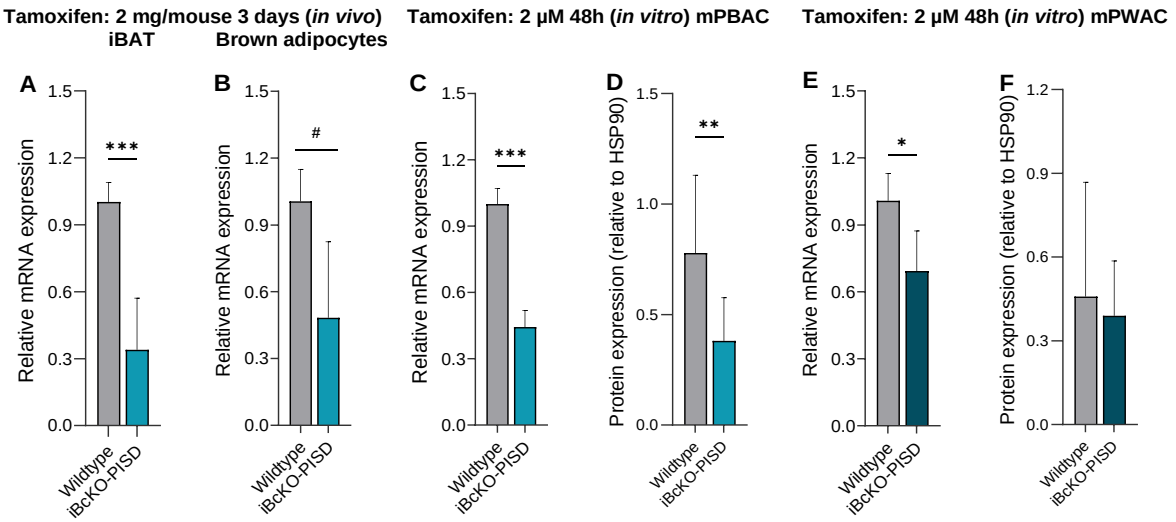

Figure 42: PISD knockout efficiency in iBAT, thereof isolated mature brown adipocytes, mPBAC and mPWAC on mRNA and protein level. *(A) Relative mRNA expression of PISD in iBAT, (B) mature brown adipocytes isolated of iBAT, (C) primary brown adipocytes differentiated from pre-adipocytes (mPBAC) and (E) primary beige adipocytes differentiated from pre-adipocytes (mPWAC) analysed using qPCR. (D) Relative protein expression of mPBAC and (F) mPWAC analysed using Western Blot. RNA and protein originated from iBcKO-PISD and WT mice which were either orally treated with 2 mg/mouse tamoxifen for three consecutive days (A-B) or ex vivo induced with 2 µM tamoxifen for 48 hours to induce conditional PISD knockout. Shown are means +SD of n= 8 (A), n= 3 (B, C, E), n= 10 (D) and n= 6 (F); $^{\#}p<0.1$, $*p<0.05$, $**p<0.01$ and $***p<0.001$ indicate significant difference to control group determined using a two-sided student's t-test with Welch's correction. Respective primers and antibodies are shown in the methods section.*

3.2.4 BODY COMPOSITION, ORAL GLUCOSE TOLERANCE TEST AND CALORIMETRY OF PISD CKO MICE

In the following chapters, *in vivo* investigations on wildtype and iBcKO-PISD mice were conducted with animals (**I-II**) fed a chow diet that were housed at (**I**) room temperature or (**II**) 8°C for four hours (short-term cold exposure), and animals (**III-IV**) fed a high fat diet for 12 weeks and housed at (**III**) room

temperature or (**IV**) 12°C for 8 days (long-term cold exposure). Wildtype (n= 5-6) and iBcKO-PISD (n= 5-6) mice of all groups (**I-IV**) received 3 consecutive doses of tamoxifen in 24 hour intervals at the age of 10 weeks, mice fed a HFD (**III-IV**) received an additional dose of tamoxifen once per month (**Figure 43** A-D):

I) Chow diet; housed at RT; sacrificed at 3 months of age.
II) Chow diet; housed at RT + last 4 hours at 8°C; sacrificed at 3 months of age.
III) Chow diet for 12 weeks + HFD for 12 weeks; housed at RT; sacrificed with 6 months of age.
IV) Chow diet for 12 weeks + HFD for 12 weeks; housed at RT + last 8 days at 12°C; sacrificed with 6 months of age.

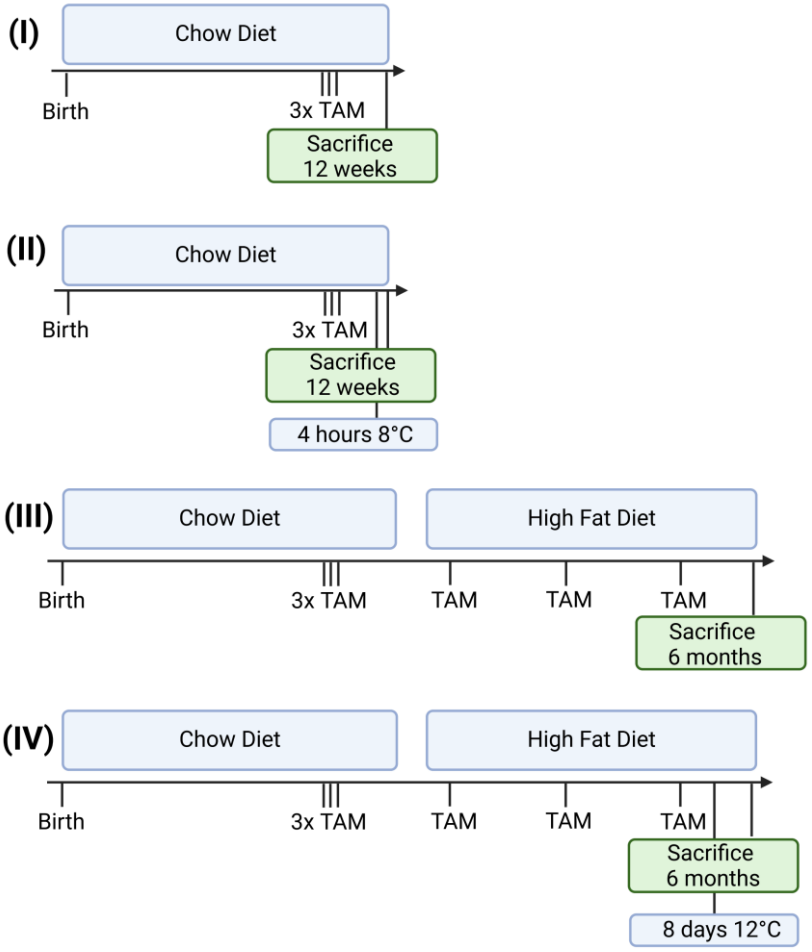

Figure 43: Schematic description of tamoxifen induction and housing conditions of iBcKO-PISD cohorts. *After birth, all mice were fed a chow diet and housed at 23°C for three months (I-IV). Ten weeks after birth, all mice received three oral gavages of 2 mg/mouse tamoxifen in sunflower oil. Two weeks later, cohort I and II were sacrificed. Group II was housed at 8°C for four hours prior sacrifice. The diet of cohort III and IV was changed to HFD for 12 weeks. During this period, tamoxifen was administered once per month via oral gavage (2 mg/mouse). Cohort III and IV were sacrificed at the age of six months. Cohort IV was housed at 12°C for the final eight days.*

BAT of iBcKO-PISD mice in groups **I-IV** exhibited a lower weight and a brighter color (**Figure 44** A, B). This phenomenon was particularly evident in mice that had been fed a high fat diet for three months (**III-IV**). In WT mice, the BAT weight was approximately 3-fold higher when fed a HFD, while in KO mice, BAT weights were similar at HFD and chow (**Figure 44** A). The weight and color of the tissue

homogenates of female iBAT (used for mature adipocyte isolation; **Figure 44** A, C) exhibited only minor differences. This finding was consistent with the very low cKO efficiencies measured via qPCR analysis (**Figure 42** B). Consequently, only male mice were used for further experiments.

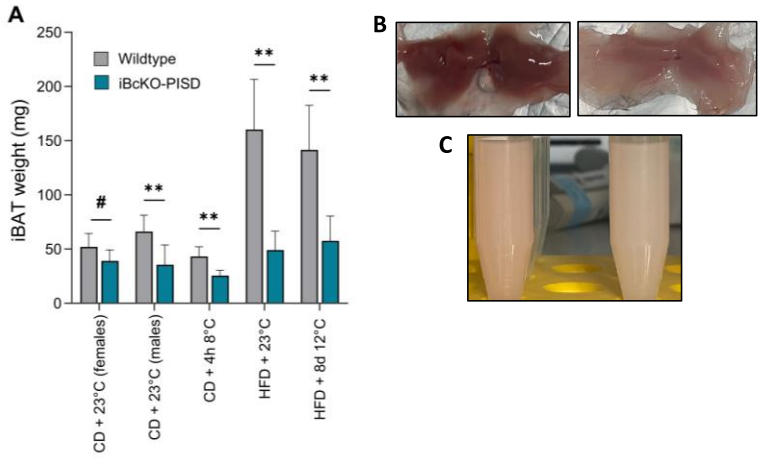

Figure 44: Brown adipose tissue of iBcKO-PISD mice has a lower weight and lighter colour compared to control group. *(A) Brown adipose tissue weight of female mice receiving 3 consecutive oral gavages, male mice of cohort A, B, C and D receiving 3 consecutive oral gavages (+ monthly refreshments). (B) Picture of iBAT dissected of wildtype (left) and iBcKO-PISD (right) mice of cohort A. (C) Homogenized iBAT for isolation of mature adipocytes of female wildtype (left) and iBcKO-PISD (right) mice receiving three consecutive oral gavages at the age of ten weeks. Shown are means +SD; #p<0.1, **p<0.01 and ***p<0.001 indicate significant differences to wildtype mice determined using two-tailed student's t-test with Welch's correction.*

The bodyweight, lean mass, and fat mass were comparable between WT and cKO mice at all conditions (**I-IV**; before cold exposure). However, cKO mice fed a high fat diet showed a slight reduction in bodyweight (~ 25%) following cold exposure (**IV**). Additionally, there was a decline in fat mass and an increase in lean mass (**Figure 45** A-D). The rectal body temperature was measured immediately after cold exposure of mice. In mice of all groups (**I-IV**) similar temperatures between the genotypes were detected (**Figure 45** E).

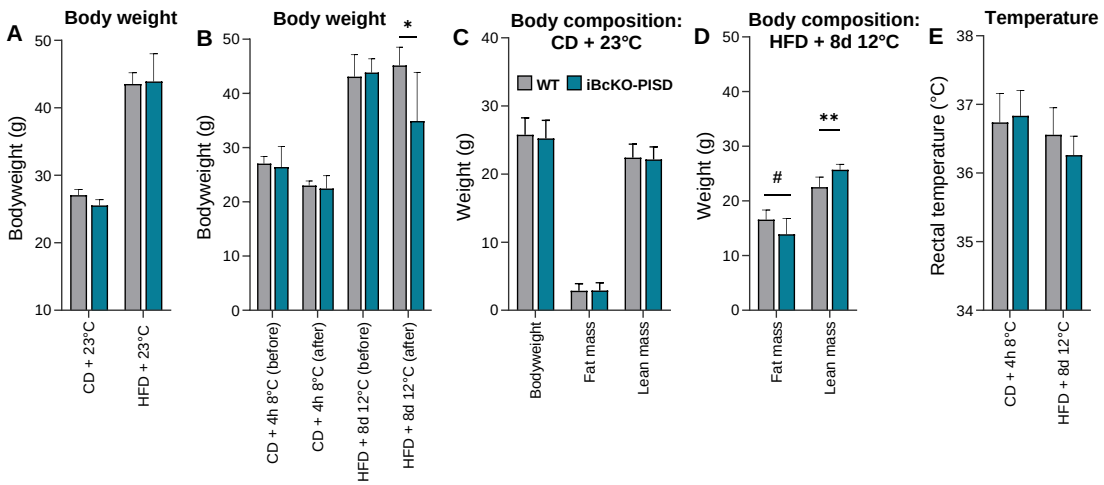

Figure 45: Bodyweight and body composition but not body temperature of iBcKO-PISD and WT mice differ after long-term cold exposure and HFD. *(A) Bodyweight of mice housed at room temperature and fed either chow or high fat diet, (B) Bodyweight before and after cold exposure of mice fed either chow or high fat diet. (C) Body composition (lean and fat mass) of mice housed at 23°C and fed a chow diet, as well as (D) of mice housed at 12°C for eight days while fed HFD. (E) Rectal temperature of mice fed a chow diet after short-term cold exposure and of mice fed a HFD after long-term cold exposure. Shown are means +SD of n= 6-8; #p<0.1, *p<0.05 and **p<0.01 indicate significant differences to control group determined using student's t-test with Welch's correction.*

To assess glucose tolerance in mice, intraperitoneal injections (i.p.) of glucose (1 mg glucose/g body weight) were administered. The blood glucose concentration was initially measured after 15 minutes, followed by measurements at 30-minute intervals for up to two hours. In mice lacking PISD in UCP1-expressing cells, glucose concentrations were increased by approximately 10% after 15 minutes when fed a chow diet (**I**). In mice fed a HFD and housed at cold (**IV**), the blood glucose levels of the cKO mice were similar to WT animals after 15 minutes, but significantly reduced at 30 and 60 minutes (**Figure 46** A-B). After 30 minutes, the cKO animals of cohort (**IV**) had already reached a glucose concentration of approximately 12.5 mg/dL, while the peak concentration (19.5 mg/dL) barely dropped at this time point in wildtype controls (> 18 mg/dL) (**Figure 46** B). It is noteworthy that, after two hours, glucose concentrations were again comparable between the genotypes (nearly at basal levels), indicating that mice lacking PISD do not display a pathological hypoglycemia but rather a reduced insulin resistance following the HFD feeding (**Figure 46** A-B).

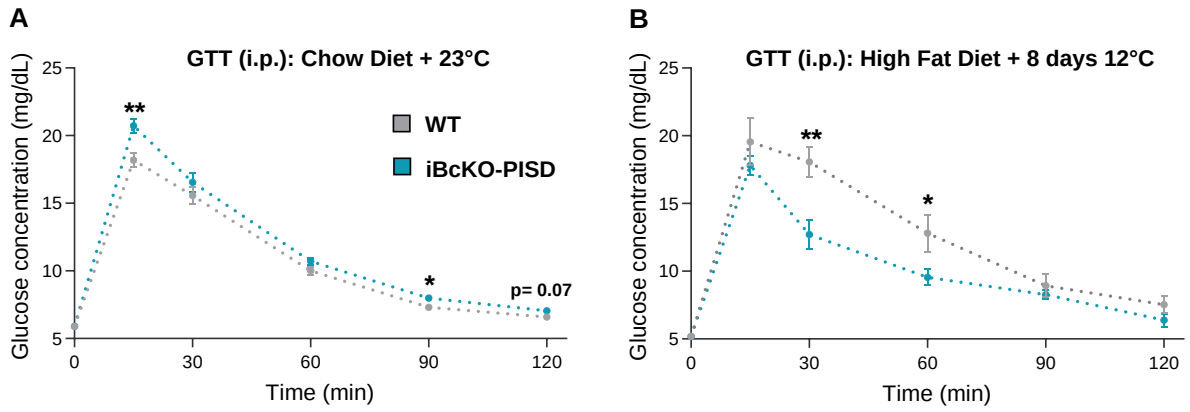

Figure 46: iBcKO-PISD mice show lower insulin resistance after receiving HFD when housed at cold compared to WT mice. *(A) GTT of mice fed a chow diet and housed at room temperature and (B) of mice fed a HFD for three months and housed at 12°C for the last eight days. Glucose was injected (1 mg glucose/g body weight) and blood was drawn and analysed after 15 minutes and subsequently in 30-minute intervals up to two hours. Shown are means ±SD of n= 6 for iBcKO-PISD and wildtype mice; *p<0.05 and **p<0.01 after two-tailed student's t-test with Welch's correction. Mice were administered 2 mg/mouse tamoxifen in sunflower oil via oral gavage for three consecutive days at ten weeks of age, followed by an oral gavage once per month (at the same concentration) to induce conditional PISD knockout.*

3.2.5 IBCKO-PISD MICE HOUSED AT ROOM TEMPERATURE OR COLD HAVE AN ALTERED RESPIRATORY CAPACITY AND LOCOMOTOR ACTIVITY COMPARED TO WILDTYPES

Mice of the iBcKO-PISD and wildtype genotypes, aged 12 weeks and fed a chow diet, were single-housed in calorimetric cages for three days at room temperature (23°C). Thereafter, they were

subjected to four hours of cold exposure at 8°C (**II**) to determine their respiratory capacities. At room temperature, the expected light-dark cycle behavior in mice of wildtype and cKO mice (nocturnal) was observed. During both phases, the respiratory exchange ratio (RER; VCO_2/VO_2) was comparable. Oxygen consumption and CO_2 production were moderately reduced in iBcKO-PISD mice (**Figure 47** A-B, E-H) as well as energy expenditure and heat production (**Figure 47** C-D, I).

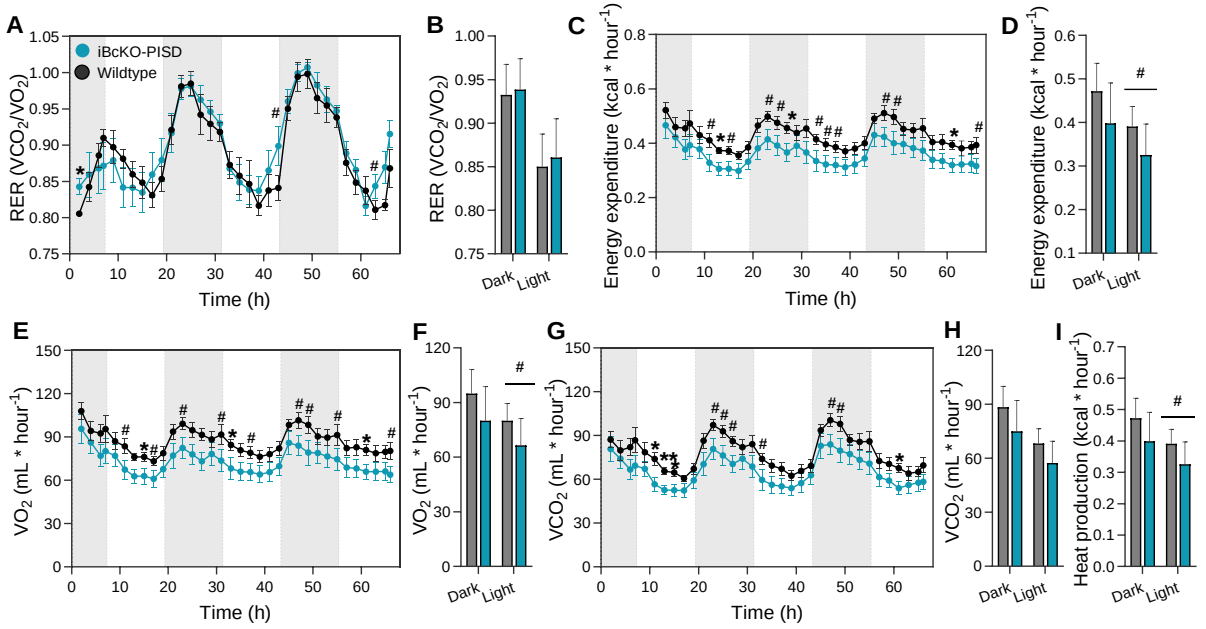

Figure 47: iBcKO-PISD mice reveal moderately reduced energy expenditure, oxygen consumption, CO_2 and heat production during light-cycle compared to control mice. *(A-B) RER, (C-D) energy expenditure, (E-F) oxygen consumption, (G-H) CO_2 production and (I) heat production of iBcKO-PISD and WT mice housed at room temperature for 72 hours. Data was gathered during single housing of mice (n= 6) using the TSE PhenoMaster system. Shown are means +SD (B, D, F, H-I) and ±SEM (A, C, E, G); #p<0.1, *p <0.05 and **p<0.01 indicate significant differences determined using two-tailed student's t-test with Welch's correction. Mice were given three consecutive oral gavages (2 mg/mouse) of tamoxifen in sunflower oil at ten weeks of age to induce conditional PISD knockout.*

All animals demonstrated comparable food and water consumption during the three-days monitoring period (**Figure 48** D-E). Locomotor activity, particularly fine movements, and rearing, as well as speed and the total distance covered, was moderately reduced in iBcKO-PISD mice by approximately 40% during their active phase (**Figure 48** A-C).

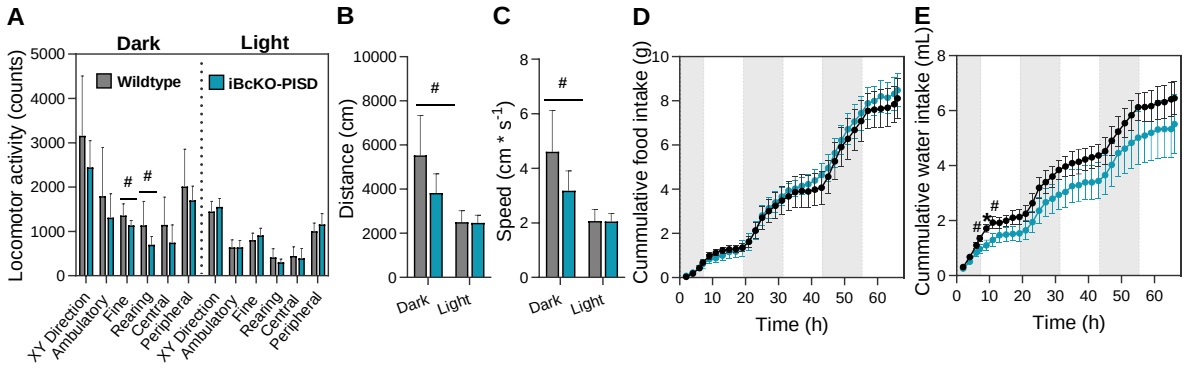

Figure 48: iBcKO-PISD mice have moderately decreased activity during dark cycle compared to wildtype mice. *(A) Locomotor activity, (B) covered distance, (C) speed, (D) cumulative food intake and (E) cumulative water consumption of iBcKO-PISD and WT mice housed at room temperature for 72 hours. Data was gathered during single housing of the mice (n= 6) using the TSE PhenoMaster system. Shown are means +SD (A-C) and ±SEM (D-E); #p<0.1 and *p <0.05 indicate significant differences to control mice determined using two-sided student's t-test with Welch's correction. Mice were given three consecutive oral gavages (2 mg/mouse) of tamoxifen in sunflower oil at ten weeks of age to induce conditional PISD knockout.*

When mice were exposed to cold (8°C, during the active/dark phase), iBcKO-PISD mice demonstrated a significantly higher (5%) respiratory exchange ratio (**Figure 49** B). At the beginning of the intervention, when the temperature had not yet reached 8°C, the iBcKO-PISD mice exhibited a markedly elevated RER, which declined more rapidly with decreasing temperature than in the wildtype mice. This resulted in comparable levels after four hours at 8°C. Three hours after the start of the intervention (when the temperature reached 8°C), the RER in iBcKO-PISD animals averaged at 0.93, while that of wildtype mice averaged at 0.82. At the end of the cold exposure period, mice of both genotypes exhibited a quotient of approximately 0.75 (**Figure 49** A).

It is well established that brown adipocytes increase the hydrolysis of lipid droplet associated TAG to FFA when exposed to cold. Concurrently, they take up a significant amount of circulating glucose, which induces the *de novo* FFA-synthesis. The results of the GTT, shown in **Figure 46** B, support the notion of a high uptake of circulating glucose. As concentrations of FFA in brown adipocytes increase, both through lipolysis and *de novo* FFA synthesis, mitochondrial β-oxidation is fueled, which in turn supports thermogenesis *(Chang 2023)*. Of note, reduced respiratory quotients indicate a preference for the oxidation of FFA over carbohydrates. Consequently, we conclude that the rapid reduction of the RER in iBcKO-PISD mice at cold exposure indicates a switch from glycolysis towards β-oxidation, which could potentially lead to an increased thermogenic capacity. The energy expenditure as well as heat production were comparable between the animals (**Figure 49** C-E).

The negative spike in **Figure 49** at 140 minutes was caused by a technical issue.

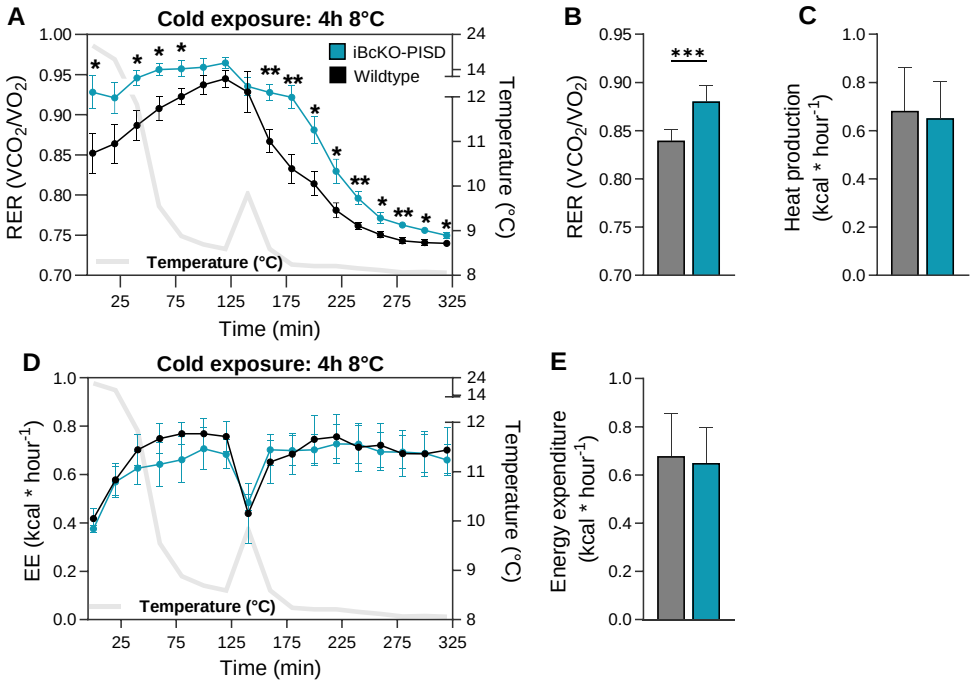

Figure 49: iBcKO-PISD mice have a significantly increased RER at the beginning of the cold intervention which rapidly converges to the RER of control animals during decreasing temperatures. *(A-B) RER, (C) heat production, and (D-E) energy expenditure of iBcKO-PISD and WT mice housed at 8°C for 4 hours. Data was gathered during single housing of the mice (n= 6) using the TSE PhenoMaster system. Shown are means +SD (B, C, E) and ±SEM (A, D); *p <0.05, **p<0.01 and ***p<0.001 indicate significant differences to control group determined using two-sided student's t-test with Welch's correction. Mice were given three consecutive oral gavages (2 mg/mouse) of tamoxifen in sunflower oil at ten weeks of age to induce conditional PISD knockout.*

The food intake was 1.5-fold increased in cKO mice when exposed to cold, whereas water consumption remained similar (**Figure 50** D-E). All parameters related to locomotor activity, including movements in all directions, fine, ambulatory, peripheral, and central movements, as well as speed and the total covered distance, were reduced by about 1.1 to 1.5-fold in cKO mice (**Figure 50** A-C).

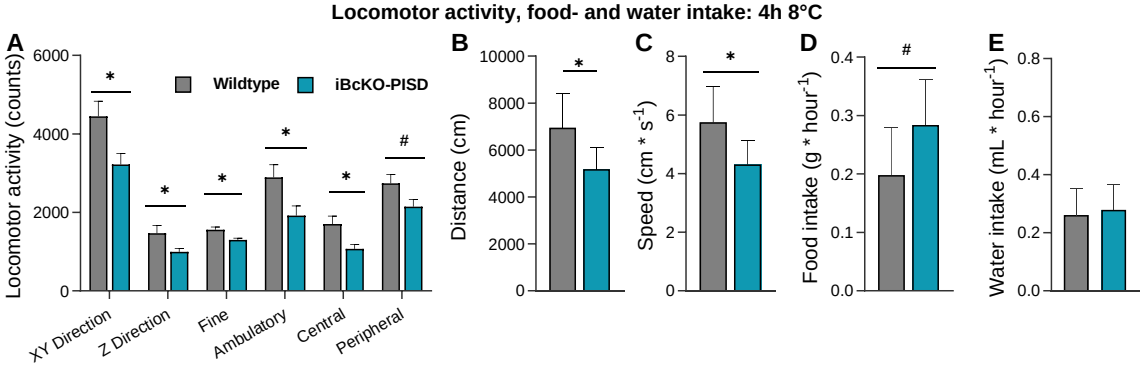

Figure 50: iBcKO-PISD mice show decreased activity and increased food consumption after short-term cold exposure compared to wildtype mice. *(A) Locomotor activity, (B) covered distance, (C) speed, (D) food intake and (E) water consumption of iBcKO-PISD and WT mice housed at 8°C for four hours. Data was gathered during single housing of the mice (n= 6) using the TSE PhenoMaster system. Shown are means +SD; #p<0.1 and *p<0.05 indicate significant differences to control group determined using two-sided student's t-test with Welch's correction. Mice were given three consecutive oral gavages (2 mg/mouse) of tamoxifen in sunflower oil at ten weeks of age to induce conditional PISD knockout.*

3.2.6 LIPID DROPLET CHARACTERISTICS OF ADIPOSE TISSUE AND LIVER

3.2.6.1 HISTOLOGY AND LIPID DROPLET QUANTIFICATION OF ADIPOSE TISSUE

To ascertain the impact of a conditional PISD knockout on adipose tissue and liver histology, hematoxylin and eosin (H&E) staining was performed. The lipid droplets in adipose tissue were quantified using the Fiji plugin Adiposoft, as previously published *(Galarraga et al. 2012)*. For each tissue, four distinct sections were quantified, with the average serving as the basis for comparison between mice. Given the considerable heterogeneity in the morphology of iWAT, with regard to lipid droplet size, the lymph nodes were used as a reference point for the selection of comparable regions for quantification.

Significant discrepancies were observed between the two genotypes with respect to housing temperatures and diet. The brown adipose tissue of iBcKO-PISD mice housed at room temperature and fed a normal chow diet (**I**) exhibited a 25% reduction in the number of lipid droplets, while the mean area/size of lipid droplets was 1.5-fold increased. The brown adipose tissue sections of cKO mice displayed an infiltration of immune cells, which potentially led to fibrosis, suggesting inflammation (**Figure 51** left panel: A-B; **Figure 53** A-B). The accumulation of lipids in brown adipose tissue may be indicative of whitening, and a reduction in thermogenic capacity. However, when mice were housed at 8°C for the final four hours prior to sacrifice (**II**), the observed morphological phenotype underwent a complete transformation. Brown adipose tissue of these mice did not show any signs of fibrosis, and the level of immune cell infiltration was comparable to that observed in wildtype tissue. Cold exposure strongly induced multilocular appearance in both wildtype and cKO mice, which made it difficult to quantify the number and area of lipid droplets. As illustrated in the magnified section of **Figure 51** (left panel: C-D), lipid droplets appeared to be even smaller/more multilocular in cKO mice compared to wildtype mice, proposing a more pronounced reduction in lipid accumulation and thus, a higher thermogenic capacity. This contradicts our observation in iBAT of mice housed at room temperature (**I**), where lipid droplets were larger, rather suggesting a reduced thermogenic capacity.

This contrast was even stronger when mice were fed a high fat diet. Wildtype mice at room temperature (**III**) displayed a 2-fold higher number of lipid droplets and a more than 50% reduction in lipid droplet area (**Figure 51** left panel: E, F; **Figure 53** A, B). Following a period of cold exposure (**IV**), mice with a conditional knockout of PISD recovered the in WT mice observed changes caused by HFD. Their tissue morphology was comparable to that of wildtype controls receiving chow diet and housed at room temperature (**I**). It is noteworthy that the observations in histological sections of group **IV** were not confirmed by the applied quantification method, which revealed a mere 20% difference between wildtype and iBcKO-PISD mice (**Figure 53** A, B). This, as well as comparable results observed in mice fed a chow diet and housed at cold temperatures (**II**), can be attributed to the limitations of the software in accurately quantifying the extremely multilocular lipid droplet structure. A large portion of lipid droplets in cKO tissue were not identified as small, single lipid droplets. Instead, they were erroneously captured as a combined single, large lipid droplet, which explains the seemingly low differences in lipid droplet number and area (**Figure 51** left panel: C, D, G, H; **Figure 53** A, B).

The findings collectively indicate a discernible morphological response of brown adipose tissue following β-adrenergic stimulation induced by cold in mice lacking PISD.

In inguinal white adipose tissue (iWAT) of mice fed a chow or high fat diet and housed at 23°C (**I, III**), comparable lipid droplet numbers and areas were observed, as well as no obvious signs of inflammation. In accordance with the findings in brown adipose tissue, cold exposure provoked a more multilocular lipid droplet distribution in all mice, with the most pronounced effect observed in iBcKO-PISD mice (**II**). Again, this effect was further elevated when mice were fed HFD (**IV**). After eight days of cold exposure, the tissue of mice lacking PISD resembled the basal phenotype (room temperature, chow diet), implying a reversal of HFD-induced conditions (**Figure 51** right panel: A-H; **Figure 53** C-D).

White adipose tissue (eWAT) of iBcKO-PISD and WT mice (**I-IV**) did not show any differences in the analyzed histological and morphological parameters (**Figure 52** left panel: A-F; **Figure 53** E, F).

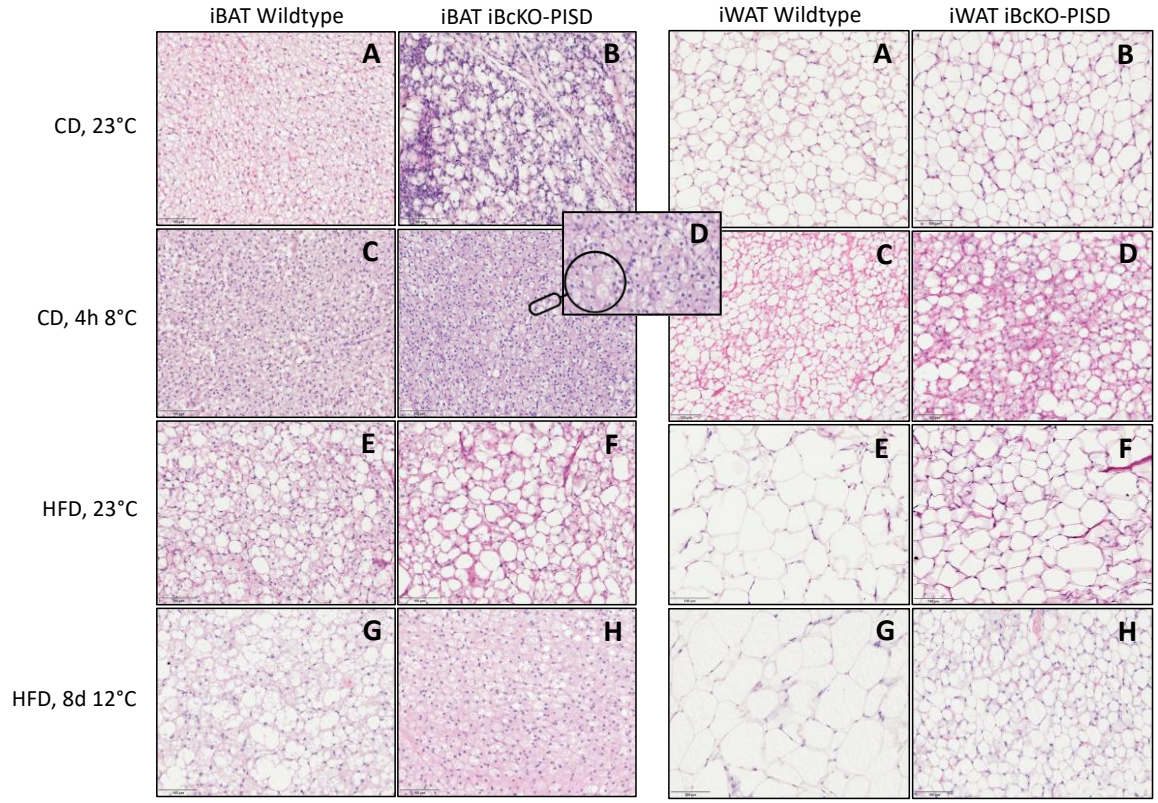

Figure 51: iBAT of iBcKO-PISD mice housed at 23°C and fed either chow or HFD shows fewer and larger lipid droplets compared to wildtypes, while the opposite is observed after cold exposure. *Images of haematoxylin and eosin stained iBAT (left) and iWAT (right) sections originating from iBcKO-PISD and wildtype mice. Histological images were comparable for n= 6 mice per group. All images are displayed at a 100 µM scale bar. Mice were given three consecutive oral gavages (2 mg/mouse) of tamoxifen in sunflower oil at ten weeks of age (+ monthly refreshments) to induce conditional PISD knockout.*

3.2.6.2 HISTOLOGY AND LIPID DROPLET QUANTIFICATION OF LIVER

UCP1 is not expressed in the liver. Nevertheless, the existing literature proposes intriguing connections between liver and BAT function. For instance, a recent study by Xiao et al. *(Xiao et al. 2023)* proposed a relationship between cold-induced BAT thermogenesis and WAT browning in male mice, with

changes in the hepatic bradykinin metabolism. To ascertain whether the knockout of PISD in iBAT affects liver morphology and function, we analyzed H&E-stained liver sections of mice.

The livers of wildtype mice fed a chow diet (**I**) had a typical polygonal structure, wherein hepatic cords encircled central veins and were distinctly separated by sinusoids. This structure was not observed in liver sections of the cKO mice, which demonstrate a very diffuse cell organization. Hepatocytes from cKO mice showed ballooning degeneration and microvesicular steatosis, which is characterized by the presence of small lipid droplets within the hepatic cytosol. Furthermore, evidence of necrotic cell death, the beginning of sinusoidal blood cell congestion, and immune cell infiltration were observed, which collectively suggests liver injury (**Figure 52** A-B).

When fed a high fat diet and housed at 12°C for eight days (**IV**), wildtype mice exhibited an extensive amount of lipid droplets and immune cell infiltration (NAFLD), while iBcKO-PISD mice exhibited a normal phenotype under those conditions, comparable to mice housed at room temperature and fed a chow diet (**Figure 52** C-D).

We conclude that a deficiency of PISD activity improves liver-related pathologies caused by calorie/fat-enriched diet after a cold stimulus.

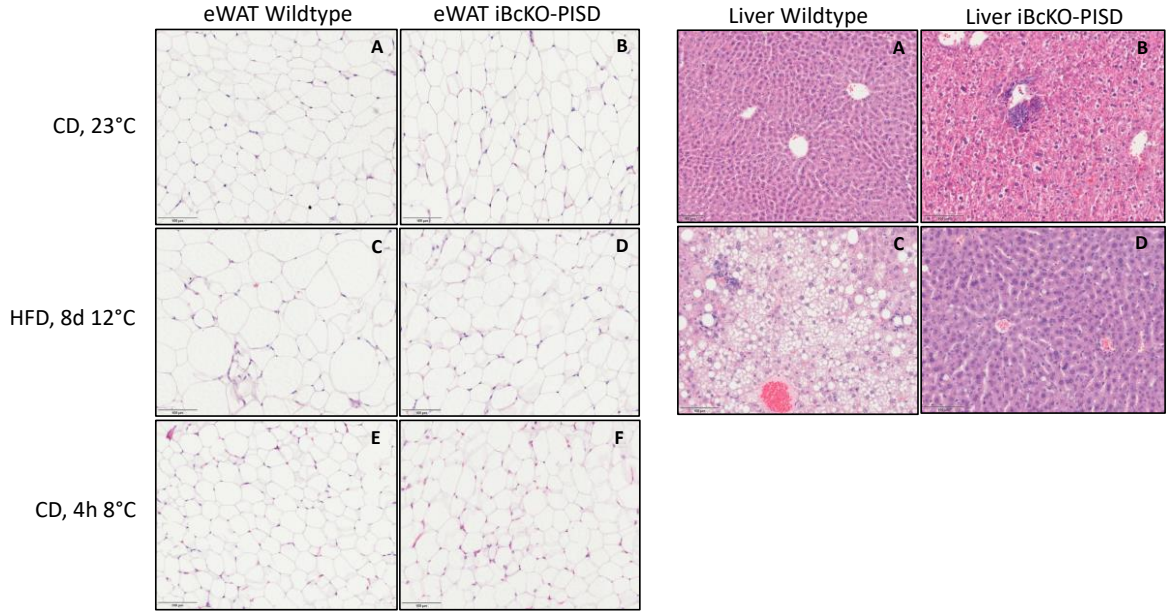

Figure 52: Liver sections of iBcKO-PISD mice housed at 23°C and fed chow diet show mild liver injury, while NAFLD of mice fed a HFD is rescued after long-term cold exposure. *Images of H&E stained eWAT (left) and liver (right) originating from iBcKO-PISD and wildtype mice. Histological images were comparable for n= 6 mice per group. All images are displayed at a 100 µM scale bar. Mice were given three consecutive oral gavages (2 mg/mouse) of tamoxifen in sunflower oil at ten weeks of age (+ monthly refreshments) to induce conditional PISD knockout.*

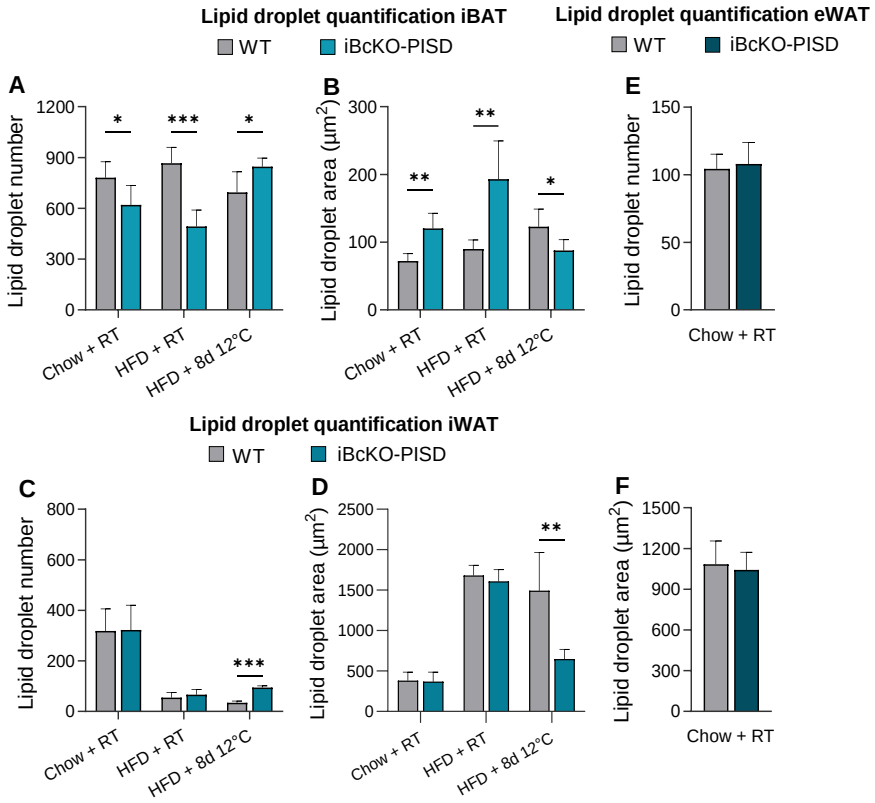

Figure 53: Lipid droplet number and area of iBAT and iWAT differ between WT and iBcKO-PISD mice, depending on diet and housing temperature. *(A, C, E) Mean lipid droplet number and (B, D, F) mean area of lipid droplets in iBAT (A-B), iWAT (C-D) and eWAT (E-F) of iBcKO-PISD and wildtype mice; For each tissue (n= 6 per cohort and genotype) four images of different tissue sections were captured, quantified, and averaged using the Fiji plugin Adiposoft. Shown are means +SD; *p<0.05, **p<0.01 and ***p<0.001 indicate significant differences to control group determined using a two-sided student's t-test with Welch's correction. Mice received oral gavages with 2 mg/mouse tamoxifen in sunflower oil for three consecutive days at ten weeks of age (+ monthly refreshments) to induce PISD knockout.*

3.2.7 PLASMA ALT AND LEPTIN OF CKO MICE ARE REDUCED WHEN HOUSED AT COLD

Next, we asked whether we could find evidence of potential liver pathology by applying an alanine aminotransferase (ALT) assay on plasma samples from mice. The pyridoxal-phosphate-dependent enzyme alanine aminotransferase (ALT) facilitates the reversible amino group transfer from alanine to alpha-ketoglutarate. Thereby, glutamate and pyruvate are generated. Elevated plasma concentrations of ALT are used as a marker for hepatocellular and liver damage *(McGill 2016)*. In this work, a coupled enzyme assay was employed to measure the colorimetric (570 nm)/fluorometric (λ_{ex}= 535/λ_{em}= 587 nm) product, which is generated in proportion to pyruvate. One unit of ALT corresponds to the amount of enzyme capable of generating 1 µM of pyruvate per minute at a temperature of 37°C.

WT and cKO mice fed a chow diet (**I, II**) did not reveal any differences in plasma ALT concentrations. However, when WT animals were fed a HFD, ALT levels rose by approximately 3-fold at 23°C and 12°C (**III-IV**). In contrast, knockout animals exhibited elevated ALT levels only when housed at room temperature (**III**). After cold exposure (**IV**), ALT activity was approximately twofold lower (comparable to the ALT activity observed in mice fed a chow diet) (**Figure 54** A). These findings are consistent with

the histological findings presented in **Figure 52**. Mice lacking PISD appear to exhibit enhanced capacity to reverse HFD-induced NAFLD, when housed at cold temperatures.

Leptin, a plasma protein secreted by adipocytes, is known to be involved in the regulation of energy metabolism by reducing the food intake and increasing the energy expenditure. However, several rodent models of obesity, such as db/db and yellow Ay/a strains, have proven an elevation in plasma leptin concentrations due to the development of leptin resistance *(Frederich et al. 1995)*.

As demonstrated in the previous sections, the conditional knockout of PISD in UCP1-expressing cells appears to develop a resistance to HFD-promoted pathologies when housed at cold temperatures (e.g. **Figure 45**). To investigate whether this could be related to leptin, an ELISA assay was employed to quantify plasma leptin levels. In accordance with the existing literature, the administration of a high fat diet (HFD) to mice housed at room temperature resulted in a significant elevation in plasma leptin concentrations, exceeding a 2-fold increase (independent of the genotype), which implies the development of leptin resistance (**III**). It has been previously reported that leptin levels can be reduced as an adaptive mechanism upon cold exposure *(Peinó et al. 2000)*. In agreement, we found a reduction in leptin levels in WT and, even more pronounced, in cKO mice fed a chow diet and housed at acute cold exposure (**II**) compared to mice housed at room temperature (**I**). In WT mice fed a HFD at 12°C (**IV**), leptin levels did not change compared to RT housed mice (**III**). In contrast, PISD cKO mice fed a HFD at 12°C (**IV**), leptin levels were 2-fold lower, compared to control mice (**Figure 54** B). Leptin resistance is not only associated with obesity but also with insulin resistance, as leptin can act as a potent insulin sensitizer, thereby improving glucose tolerance *(Koch et al. 2014)*. In this context, the reduced leptin levels observed in cold-exposed cKO mice (**II, IV**) fit well to the results of the glucose tolerance test presented in **Figure 46** B, which demonstrate a faster reduction in blood glucose concentrations.

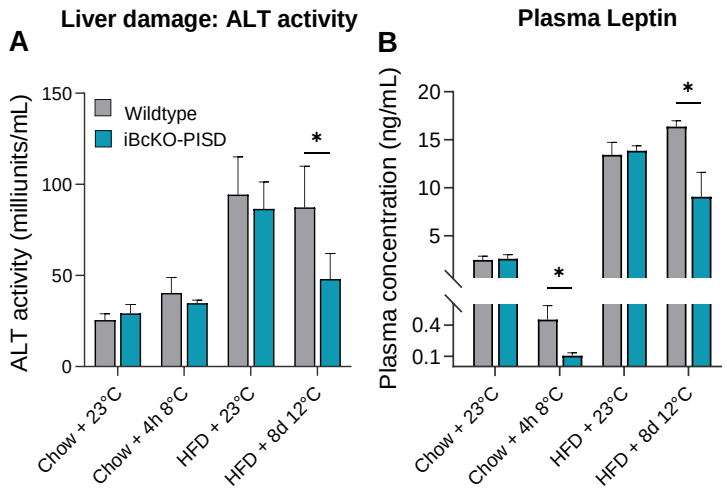

Figure 54: Plasma leptin levels and ALT activity are reduced in iBcKO-PISD mice when fed a HFD and housed at cold. *(A) ALT activity and (B) leptin concentration in plasma of iBcKO-PISD and wildtype mice of cohort I-IV; shown are means +SD of n= 4-10, *p<0.05 indicates significant differences to wildtype mice determined using student's t-test with Welch's correction. Mice were orally given 2 mg/mouse tamoxifen in sunflower oil for three consecutive days at ten weeks of age (+ monthly refreshments) to induce PISD knockout.*

3.2.8 ADIPOCYTE DIFFERENTIATION- AND LIPID METABOLISM- RELATED GENE EXPRESSION PROFILES IN BROWN AND BEIGE ADIPOSE TISSUE OF IBCKO-PISD MICE

Next, the mRNA expression levels for white (ADIPOQ, FABP4, ADCY5) and brown (UCP1, COX7A1, DIO2, CTP1B, CIDEA, PPARγ, ELOVL3) adipocyte markers, relevant genes involved in phospholipid metabolism (PSS1, PSS2, PEMT), glycerolipid synthesis (DGAT1, DGAT2), lipolysis (ATGL, HSL), FA synthesis (FAS, SCD1, ELOVL6, SREBP1-c) as well as cholesterol biosynthesis (ACAT2, HMGCR, SREBP-2c) were analyzed in brown and beige adipose tissue of iBcKO-PISD mice. Further, the gene expression of PGAM5 was studied, a known regulator of the continuous processes of mitochondrial fusion and fission (mitochondrial dynamics), which was previously identified as a suppressor of UCP1 expression regulated by PISD *(Sugawara et al. 2020)*.

When mice were housed at room temperature and fed a chow diet (**I**), the majority of the studied genes exhibited a significant downregulation in iBcKO-PISD mice. Consistent to the histological sections shown in **Figure 51**, all brown adipocyte markers, particularly UCP1 (~80%) and CTP1B (~90%), were substantially reduced in mice expressing the conditional PISD knockout. The mRNA expression of ATGL, HSL, DGAT1 and DGAT2 was higher in wildtype mice, indicating a suppression of both lipolysis and glycerolipid synthesis in mice lacking PISD. Enzymes involved in the synthesis of phosphatidylserine (PSS1, PSS2) were ~3-fold reduced at a lower level of PISD activity. This is coherent considering the role of PS as a substrate for PISD action. The enzymes involved in FA synthesis were downregulated by approximately 80-90% (FAS, SCD1, ELOVL6, SREBP1-c), while the enzymes involved in cholesterol biosynthesis were upregulated 1.2-fold (SREBP2-c) and 3-fold (HMGCOAR). ACAT2, which is responsible for the esterification of FC to yield CE, was about 5-fold higher in wildtype mice (**Figure 55** A-B).

Following four hours of acute cold exposure (**II**), the mRNA expression of most investigated adipocyte differentiation marker genes was unchanged between WT and cKO. The histological stainings (**Figure 51** C, D) were corroborated by the observation that brown adipocyte marker gene expression was not reduced but instead elevated in the cKO compared to wildtype tissue (ELOVL3, DIO2). UCP1 was expressed at comparable levels between the genotypes. All genes involved in lipid metabolism (except for DGAT2) displayed similar levels in cKO and wildtype mice, which is, again, in contrast to the results observed in mice housed at room temperature (**Figure 55** C-D).

WT and cKO mice that were fed a HFD and exposed to 12°C (**IV**) did not display differential mRNA expression for lipid metabolism-related genes in BAT, except for DGAT2 and ACAT2. These enzymes were downregulated in cKO mice. Genes related to adipose tissue browning (DIO2, ELOVL3) were significantly reduced (3-fold and 6-fold, respectively) in control mice compared to iBcKO-PISD animals, whereas the white adipocyte marker ADIPOQ revealed the opposite. Interestingly, mice lacking PISD displayed a 20% increase in UCP1 abundance, while PGAM5, which suppresses UCP1, was downregulated (**Figure 55** E-F).

At room temperature, HFD feeding (**III**) induced mRNA expression of most browning markers as well as genes involved in lipolysis and TG synthesis (ATGL, HSL, DGAT1, DGAT2) in wildtype mice. Transcription of genes involved in FFA synthesis, cholesterol synthesis, and phospholipid metabolism was largely unaffected, except for ACAT2 (50% reduction in cKO). UCP1 expression was approximately 2-fold lower in iBcKO-PISD tissue compared to WT BAT (**Figure 55** G-H).

Inguinal white adipose tissue exhibited comparable mRNA levels of all tested genes in WT and cKO mice maintained at room temperature and fed a chow diet (**I**). However, when mice were housed at 8°C for 4h (**II**), UCP1 (along with all analyzed browning markers) displayed a 5-fold increase in the cKO mice. This may suggest that iWAT at a basal state (without β-adrenergic stimulation) does not express sufficient UCP1-expressing cells (beige adipocytes) to induce the conditional knockout. The mRNA levels of DGAT2, FAS, SCD1, ELOVL6, and ACAT2 were higher in cKO compared to wildtype mice (**Figure 56** A-D).

The mRNA expression levels of primary brown and beige adipocytes, which were differentiated from pre-adipocytes originating from iBcKO-PISD and wildtype mice (both treated with 2 µM Tamoxifen for 48 hours), demonstrated a 2.5-fold downregulation of UCP1 when PISD was absent, while the browning marker COX7A1 was approximately 50% reduced. These findings are consistent with those of cohort **I** (shown in **Figure 55** A). In mPWAC, no significant differences between the genotypes were observed (**Figure 56** E-F).

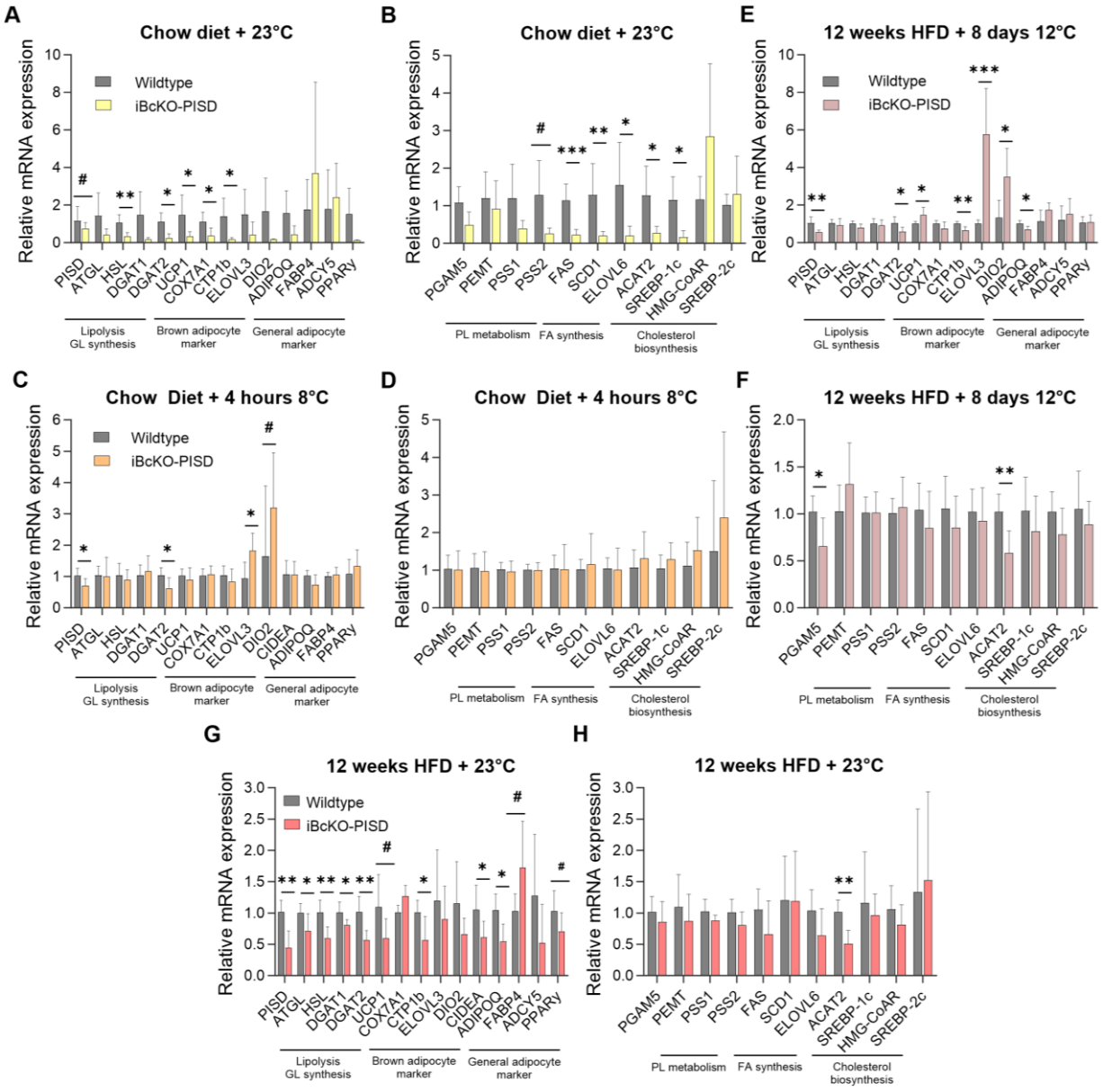

Figure 55: Brown and white adipocyte marker genes as well as genes involved in lipid metabolism differ between iBAT of iBcKO-PISD and WT mice depending on the housing condition. *(A-B) mRNA expression of relevant genes in iBAT of iBcKO-PISD and wildtype mice of cohort I, (C-D) cohort II, (E-F) cohort IV and (G-H) cohort III; shown are means +SD of n= 5-6 per group; #p<0.1, *p<0.05, **p<0.01 and ***p<0.001 indicate significant differences to wildtype mice determined using student's t-test with Welch's correction. Mice were treated with three consecutive oral gavages (2 mg/mouse) of tamoxifen in sunflower oil at ten weeks of age (+ monthly refreshments) to induce PISD knockout. Data was quantified relative to wildtype mice using TBD as housekeeper.*

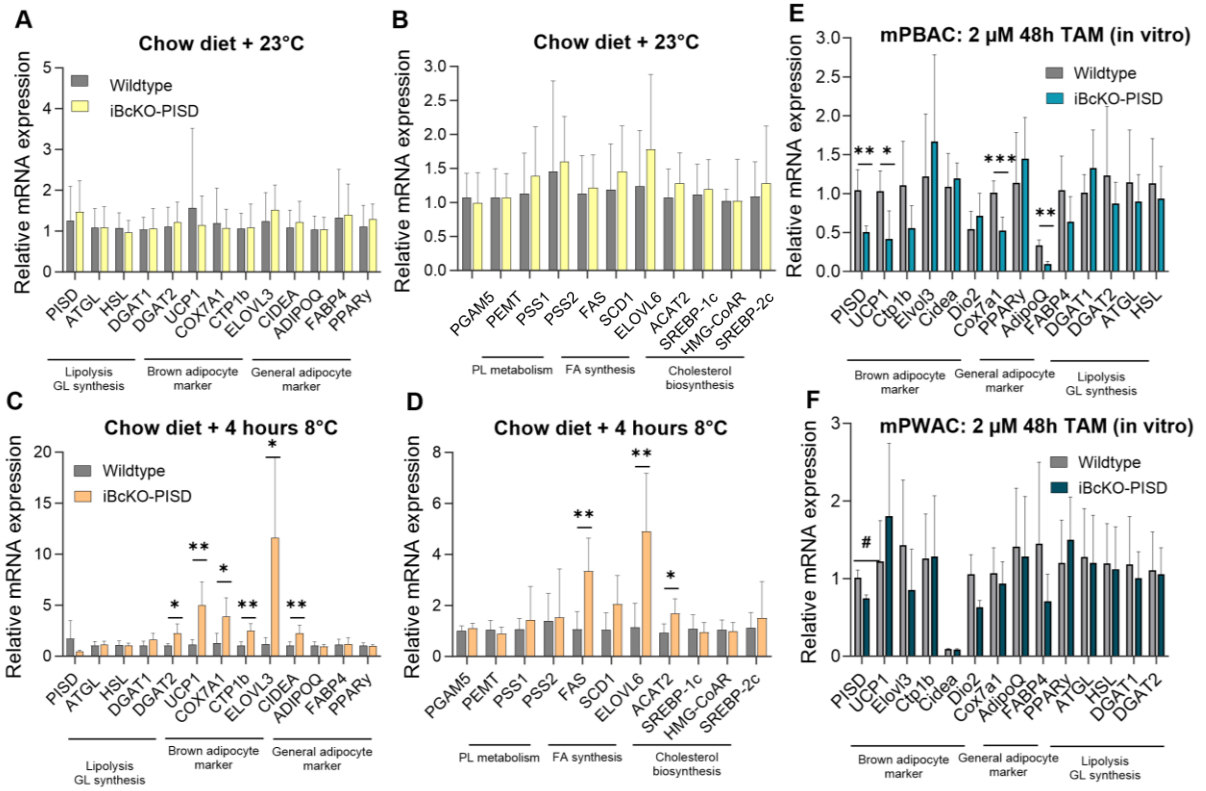

Figure 56: Brown and white adipocyte marker genes as well as genes involved in lipid metabolism differ between iWAT of iBcKO-PISD and WT mice after cold exposure. *(A-B) mRNA expression of relevant genes in iWAT of iBcKO-PISD and wildtype mice of cohort I and (C-D) cohort II. Mice were treated with three consecutive oral gavages (2 mg/mouse) of tamoxifen in sunflower oil at ten weeks of age to induce PISD knockout. (E) mRNA expression of relevant genes in mPBAC and (F) mPWAC isolated of iBcKO-PISD and wildtype mice and induced with 2 µM tamoxifen for 48 hours to induce PISD knockout (in vitro); shown are means +SD of n= 4-6 per group; #p<0.1, *p<0.05, **p<0.01 and ***p<0.001 indicate significant differences to wildtype mice determined using student's t-test with Welch's correction. Data was quantified relative to wildtype mice using TBD as housekeeper.*

3.2.9 PISD, PERILIPIN, VDAC$_1$ AND CYTOCHROME C PROTEIN EXPRESSION IN PRIMARY BROWN AND BEIGE ADIPOCYTES OF PISD CKO AND WILDTYPE MICE

To strengthen the transcriptomic results, protein abundance of selected candidates was determined using Western Blot analyses on primary brown and beige adipocytes previously treated with tamoxifen (*in vitro*). Consistent with **Figure 42** D, PISD was approximately 2-fold decreased in adipocytes lacking PISD in UCP1 expressing cells. Nonetheless, neither brown nor beige adipocytes revealed differences in UCP1 protein (**Figure 57** A, C). The lipid droplet-associated protein perilipin was increased in

adipocytes lacking PISD (~30%), further substantiating the increased lipid storage observed in the histological stainings of mice housed at 23°C and fed a chow or high fat diet (**Figure 57** A, C; **Figure 51**). The mitochondrial marker proteins VDAC1 and cytochrome C were initially investigated with the intention of evaluating mitochondrial mass. As iBcKO-PISD mice had a "whiter" phenotype under basal conditions, we expected a reduction in mitochondrial density. Also, a recent study by Johnson et al. *(Johnson et al. 2023)* demonstrated that a conditional knockout of PISD in brown adipose tissue substantially reduces the mitochondrial mass and causes a reduced density of cristae and therefore a disorganization of the inner mitochondrial membrane. Surprisingly, in our study, cytochrome C and VDAC1 protein levels were 2.0-2.5-fold elevated in brown and beige adipocytes of iBcKO-PISD mice (**Figure 57** A-D). This finding may not necessarily reflect an increase in mitochondrial density, but rather an induction of mitochondrial damage. The voltage-dependent anion channel VDAC1 is known to be overexpressed during pathological conditions, such as mitochondrial dysfunction, leading to elevated permeability of the outer mitochondrial membrane for the release of pro-apoptotic proteins and ultimately induces cell death *(Shoshan-Barmatz et al. 2020; Shoshan-Barmatz et al. 2018)*. Cytochrome C is a soluble electron carrier between complexes III and IV of the oxidative phosphorylation chain. Its release into the cytosol increases with the permeability of outer mitochondrial membranes, resulting in the execution of pro-apoptotic functions *(Eleftheriadis et al. 2016)*.

In summary, these results provide further evidence that brown and beige adipocytes lacking PISD exhibit elevated lipid storage and potentially mitochondrial dysfunction under basal conditions.

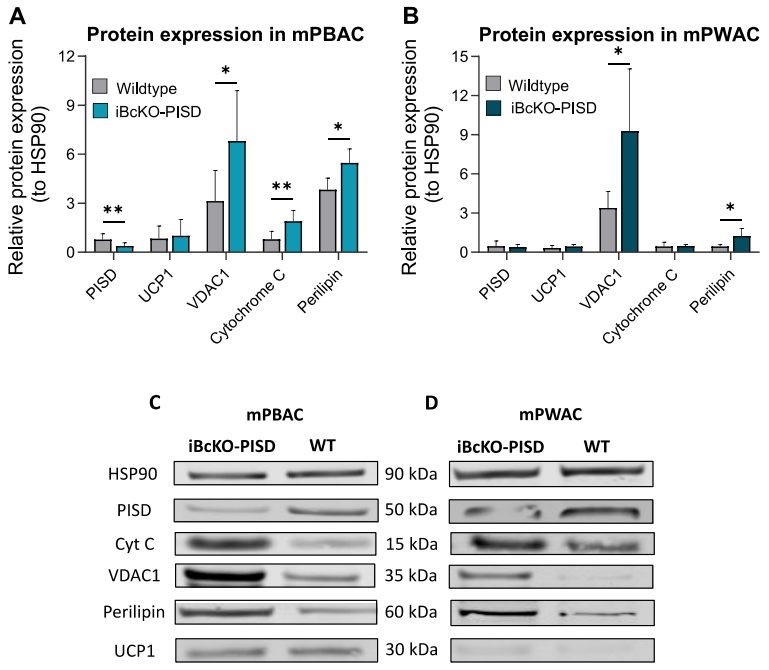

Figure 57: UCP1 protein abundance in mPBAC and mPWAC is similar in iBcKO-PISD and WT mice, whereas VDAC1 and cytochrome C as well as lipid droplet marker perilipin are higher expressed in iBcKO-PISD mice. *(A, C) Quantified and exemplary blotted protein abundance relative to HSP90 expression in primary brown and (B, D) beige adipocytes induced with 2 µM tamoxifen for 48h (in vitro). Analysed using Western Blot; shown are means +SD of n= 10 (PISD), n= 6-7 (UCP1, VDAC1, Cytochrome C) and n= 4 (Perilipin); *p<0.05 and **p<0.01 indicate significant differences to control group determined using student's t-test with Welch's correction.*

3.2.10 LIPID COMPOSITION OF MITOCHONDRIA ISOLATED FROM BROWN AND BEIGE ADIPOCYTES DERIVED FROM IBCKO-PISD AND WILDTYPE MICE

To analyze whether the conditional knockout of PISD alters the mitochondrial lipid composition, mitochondria where isolated from adipocytes differentiated from pre-adipocytes of BAT after cultivation and treatment with tamoxifen using an antibody-based isolation kit. The lipidome was quantified using a comprehensive MS-based lipidomic analysis.

Surprisingly, mPBAC cKO cells had unaltered total concentrations of PE and PS (**Figure 58** B). Moreover, the PE/PS ratio was found to be approximately 2-fold reduced in wildtype brown adipocytes compared to cKO adipocytes (expected would have been the opposite), which was provoked through a significant elevation of the phospholipid species PE 32:1, PE 34:1, together with a decrease in PS 36:1, PS 36:2, PS 38:1, PS 38:2, PS 40:3, PS 42:6 and PS 42:7 (**Figure 58** A, C, D). This may be attributed to a compensatory effect of the Kennedy pathway, which is located outside of mitochondria. Potential explanations could be an increase in PE *de novo* synthesis, a reduction in PS synthesis from PE, or a diminished PEMT-mediated conversion of PE to PC. An alternative hypothesis could be a change in the transport of lipids into mitochondria upon PISD knockout. Nevertheless, mechanisms governing the transport of PE into mitochondria remain elusive. The levels of PA, specifically PA 32:0, PA 32:1, and PA 34:1, were found to be more than 2-fold higher in the cKO mice (**Figure 58** G). Other phospholipid classes, sterols, ceramides, as well as glycerolipids revealed no substantial differences between the genotypes (**Figure 58** B, E, F; **Supplementary Figure 7**; **Supplementary Figure 8**). It is particularly noteworthy that in cKO mitochondria, PE/FC, PC/FC, and GPL/FC species were found to be almost 2-fold increased (**Figure 58** A).

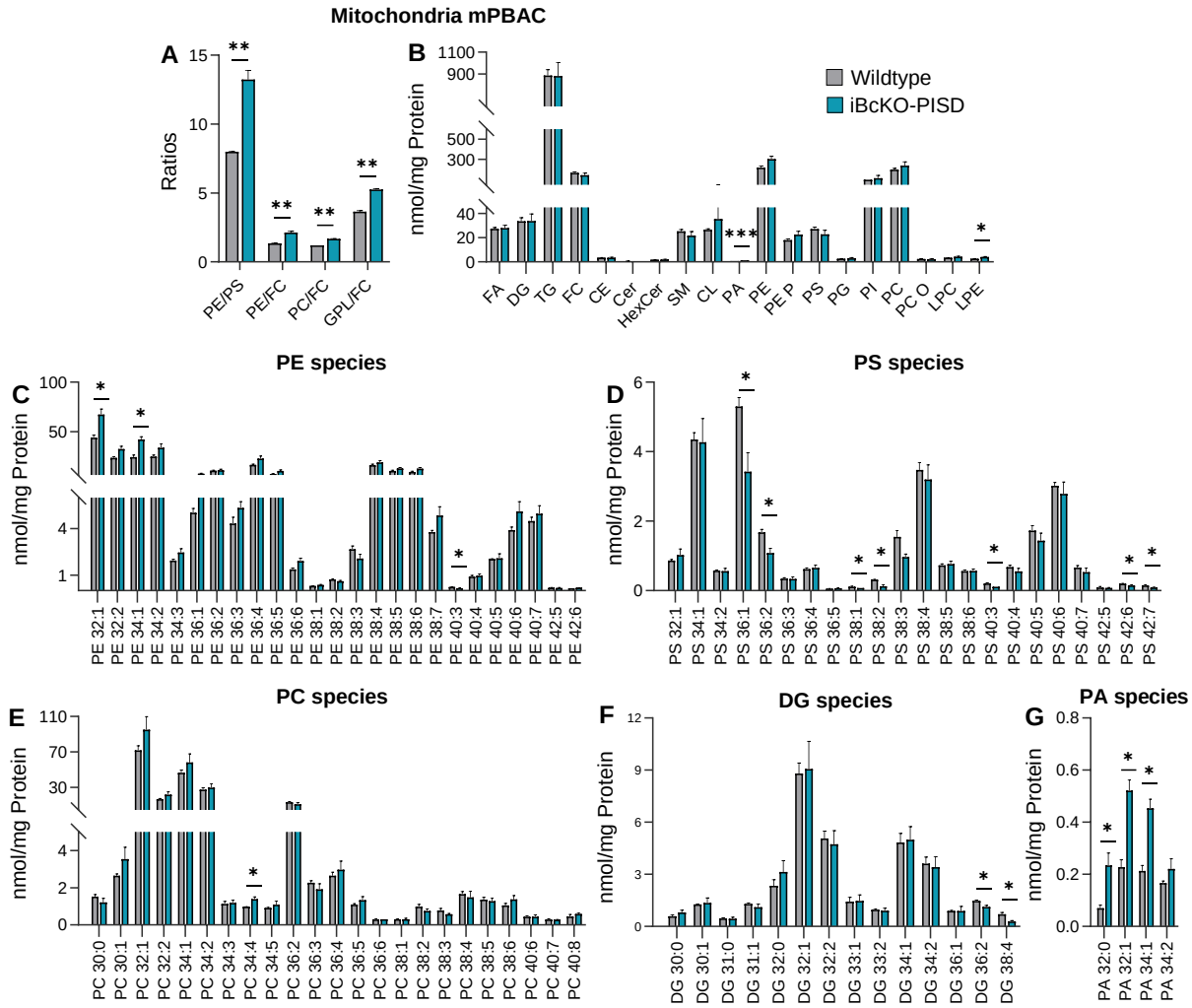

Figure 58: Common membrane lipids are differentially distributed between mPBAC mitochondria of iBcKO-PISD and WT mice. *(A) Lipid ratios, (B) common membrane lipids, (C) PE species, (D) PS species, (E) PC species, (F) DG species and (G) PA species in mitochondria isolated of mPBAC which were previously treated with 2 µM tamoxifen for 48 hours to induce PISD cKO; lipids were analysed using mass spectrometry. Shown are means +SD of n= 2 per group; *p<0.05, **p<0.01 and ***p<0.001 indicate significant differences to control, determined with a student's two-tailed t-test with Welch's correction. Each mitochondrial sample was pooled from adipocytes originating from n= 4 mice.*

In mitochondria isolated from primary beige adipocytes (mPWAC), the PE/PS ratio was also lower in wildtype mice, although not as pronounced as it was observed in brown adipocytes (2-fold vs. 1.1-fold) (**Figure 59** A). Here, this finding can be attributed to the unequal increases observed in mice lacking PISD in both PE species (e.g. PE 34:1, PE 38:4) and PS species (e.g. PS 40:5, PS 40:6) (**Figure 59** B-D). As observed in brown adipocytes, the GPL/FC ratio was elevated by approximately 20% in beige adipocytes from iBcKO-PISD mice, which was (besides PE and PS) due to increased levels in PE P, PC, and PA species (e.g. PC 30:1, PC 34:1, PC 34:4, PA 32:0, PA 34:1, PA 34:2) (**Figure 59** A, B, E, G). SM was found to be almost 2-fold reduced in wildtype adipocytes, while other lipid classes and species were comparable between the genotypes (**Figure 59** B; **Supplementary Figure 9**; **Supplementary Figure 10**).

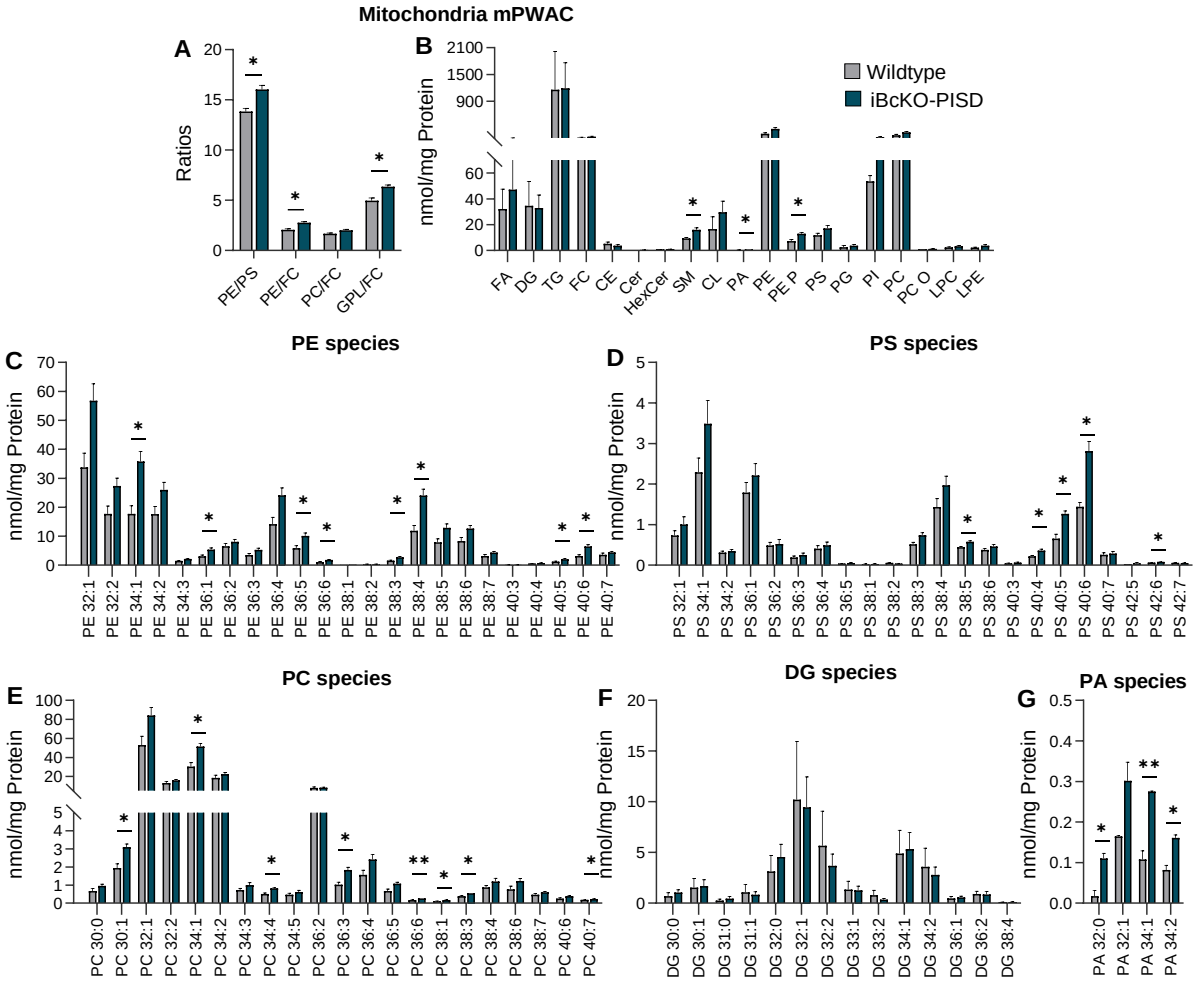

Figure 59: Common membrane lipids are differentially distributed between mPWAC mitochondria of iBcKO-PISD and WT mice. *(A) Lipid ratios, (B) common membrane lipids, (C) PE species, (D) PS species, (E) PC species, (F) DG species and (G) PA species in mitochondria isolated of mPWAC which were previously treated with 2 µM tamoxifen for 48 hours to induce PISD cKO; lipids were analysed using mass spectrometry. Shown are means +SD of n= 2 per group; *p<0.05 and **p<0.01 indicate significant differences to control, determined using a student's two-tailed t-test with Welch's correction. Each mitochondrial sample was pooled from adipocytes originating from n= 2 mice.*

3.2.11 ISOPROTERENOL-INDUCED UCP$_1$ ACTIVITY OF PRIMARY BROWN ADIPOCYTES IS INCREASED WHEN PISD IS KNOCKED DOWN OR KNOCKED OUT

To study whether the modulation of PISD activity in primary brown and beige adipocytes affects UCP1 and thereby thermogenic function, the mitochondrial respiratory capacity was assessed using microplate-based respirometry in (1) siRNA-treated PISD knockdown and (2) PISD cKO cells. Therefore, a similar assay was employed as previously utilized in **section 3.1**.

The following measurements were taken: Measurement of [1] basal respiration; [2] basal uncoupled respiration after blocking ATP synthase using oligomycin; [3] induction of UCP1 by addition of isoproterenol (ISO) as β-adrenergic agonist; [4] assessment of the maximal respiratory capacity by using carbonyl cyanide 4-(trifluoromethoxy) phenylhydrazone (FCCP) as uncoupling agent; and [5] non-

mitochondrial O_2 consumption applying antimycin A (Anti A). The activity of UCP1 was estimated by calculating the isoproterenol-induced increase over proton leak-linked oxygen consumption.

PISD expression was silenced using RNAi, resulting in a 5-fold reduction of its transcription levels (**Figure 60** C). The tamoxifen-induced knockout of PISD in brown adipocytes differentiated from pre-adipocytes isolated from BAT of iBcKO-PISD mice, resulted in a 50% reduction of PISD on mRNA and protein levels as shown in **Figure 42** C and D. In both cases, when PISD was knocked down or knocked out, increased PC/FC, PE/FC and most importantly GPL/FC ratios (**Figure 58** A, **Figure 60** D), together with isoproterenol-induced UCP1-dependent OCR were found (cKO: 1.5-fold, KD: 1.3-fold) (**Figure 60** A-B, **Figure 61** A-B). Interestingly, both in PISD KD and PISD KO brown adipocytes, also PE/PS was elevated (**Figure 58** A, **Figure 60** D).

This essentially supports our previous findings that brown adipose tissue of iBcKO-PISD mice housed at cold temperatures, as a condition comparable to isoproterenol treated cells, have a higher browning capacity compared to wildtypes. Moreover, these results further strengthen a potential correlation between the mitochondrial GPL/FC and UCP1 activity.

Primary beige adipocytes did not reveal an impact on UCP1 activity after modulation of PISD activity (**Figure 61** C, D).

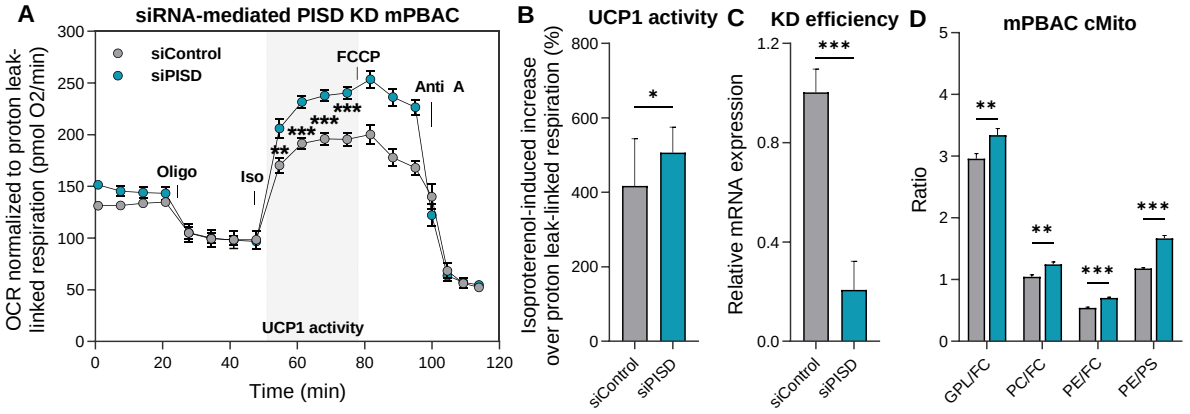

Figure 60: Primary brown adipocytes with siRNA-mediated PISD inhibition show increased isoproterenol induced UCP1-mediated respiration compared to non-targeting control. *(A) Microplate-based respirometry was applied on primary brown adipocytes (n= 12-16) treated with siRNA against PISD or non-targeting control; The oxygen consumption rate (OCR) was measured at basal conditions, at proton leak-linked respiration (oligomycin; CV inhibition), UCP1-mediated respiration (isoproterenol; β-adrenergic agonist), maximal respiratory capacity (FCCP; uncoupling reagent) and after inhibition of the electron transport chain (antimycin A; CIII inhibitor). (B) UCP1 activity was calculated as isoproterenol induced increase over proton leak-linked respiration. (C) Relative mRNA expression of PISD after siRNA mediated knockdown in primary brown adipocytes (n= 3). (D) Lipid ratios of mitochondria isolated of respective cells (n= 3). Shown are means ±SEM (A) and means +SD (bar plots); *p<0.05, **p<0.01 and ***p<0.001 indicate significate differences relative to controls, determined using two-sided student's t-test with Welch's correction.*

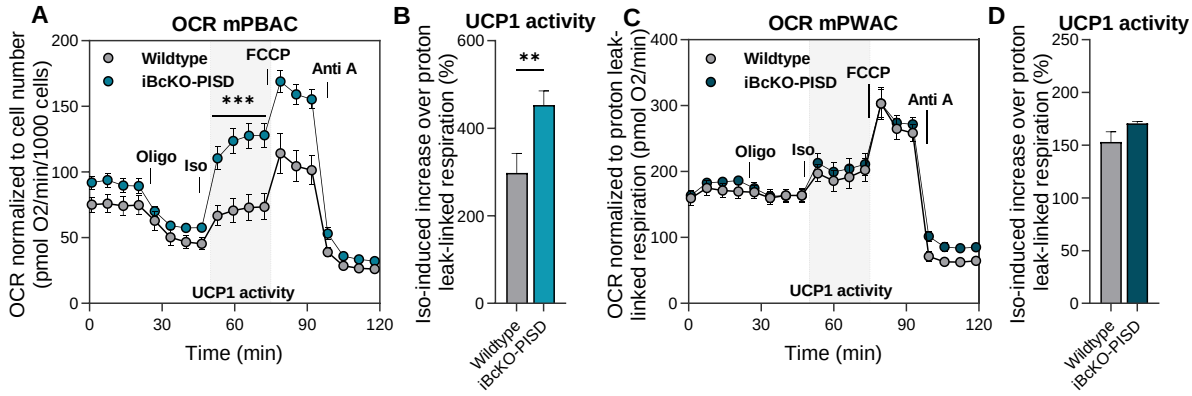

Figure 61: Primary brown adipocytes of iBcKO-PISD mice display increased isoproterenol-induced UCP1-mediated respiration compared to wildtypes, whereas in beige adipocytes UCP1 function is unchanged. *(A, C) Microplate-based respirometry was applied on (A) primary brown adipocytes and (C) primary beige adipocytes originating from iBcKO-PISD or wildtype mice. Cells were previously treated with 2 µM tamoxifen for 48 hours to induce PISD cKO; The oxygen consumption rate (OCR) was measured at basal conditions, at proton leak-linked respiration (oligomycin; CV inhibition), UCP1-mediated respiration (isoproterenol; adrenergic agonist), maximal respiratory capacity (FCCP; uncoupling reagent) and after inhibition of the electron transport chain (antimycin A; CIII inhibitor). (B, D) UCP1 activity was calculated as isoproterenol-induced increase over proton leak-linked respiration. Shown are means ±SEM (A, C) and means +SD (B, D) of n= 15 WT, n= 40 cKO (mPBAC) and n= 10 (mPWAC); **p<0.01 and ***p<0.001 indicate significate differences relative to controls, determined using a two-sided t-test with Welch's correction.*

4 DISCUSSION

The metabolic syndrome, particularly characterized by central obesity, represents a substantial public health burden, with an increased risk of all-cause mortality observed in both adults and children worldwide. This condition is associated with a number of complications, including cardiovascular disease, inflammation, insulin resistance, hyperglycemia, hypertension, and dyslipidemia. Overweight and obesity are defined as having a persistent positive energy balance, which is caused by genetic factors, reduced energy expenditure, and excessive energy intake from food. This subsequently leads to lipid accumulation in adipose tissue *(Eckel et al. 2005; Després und Lemieux 2006)*. Typical measures to combat obesity include increasing physical activity levels and implementing caloric restriction. In order to improve quality of life and reduce obesity-related complications, it is necessary to achieve sustained weight loss of more than 10%. This can be very challenging for the majority of individuals over extended periods. Moreover, the human body is capable in opposing such efforts through physiological adaptations, emphasizing the necessity of medical assistance in addition to lifestyle interventions *(Perdomo et al. 2023)*. In recent years, drugs such as glucagon-like peptide-1 (GLP-1) receptor analogues (e.g. Semaglutides/ Ozempic) have emerged as potential treatment options for obesity. By mimicking the natural hormone GLP-1, these drugs promote weight loss through a combination of appetite reduction, slowing gastric emptying, and improving insulin sensitivity. Nevertheless, due to the potential for adverse (side) effects, high costs, the low accessibility to patients because of high demand and limited knowledge on long-term consequences, current drugs are inadequate to address the surging prevalence of metabolic disorders, indicating the necessity for the implementation of novel and innovative treatment approaches *(Ryan 2022)*.

Over the past two decades, there has been a major debate surrounding the relevance of brown adipose tissue in humans, which is involved in regulating body temperature. The mitochondrial protein uncoupling protein 1 (UCP1) is highly expressed and has the capacity to uncouple oxidative phosphorylation, thereby dissipating chemical energy in the form of heat *(Cohen und Kajimura 2021; Wu et al. 2013)*. As a consequence of the increased energy expenditure resulting from this process, brown adipose tissue has been identified as a potential novel therapeutic target for the treatment of metabolic dysfunction, including obesity *(Liu et al. 2022)*. The debate also extends to the activation of BAT function and the 'browning' of white adipose tissue under certain conditions, such as β-adrenergic stimulation. The direct clinical use of sympathomimetic agents is precluded due to serious side effects associated with the required doses *(Wu et al. 2013)*. To develop novel drugs that promote adipose tissue thermogenesis, it is key to gain a deeper understanding of the function of brown and beige adipocyte UCP1.

This work aims to investigate the role of mitochondrial glycerophospholipids, including PC, PE and PS, and cholesterol in the metabolism and activity of brown adipose tissue.

4.1 BAT MITOCHONDRIA HAVE A UNIQUE LIPID COMPOSITION

The composition of lipids in different tissue and cell types varies to comply with their respective functionality. This is even conserved on the subcellular level *(Schweizer et al. 2019; van Meer et al. 2008)*. To date, it remains unclear whether the lipid distribution of organelles in different tissue and

cell types is similar. This study demonstrates that the lipid composition of mitochondrial membranes differs significantly between different organs.

To ascertain that the observed differences in the membrane lipid composition are primarily derived from mitochondrial membranes and not from contaminations with other organelles, crude mitochondrial fractions were isolated using differential centrifugation and further purified into ER, MAM and purer mitochondrial fractions using density gradient centrifugation. The separation of mitochondria and ER can be achieved using density gradients, as these organelles exist as separate structures without direct fusion between their membranes. However, separating mitochondria from mitochondria-associated membranes (MAM) is more challenging due to the direct association of this membrane with the mitochondrial outer membrane, as first described by Jean Vance *(Vance 1990)*. Previous reports on mitochondrial purification unveil that the biochemical separation of MAM from ER is even more complicated than from mitochondria *(Giacomello und Pellegrini 2016; Wieckowski et al. 2009; Ma et al. 2017)*. Here, a protocol originally developed to separate liver MAM fractions from the mitochondrial outer membrane, was employed and adjusted to purify mitochondria from brown adipose tissue (referred to as pMito) *(Wieckowski et al. 2009)*. Regardless, due to its considerable time-consuming nature and the preclusion of isolating respiring mitochondria, this procedure is not a practicable approach for functional analyses, such as mitochondrial respirometry. Additionally, it requires an excessive number of animals, with 15 mice needed per isolate of iBAT mitochondria. Consequently, we developed a protocol for enrichment of mitochondria based on differential centrifugation (referred to as cMito), which is less time-consuming and requires fewer animals. Proteomic, western blot and lipidomic analyses confirmed that the proteomes and lipidomes were largely comparable between cMito and pMito fractions. The presence of MAM and ER in cMito was found to be negligible. Hence, cMito isolates were used for the subsequent experiments.

Our findings unveil that the lipidomic organization of mitochondria is critical for brown adipocyte function. The application of an established data analysis strategy *(Kindt et al. 2018; Ecker et al. 2021)* in combination with an independent approach based on machine learning has revealed that brown adipose tissue mitochondria comprise more GPL (especially PC and PE) and almost no free cholesterol compared to WAT mitochondria, resulting in a significantly higher GPL/FC ratio. It is well established that mitochondria contain relatively low levels of cholesterol, with a concentration of approximately 10% compared to 50% in plasma membranes. However, the detection of a cholesterol concentration of only 2% in brown adipose tissue (BAT) mitochondria represents a previously unreported finding. Our findings indicate that there is no systemic difference in the expression levels of genes involved in cholesterol biosynthesis across different adipose tissue depots. However, we did observe a notable elevation in the *de novo* synthesis of glycerophospholipids PC and PE in BAT. This observation leads us to conclude that the high mitochondrial GPL/FC ratios observed in BAT may originate from distinct phospholipid metabolic capacities across different adipose tissue depots. Importantly, iBAT mitochondria of mice housed at 4°C displayed significantly higher portions of GPL, particularly PC, PE, PG and PI compared to mice housed at room temperature and thermoneutrality. In beige adipose tissue, this observation was similar, although less pronounced (only observed for PE and PG). In mitochondria from white adipose tissue, temperature differences did not affect the distribution of lipids. This evidence provides clear indication of a correlation between the mitochondrial GPL composition and BAT activity/WAT browning. In agreement with previous findings, it was demonstrated that cold exposure induces alterations in the expression of genes involved in glycerophospholipid (GPL) metabolism, as well as in the levels of phosphatidylcholine (PC),

phosphatidylethanolamine (PE) and cardiolipin (CL) in murine brown adipose tissue. In human serum, levels of polyunsaturated PE and PG species are elevated upon cold exposure *(Lynes et al. 2018; Marcher et al. 2015)*.

Murine UCP1 knockout models, initially described in the Kozak laboratory, have been observed to be unable to maintain body temperature upon acute cold exposure unless the temperature is gradually decreased, allowing sufficient time for the mice to adapt. Consequently, UCP1 has been identified as principal mediator of non-shivering thermogenesis *(Enerbäck et al. 1997; Nedergaard et al. 2001)*. Several theories on how UCP1 is activated have been proposed in the literature, but the precise mechanisms remain elusive. Proposed models for the generation of heat by the dissipation of the proton current through the inner mitochondrial membranes include the following: (1) UCP1 operates as an OH^- uniporter, binding fatty acids allosterically *(Nicholls 2006)*. (2) Upon allosteric binding of FFA, UCP1 functions as a H^+ uniporter, transporting protons into the mitochondrial matrix *(Rial und González-Barroso 2001; Cannon und Nedergaard 2004; Shabalina et al. 2004)*. (3) UCP1 interacts with long-chain fatty acids, which cannot dissociate from it due to their hydrophobic characteristics. This interaction induces a conformational change, thereby releasing H^+ into the mitochondrial matrix *(Fedorenko et al. 2012)*. (4) UCP1 protonates carboxylate groups delivered by direct fatty acid binding and carries them into the mitochondrial matrix (H^+-buffering model) *(Klingenberg und Huang 1999)*. (5) UCP1 facilitates the transport of deprotonated fatty acids from the matrix to the intermembrane space, thereby providing anions that can be protonated and flip-flop through lipid bilayers back into the mitochondrial matrix (fatty acid cycling model) *(Garlid et al. 1998)*.

The flip-flop of protonated fatty acids across lipid bilayers essentially depends on its lipid composition, with the ratio between glycerophospholipids and free cholesterol (GPL/FC) being of particular significance. In 1972, Singer and Nicolson described how cholesterol regulates membrane fluidity. At elevated temperatures, cholesterol serves to stabilize cell membranes. Conversely, at lower temperatures, cholesterol intercalates between phospholipids, preventing them from interfering with each other. Consequently, cholesterol either decreases or increases membrane fluidity, respectively *(Singer und Nicolson 1972)*. In more precise terms, cholesterol can facilitate the ordered arrangement of acyl chains in GPL, thereby restricting their mobility within the membrane. This leads to an elevation of lipid packing density and an increase in the energy required to create a void in the leaflet, through which FFA can flip-flop *(Brunaldi et al. 2005; Kleinfeld et al. 1997)*. Therefore, a low cholesterol content in mitochondrial membranes (i.e. high GPL/FC ratio) is likely to increase FFA flip-flop, potentially leading to UCP1 activation via the fatty acid cycling model.

Moreover, an increase in cholesterol within mitochondrial membranes could not only influence the flip-flop capacity of fatty acids, but also other processes. An increase in membrane rigidity may result in restricted mobility of UCP1 and reduced accessibility of protons to the uncoupling site.

4.2 GPL/FC AFFECTS UCP_1 ACTIVITY IN BROWN ADIPOSE TISSUE MITOCHONDRIA

4.2.1 MODULATION OF MITOCHONDRIAL GPL/FC VIA GPL AND FC ENRICHMENT

The main objective was to investigate the potential relationship between the elevated GPL/FC ratio in brown adipose tissue mitochondria and UCP1 function. To this end, mitochondrial respiration was analyzed using high-resolution and microplate-based respirometry. The lipid composition of

mitochondrial membranes was modulated through various strategies. Attempts to decrease the GPL/FC ratio were as follows: Incubation with a cholesterol-BSA complex, a me-β-CD-Cholesterol complex ("water-soluble cholesterol") and by overexpressing STARD3 (mitochondrial cholesterol transporter). The GPL/FC ratio was increased by using me-β-CD and by inhibiting STARD3 using siRNA-mediated RNA interference.

The incubation of iBAT mitochondria with a BSA-cholesterol complex resulted in a reduction in UCP1 activity, basal respiration, and G3P-induced respiration. BSA is frequently employed as a carrier protein, as it facilitates the solubilization and delivery of molecules such as cholesterol to cells and cellular compartments. However, BSA is not a specific carrier for cholesterol. It binds various types of lipids, including phospholipids and fatty acids. It cannot be excluded, that BSA wasn't fully saturated with the applied concentration of free cholesterol. Hence, unsaturated BSA might have extracted a bulk of other molecules from the mitochondrial membranes, potentially perforating lipid bilayers and thereby causing a general inhibition of mitochondrial respiration. Consequently, alternative approaches were employed to modify mitochondrial lipid compositions. Methyl-β-cyclodextrin is a commonly utilized compound for the depletion of cholesterol in cellular and organelle membranes. Its structure is composed of a hydrophilic oligosaccharide, consisting of α-(1-4)-linked D-glucopyranose units, which form heptamers. These heptamers create a hydrophobic central cavity that can form a 2:1 complex with cholesterol at membrane surfaces *(Mahammad und Parmryd 2015)*. Methyl-β-cyclodextrin can not only be used to deplete cholesterol from membranes but also to enrich them with exogenous cholesterol. Typically, cholesterol is conjugated with me-β-CD in a 1:25 ratio (960 mg me-β-CD + 40 mg cholesterol), which provides saturated cyclodextrin. Saturated cyclodextrin is uncapable to bind membrane lipids and therefore only delivers "water-soluble" cholesterol to membranes *(Barman und Nayak 2007; Chiu et al. 2021)*. Both approaches demonstrated a significant impact on UCP1 activity. The enrichment of mitochondria with cholesterol resulted in a reduction in UCP1 activity, whereas the depletion of cholesterol led to an increase in UCP1 activity at concentrations between 1 µM and 10 µM me-β-CD. It is worth noting that the results were highly dependent on the dose used (0.5 µM – 50 µM). Outside of the previously shown range (1 µM-10 µM), the effect on UCP1 was rather opponent to what was expected. One significant drawback of methyl-β-cyclodextrin is that, under certain conditions, it may not be entirely specific to cholesterol. For instance, at high concentrations, it may remove phospholipids from membranes and redistribute phospholipids in membranes that typically do not undergo rapid lipid exchange *(Leventis und Silvius 2001; Sanchez et al. 2011)*. A previous study reported that, for reasons that remain unknown, also very low concentrations of cyclodextrin (0.5 µM, 30 minutes) reduce cellular cholesterol extraction in T lymphocytes *(Fülöp et al. 2001)*.

To address these challenges and potential drawbacks, we conducted an incubation experiment with isolated mitochondria and donor vesicles containing varying ratios of glycerophospholipids and free cholesterol. To facilitate the lipid exchange between mitochondrial membranes and vesicles, methyl-α- *c*yclodextrin was here employed. This form of cyclodextrin is, as methyl-β-cyclodextrin, hydrophilic on its outer shell, which is exposed to the mitochondria, whereas its inner core is hydrophobic (**Figure 34**). However, the major distinction between this oligosaccharide and me-β-CD is that the former forms a hexamer rather than a heptamer, which results in a cavity incapable in binding sterols. It primarily forms soluble complexes with phospholipid-containing vesicles to facilitate their incorporation into membranes, without extracting cholesterol from membranes *(Kainu et al. 2010; Li et al. 2016; Lin und*

London 2014). To accelerate the fusion of vesicles with mitochondria, donor vesicles were extensively sonicated to yield small unilamellar vesicles (SUVs). To further decrease their size, 5% phosphatidic acid, which has a conical shape and a very small headgroup, was added to each vesicle *(Clark et al. 2020; Hauser und Gains 1982)*. This approach enabled the modulation of the mitochondria's GPL and FC contents and could demonstrate that increasing GPL/FC ratios in brown adipose tissue mitochondria drive the activity of UCP1. It was not clear whether the lipid exchange mediated by cyclodextrins solely affects the OMM or also the IMM, where OXPHOS and UCP1 are located. To consider this uncertainty, mitoplasts were prepared after incubating mitochondria with SUVs by detaching the OMM using digitonin. The mitoplast lipidome revealed comparable GPL/FC ratios to those observed in mitochondria prior to digitonin treatment, contingent on the lipid composition of the vesicles. This suggests that the lipid exchange was not limited to the outer mitochondrial membranes but also occurred in inner mitochondrial membranes. Digitonin is a detergent that is prominently used to permeabilize membranes, especially plasma membranes, by extracting membrane components *(Adam 2016; Niklas et al. 2011)*. It has been reported that digitonin is also effective in permeabilizing mitochondrial outer membranes *(Vander Heiden et al. 2000; Schnaitman und Greenawalt 1968)*. A recent publication has indicated that digitonin treatment primarily relies on its interaction with sterols, and therefore, it may eventually be unable to flip across cholesterol-poor membranes *(Fan und Heerklotz 2017)*. Our western blotting data (e.g. VDAC1-OMM marker; data not shown) demonstrated that, despite the presence of only marginal cholesterol, digitonin was able to extract the outer mitochondrial membrane (OMM) from brown adipose tissue mitochondria.

4.2.2 MODULATION OF MITOCHONDRIAL GPL/FC BY AFFECTING LIPID TRAFFICKING

Given that mitochondria are dynamic organelles that rely substantially on intracellular lipid trafficking, we also conducted research on intact adipocytes. The cholesterol contents of mitochondria depend on the proteins of the StAR family, primarily STARD1 and STARD3. Previous studies have indicated that imbalances in cholesterol trafficking can lead to the accumulation of cholesterol in mitochondria *(van Meer et al. 2008; Elustondo et al. 2017; Miller 2007)*. Thereby, membrane fluidity and membrane physical properties can be affected, ultimately resulting in mitochondrial dysfunction and associated diseases such as Alzheimer's and cardiovascular disease *(Elustondo et al. 2017; van Meer et al. 2008; Ballinger 2005)*. A recent study demonstrated that feeding mice a diet enriched in cholesterol resulted in the upregulation of STARD1 and STARD3 expression, which in turn led to an accumulation of cholesterol in liver mitochondria. This impairs oxidative phosphorylation by disrupting the assembly of mitochondrial respiratory supercomplexes *(Solsona-Vilarrasa et al. 2019)*, thereby corroborating our findings on liver mitochondrial respiration (data not shown). To ascertain whether STARD3 impacts oxidative phosphorylation and/or UCP1 activity in brown adipose tissue, we manipulated STARD3 expression in primary brown adipocytes. The overexpression of STARD3 resulted in a decrease in the GPL/FC ratios, which was accompanied by an increase in FC in the mitochondria. This ultimately led to a reduction in UCP1 activity. The knockdown of STARD3 demonstrated an opposing scenario. The proton leak-linked respiration, as measured via oligomycin-mediated inhibition of complex V of the ETC, was not affected by STARD3. This suggests that the change in brown adipocyte mitochondrial respiration was specifically due to UCP1 and not due to any OXPHOS complexes. This was subsequently validated through the conduct of analog respiratory experiments on UCP1 knockout mice.

These results imply that STARD3 may be a promising therapeutic target for modifying mitochondrial GPL/FC ratios and, consequently, BAT function. It is of note that this process does not interfere with

major cellular functions such as cholesterol biosynthesis. In contrast, the inhibition of 3-hydroxy-3-methylglutaryl-coenzyme A reductase (HMGCR) via statins has been demonstrated to inhibit BAT activity in humans by inhibiting the mevalonate pathway intermediate geranylgeranyl pyrophosphate, which is driving adipocyte browning *(Balaz et al. 2019)*. This is consistent with our observation that simvastatin treatment of murine primary brown adipocytes results in a reduction in isoproterenol-induced UCP1-mediated respiration (data not shown). STARD3 has already been proposed as a molecular target against colorectal, prostate, and gastric tumors. A recent pharmacophore-based virtual screening identified "VD1" as a potent inhibitor of STARD3 *(Asif et al. 2021; Lapillo et al. 2019)*.

To investigate whether mitochondrial phospholipid transport affects the GPL/FC ratio and UCP1 activity in primary brown adipocytes, we conducted a series of experiments targeting STARD7, which has been suggested to facilitate the transport of phosphatidylcholine into mitochondria *(Horibata und Sugimoto 2010)*. Following overexpression and inhibition of STARD7, no change in UCP1 activity was observed (data not shown). PC is the most abundant phospholipid in mitochondrial membranes, making it vital for cell survival. It is synthesized in the endoplasmic reticulum and therefore transport mechanisms into mitochondria are essential *(Sperka-Gottlieb et al. 1988; Zinser et al. 1991; Schuler et al. 2016)*. The mechanisms of mitochondrial PC trafficking remain poorly understood, and other proteins that potentially transport PC into mitochondria have been described (e.g. STARD2 and STARD10) *(Kanno et al. 2007; Olayioye et al. 2005)*. The high abundance of PC and its importance for mitochondrial function imply the existence of compensatory mechanisms for STARD7 overexpression and inhibition. These mechanisms might maintain the equilibrium of the mitochondrial phospholipid distribution, which in turn, could explain an unaltered UCP1 activity.

4.3 THE ROLE OF PISD FOR MITOCHONDRIAL LIPID METABOLISM AND LIPID COMPOSITION OF BROWN AND BEIGE ADIPOSE TISSUE

Phosphatidylserine decarboxylase (PISD) plays a pivotal role in mammalian phospholipid metabolism. It is an integral membrane protein of the inner mitochondrial membrane and catalyzes the decarboxylation of phosphatidylserine to phosphatidylethanolamine. PE is a vital component of cellular function. It plays a role in the folding of membrane proteins and supports the activity of respiratory complexes *(Patel und Witt 2017)*. In rat liver mitochondria, PE represents a major GPL as it makes up 38% of phospholipids in the IMM and 34% of the OMM *(Vance 2015)*. To date, the only known source of mitochondrial phosphatidylethanolamine synthesis is PISD activity. PE can be *de novo* synthesized in the endoplasmic reticulum (Kennedy pathway) from ethanolamine, catalyzed via ethanolamine phosphotransferase (EPT) *(Voelker 1997)*. So far, no transport mechanism of PE into mitochondria has been identified. Voelker and colleagues demonstrated that the growth and division of cells in the baby hamster kidney (BHK-21) cell line does not necessarily require exogenous ethanolamine. This suggests that EPT activity (*de novo* synthesis) is not essential and that PISD activity can even supply PE required for all cellular membranes in mammals, not only for mitochondria, but also for other organelles *(Voelker 1984)*. Since PISD is highly expressed and active in brown and beige adipose tissue, the question emerged whether it is critical for its function, specifically for UCP1 activity. In previous studies, it was found that disrupting PISD in mice results in embryonic lethality between day 8 and 10 of embryonic development. This is likely due to the presence of misshapen and

fragmented mitochondria *(Steenbergen et al. 2005)*. Therefore, here, a mouse line was generated that expressed an inducible knockout of PISD specifically in UCP1-expressing cells.

This mouse strain revealed a knockout efficiency of approximately 70% (mRNA) and 50% (protein) in brown adipose tissue. A complete tamoxifen-induced knockout in iBAT could not be expected, given it contains only 25-30% brown adipocytes expressing UCP1, as shown in the UCP1-CreER mouse strain. This remains unchanged even upon cold exposure. Further, room temperature can be considered as mild cold exposure for mice, causing hyperplasia of brown adipose tissue cells. Because this cell biogenesis (partly) occurs after tamoxifen treatment, no KO can be induced in those newly generated cells. In inguinal white adipose tissue, the population of adipocytes exhibits considerable heterogeneity, with some cells exhibiting low and others exhibiting high levels of UCP1 expression. Overall, the fraction of UCP1-expressing cells in iWAT is very low (<1%), but increases approximately 5-fold during cold exposure *(Rosenwald et al. 2013; Song et al. 2020)*. This explains why the knockout efficiency of our mouse strain was very low in beige adipose tissue at basal conditions but increased after cold exposure. Other cell types present in adipose tissue are collectively referred to as stromal vascular fraction (SVF), which encompasses a diverse array of immune cells, fibroblasts, pre-adipocytes, macrophages, neutrophils, lymphocytes, stem cells and pericytes *(Esteve Ràfols 2014; Saetang und Sangkhathat 2018)*.

Given the absence of UCP1-expressing cells, the histological characteristics of white adipose tissue (eWAT) were found to be similar between wildtype and iBcKO-PISD mice. In contrast, staining of brown and beige adipose tissue and liver revealed substantial morphological differences between the two genotypes. These differences were found to be dependent on the diet fed and the temperature the mice were housed at. In the absence of PISD in brown adipose tissue, mice exhibited a significant increase in lipid droplet size and a reduction in their numbers, which resembled a phenotype towards white adipose tissue. This was observed under normal conditions (room temperature and chow diet; condition **I**). It was accompanied by a significant infiltration of immune cells and fibrosis. In a recent publication, Johnson et al. published a similar finding. Further, the group suggests impaired BAT thermogenesis in mice lacking PISD in brown adipose tissue *(Johnson et al. 2023)*. However, we cannot support their assertion that mice lacking PISD are generally restricted in their BAT activity (independent of housing conditions such as diet and temperature). Firstly, because we observed a strong upregulation of PISD expression following intraperitoneal injections of CL-316,243 in wildtype mice of the 129Sv/ev tac strain. Therefore, the observed discrepancy in thermogenic capacity between wildtype and cKO mice may not be attributed due their genotype per se, but rather to a direct impact of the β-adrenergic agonist on PISD expression. Secondly, because of our cold housing experiments (**II, IV**). Cold exposure activates the sympathetic nervous system which releases norepinephrine from sympathetic nerves, inducing the cyclic adenosine monophosphate (cAMP)-dependent signaling pathway *(Chartoumpekis et al. 2011)*. Norepinephrine is an agonist to all β-adrenergic receptors, while CL-316,243 specifically binds β_3-adrenergic receptors *(Himms-Hagen et al. 1994)*. When mice were exposed to cold (short-term; **II**), PISD cKO led to a more multilocular phenotype, indicating a higher thermogenic capacity compared to wildtype mice. Upon feeding mice a HFD for 12 weeks and long-term cold exposure (**IV**), brown adipose tissue from cKO mice even exhibited characteristics similar to that of mice fed a normal chow diet (**I**). This implies that mice lacking PISD may be better able to cope with the dietary overload of a HFD, i.e. obesity, after cold exposure than WT mice. This is corroborated by a reduction in total body weight and an increase in lean mass, accompanied by a decrease in fat mass. The weight of brown adipose tissue in mice fed a HFD (**III, IV**) was approximately three times

greater in wildtype mice compared to those fed a standard diet (**I, II**). In contrast, iBcKO-PISD mice displayed comparable tissue weights between chow (**I, II**) and high fat diet (**III, IV**).

But how could diet induced differences in lipid accumulation between wildtype mice and mice lacking PISD be explained? Although PISD is most prominently known as a mitochondrial enzyme, a second alternative splicing variant of PISD was recently identified using proteomics and PCR-based tests in various vertebrates such as humans and mice. This variant is not localized to inner mitochondrial membranes but to lipid droplet surfaces. As observed in HeLa cells, deriving from a human cervical carcinoma, the expression of both PISD variants depends on the nutritional state. An increase in cellular lipid droplet area induced by supplementation of growth medium with free fatty acids ('lipid storage state'), favors the localization of PISD to lipid droplets, while a reduction of LD area after using lipid-free medium ('lipid droplet shrinkage state') harbors PISD mainly at mitochondria. Additionally, it was demonstrated that PISD promotes the storage of triacylglycerols in lipid droplets, which could be explained by the increased fusion of small lipid droplets to larger ones when lipid droplets harbor more PE on their surfaces (i.e. higher PISD activity). After depletion of both forms of PISD, TAG synthesis was impaired after a FFA challenge, indicating an essential role of PISD in the storage of neutral lipids and thus, lipid droplet biogenesis *(Kumar et al. 2021)van der Veen et al. 2017)*. These findings can be related to the histological differences of brown adipose tissue from iBcKO-PISD and wildtype mice when fed either a chow or high fat diet. When mice were fed a chow diet (**I**), PISD KO led to significantly larger lipid droplets, immune cell infiltration and fibrosis compared to control mice. In contrast, when mice were fed a HFD (**III**), the differences in lipid droplet size (and immune cell infiltration and/or fibrosis) were not detected anymore. When mice were fed HFD and were additionally housed at cold temperatures (**IV**), this observation was even more pronounced. Lipid droplet size and number of the cKO animals was comparable to wildtype mice at room temperature and chow diet (**I**). The negative effects of HFD on brown adipose tissue were completely recovered. This might imply that PISD in murine brown adipose tissue, especially after cold stimulation, primarily localizes to lipid droplets and thereby promotes lipid storage upon high lipid dietary conditions.

The phenotype of iWAT in iBcKO-PISD mice exhibited a greater shift towards a brown adipose tissue phenotype following cold exposure (**II, IV**). At room temperature (**I, III**), the phenotype was comparable between the genotypes, which is consistent with the low expression of UCP1 in inguinal white adipose tissue under basal conditions. The Nedergaard and Cannon laboratory reported that no UCP1 protein absorbance units (a.u.) per mg of iWAT protein could be detected at room temperature, whereas they observed an elevation to ~50 UCP1 protein a.u. per mg of iWAT protein after exposure to 4°C *(Kalinovich et al. 2017)*. We observed a comparable body temperature (rectal) and heat production in WT and cKO mice following cold exposure (**II**), in contrast to the impaired resistance against cold as described by Johnson et al. They determined a significant decline in core temperature in cold-exposed mice with PISD deletion. After four hours of cold exposure, a core temperature of ~21°C was detected, which remained stable for an additional four hours *(Johnson et al. 2023, 2023)*. However, it is unclear how mice can survive a core temperature of 21°C for several hours. Most likely, these reported findings are due to the location of the temperature-sensitive transponders implanted in dorsal subcutaneous adipose tissue, which may not be a reliable indicator of core temperature.

In our work, the morphology of brown adipose tissue determined by H&E staining aligns closely with the results of gene expression analyses. Mice with the iBcKO-PISD genotype displayed a pronounced downregulation of brown adipocyte marker genes, including UCP1, COX7A1, CTP1b, ELOVL3 and DIO2.

In contrast, white adipocyte markers, such as Adcy5, ADIPOQ and FABP4, were upregulated when mice were housed at room temperature (**I, III**), implying a shift towards a morphology resembling white adipocytes. This observation was reversed after cold exposure (**II, IV**) for both brown and beige adipose tissue of mice lacking PISD. These results are evidenced by a significant upregulation of brown adipocyte marker genes, which implies an increase in adipose tissue browning capacity.

4.4 THE RELEVANCE OF BROWN ADIPOSE TISSUE LOCATED PISD FOR WHOLE-BODY METABOLISM

4.4.1 BROWN ADIPOSE TISSUE PISD IN THE LIGHT OF INTER-ORGAN COMMUNICATION WITH LIVER

Surprisingly, histological liver sections from conditional PISD knockout mice exhibited a markedly altered phenotype. A knockout in the liver is not a viable option, as numerous publications *(Mills et al. 2021)* and gene/protein databases (e.g. *Bgee, UniProt, The Human Protein Atlas*) indicate that it is not an UCP1-expressing tissue. But, in recent years, several publications have indicated interorgan-communication between brown adipose tissue and liver. For example, it has been demonstrated that cold-induced WAT browning and BAT thermogenesis in male mice are linked to the bradykinin metabolism. In response to cold, hepatic cells reduce bradykinin degradation, thereby increasing its serum levels. This ultimately increases the expression of UCP1 in adipose tissue *(Xiao et al. 2023)*. Bradykinin is a peptide hormone involved in regulating inflammatory processes, vasodilation, and pain *(Dutra 2017)*. The generation of ectopic UCP1 in the liver via adenovirus-mediated overexpression resulted in an increase in energy expenditure, thereby improving obesity, insulin resistance, and dyslipidemia. Furthermore, it reversed leptin resistance and hyperphagia induced by a high fat diet in mice *(Ishigaki et al. 2005)*. Beyond thermogenesis, cross-organ communication between liver and BAT was also suggested to control inflammatory processes to improve non-alcoholic fatty liver disease (NAFLD). It was discovered that UCP1 is essential for the clearance of succinate from the circulation. UCP1 KO mice exhibited elevated extracellular succinate concentrations in the liver, resulting in extensive ligation to the succinate receptor 1 (SUCNR1). This, in turn, led to an increase in immune cell infiltration and glucose intolerance *(Mills et al. 2021)*. Mice with a conditional adipose tissue knockout of SUCNR1 (AdipoQ-Cre driven) exhibited enhanced brown adipocyte differentiation compared to wildtypes, leading to browning of white adipose tissue and succinate accumulation. Additionally, they observed improved glucose homeostasis, less adiposity, and lower leptin levels, which are usually proportional to body fat mass. SUCNR1 is proposed to function as an anti-lipolytic effector in adipocytes, whereas the pharmacological elevation of plasma succinate can be linked with an enhanced UCP1-driven thermogenesis in brown adipose tissue (BAT). In response to HFD on the other hand, mice lacking SUCNR1 show a disturbed glucose homeostasis and elevated liver steatosis *(Villanueva-Carmona et al. 2023; Mills et al. 2018)*. These data collectively strengthen the idea of communication between the liver, circulation, and brown/beige adipose tissue. A human study in 60 adults (NAFLD patients: 29; healthy controls: 31) described an inverse correlation between BAT activity and hepatic lipid accumulation *(Ahmed et al. 2021)*. In this work, a recovery of the NAFLD-like phenotype in HFD fed mice lacking PISD in UCP1-expressing cells after long-term cold exposure was observed. Furthermore, we demonstrate a reduction in alanine aminotransferase (ALT) activity, a marker for liver injury, in plasma, suggesting that PISD may be critical for inflammatory processes in the liver. It is currently unclear whether this observation depends on the lack of PISD protein, altered GPL/FC or an increased UCP1 function and thermogenesis in BAT.

4.4.2 BROWN ADIPOSE TISSUE PISD IN THE LIGHT OF ENERGY METABOLISM

Leptin is a plasma protein derived from adipocytes that is known to be involved in energy metabolism. It reduces food intake, but increases energy expenditure *(Obradovic et al. 2021)*. We found higher plasma leptin levels after feeding HFD (**III, IV**), in both tested genotypes. This is consistent with results from other groups, as several obesity models in rodents (e.g. db/db or yellow Ay/a) have proven an increase in plasma leptin concentrations due to the development of leptin resistance *(Frederich et al. 1995)*. We observed a reduction in plasma leptin levels in iBcKO-PISD mice receiving either a chow diet in conjunction with acute cold exposure (**II**) or an HFD with long-term cold exposure (**IV**), compared to the wildtype controls. As cKO mice (chow + cold) additionally exhibited a reduced locomotor activity and an increased food intake, an impact of PISD on whole-body energy metabolism can be concluded. Body weight and composition (lean/fat mass) were unaffected by PISD cKO. Several studies have reported that cold exposure can result in a reduction in leptin secretion from adipose tissue in both rodents and humans as adaptive mechanism *(Hardie et al. 1996; Trayhurn et al. 1995; Peinó et al. 2000; Ricci et al. 2000; Blondin et al. 2017; Mengel et al. 2020; Sun et al. 2020; Castellani und Tipton 2015)*. Leptin secretion is inhibited by sympathomimetic agents, and cold exposure is known to increase the sympathetic activity to adipose tissue, potentially explaining this observation *(Bing et al. 1998)*. Another potential explanation is the regulation of leptin receptors (OB-Rb). During high-fat diet feeding, leptin receptor (OB-Rb) expression is downregulated, whereas during cold exposure, it is upregulated *(Dutra et al. 2007; Priego et al. 2009)*.

Brown adipose tissue activity has been demonstrated to correlate with improved insulin resistance *(Cheng et al. 2021)*, to which leptin has been linked. It acts as a potent insulin sensitizer, thereby improving glucose tolerance *(Koch et al. 2014)*. PISD cKO mice fed HFD and housed at cold temperatures (**IV**) revealed a markedly accelerated glucose clearance in a glucose tolerance test compared to wildtype controls. This observation may, at least partly, be attributed to a reduced leptin resistance in these mice. Insulin resistance elevates the release of free fatty acids from adipose tissue, thereby inducing a higher lipid storage in the liver *(Cetin et al. 2020)*. Consequently, the improvement of insulin resistance may be a further contributing factor to the observed phenotypic changes in liver sections, including the recovery of NAFLD in iBcKO-PISD mice.

VDAC1, cytochrome c and perilipin were found to be elevated in primary brown and beige adipocytes isolated from iBcKO-PISD mice at room temperature and on chow diet, compared to the wildtype controls (**I**). Voltage-dependent anion channel 1 (VDAC1) is the most common protein in the outer mitochondrial membrane. It is linked with mitochondrial dysfunction due to its involvement in the regulation of oxidative stress and apoptosis. A number of pathological conditions and diseases have been associated with increased levels of VDAC1. For instance, post-mortem examination of the brains of Alzheimer's disease patients has revealed elevated levels of VDAC1, which lends support to the hypothesis that it plays a role in inducing cell death *(Shoshan-Barmatz et al. 2018)*. Another study has indicated, that VDAC1 is involved in insulin secretion, as an upregulation of VDAC1 in islets of diabetic patients (type 2) can be determined *(Zhang et al. 2019)*. Cytochrome C is a molecule that is involved in the electron transport chain located in the inner mitochondrial membrane. In pathological conditions associated with apoptosis and inflammation, there is an elevated release of cytochrome c into the cytoplasm and extracellular spaces *(Eleftheriadis et al. 2016)*. Consequently, the observed upregulation of both proteins in adipocytes of iBcKO-PISD mice is consistent with the histological images of cohort **I**, suggesting the presence of cellular and mitochondrial damage. Perilipin is a lipid droplet-bound

protein that promotes the interaction between lipid droplets and mitochondria. Multiple studies have revealed that perilipin overexpression results in increased lipid droplet storage, as observed here in brown adipose tissue of iBcKO-PISD mice *(Londos et al. 2005; Sztalryd und Kimmel 2014; Kimmel und Sztalryd 2014; Bickel et al. 2009)*.

4.5 THE IMPACT OF BAT LOCATED PISD FOR THE RESPIRATORY EXCHANGE RATIO

The RER is defined as the ratio between the volume of produced CO_2 and consumed O_2. This ratio provides indirect information on the relative contribution of macronutrients to energy expenditure *(Ramos-Jiménez et al. 2008)*. A lower ratio indicates a greater reliance on lipid oxidation, while a ratio approaching 1 suggests a predominant use of carbohydrates *(Pendergast et al. 2000; Simonson und DeFronzo 1990)*. As demonstrated by Symonds et al., 20% of the daily diet and/or cold exposure-induced glucose oxidation can take place in brown adipose tissue of adult humans *(Symonds et al. 2019)*. Cold-induced BAT activity has been demonstrated to improve glucose metabolism in both diabetic and lean/healthy subjects by regulating glucose homeostasis *(Hanssen et al. 2015; Hankir und Klingenspor 2018; Iwen et al. 2017)*. In addition to thermogenesis, glucose utilization pathways in brown and beige adipocytes include glycolysis, the tricarboxylic acid cycle (TCA), lipogenesis, as well as lipolysis *(Symonds et al. 2019)*. We identified that iBcKO-PISD mice fed on a chow diet exhibited a significantly higher mean respiratory exchange ratio (RER) when housed at acute cold exposure (**II**). This suggests that mice lacking PISD may metabolize more carbohydrates in UCP1-expressing cells at cold exposure in order to supply the body with energy in comparison to wildtype mice. However, a comparison of the RER curve with the development of the cage temperature raises the question of whether this observation is solely induced by cold exposure. Prior to the temperature decline in the cages (before ~15 minutes), cKO mice displayed a higher RER compared to wildtypes. As soon as the cage temperature started to descend (after ~15 minutes), the RER increased in wildtype mice. Upon reaching a temperature of 8°C (after ~2 hours), the RER began to decline. This found metabolic response is consistent with previous publications in the field. A study on human males reported, that cold exposure in the first two hours increases the reliance on carbohydrate metabolism due to the immediate energy demand for generating heat throughout shivering thermogenesis, which temporarily increases the RER *(Vallerand und Jacobs 1989)*. During periods of cold exposure, the body undergoes physiological adaptations to accommodate the external environment. Thus, a shift towards the more efficient, non-shivering thermogenesis in BAT can be observed, which is primarily fueled by the lipolysis of intracellular TAG and fatty acids derived from WAT lipolysis. This results in a decreasing respiratory exchange ratio *(Peres Valgas da Silva et al. 2019)*. In iBcKO-PISD mice, the initial rise in RER occurred at a markedly slower rate, resulting in a respiratory exchange ratio that was nearly identical between both genotypes at the end of the intervention. In cKO mice, this might lead to a higher oxidation of carbohydrates at room temperature, accompanied by a rapid switch from carbohydrate utilization towards lipid utilization during cold exposure. Since the primary fuel for non-shivering thermogenesis in BAT are free fatty acids liberated from brown or white adipocyte TAG, the fast reduction in RER of cKO mice indicates a higher level of brown adipose tissue activity upon cold exposure compared to wildtype mice.

4.6 THE RELEVANCE OF BROWN ADIPOSE TISSUE LOCATED PISD FOR LIPID METABOLISM

A downregulation of several genes involved in lipid metabolism was observed in iBcKO-PISD mice housed at room temperature (**I**), but not after cold exposure (**II**). For example, the mRNA expression of the C16 and C18 FA desaturase SCD1 and elongase ELOVL6 is downregulated. It has been previously proposed that UCP1 has a strong affinity for long chain and unsaturated C18-fatty acids *(Huang 2003)*, supporting the idea that mice lacking PISD may primarily oxidize glucose at room temperature and rather metabolize lipids at cold exposure due to an activation of BAT. Long-term cold exposure + HFD (**IV**) resulted in a notable increase in UCP1 expression.

As PISD decarboxylates PS to synthesize mitochondrial PE, it was hypothesized that an inhibition of PISD activity would result in a reduction in the generation of mitochondrial phosphatidylethanolamine. It was unexpected that mitochondria isolated from primary brown and beige adipocytes lacking PISD revealed elevated PE/PS ratios due to an increase in PE, especially PE 32:1 and PE 34:1, while PS levels decreased, especially PS 36:1 and 36:2. To date, the PISD pathway is the only known pathway for mitochondrial PE synthesis and is critical for mitochondrial function and morphology *(Steenbergen et al. 2005; Tasseva et al. 2013)*. Other pathways of PE and PS synthesis (outside of mitochondria), as well as import and export processes from ER or MAM to mitochondria, may serve to compensate for the deficient intra-mitochondrial PE synthesis observed in PISD cKO cells. Although cellular PE is primarily synthesized via the CDP-ethanolamine (Kennedy) pathway, PISD-derived PE can also be exported to the ER via endoplasmic reticulum-mitochondria contact sites (ERMCS), thereby supplying the cells with PE *(Kainu et al. 2013)*. Both PE synthesis pathways are highly efficient. In Drosophila mutants lacking the CDP-ethanolamine pathway, it was demonstrated, that inducing PISD can fully compensate for this mutation *(Zhao und Wang 2020)*. In yeast, it was reported, that Ups1 and Ups2 (PRELID3b in mammals) regulate the transfer of PE from mitochondria to the ER by either accelerating or decelerating PE to PC conversion outside of mitochondria (via PEMT), thereby maintaining normal levels of PE *(Tamura et al. 2014)*. It was further proposed that Ups1 and Ups2 are involved in the synthesis of PS and PA, which are functioning as PE precursors *(Tamura et al. 2020)*. Given that PS is not synthesized within mitochondria, but serves as a major substrate for mitochondrial PE, the import mechanisms of PS into mitochondria are essential for PISD activity. PS translocation is promoted by an increase in its synthesis outside of mitochondria. Consequently, the PS synthesis enzymes (PSS1 and PSS2) may also serve to compensate for mitochondrial PE deficiencies by elevating the substrate availability for PISD. This hypothesis is supported by the finding that a knockdown of PSS1 inhibits PS decarboxylation in mitochondria of mammalian HeLa cells *(Kainu et al. 2013)*. Our mRNA expression analysis of brown and beige adipose tissue showed a pronounced downregulation of PSS1 and PSS2, suggesting that the mitochondrial PE synthesis in iBcKO-PISD mice might not be as dependent on PS import and PISD activity as previously thought. Instead, it may be covered by alternative mechanisms. Even though the results of studies investigating the import of PE to mitochondria are contradictory, some metabolic analyses in mammalian cells indicate that PE generated in the CDP-ethanolamine pathway is transferred into mitochondria *(Bleijerveld et al. 2007; Yaffe und Kennedy 1983; Kainu et al. 2013; Camici und Corazzi 1995; Blok et al. 1971)*. It is noteworthy that the import of PE into mitochondria is facilitated by PE plasmalogens *(Kainu et al. 2013)*. Upon oxidative stress and/or when phospholipases are highly active, PE P can be converted into lyso-phosphatidylethanolamine (LPE) by cleavage of the vinyl-ether bond *(Morel et al. 2021)*. This is a process that is catalyzed by plasmalogenases. Recently, for cytochrome C a plasmalogenase activity was discovered *(Dorninger et al. 2022)*. In this work, we

determined an increased cytochrome C expression in brown adipocytes of PISD cKO mice. LPE can be re-acylated back to PE using acyltransferases (Lands cycle) *(O'Donnell 2022; LANDS 1958)*. To date, it remains unclear whether the degradation of PE P to LPE can take place in brown adipose tissue mitochondria. Our lipidomic results of primary brown and beige adipocyte mitochondria originating from iBcKO-PISD mice exhibited elevated levels of PE P (e.g. PE P 16:0/16:1, PE P 16:0/20:4, PE P 16:0/22:6 and PE P 18:1/16:1), as well as increased levels of LPE (e.g. LPE 16:1, LPE 18:1, LPE 22:6). Consequently, too low mitochondrial PE levels may be (over) compensated by PE P degradation to LPE and subsequent re-acylation to PE. The hypothesis of increased PE and PE P syntheses in ER membranes could further reduce the PE efflux of mitochondria, due to a steeper concentration gradient, making the PE export less energetically favorable.

Also, we identified a higher abundance of PA species in brown and beige adipocytes of cKO mice, which serves as a substrate for PE synthesis in the Kennedy pathway *(Gibellini und Smith 2010)*. PA derives from glycerol-3-phosphate, which is an intermediate of glycolysis *(Possik et al. 2017)*. This is in line with the elevated respiratory exchange ratio observed in PISD cKO mice at room temperature, which indicates an elevation in glucose utilization.

4.7 THE IMPORTANCE OF PISD IN BROWN ADIPOCYTES FOR UCP$_1$ ACTIVITY

The finding that GPL/FC ratios and UCP1-dependent respiration are significantly elevated in mitochondria of mice lacking PISD in UCP1-expressing cells provides further evidence that FC and phospholipids regulate UCP1 function. When the PISD cKO was induced in primary brown adipocytes, isoproterenol-induced UCP1 activity in brown adipocytes was significantly higher. This likely explains the increased thermogenic capacity observed in cold exposed iBcKO-PISD mice. Recently, Johnson and colleagues proposed that mitochondrial PE content, which is mediated by PISD activity, affects UCP1 directly by altering the proton flux through the inner mitochondrial membrane via UCP1. This was investigated by patch clamp analysis on isolated mitoplasts of brown adipose tissue originating from mice lacking PISD, which revealed a substantial reduction of the proton current compared to wildtype mice *(Johnson et al. 2023)*. This is consistent with our hypothesis of reduced thermogenic capacity in iBcKO-PISD mice at basal conditions (without isoproterenol induction). So far, it is unclear whether patch clamp analysis of mitochondria isolated from iBcKO-PISD mice housed at cold (resembling isoproterenol induction) and feeding these mice HFD would reveal contradictory results. A mechanistic explanation could be PISD regulated alterations in brown adipose tissue lipid droplet size and number (i.e. TAG storage), thereby affecting the release of free fatty acids which, in turn, might alter the UCP1-mediated proton flux.

In addition to alterations in the brown adipocyte lipid composition, UCP1 may also be regulated at the transcriptional or translational level by a PISD-dependent mechanism. In a recent study, Sugawara et al. demonstrated that the mitochondrial serine/threonine phosphatase PGAM5 inhibits the expression of UCP1 by its phosphatase and intramembrane cleavage activity, thereby suppressing energy consumption in brown adipocytes. In brown adipocytes with a knockout of PGAM5, there is an increase in oxygen consumption due to the accumulation of UCP1 protein. PISD controls PGAM5 cleavage, which was identified by executing a genome-wide siRNA screening in HeLa cells *(Sugawara et al. 2020)*. Thus, the conditional knockout of PISD may inhibit PGAM5, which could subsequently result in increased UCP1-mediated respiration.

5 CONCLUSION AND OUTLOOK

We identified a unique lipid species signature of brown adipose tissue mitochondria. The high glycerophospholipid (i.e. PC, PE) and low free cholesterol levels observed in brown compared to white adipose tissue, liver and muscle mitochondria can be related to brown adipose tissue function and adipose tissue browning as well as UCP1 activity. A mouse model having a tamoxifen-inducible knockout of PISD in UCP1 expressing cells did not only reveal elevated UCP1 activity in mice lacking PISD in brown adipose tissue upon isoproterenol induction, but also an improved whole-body metabolism in obese animals after cold stimulation.

We conclude that the mitochondrial lipid composition regulated by phosphatidylserine decarboxylase in brown adipose tissue affects the activity of UCP1 and non-shivering thermogenesis. The activity of brown adipose tissue in humans can be related to the improvement of metabolic health, including obesity and coronary artery disease *(Becher et al. 2021)*. Recent studies even provide evidence on its positive impact on other pathological conditions such as liver disease and intestinal cancer *(Seki et al. 2022; Chen and Kang 2023)*. The present thesis provides novel insights that contribute to the deciphering of the complicated and still largely elusive picture of brown adipose tissue in the light of health and disease.

In future studies, one major aim will be to decrypt mechanisms underlying the link between the mitochondrial lipidome and UCP1 function. A first step could be patch-clamp analyses to investigate the proton flux through UCP1 of BAT mitoplasts isolated from our PISD cKO mouse model after cold exposure and high lipid dietary conditions, or after incubation with SUVs containing different amounts of PC, PE and FC.

6 BIBLIOGRAPHY

Adam, Stephen A. (2016): Nuclear Protein Transport in Digitonin Permeabilized Cells. In: Methods in molecular biology (Clifton, N.J.) 1411, S. 479–487. DOI: 10.1007/978-1-4939-3530-7_29.

Afzal, Nasrin; Lederer, W. Jonathan; Jafri, M. Saleet; Mannella, Carmen A. (2021): Effect of crista morphology on mitochondrial ATP output: A computational study. In: Current research in physiology 4, S. 163–176. DOI: 10.1016/j.crphys.2021.03.005.

Ahmed, Basma A.; Ong, Frank J.; Barra, Nicole G.; Blondin, Denis P.; Gunn, Elizabeth; Oreskovich, Stephan M. et al. (2021): Lower brown adipose tissue activity is associated with non-alcoholic fatty liver disease but not changes in the gut microbiota. In: Cell reports. Medicine 2 (9), S. 100397. DOI: 10.1016/j.xcrm.2021.100397.

Arch, Jonathan R. S. (2008): The discovery of drugs for obesity, the metabolic effects of leptin and v 1ariable receptor pharmacology: perspectives from beta3-adrenoceptor agonists. In: Naunyn-Schmiedeberg's archives of pharmacology 378 (2), S. 225–240. DOI: 10.1007/s00210-008-0271-1. Arikketh, Devi; Nelson, Randy; Vance, Jean E. (2008): Defining the importance of phosphatidylserine synthase-1 (PSS1): unexpected viability of PSS1-deficient mice. In: The Journal of biological chemistry 283 (19), S. 12888–12897. DOI: 10.1074/jbc.M800714200.

Arner, Peter; Langin, Dominique (2014): Lipolysis in lipid turnover, cancer cachexia, and obesity-induced insulin resistance. In: Trends in endocrinology and metabolism: TEM 25 (5), S. 255–262. DOI: 10.1016/j.tem.2014.03.002.

Asif, Kanwal; Memeo, Lorenzo; Palazzolo, Stefano; Frión-Herrera, Yahima; Parisi, Salvatore; Caligiuri, Isabella et al. (2021): STARD3: A Prospective Target for Cancer Therapy. In: Cancers 13 (18). DOI: 10.3390/cancers13184693.

Baker, Michael J.; Tatsuta, Takashi; Langer, Thomas (2011): Quality control of mitochondrial proteostasis. In: Cold Spring Harbor perspectives in biology 3 (7). DOI: 10.1101/cshperspect.a007559.

Bal, Naresh C.; Maurya, Santosh K.; Sopariwala, Danesh H.; Sahoo, Sanjaya K.; Gupta, Subash C.; Shaikh, Sana A. et al. (2012): Sarcolipin is a newly identified regulator of muscle-based thermogenesis in mammals. In: Nature medicine 18 (10), S. 1575–1579. DOI: 10.1038/nm.2897.

Balaz, Miroslav; Becker, Anton S.; Balazova, Lucia; Straub, Leon; Müller, Julian; Gashi, Gani et al. (2019): Inhibition of Mevalonate Pathway Prevents Adipocyte Browning in Mice and Men by Affecting Protein Prenylation. In: Cell metabolism 29 (4), 901-916.e8. DOI: 10.1016/j.cmet.2018.11.017.

Balboa, Elisa; Castro, Juan; Pinochet, María-José; Cancino, Gonzalo I.; Matías, Nuria; Sáez, P. J. et al. (2017): MLN64 induces mitochondrial dysfunction associated with increased mitochondrial cholesterol content. In: Redox biology 12, S. 274–284. DOI: 10.1016/j.redox.2017.02.024.

Ballinger, Scott W. (2005): Mitochondrial dysfunction in cardiovascular disease. In: Free radical biology & medicine 38 (10), S. 1278–1295. DOI: 10.1016/j.freeradbiomed.2005.02.014.

Barman, Subrata; Nayak, Debi P. (2007): Lipid raft disruption by cholesterol depletion enhances influenza A virus budding from MDCK cells. In: Journal of virology 81 (22), S. 12169–12178. DOI: 10.1128/JVI.00835-07.

Bartelt, Alexander; Bruns, Oliver T.; Reimer, Rudolph; Hohenberg, Heinz; Ittrich, Harald; Peldschus, Kersten et al. (2011): Brown adipose tissue activity controls triglyceride clearance. In: Nature medicine 17 (2), S. 200–205. DOI: 10.1038/nm.2297.

Becher T, Palanisamy S, Kramer DJ, Eljalby M, Marx SJ, Wibmer AG, Butler SD, Jiang CS, Vaughan R, Schöder H, Mark A, Cohen P, 2021. Brown adipose tissue is associated with cardiometabolic health. Nature medicine, 27 (1), 58–65.

Berbée, Jimmy F. P.; Boon, Mariëtte R.; Khedoe, P. Padmini S. J.; Bartelt, Alexander; Schlein, Christian; Worthmann, Anna et al. (2015): Brown fat activation reduces hypercholesterolaemia and protects from atherosclerosis development. In: Nature communications 6, S. 6356. DOI: 10.1038/ncomms7356.

Bian, Yangyang; Zheng, Runsheng; Bayer, Florian P.; Wong, Cassandra; Chang, Yun-Chien; Meng, Chen et al. (2020): Robust, reproducible and quantitative analysis of thousands of proteomes by micro-flow LC-MS/MS. In: Nature communications 11 (1), S. 157. DOI: 10.1038/s41467-019-13973-x.

Biau, Gérard (2010): Analysis of a Random Forests Model.

Bickel, Perry E.; Tansey, John T.; Welte, Michael A. (2009): PAT proteins, an ancient family of lipid droplet proteins that regulate cellular lipid stores. In: Biochimica et biophysica acta 1791 (6), S. 419–440. DOI: 10.1016/j.bbalip.2009.04.002.

Bing, C.; Frankish, H. M.; Pickavance, L.; Wang, Q.; Hopkins, D. F.; Stock, M. J.; Williams, G. (1998): Hyperphagia in cold-exposed rats is accompanied by decreased plasma leptin but unchanged hypothalamic NPY. In: The American journal of physiology 274 (1), R62-8. DOI: 10.1152/ajpregu.1998.274.1.R62.

Birner, R.; Bürgermeister, M.; Schneiter, R.; Daum, G. (2001): Roles of phosphatidylethanolamine and of its several biosynthetic pathways in Saccharomyces cerevisiae. In: Molecular biology of the cell 12 (4), S. 997–1007. DOI: 10.1091/mbc.12.4.997.

Bleijerveld, Onno B.; Brouwers, Jos F. H. M.; Vaandrager, Arie B.; Helms, J. Bernd; Houweling, Martin (2007): The CDP-ethanolamine pathway and phosphatidylserine decarboxylation generate different phosphatidylethanolamine molecular species. In: The Journal of biological chemistry 282 (39), S. 28362–28372. DOI: 10.1074/jbc.M703786200.

BLIGH, E. G.; DYER, W. J. (1959): A rapid method of total lipid extraction and purification. In: Canadian journal of biochemistry and physiology 37 (8), S. 911–917. DOI: 10.1139/o59-099.

Blok, M. C.; Wirtz, K. W.; Scherphof, G. L. (1971): Exchange of phospholipids between microsomes and inner and outer mitochondrial membranes of rat liver. In: Biochimica et biophysica acta 233 (1), S. 61–75. DOI: 10.1016/0005-2736(71)90358-0.

Blondin, Denis P.; Frisch, Frédérique; Phoenix, Serge; Guérin, Brigitte; Turcotte, Éric E.; Haman, François et al. (2017): Inhibition of Intracellular Triglyceride Lipolysis Suppresses Cold-Induced Brown Adipose Tissue Metabolism and Increases Shivering in Humans. In: Cell metabolism 25 (2), S. 438–447. DOI: 10.1016/j.cmet.2016.12.005.

Blondin, Denis P.; Nielsen, Soren; Kuipers, Eline N.; Severinsen, Mai C.; Jensen, Verena H.; Miard, Stéphanie et al. (2020): Human Brown Adipocyte Thermogenesis Is Driven by β2-AR Stimulation. In: Cell metabolism 32 (2), 287-300.e7. DOI: 10.1016/j.cmet.2020.07.005.

Bouillaud, F.; Ricquier, D.; Mory, G.; Thibault, J. (1984): Increased level of mRNA for the uncoupling protein in brown adipose tissue of rats during thermogenesis induced by cold exposure or norepinephrine infusion. In: The Journal of biological chemistry 259 (18), S. 11583–11586.

Breiman, Leo (2001). In: Machine Learning 45 (1), S. 5–32. DOI: 10.1023/A:1010933404324.

Breining, Peter; Jensen, Jonas B.; Sundelin, Elias I.; Gormsen, Lars C.; Jakobsen, Steen; Busk, Morten et al. (2018): Metformin targets brown adipose tissue in vivo and reduces oxygen consumption in vitro. In: Diabetes, obesity & metabolism 20 (9), S. 2264–2273. DOI: 10.1111/dom.13362.

Brown, Michael S.; Goldstein, Joseph L. (2009): Cholesterol feedback: from Schoenheimer's bottle to Scap's MELADL. In: Journal of lipid research 50 Suppl (Suppl), S15-27. DOI: 10.1194/jlr.R800054-JLR200.

Brunaldi, Kellen; Miranda, Manoel Arcisio; Abdulkader, Fernando; Curi, Rui; Procopio, Joaquim (2005): Fatty acid flip-flop and proton transport determined by short-circuit current in planar bilayers. In: Journal of lipid research 46 (2), S. 245–251. DOI: 10.1194/jlr.M400155-JLR200.

Bürgermeister, Maria; Birner-Grünberger, Ruth; Nebauer, Ruth; Daum, Günther (2004): Contribution of different pathways to the supply of phosphatidylethanolamine and phosphatidylcholine to mitochondrial membranes of the yeast Saccharomyces cerevisiae. In: Biochimica et biophysica acta 1686 (1-2), S. 161–168. DOI: 10.1016/j.bbalip.2004.09.007.

Camici, O.; Corazzi, L. (1995): Import of phosphatidylethanolamine for the assembly of rat brain mitochondrial membranes. In: The Journal of membrane biology 148 (2), S. 169–176. DOI: 10.1007/BF00207272.

Cannon, Barbara; Nedergaard, Jan (2004): Brown adipose tissue: function and physiological significance. In: Physiological reviews 84 (1), S. 277–359. DOI: 10.1152/physrev.00015.2003.

Cannon, Barbara; Nedergaard, Jan (2017): What Ignites UCP1? In: Cell metabolism 26 (5), S. 697–698. DOI: 10.1016/j.cmet.2017.10.012.

Carper, Deborah; Coué, Marine; Nascimento, Emmani B. M.; Barquissau, Valentin; Lagarde, Damien; Pestourie, Carine et al. (2020): Atrial Natriuretic Peptide Orchestrates a Coordinated Physiological Response to Fuel Non-shivering Thermogenesis. In: Cell reports 32 (8), S. 108075. DOI: 10.1016/j.celrep.2020.108075.

Casares, Doralicia; Escribá, Pablo V.; Rosselló, Catalina Ana (2019): Membrane Lipid Composition: Effect on Membrane and Organelle Structure, Function and Compartmentalization and Therapeutic Avenues. In: International journal of molecular sciences 20 (9). DOI: 10.3390/ijms20092167.

Castellani, John W.; Tipton, Michael J. (2015): Cold Stress Effects on Exposure Tolerance and Exercise Performance. In: Comprehensive Physiology 6 (1), S. 443–469. DOI: 10.1002/cphy.c140081.

Cates, Charles C.; McCabe, James G.; Lawson, Gregory W.; Couto, Marcelo A. (2014): Core body temperature as adjunct to endpoint determination in murine median lethal dose testing of rattlesnake venom. In: Comparative medicine 64 (6), S. 440–447.

Cetin, Elif Guven; Demir, Nazan; Sen, Ilker (2020): The Relationship between Insulin Resistance and Liver Damage in non-alcoholic Fatty Liver Patients. In: Sisli Etfal Hastanesi tip bulteni 54 (4), S. 411–415. DOI: 10.14744/SEMB.2018.83604.

Chacinska, Agnieszka; Koehler, Carla M.; Milenkovic, Dusanka; Lithgow, Trevor; Pfanner, Nikolaus (2009): Importing mitochondrial proteins: machineries and mechanisms. In: Cell 138 (4), S. 628–644. DOI: 10.1016/j.cell.2009.08.005.

Chan, David C. (2012): Fusion and fission: interlinked processes critical for mitochondrial health. In: Annual review of genetics 46, S. 265–287. DOI: 10.1146/annurev-genet-110410-132529.

Chang, Ji Suk (2023): Recent insights into the molecular mechanisms of simultaneous fatty acid oxidation and synthesis in brown adipocytes. In: Frontiers in endocrinology 14, S. 1106544. DOI: 10.3389/fendo.2023.1106544.

Chapman, James; Fielder, Edward; Passos, João F. (2019): Mitochondrial dysfunction and cell senescence: deciphering a complex relationship. In: FEBS letters 593 (13), S. 1566–1579. DOI: 10.1002/1873-3468.13498.

Chartoumpekis, Dionysios V.; Habeos, Ioannis G.; Ziros, Panos G.; Psyrogiannis, Agathoklis I.; Kyriazopoulou, Venetsana E.; Papavassiliou, Athanasios G. (2011): Brown adipose tissue responds to cold and adrenergic stimulation by induction of FGF21. In: Molecular medicine (Cambridge, Mass.) 17 (7-8), S. 736–740. DOI: 10.2119/molmed.2011.00075.

Chen Z, Kang Y, 2023. Cold snap for cancer: cold-induced brown fat thermogenesis starves tumor growth. Signal transduction and targeted therapy, 8 (1), 10.

Cheng, Long; Wang, Jingkang; Dai, Hongyu; Duan, Yuhui; An, Yongcheng; Shi, Lu et al. (2021): Brown and beige adipose tissue: a novel therapeutic strategy for obesity and type 2 diabetes mellitus. In: Adipocyte 10 (1), S. 48–65. DOI: 10.1080/21623945.2020.1870060.

Chiu, Yi-Chou; Chu, Pei-Wen; Lin, Hua-Ching; Chen, Shau-Kwaun (2021): Accumulation of cholesterol suppresses oxidative phosphorylation and altered responses to inflammatory stimuli of macrophages. In: Biochemistry and biophysics reports 28, S. 101166. DOI: 10.1016/j.bbrep.2021.101166.

Chu, Charleen T.; Ji, Jing; Dagda, Ruben K.; Jiang, Jian Fei; Tyurina, Yulia Y.; Kapralov, Alexandr A. et al. (2013): Cardiolipin externalization to the outer mitochondrial membrane acts as an elimination signal for mitophagy in neuronal cells. In: Nature cell biology 15 (10), S. 1197–1205. DOI: 10.1038/ncb2837.

Cinti, Saverio (2012): The adipose organ at a glance. In: Disease models & mechanisms 5 (5), S. 588–594. DOI: 10.1242/dmm.009662.

Clancey, C. J.; Chang, S. C.; Dowhan, W. (1993): Cloning of a gene (PSD1) encoding phosphatidylserine decarboxylase from Saccharomyces cerevisiae by complementation of an Escherichia coli mutant. In: The Journal of biological chemistry 268 (33), S. 24580–24590.

Clark, Samantha T.; Arras, Matthias M. L.; Sarles, Stephen A.; Frymier, Paul D. (2020): Lipid shape determination of detergent solubilization in mixed-lipid liposomes. In: Colloids and surfaces. B, Biointerfaces 187, S. 110609. DOI: 10.1016/j.colsurfb.2019.110609.

Cohen, Paul; Kajimura, Shingo (2021): The cellular and functional complexity of thermogenic fat. In: Nature reviews. Molecular cell biology 22 (6), S. 393–409. DOI: 10.1038/s41580-021-00350-0.

Cole, Laura K.; Vance, Dennis E. (2010): A role for Sp1 in transcriptional regulation of phosphatidylethanolamine N-methyltransferase in liver and 3T3-L1 adipocytes. In: The Journal of biological chemistry 285 (16), S. 11880–11891. DOI: 10.1074/jbc.M110.109843.

Collins, S.; Yehuda-Shnaidman, E.; Wang, H. (2010): Positive and negative control of Ucp1 gene transcription and the role of β-adrenergic signaling networks. In: International journal of obesity (2005) 34 Suppl 1, S28-33. DOI: 10.1038/ijo.2010.180.

Cox, Jürgen; Mann, Matthias (2008): MaxQuant enables high peptide identification rates, individualized p.p.b.-range mass accuracies and proteome-wide protein quantification. In: Nature biotechnology 26 (12), S. 1367–1372. DOI: 10.1038/nbt.1511.

Cristancho, Ana G.; Lazar, Mitchell A. (2011): Forming functional fat: a growing understanding of adipocyte differentiation. In: Nature reviews. Molecular cell biology 12 (11), S. 722–734. DOI: 10.1038/nrm3198.

Cypess, Aaron M.; Lehman, Sanaz; Williams, Gethin; Tal, Ilan; Rodman, Dean; Goldfine, Allison B. et al. (2009): Identification and importance of brown adipose tissue in adult humans. In: The New England journal of medicine 360 (15), S. 1509–1517. DOI: 10.1056/NEJMoa0810780.

D'Arrigo, Paola; Servi, Stefano (2010): Synthesis of lysophospholipids. In: Molecules (Basel, Switzerland) 15 (3), S. 1354–1377. DOI: 10.3390/molecules15031354.

Després, Jean-Pierre; Lemieux, Isabelle (2006): Abdominal obesity and metabolic syndrome. In: Nature 444 (7121), S. 881–887. DOI: 10.1038/nature05488.

Dieterle, Frank; Ross, Alfred; Schlotterbeck, Götz; Senn, Hans (2006): Probabilistic quotient normalization as robust method to account for dilution of complex biological mixtures. Application in 1H NMR metabonomics. In: Analytical chemistry 78 (13), S. 4281–4290. DOI: 10.1021/ac051632c.

Dolis, D.; Kroon, A. I. de; Kruijff, B. de (1996): Transmembrane movement of phosphatidylcholine in mitochondrial outer membrane vesicles. In: The Journal of biological chemistry 271 (20), S. 11879–11883. DOI: 10.1074/jbc.271.20.11879.

Dorninger, Fabian; Werner, Ernst R.; Berger, Johannes; Watschinger, Katrin (2022): Regulation of plasmalogen metabolism and traffic in mammals: The fog begins to lift. In: Frontiers in cell and developmental biology 10, S. 946393. DOI: 10.3389/fcell.2022.946393.

Duan, Yajun; Gong, Ke; Xu, Suowen; Zhang, Feng; Meng, Xianshe; Han, Jihong (2022): Regulation of cholesterol homeostasis in health and diseases: from mechanisms to targeted therapeutics. In: Signal transduction and targeted therapy 7 (1), S. 265. DOI: 10.1038/s41392-022-01125-5.

Dutra, Rafael Cypriano (2017): Kinin receptors: Key regulators of autoimmunity. In: Autoimmunity reviews 16 (2), S. 192–207. DOI: 10.1016/j.autrev.2016.12.011.

Dutra, S. C. P.; Moura, E. G.; Rodrigues, A. L.; Lisboa, P. C.; Bonomo, I.; Toste, F. P.; Passos, M. C. F. (2007): Cold exposure restores the decrease in leptin receptors (OB-Rb) caused by neonatal leptin treatment in 30-day-old rats. In: The Journal of endocrinology 195 (2), S. 351–358. DOI: 10.1677/JOE-07-0366.

Dykxhoorn, Derek M.; Novina, Carl D.; Sharp, Phillip A. (2003): Killing the messenger: short RNAs that silence gene expression. In: Nature reviews. Molecular cell biology 4 (6), S. 457–467. DOI: 10.1038/nrm1129.

Ebeling, P.; Koistinen, H. A.; Koivisto, V. A. (1998): Insulin-independent glucose transport regulates insulin sensitivity. In: FEBS letters 436 (3), S. 301–303. DOI: 10.1016/s0014-5793(98)01149-1.

Eckel, Robert H.; Grundy, Scott M.; Zimmet, Paul Z. (2005): The metabolic syndrome. In: Lancet (London, England) 365 (9468), S. 1415–1428. DOI: 10.1016/S0140-6736(05)66378-7.

Ecker, Josef; Benedetti, Elisa; Kindt, Alida S. D.; Höring, Marcus; Perl, Markus; Machmüller, Andrea Christel et al. (2021): The Colorectal Cancer Lipidome: Identification of a Robust Tumor-Specific Lipid Species Signature. In: Gastroenterology 161 (3), 910-923.e19. DOI: 10.1053/j.gastro.2021.05.009.

Eleftheriadis, Theodoros; Pissas, Georgios; Liakopoulos, Vassilios; Stefanidis, Ioannis (2016): Cytochrome c as a Potentially Clinical Useful Marker of Mitochondrial and Cellular Damage. In: Frontiers in immunology 7, S. 279. DOI: 10.3389/fimmu.2016.00279.

Elustondo, Pia; Martin, Laura A.; Karten, Barbara (2017): Mitochondrial cholesterol import. In: Biochimica et biophysica acta. Molecular and cell biology of lipids 1862 (1), S. 90–101. DOI: 10.1016/j.bbalip.2016.08.012.

Emanuelli, Brice; Vienberg, Sara G.; Smyth, Graham; Cheng, Christine; Stanford, Kristin I.; Arumugam, Manimozhiyan et al. (2014): Interplay between FGF21 and insulin action in the liver regulates metabolism. In: The Journal of clinical investigation 124 (2), S. 515–527. DOI: 10.1172/JCI67353.

Emont, Margo P.; Jacobs, Christopher; Essene, Adam L.; Pant, Deepti; Tenen, Danielle; Colleluori, Georgia et al. (2023): Author Correction: A single-cell atlas of human and mouse white adipose tissue. In: Nature 620 (7973), E14. DOI: 10.1038/s41586-023-06445-2.

Enerbäck, S.; Jacobsson, A.; Simpson, E. M.; Guerra, C.; Yamashita, H.; Harper, M. E.; Kozak, L. P. (1997): Mice lacking mitochondrial uncoupling protein are cold-sensitive but not obese. In: Nature 387 (6628), S. 90–94. DOI: 10.1038/387090a0.

English, J. T.; Patel, S. K.; Flanagan, M. J. (1973): Association of pheochromocytomas with brown fat tumors. In: Radiology 107 (2), S. 279–281. DOI: 10.1148/107.2.279.

Ernst, Robert; Ejsing, Christer S.; Antonny, Bruno (2016): Homeoviscous Adaptation and the Regulation of Membrane Lipids. In: Journal of molecular biology 428 (24 Pt A), S. 4776–4791. DOI: 10.1016/j.jmb.2016.08.013.

Esteve Ràfols, Montserrat (2014): Adipose tissue: cell heterogeneity and functional diversity. In: Endocrinologia y nutricion: organo de la Sociedad Espanola de Endocrinologia y Nutricion 61 (2), S. 100–112. DOI: 10.1016/j.endonu.2013.03.011.

Fadeel, Bengt; Xue, Ding (2009): The ins and outs of phospholipid asymmetry in the plasma membrane: roles in health and disease. In: Critical reviews in biochemistry and molecular biology 44 (5), S. 264–277. DOI: 10.1080/10409230903193307.

Fadok, V. A.; Bratton, D. L.; Frasch, S. C.; Warner, M. L.; Henson, P. M. (1998): The role of phosphatidylserine in recognition of apoptotic cells by phagocytes. In: Cell death and differentiation 5 (7), S. 551–562. DOI: 10.1038/sj.cdd.4400404.

Fan, Helen Y.; Heerklotz, Heiko (2017): Digitonin does not flip across cholesterol-poor membranes. In: Journal of colloid and interface science 504, S. 283–293. DOI: 10.1016/j.jcis.2017.05.034.

Fedorenko, Andriy; Lishko, Polina V.; Kirichok, Yuriy (2012): Mechanism of fatty-acid-dependent UCP1 uncoupling in brown fat mitochondria. In: Cell 151 (2), S. 400–413. DOI: 10.1016/j.cell.2012.09.010.

Feldmann, Helena M.; Golozoubova, Valeria; Cannon, Barbara; Nedergaard, Jan (2009): UCP1 ablation induces obesity and abolishes diet-induced thermogenesis in mice exempt from thermal stress by living at thermoneutrality. In: Cell metabolism 9 (2), S. 203–209. DOI: 10.1016/j.cmet.2008.12.014.

Flis, Vid V.; Daum, Günther (2013): Lipid transport between the endoplasmic reticulum and mitochondria. In: Cold Spring Harbor perspectives in biology 5 (6). DOI: 10.1101/cshperspect.a013235.

Frank, S.; Gaume, B.; Bergmann-Leitner, E. S.; Leitner, W. W.; Robert, E. G.; Catez, F. et al. (2001): The role of dynamin-related protein 1, a mediator of mitochondrial fission, in apoptosis. In: Developmental cell 1 (4), S. 515–525. DOI: 10.1016/s1534-5807(01)00055-7.

Frederich, R. C.; Hamann, A.; Anderson, S.; Löllmann, B.; Lowell, B. B.; Flier, J. S. (1995): Leptin levels reflect body lipid content in mice: evidence for diet-induced resistance to leptin action. In: Nature medicine 1 (12), S. 1311–1314. DOI: 10.1038/nm1295-1311.

Friedman, Jonathan R.; Kannan, Muthukumar; Toulmay, Alexandre; Jan, Calvin H.; Weissman, Jonathan S.; Prinz, William A.; Nunnari, Jodi (2018): Lipid Homeostasis Is Maintained by Dual Targeting of the Mitochondrial PE Biosynthesis Enzyme to the ER. In: Developmental cell 44 (2), 261-270.e6. DOI: 10.1016/j.devcel.2017.11.023.

Fujimoto, Y.; Nishioka, K.; Hase, Y.; Sado, K.; Fujita, T. (1988): Triacylglycerol lipase-mediated release of arachidonic acid for renal medullary prostaglandin synthesis. In: Archives of biochemistry and biophysics 261 (2), S. 368–374. DOI: 10.1016/0003-9861(88)90352-9.

Fülöp, T.; Douziech, N.; Goulet, A. C.; Desgeorges, S.; Linteau, A.; Lacombe, G.; Dupuis, G. (2001): Cyclodextrin modulation of T lymphocyte signal transduction with aging. In: Mechanisms of ageing and development 122 (13), S. 1413–1430. DOI: 10.1016/s0047-6374(01)00274-3.

Galarraga, Miguel; Campión, Javier; Muñoz-Barrutia, Arrate; Boqué, Noemí; Moreno, Haritz; Martínez, José Alfredo et al. (2012): Adiposoft: automated software for the analysis of white adipose tissue cellularity in histological sections. In: Journal of lipid research 53 (12), S. 2791–2796. DOI: 10.1194/jlr.D023788.

Garlid, K. D.; Jabůrek, M.; Jezek, P. (1998): The mechanism of proton transport mediated by mitochondrial uncoupling proteins. In: FEBS letters 438 (1-2), S. 10–14. DOI: 10.1016/s0014-5793(98)01246-0.

Ge, Xuan; Chen, Cheng; Hui, Xiaoyan; Wang, Yu; Lam, Karen S. L.; Xu, Aimin (2011): Fibroblast growth factor 21 induces glucose transporter-1 expression through activation of the serum response factor/Ets-like protein-1 in adipocytes. In: The Journal of biological chemistry 286 (40), S. 34533–34541. DOI: 10.1074/jbc.M111.248591.

Gebert, Natalia; Joshi, Amit S.; Kutik, Stephan; Becker, Thomas; McKenzie, Matthew; Guan, Xue Li et al. (2009): Mitochondrial cardiolipin involved in outer-membrane protein biogenesis: implications for Barth syndrome. In: Current biology : CB 19 (24), S. 2133–2139. DOI: 10.1016/j.cub.2009.10.074.

Gellerich, F. N.; Trumbeckaite, S.; Opalka, J. R.; Seppet, E.; Rasmussen, H. N.; Neuhoff, C.; Zierz, S. (2000): Function of the mitochondrial outer membrane as a diffusion barrier in health and diseases. In: Biochemical Society transactions 28 (2), S. 164–169. DOI: 10.1042/bst0280164.

Giacomello, M.; Pellegrini, L. (2016): The coming of age of the mitochondria-ER contact: a matter of thickness. In: Cell death and differentiation 23 (9), S. 1417–1427. DOI: 10.1038/cdd.2016.52.

Giacomello, Marta; Pyakurel, Aswin; Glytsou, Christina; Scorrano, Luca (2020): The cell biology of mitochondrial membrane dynamics. In: Nature reviews. Molecular cell biology 21 (4), S. 204–224. DOI: 10.1038/s41580-020-0210-7.

Gibellini, Federica; Smith, Terry K. (2010): The Kennedy pathway--De novo synthesis of phosphatidylethanolamine and phosphatidylcholine. In: IUBMB life 62 (6), S. 414–428. DOI: 10.1002/iub.337.

Giles, Daniel A.; Moreno-Fernandez, Maria E.; Stankiewicz, Traci E.; Graspeuntner, Simon; Cappelletti, Monica; Wu, David et al. (2017): Thermoneutral housing exacerbates nonalcoholic fatty liver disease in mice and allows for sex-independent disease modeling. In: Nature medicine 23 (7), S. 829–838. DOI: 10.1038/nm.4346.

Girousse, A.; Langin, D. (2012): Adipocyte lipases and lipid droplet-associated proteins: insight from transgenic mouse models. In: International journal of obesity (2005) 36 (4), S. 581–594. DOI: 10.1038/ijo.2011.113.

Gomes, Ligia C.; Di Benedetto, Giulietta; Scorrano, Luca (2011): During autophagy mitochondria elongate, are spared from degradation and sustain cell viability. In: Nature cell biology 13 (5), S. 589–598. DOI: 10.1038/ncb2220.

Greenberg, A. S.; Shen, W. J.; Muliro, K.; Patel, S.; Souza, S. C.; Roth, R. A.; Kraemer, F. B. (2001): Stimulation of lipolysis and hormone-sensitive lipase via the extracellular signal-regulated kinase pathway. In: The Journal of biological chemistry 276 (48), S. 45456–45461. DOI: 10.1074/jbc.M104436200.

Hagen, T.; Lowell, B. B. (2000): Chimeric proteins between UCP1 and UCP3: the middle third of UCP1 is necessary and sufficient for activation by fatty acids. In: Biochemical and biophysical research communications 276 (2), S. 642–648. DOI: 10.1006/bbrc.2000.3535.

Hankir, Mohammed K.; Klingenspor, Martin (2018): Brown adipocyte glucose metabolism: a heated subject. In: EMBO reports 19 (9). DOI: 10.15252/embr.201846404.

Hannon, Gregory J.; Rossi, John J. (2004): Unlocking the potential of the human genome with RNA interference. In: Nature 431 (7006), S. 371–378. DOI: 10.1038/nature02870.

Hanssen, Mark J. W.; Hoeks, Joris; Brans, Boudewijn; van der Lans, Anouk A. J. J.; Schaart, Gert; van den Driessche, José J. et al. (2015): Short-term cold acclimation improves insulin sensitivity in patients with type 2 diabetes mellitus. In: Nature medicine 21 (8), S. 863–865. DOI: 10.1038/nm.3891.

Hardie, L. J.; Rayner, D. V.; Holmes, S.; Trayhurn, P. (1996): Circulating leptin levels are modulated by fasting, cold exposure and insulin administration in lean but not Zucker (fa/fa) rats as measured by ELISA. In: Biochemical and biophysical research communications 223 (3), S. 660–665. DOI: 10.1006/bbrc.1996.0951.

Hauser, H.; Gains, N. (1982): Spontaneous vesiculation of phospholipids: a simple and quick method of forming unilamellar vesicles. In: Proceedings of the National Academy of Sciences of the United States of America 79 (6), S. 1683–1687. DOI: 10.1073/pnas.79.6.1683.

Heikinheimo, L.; Somerharju, P. (1998): Preferential decarboxylation of hydrophilic phosphatidylserine species in cultured cells. Implications on the mechanism of transport to mitochondria and cellular aminophospholipid species compositions. In: The Journal of biological chemistry 273 (6), S. 3327–3335. DOI: 10.1074/jbc.273.6.3327.

Herranz, Nicolás; Gil, Jesús (2016): Mitochondria and senescence: new actors for an old play. In: The EMBO journal 35 (7), S. 701–702. DOI: 10.15252/embj.201694025.

Himms-Hagen, J.; Cui, J.; Danforth, E.; Taatjes, D. J.; Lang, S. S.; Waters, B. L.; Claus, T. H. (1994): Effect of CL-316,243, a thermogenic beta 3-agonist, on energy balance and brown and white adipose tissues in rats. In: The American journal of physiology 266 (4 Pt 2), R1371-82. DOI: 10.1152/ajpregu.1994.266.4.R1371.

Himms-Hagen, J.; Melnyk, A.; Zingaretti, M. C.; Ceresi, E.; Barbatelli, G.; Cinti, S. (2000): Multilocular fat cells in WAT of CL-316243-treated rats derive directly from white adipocytes. In: American journal of physiology. Cell physiology 279 (3), C670-81. DOI: 10.1152/ajpcell.2000.279.3.C670.

Horibata, Yasuhiro; Ando, Hiromi; Zhang, Peixiang; Vergnes, Laurent; Aoyama, Chieko; Itoh, Masahiko et al. (2016): StarD7 Protein Deficiency Adversely Affects the Phosphatidylcholine Composition, Respiratory Activity, and Cristae Structure of Mitochondria. In: The Journal of biological chemistry 291 (48), S. 24880–24891. DOI: 10.1074/jbc.M116.736793.

Horibata, Yasuhiro; Sugimoto, Hiroyuki (2010): StarD7 mediates the intracellular trafficking of phosphatidylcholine to mitochondria. In: The Journal of biological chemistry 285 (10), S. 7358–7365. DOI: 10.1074/jbc.M109.056960.

Höring, Marcus; Ejsing, Christer S.; Hermansson, Martin; Liebisch, Gerhard (2019): Quantification of Cholesterol and Cholesteryl Ester by Direct Flow Injection High-Resolution Fourier Transform Mass Spectrometry Utilizing Species-Specific Response Factors. In: Analytical chemistry 91 (5), S. 3459–3466. DOI: 10.1021/acs.analchem.8b05013.

Höring, Marcus; Ejsing, Christer S.; Krautbauer, Sabrina; Ertl, Verena M.; Burkhardt, Ralph; Liebisch, Gerhard (2021): Accurate quantification of lipid species affected by isobaric overlap in Fourier-transform mass spectrometry. In: Journal of lipid research 62, S. 100050. DOI: 10.1016/j.jlr.2021.100050.

Hörl, Gerd; Wagner, Andrea; Cole, Laura K.; Malli, Roland; Reicher, Helga; Kotzbeck, Petra et al. (2011): Sequential synthesis and methylation of phosphatidylethanolamine promote lipid droplet biosynthesis and stability in tissue culture and in vivo. In: The Journal of biological chemistry 286 (19), S. 17338–17350. DOI: 10.1074/jbc.M111.234534.

Huang, Shu-Gui (2003): Binding of fatty acids to the uncoupling protein from brown adipose tissue mitochondria. In: Archives of biochemistry and biophysics 412 (1), S. 142–146. DOI: 10.1016/s0003-9861(03)00031-6.

Ikeda, Kenji; Maretich, Pema; Kajimura, Shingo (2018): The Common and Distinct Features of Brown and Beige Adipocytes. In: Trends in endocrinology and metabolism: TEM 29 (3), S. 191–200. DOI: 10.1016/j.tem.2018.01.001.

Ikeda, Kenji; Yamada, Tetsuya (2020): UCP1 Dependent and Independent Thermogenesis in Brown and Beige Adipocytes. In: Frontiers in endocrinology 11, S. 498. DOI: 10.3389/fendo.2020.00498.

Ishigaki, Yasushi; Katagiri, Hideki; Yamada, Tetsuya; Ogihara, Takehide; Imai, Junta; Uno, Kenji et al. (2005): Dissipating excess energy stored in the liver is a potential treatment strategy for diabetes associated with obesity. In: Diabetes 54 (2), S. 322–332. DOI: 10.2337/diabetes.54.2.322.

Isidor, Marie S.; Winther, Sally; Basse, Astrid L.; Petersen, M. Christine H.; Cannon, Barbara; Nedergaard, Jan; Hansen, Jacob B. (2016): An siRNA-based method for efficient silencing of gene expression in mature brown adipocytes. In: Adipocyte 5 (2), S. 175–185. DOI: 10.1080/21623945.2015.1111972.

Iwen, K. Alexander; Backhaus, Jenny; Cassens, Melanie; Waltl, Maren; Hedesan, Oana C.; Merkel, Martin et al. (2017): Cold-Induced Brown Adipose Tissue Activity Alters Plasma Fatty Acids and Improves Glucose Metabolism in Men. In: The Journal of clinical endocrinology and metabolism 102 (11), S. 4226–4234. DOI: 10.1210/jc.2017-01250.

Jennings, William; Epand, Richard M. (2020): CDP-diacylglycerol, a critical intermediate in lipid metabolism. In: Chemistry and physics of lipids 230, S. 104914. DOI: 10.1016/j.chemphyslip.2020.104914.

Johnson, Jordan M.; Peterlin, Alek D.; Balderas, Enrique; Sustarsic, Elahu G.; Maschek, J. Alan; Lang, Marisa J. et al. (2023): Mitochondrial phosphatidylethanolamine modulates UCP1 to promote brown adipose thermogenesis. In: Science advances 9 (8), eade7864. DOI: 10.1126/sciadv.ade7864.

Johnson, Jordan M.; Verkerke, Anthony R. P.; Maschek, J. Alan; Ferrara, Patrick J.; Lin, Chien-Te; Kew, Kimberly A. et al. (2020): Alternative splicing of UCP1 by non-cell-autonomous action of PEMT. In: Molecular metabolism 31, S. 55–66. DOI: 10.1016/j.molmet.2019.10.007.

Joshi, Amit S.; Thompson, Morgan N.; Fei, Naomi; Hüttemann, Maik; Greenberg, Miriam L. (2012): Cardiolipin and mitochondrial phosphatidylethanolamine have overlapping functions in mitochondrial fusion in Saccharomyces cerevisiae. In: The Journal of biological chemistry 287 (21), S. 17589–17597. DOI: 10.1074/jbc.M111.330167.

Kainu, Ville; Hermansson, Martin; Hänninen, Satu; Hokynar, Kati; Somerharju, Pentti (2013): Import of phosphatidylserine to and export of phosphatidylethanolamine molecular species from mitochondria. In: Biochimica et biophysica acta 1831 (2), S. 429–437. DOI: 10.1016/j.bbalip.2012.11.003.

Kainu, Ville; Hermansson, Martin; Somerharju, Pentti (2010): Introduction of phospholipids to cultured cells with cyclodextrin. In: Journal of lipid research 51 (12), S. 3533–3541. DOI: 10.1194/jlr.D009373.

Kalinovich, Anastasia V.; Jong, Jasper M. A. de; Cannon, Barbara; Nedergaard, Jan (2017): UCP1 in adipose tissues: two steps to full browning. In: Biochimie 134, S. 127–137. DOI: 10.1016/j.biochi.2017.01.007.

Kannan, Muthukumar; Sivaprakasam, Chinnarasu; Prinz, William A.; Nachiappan, Vasanthi (2016): Endoplasmic reticulum stress affects the transport of phosphatidylethanolamine from mitochondria to the endoplasmic reticulum in S.cerevisiae. In: Biochimica et biophysica acta 1861 (12 Pt A), S. 1959–1967. DOI: 10.1016/j.bbalip.2016.09.015.

Kanno, Keishi; Wu, Michele K.; Scapa, Erez F.; Roderick, Steven L.; Cohen, David E. (2007): Structure and function of phosphatidylcholine transfer protein (PC-TP)/StarD2. In: Biochimica et biophysica acta 1771 (6), S. 654–662. DOI: 10.1016/j.bbalip.2007.04.003.

Karise, Iara; Bargut, Thereza Cristina; Del Sol, Mariano; Aguila, Marcia Barbosa; Mandarim-de-Lacerda, Carlos A. (2019): Metformin enhances mitochondrial biogenesis and thermogenesis in brown adipocytes of mice. In: Biomedicine & pharmacotherapy = Biomedecine & pharmacotherapie 111, S. 1156–1165. DOI: 10.1016/j.biopha.2019.01.021.

Kazak, Lawrence; Chouchani, Edward T.; Lu, Gina Z.; Jedrychowski, Mark P.; Bare, Curtis J.; Mina, Amir I. et al. (2017): Genetic Depletion of Adipocyte Creatine Metabolism Inhibits Diet-Induced Thermogenesis and Drives Obesity. In: Cell metabolism 26 (4), S. 693. DOI: 10.1016/j.cmet.2017.09.007.

Kennedy, E. P.; Westheimer, F. H. (1964): Nobel Laureates: Bloch and Lynen Win Prize in Medicine and Physiology. In: Science (New York, N.Y.) 146 (3643), S. 504–506. DOI: 10.1126/science.146.3643.504.

Kersten, S.; Mandard, S.; Tan, N. S.; Escher, P.; Metzger, D.; Chambon, P. et al. (2000): Characterization of the fasting-induced adipose factor FIAF, a novel peroxisome proliferator-activated receptor target gene. In: The Journal of biological chemistry 275 (37), S. 28488–28493. DOI: 10.1074/jbc.M004029200.

Khacho, Mireille; Clark, Alysen; Svoboda, Devon S.; Azzi, Joelle; MacLaurin, Jason G.; Meghaizel, Cynthia et al. (2016): Mitochondrial Dynamics Impacts Stem Cell Identity and Fate Decisions by Regulating a Nuclear Transcriptional Program. In: Cell stem cell 19 (2), S. 232–247. DOI: 10.1016/j.stem.2016.04.015.

Khan, M.; Contreras, M.; Singh, I. (2000): Endotoxin-induced alterations of lipid and fatty acid compositions in rat liver peroxisomes. In: Journal of endotoxin research 6 (1), S. 41–50. DOI: 10.1177/09680519000060010601.

Kim, Dong-Ho; Behlke, Mark A.; Rose, Scott D.; Chang, Mi-Sook; Choi, Sangdun; Rossi, John J. (2005): Synthetic dsRNA Dicer substrates enhance RNAi potency and efficacy. In: Nature biotechnology 23 (2), S. 222–226. DOI: 10.1038/nbt1051.

Kimmel, Alan R.; Sztalryd, Carole (2014): Perilipin 5, a lipid droplet protein adapted to mitochondrial energy utilization. In: Current opinion in lipidology 25 (2), S. 110–117. DOI: 10.1097/MOL.0000000000000057.

Kindt, Alida; Liebisch, Gerhard; Clavel, Thomas; Haller, Dirk; Hörmannsperger, Gabriele; Yoon, Hongsup et al. (2018): The gut microbiota promotes hepatic fatty acid desaturation and elongation in mice. In: Nature communications 9 (1), S. 3760. DOI: 10.1038/s41467-018-05767-4.

Klaus, S.; Casteilla, L.; Bouillaud, F.; Ricquier, D. (1991): The uncoupling protein UCP: a membraneous mitochondrial ion carrier exclusively expressed in brown adipose tissue. In: The International journal of biochemistry 23 (9), S. 791–801. DOI: 10.1016/0020-711x(91)90062-r.

Kleinfeld, A. M.; Chu, P.; Romero, C. (1997): Transport of long-chain native fatty acids across lipid bilayer membranes indicates that transbilayer flip-flop is rate limiting. In: Biochemistry 36 (46), S. 14146–14158. DOI: 10.1021/bi971440e.

Klingenberg, M.; Huang, S. G. (1999): Structure and function of the uncoupling protein from brown adipose tissue. In: Biochimica et biophysica acta 1415 (2), S. 271–296. DOI: 10.1016/s0005-2736(98)00232-6.

Klingenspor, M.; Bast, A.; Bolze, F.; Li, Y.; Maurer, S.; Schweizer, S. (2017): Brown Adipose Tissue. In: Michael E. Symonds (Hg.): Adipose Tissue Biology. Cham: Springer International Publishing, S. 91-147.

Kobayashi, Toshihide; Menon, Anant K. (2018): Transbilayer lipid asymmetry. In: Current biology: CB 28 (8), R386-R391. DOI: 10.1016/j.cub.2018.01.007.

Koch, C. E.; Lowe, C.; Pretz, D.; Steger, J.; Williams, L. M.; Tups, A. (2014): High-fat diet induces leptin resistance in leptin-deficient mice. In: Journal of neuroendocrinology 26 (2), S. 58–67. DOI: 10.1111/jne.12131.

Koenen, Mascha; Hill, Michael A.; Cohen, Paul; Sowers, James R. (2021): Obesity, Adipose Tissue and Vascular Dysfunction. In: Circulation research 128 (7), S. 951–968. DOI: 10.1161/CIRCRESAHA.121.318093.

Komissarenko, S. V.; Gulaia, N. M.; Gubenko, E. P. (1977): Ingibirovanie metilendifosfonovoĭ kislotoĭ aktivnosti neorganicheskoĭ pirofosfatazy selezenki mysheĭ. In: Biokhimiia (Moscow, Russia) 42 (2), S. 238–242.

Kornmann, Benoît (2013): The molecular hug between the ER and the mitochondria. In: Current opinion in cell biology 25 (4), S. 443–448. DOI: 10.1016/j.ceb.2013.02.010.

Kornmann, Benoît; Currie, Erin; Collins, Sean R.; Schuldiner, Maya; Nunnari, Jodi; Weissman, Jonathan S.; Walter, Peter (2009): An ER-mitochondria tethering complex revealed by a synthetic biology screen. In: Science (New York, N.Y.) 325 (5939), S. 477–481. DOI: 10.1126/science.1175088.

Kuge, O.; Nishijima, M.; Akamatsu, Y. (1991): A cloned gene encoding phosphatidylserine decarboxylase complements the phosphatidylserine biosynthetic defect of a Chinese hamster ovary cell mutant. In: The Journal of biological chemistry 266 (10), S. 6370–6376.

Kumar, Santosh; Chitraju, Chandramohan; Farese, Robert V.; Walther, Tobias C.; Burd, Christopher G. (2021): Conditional targeting of phosphatidylserine decarboxylase to lipid droplets. In: Biology open 10 (3). DOI: 10.1242/bio.058516.

Lackner, Laura L. (2019): The Expanding and Unexpected Functions of Mitochondria Contact Sites. In: Trends in cell biology 29 (7), S. 580–590. DOI: 10.1016/j.tcb.2019.02.009.

Laganà, Alessandro; Veneziano, Dario; Russo, Francesco; Pulvirenti, Alfredo; Giugno, Rosalba; Croce, Carlo Maria; Ferro, Alfredo (2015): Computational design of artificial RNA molecules for gene regulation. In: Methods in molecular biology (Clifton, N.J.) 1269, S. 393–412. DOI: 10.1007/978-1-4939-2291-8_25.

Lampl, M.; Leber, A.; Paltauf, F.; Daum, G. (1994): Import of phosphatidylinositol and phosphatidylcholine into mitochondria of the yeast, Saccharomyces cerevisiae. In: FEBS letters 356 (1), S. 1–4. DOI: 10.1016/0014-5793(94)01197-4.

LANDS, W. E. (1958): Metabolism of glycerolipides; a comparison of lecithin and triglyceride synthesis. In: The Journal of biological chemistry 231 (2), S. 883–888.

Langin, Dominique (2006): Control of fatty acid and glycerol release in adipose tissue lipolysis. In: Comptes rendus biologies 329 (8), 598-607; discussion 653-5. DOI: 10.1016/j.crvi.2005.10.008.

Langmann, Thomas; Mauerer, Richard; Schmitz, Gerd (2006): Human ATP-binding cassette transporter TaqMan low-density array: analysis of macrophage differentiation and foam cell formation. In: Clinical chemistry 52 (2), S. 310–313. DOI: 10.1373/clinchem.2005.059774.

Lapillo, Margherita; Salis, Barbara; Palazzolo, Stefano; Poli, Giulio; Granchi, Carlotta; Minutolo, Filippo et al. (2019): First-of-its-kind STARD3 Inhibitor: In Silico Identification and Biological Evaluation as Anticancer Agent. In: ACS medicinal chemistry letters 10 (4), S. 475–480. DOI: 10.1021/acsmedchemlett.8b00509.

Larsen, Thomas M.; Toubro, Søren; van Baak, Marleen A.; Gottesdiener, Keith M.; Larson, Patrick; Saris, Wim H. M.; Astrup, Arne (2002): Effect of a 28-d treatment with L-796568, a novel beta(3)-adrenergic receptor agonist, on energy expenditure and body composition in obese men. In: The American journal of clinical nutrition 76 (4), S. 780–788. DOI: 10.1093/ajcn/76.4.780.

Lass, Achim; Zimmermann, Robert; Haemmerle, Guenter; Riederer, Monika; Schoiswohl, Gabriele; Schweiger, Martina et al. (2006): Adipose triglyceride lipase-mediated lipolysis of cellular fat stores is activated by CGI-58 and defective in Chanarin-Dorfman Syndrome. In: Cell metabolism 3 (5), S. 309–319. DOI: 10.1016/j.cmet.2006.03.005.

Lean, M. E.; James, W. P.; Jennings, G.; Trayhurn, P. (1986): Brown adipose tissue in patients with phaeochromocytoma. In: International journal of obesity 10 (3), S. 219–227.

Leitner, Brooks P.; Huang, Shan; Brychta, Robert J.; Duckworth, Courtney J.; Baskin, Alison S.; McGehee, Suzanne et al. (2017): Mapping of human brown adipose tissue in lean and obese young men. In: Proceedings of the National Academy of Sciences of the United States of America 114 (32), S. 8649–8654. DOI: 10.1073/pnas.1705287114.

Leventis, R.; Silvius, J. R. (2001): Use of cyclodextrins to monitor transbilayer movement and differential lipid affinities of cholesterol. In: Biophysical journal 81 (4), S. 2257–2267. DOI: 10.1016/S0006-3495(01)75873-0.

Li, Guangtao; Kim, JiHyun; Huang, Zhen; St Clair, Johnna R.; Brown, Deborah A.; London, Erwin (2016): Efficient replacement of plasma membrane outer leaflet phospholipids and sphingolipids in cells with exogenous lipids. In: Proceedings of the National Academy of Sciences of the United States of America 113 (49), S. 14025–14030. DOI: 10.1073/pnas.1610705113.

Li, Q. X.; Dowhan, W. (1988): Structural characterization of Escherichia coli phosphatidylserine decarboxylase. In: The Journal of biological chemistry 263 (23), S. 11516–11522.

Li, Yongguo; Schnabl, Katharina; Gabler, Sarah-Madeleine; Willershäuser, Monja; Reber, Josefine; Karlas, Angelos et al. (2018): Secretin-Activated Brown Fat Mediates Prandial Thermogenesis to Induce Satiation. In: Cell 175 (6), 1561-1574.e12. DOI: 10.1016/j.cell.2018.10.016.

Liang, Xingwei; Yang, Qiyuan; Zhang, Lupei; Maricelli, Joseph W.; Rodgers, Buel D.; Zhu, Mei-Jun; Du, Min (2016): Maternal high-fat diet during lactation impairs thermogenic function of brown adipose tissue in offspring mice. In: Scientific reports 6, S. 34345. DOI: 10.1038/srep34345.

Lidell, Martin E.; Betz, Matthias J.; Dahlqvist Leinhard, Olof; Heglind, Mikael; Elander, Louise; Slawik, Marc et al. (2013): Evidence for two types of brown adipose tissue in humans. In: Nature medicine 19 (5), S. 631–634. DOI: 10.1038/nm.3017.

Liebisch, Gerhard; Fahy, Eoin; Aoki, Junken; Dennis, Edward A.; Durand, Thierry; Ejsing, Christer S. et al. (2020): Update on LIPID MAPS classification, nomenclature, and shorthand notation for MS-derived lipid structures. In: Journal of lipid research 61 (12), S. 1539–1555. DOI: 10.1194/jlr.S120001025.

Liebisch, Gerhard; Lieser, Bernd; Rathenberg, Jan; Drobnik, Wolfgang; Schmitz, Gerd (2004): High-throughput quantification of phosphatidylcholine and sphingomyelin by electrospray ionization tandem mass spectrometry coupled with isotope correction algorithm. In: Biochimica et biophysica acta 1686 (1-2), S. 108–117. DOI: 10.1016/j.bbalip.2004.09.003.

Lin, Qingqing; London, Erwin (2014): Preparation of artificial plasma membrane mimicking vesicles with lipid asymmetry. In: PloS one 9 (1), e87903. DOI: 10.1371/journal.pone.0087903.

Liu, Xiaomeng; Zhang, Zhi; Song, Yajie; Xie, Hengchang; Dong, Meng (2022): An update on brown adipose tissue and obesity intervention: Function, regulation and therapeutic implications. In: Frontiers in endocrinology 13, S. 1065263. DOI: 10.3389/fendo.2022.1065263.

Liu, Xiaomeng; Zheng, Zongji; Zhu, Xiaoming; Meng, Minghui; Li, Lan; Shen, Yanyan et al. (2013): Brown adipose tissue transplantation improves whole-body energy metabolism. In: Cell research 23 (6), S. 851–854. DOI: 10.1038/cr.2013.64.

Livak, K. J.; Schmittgen, T. D. (2001): Analysis of relative gene expression data using real-time quantitative PCR and the 2(-Delta Delta C(T)) Method. In: Methods (San Diego, Calif.) 25 (4), S. 402–408. DOI: 10.1006/meth.2001.1262.

Londos, C.; Sztalryd, C.; Tansey, J. T.; Kimmel, A. R. (2005): Role of PAT proteins in lipid metabolism. In: Biochimie 87 (1), S. 45–49. DOI: 10.1016/j.biochi.2004.12.010.

Luijten, Ineke H. N.; Feldmann, Helena M.; Essen, Gabriella von; Cannon, Barbara; Nedergaard, Jan (2019): In the absence of UCP1-mediated diet-induced thermogenesis, obesity is augmented even in the obesity-resistant 129S mouse strain. In: American journal of physiology. Endocrinology and metabolism 316 (5), E729-E740. DOI: 10.1152/ajpendo.00020.2019.

Lynes, Matthew D.; Shamsi, Farnaz; Sustarsic, Elahu Gosney; Leiria, Luiz O.; Wang, Chih-Hao; Su, Sheng-Chiang et al. (2018): Cold-Activated Lipid Dynamics in Adipose Tissue Highlights a Role for Cardiolipin in Thermogenic Metabolism. In: Cell reports 24 (3), S. 781–790. DOI: 10.1016/j.celrep.2018.06.073.

Ma, Jacey Hongjie; Shen, Shichen; Wang, Joshua J.; He, Zhanwen; Poon, Amanda; Li, Jun et al. (2017): Comparative Proteomic Analysis of the Mitochondria-associated ER Membrane (MAM) in a Long-term Type 2 Diabetic Rodent Model. In: Scientific reports 7 (1), S. 2062. DOI: 10.1038/s41598-017-02213-1.

Mahammad, Saleemulla; Parmryd, Ingela (2015): Cholesterol depletion using methyl-β-cyclodextrin. In: Methods in molecular biology (Clifton, N.J.) 1232, S. 91–102. DOI: 10.1007/978-1-4939-1752-5_8.

Man, Weng Chi; Miyazaki, Makoto; Chu, Kiki; Ntambi, James M. (2006): Membrane topology of mouse stearoyl-CoA desaturase 1. In: The Journal of biological chemistry 281 (2), S. 1251–1260. DOI: 10.1074/jbc.M508733200.

Marcher, Ann-Britt; Loft, Anne; Nielsen, Ronni; Vihervaara, Terhi; Madsen, Jesper Grud Skat; Sysi-Aho, Marko et al. (2015): RNA-Seq and Mass-Spectrometry-Based Lipidomics Reveal Extensive Changes of Glycerolipid Pathways in Brown Adipose Tissue in Response to Cold. In: Cell reports 13 (9), S. 2000–2013. DOI: 10.1016/j.celrep.2015.10.069.

Marzolla, Vincenzo; Armani, Andrea; Zennaro, Maria-Christina; Cinti, Francesca; Mammi, Caterina; Fabbri, Andrea et al. (2012): The role of the mineralocorticoid receptor in adipocyte biology and fat metabolism. In: Molecular and cellular endocrinology 350 (2), S. 281–288. DOI: 10.1016/j.mce.2011.09.011.

McGill, Mitchell R. (2016): The past and present of serum aminotransferases and the future of liver injury biomarkers. In: EXCLI journal 15, S. 817–828. DOI: 10.17179/excli2016-800.

Meister, Gunter; Tuschl, Thomas (2004): Mechanisms of gene silencing by double-stranded RNA. In: Nature 431 (7006), S. 343–349. DOI: 10.1038/nature02873.

MELICOW, M. M. (1957): Hibernating fat and pheochromocytoma. In: A.M.A. archives of pathology 63 (4), S. 367–372.

Mengel, Laura A.; Seidl, Hatti; Brandl, Beate; Skurk, Thomas; Holzapfel, Christina; Stecher, Lynne et al. (2020): Gender Differences in the Response to Short-term Cold Exposure in Young Adults. In: The Journal of clinical endocrinology and metabolism 105 (5). DOI: 10.1210/clinem/dgaa110.

Miller, Walter L. (2007): Steroidogenic acute regulatory protein (StAR), a novel mitochondrial cholesterol transporter. In: Biochimica et biophysica acta 1771 (6), S. 663–676. DOI: 10.1016/j.bbalip.2007.02.012.

Mills, Evanna L.; Harmon, Cathal; Jedrychowski, Mark P.; Xiao, Haopeng; Garrity, Ryan; Tran, Nhien V. et al. (2021): UCP1 governs liver extracellular succinate and inflammatory pathogenesis. In: Nature metabolism 3 (5), S. 604–617. DOI: 10.1038/s42255-021-00389-5.

Mills, Evanna L.; Pierce, Kerry A.; Jedrychowski, Mark P.; Garrity, Ryan; Winther, Sally; Vidoni, Sara et al. (2018): Accumulation of succinate controls activation of adipose tissue thermogenesis. In: Nature 560 (7716), S. 102–106. DOI: 10.1038/s41586-018-0353-2.

Morel, Yulemni; Hegdekar, Nivedita; Sarkar, Chinmoy; Lipinski, Marta M.; Kane, Maureen A.; Jones, Jace W. (2021): Structure-specific, accurate quantitation of plasmalogen glycerophosphoethanolamine. In: Analytica chimica acta 1186, S. 339088. DOI: 10.1016/j.aca.2021.339088.

Nedergaard, J.; Golozoubova, V.; Matthias, A.; Asadi, A.; Jacobsson, A.; Cannon, B. (2001): UCP1: the only protein able to mediate adaptive non-shivering thermogenesis and metabolic inefficiency. In: Biochimica et biophysica acta 1504 (1), S. 82–106. DOI: 10.1016/s0005-2728(00)00247-4.

Nicholls, David G. (2006): The physiological regulation of uncoupling proteins. In: Biochimica et biophysica acta 1757 (5-6), S. 459–466. DOI: 10.1016/j.bbabio.2006.02.005.

Nicolson, Garth L.; Ferreira de Mattos, Gonzalo; Ash, Michael; Settineri, Robert; Escribá, Pablo V. (2021): Fundamentals of Membrane Lipid Replacement: A Natural Medicine Approach to Repairing Cellular Membranes and Reducing Fatigue, Pain, and Other Symptoms While Restoring Function in Chronic Illnesses and Aging. In: Membranes 11 (12). DOI: 10.3390/membranes11120944.

Niklas, Jens; Melnyk, Armin; Yuan, Yongbo; Heinzle, Elmar (2011): Selective permeabilization for the high-throughput measurement of compartmented enzyme activities in mammalian cells. In: Analytical biochemistry 416 (2), S. 218–227. DOI: 10.1016/j.ab.2011.05.039.

Nishio, Miwako; Yoneshiro, Takeshi; Nakahara, Masako; Suzuki, Shinnosuke; Saeki, Koichi; Hasegawa, Mamoru et al. (2012): Production of functional classical brown adipocytes from human pluripotent stem cells using specific hemopoietin cocktail without gene transfer. In: Cell metabolism 16 (3), S. 394–406. DOI: 10.1016/j.cmet.2012.08.001.

Nishitoh, Hideki; Matsuzawa, Atsushi; Tobiume, Kei; Saegusa, Kaoru; Takeda, Kohsuke; Inoue, Kiyoshi et al. (2002): ASK1 is essential for endoplasmic reticulum stress-induced neuronal cell death triggered by expanded polyglutamine repeats. In: Genes & development 16 (11), S. 1345–1355. DOI: 10.1101/gad.992302.

Obradovic, Milan; Sudar-Milovanovic, Emina; Soskic, Sanja; Essack, Magbubah; Arya, Swati; Stewart, Alan J. et al. (2021): Leptin and Obesity: Role and Clinical Implication. In: Frontiers in endocrinology 12, S. 585887. DOI: 10.3389/fendo.2021.585887.

O'Donnell, Valerie B. (2022): New appreciation for an old pathway: the Lands Cycle moves into new arenas in health and disease. In: Biochemical Society transactions 50 (1), S. 1–11. DOI: 10.1042/BST20210579.

Oeckl, Josef; Bast-Habersbrunner, Andrea; Fromme, Tobias; Klingenspor, Martin; Li, Yongguo (2020): Isolation, Culture, and Functional Analysis of Murine Thermogenic Adipocytes. In: STAR protocols 1 (3), S. 100118. DOI: 10.1016/j.xpro.2020.100118.

Oeckl, Josef; Janovska, Petra; Adamcova, Katerina; Bardova, Kristina; Brunner, Sarah; Dieckmann, Sebastian et al. (2022): Loss of UCP1 function augments recruitment of futile lipid cycling for thermogenesis in murine brown fat. In: Molecular metabolism 61, S. 101499. DOI: 10.1016/j.molmet.2022.101499.

Olayioye, Monilola A.; Vehring, Stefanie; Müller, Peter; Herrmann, Andreas; Schiller, Jürgen; Thiele, Christoph et al. (2005): StarD10, a START domain protein overexpressed in breast cancer, functions as a phospholipid transfer protein. In: The Journal of biological chemistry 280 (29), S. 27436–27442. DOI: 10.1074/jbc.M413330200.

Ottaviani, Enzo; Malagoli, Davide; Franceschi, Claudio (2011): The evolution of the adipose tissue: a neglected enigma. In: General and comparative endocrinology 174 (1), S. 1–4. DOI: 10.1016/j.ygcen.2011.06.018.

Patel, Dhaval; Witt, Stephan N. (2017): Ethanolamine and Phosphatidylethanolamine: Partners in Health and Disease. In: Oxidative medicine and cellular longevity 2017, S. 4829180. DOI: 10.1155/2017/4829180.

Peinó, R.; Piñeiro, V.; Gualillo, O.; Menéndez, C.; Brenlla, J.; Casabiell, X. et al. (2000): Cold exposure inhibits leptin secretion in vitro by a direct and non-specific action on adipose tissue. In: European journal of endocrinology 142 (2), S. 195–199. DOI: 10.1530/eje.0.1420195.

Pendergast, D. R.; Leddy, J. J.; Venkatraman, J. T. (2000): A perspective on fat intake in athletes. In: Journal of the American College of Nutrition 19 (3), S. 345–350. DOI: 10.1080/07315724.2000.10718930.

Percy, A. K.; Moore, J. F.; Carson, M. A.; Waechter, C. J. (1983): Characterization of brain phosphatidylserine decarboxylase: localization in the mitochondrial inner membrane. In: Archives of biochemistry and biophysics 223 (2), S. 484–494. DOI: 10.1016/0003-9861(83)90613-6.

Perdomo, Carolina M.; Cohen, Ricardo V.; Sumithran, Priya; Clément, Karine; Frühbeck, Gema (2023): Contemporary medical, device, and surgical therapies for obesity in adults. In: Lancet (London, England) 401 (10382), S. 1116–1130. DOI: 10.1016/S0140-6736(22)02403-5.

Peres Valgas da Silva, Carmem; Hernández-Saavedra, Diego; White, Joseph D.; Stanford, Kristin I. (2019): Cold and Exercise: Therapeutic Tools to Activate Brown Adipose Tissue and Combat Obesity. In: Biology 8 (1). DOI: 10.3390/biology8010009.

Petruzzelli, Michele; Schweiger, Martina; Schreiber, Renate; Campos-Olivas, Ramon; Tsoli, Maria; Allen, John et al. (2014): A switch from white to brown fat increases energy expenditure in cancer-associated cachexia. In: Cell metabolism 20 (3), S. 433–447. DOI: 10.1016/j.cmet.2014.06.011.

Pham, John W.; Pellino, Janice L.; Lee, Young Sik; Carthew, Richard W.; Sontheimer, Erik J. (2004): A Dicer-2-dependent 80s complex cleaves targeted mRNAs during RNAi in Drosophila. In: Cell 117 (1), S. 83–94. DOI:10.1016/s0092-8674(04)00258-2.

Pipitone RM, Ciccioli C, Infantino G, La Mantia C, Parisi S, Tulone A, Pennisi G, Grimaudo S, Petta S, 2023. MAFLD: a multisystem disease. Therapeutic advances in endocrinology and metabolism, 14, 20420188221145549.

Possik, Elite; Madiraju, S. R. Murthy; Prentki, Marc (2017): Glycerol-3-phosphate phosphatase/PGP: Role in intermediary metabolism and target for cardiometabolic diseases. In: Biochimie 143, S. 18–28. DOI: 10.1016/j.biochi.2017.08.001.

Pouwels, Sjaak; Sakran, Nasser; Graham, Yitka; Leal, Angela; Pintar, Tadeja; Yang, Wah et al. (2022): Non-alcoholic fatty liver disease (NAFLD): a review of pathophysiology, clinical management and effects of weight loss. In: BMC endocrine disorders 22 (1), S. 63. DOI: 10.1186/s12902-022-00980-1.

Priego, T.; Sánchez, J.; Palou, A.; Picó, C. (2009): Effect of high-fat diet feeding on leptin receptor expression in white adipose tissue in rats: depot- and sex-related differential response. In: Genes & nutrition 4 (2), S. 151–156. DOI: 10.1007/s12263-009-0114-9.

Qing, Hua; Desrouleaux, Reina; Israni-Winger, Kavita; Mineur, Yann S.; Fogelman, Nia; Zhang, Cuiling et al. (2020): Origin and Function of Stress-Induced IL-6 in Murine Models. In: Cell 182 (2), 372-387.e14. DOI: 10.1016/j.cell.2020.05.054.

Ramjiawan, B.; Czubryt, M. P.; Gilchrist, J. S.; Pierce, G. N. (1996): Nuclear membrane cholesterol can modulate nuclear nucleoside triphosphatase activity. In: Journal of cellular biochemistry 63 (4), S. 442–452. DOI: 10.1002/(sici)1097-4644(19961215)63:4<442::aid-jcb6>3.0.co;2-t.

Ramos-Jiménez, Arnulfo; Hernández-Torres, Rosa P.; Torres-Durán, Patricia V.; Romero-Gonzalez, Jaime; Mascher, Dieter; Posadas-Romero, Carlos; Juárez-Oropeza, Marco A. (2008): The Respiratory Exchange Ratio is Associated with Fitness Indicators Both in Trained and Untrained Men: A Possible Application for People with Reduced Exercise Tolerance. In: Clinical medicine. Circulatory, respiratory and pulmonary medicine 2, S. 1–9. DOI: 10.4137/ccrpm.s449.

Reddy, Narendra L.; Tan, Bee K.; Barber, Thomas M.; Randeva, Harpal S. (2014): Brown adipose tissue: endocrine determinants of function and therapeutic manipulation as a novel treatment strategy for obesity. In: BMC obesity 1, S. 13. DOI: 10.1186/s40608-014-0013-5.

Rial, E.; González-Barroso, M. M. (2001): Physiological regulation of the transport activity in the uncoupling proteins UCP1 and UCP2. In: Biochimica et biophysica acta 1504 (1), S. 70–81. DOI: 10.1016/s0005-2728(00)00240-1.

Ricci, M. R.; Fried, S. K.; Mittleman, K. D. (2000): Acute cold exposure decreases plasma leptin in women. In: Metabolism: clinical and experimental 49 (4), S. 421–423. DOI: 10.1016/s0026-0495(00)80001-3.

Ricquier, D.; Nechad, M.; Mory, G. (1982): Ultrastructural and biochemical characterization of human brown adipose tissue in pheochromocytoma. In: The Journal of clinical endocrinology and metabolism 54 (4), S. 803–807. DOI: 10.1210/jcem-54-4-803.

Riekhof, Wayne R.; Voelker, Dennis R. (2006): Uptake and utilization of lyso-phosphatidylethanolamine by Saccharomyces cerevisiae. In: The Journal of biological chemistry 281 (48), S. 36588–36596. DOI: 10.1074/jbc.M608851200.

Riis-Vestergaard, Mette Ji; Richelsen, Bjørn; Bruun, Jens Meldgaard; Li, Wei; Hansen, Jacob B.; Pedersen, Steen Bønløkke (2020): Beta-1 and Not Beta-3 Adrenergic Receptors May Be the Primary Regulator of Human Brown Adipocyte Metabolism. In: The Journal of clinical endocrinology and metabolism 105 (4). DOI: 10.1210/clinem/dgz298.

Rodriguez, A. M.; Monjo, M.; Roca, P.; Palou, A. (2002): Opposite actions of testosterone and progesterone on UCP1 mRNA expression in cultured brown adipocytes. In: Cellular and molecular life sciences : CMLS 59 (10), S. 1714–1723. DOI: 10.1007/pl00012499.

Rodríguez-Cuenca, S.; Monjo, M.; Gianotti, M.; Proenza, A. M.; Roca, P. (2007): Expression of mitochondrial biogenesis-signaling factors in brown adipocytes is influenced specifically by 17beta-estradiol, testosterone, and progesterone. In: American journal of physiology. Endocrinology and metabolism 292 (1), E340-6. DOI: 10.1152/ajpendo.00175.2006.

Rosenwald, Matthias; Perdikari, Aliki; Rülicke, Thomas; Wolfrum, Christian (2013): Bi-directional interconversion of brite and white adipocytes. In: Nature cell biology 15 (6), S. 659–667. DOI: 10.1038/ncb2740.

Rosenwald, Matthias; Wolfrum, Christian (2014): The origin and definition of brite versus white and classical brown adipocytes. In: Adipocyte 3 (1), S. 4–9. DOI: 10.4161/adip.26232.

Rotter, Victoria; Nagaev, Ivan; Smith, Ulf (2003): Interleukin-6 (IL-6) induces insulin resistance in 3T3-L1 adipocytes and is, like IL-8 and tumor necrosis factor-alpha, overexpressed in human fat cells from insulin-resistant subjects. In: The Journal of biological chemistry 278 (46), S. 45777–45784. DOI: 10.1074/jbc.M301977200.

Ryan, Donna H. (2022): Drugs for Treating Obesity. In: Handbook of experimental pharmacology 274, S. 387–414. DOI: 10.1007/164_2021_560.

Saetang, Jirakrit; Sangkhathat, Surasak (2018): Role of innate lymphoid cells in obesity and metabolic disease (Review). In: Molecular medicine reports 17 (1), S. 1403–1412. DOI: 10.3892/mmr.2017.8038.

Sam, Pingdewinde N.; Calzada, Elizabeth; Acoba, Michelle Grace; Zhao, Tian; Watanabe, Yasunori; Nejatfard, Anahita et al. (2021): Impaired phosphatidylethanolamine metabolism activates a reversible stress response that detects and resolves mutant mitochondrial precursors. In: iScience 24 (3), S. 102196. DOI: 10.1016/j.isci.2021.102196.

Sanchez, Susana A.; Gunther, German; Tricerri, Maria A.; Gratton, Enrico (2011): Methyl-β-cyclodextrins preferentially remove cholesterol from the liquid disordered phase in giant unilamellar vesicles. In: The Journal of membrane biology 241 (1), S. 1–10. DOI: 10.1007/s00232-011-9348-8.

Schnaitman, C.; Greenawalt, J. W. (1968): Enzymatic properties of the inner and outer membranes of rat liver mitochondria. In: The Journal of cell biology 38 (1), S. 158–175. DOI: 10.1083/jcb.38.1.158.

Schoer, J. K.; Gallegos, A. M.; McIntosh, A. L.; Starodub, O.; Kier, A. B.; Billheimer, J. T.; Schroeder, F. (2000): Lysosomal membrane cholesterol dynamics. In: Biochemistry 39 (26), S. 7662–7677. DOI: 10.1021/bi992686h.

Schreiber, Renate; Diwoky, Clemens; Schoiswohl, Gabriele; Feiler, Ursula; Wongsiriroj, Nuttaporn; Abdellatif, Mahmoud et al. (2017): Cold-Induced Thermogenesis Depends on ATGL-Mediated Lipolysis in Cardiac Muscle, but Not Brown Adipose Tissue. In: Cell metabolism 26 (5), 753-763.e7. DOI: 10.1016/j.cmet.2017.09.004.

Schuler, Max-Hinderk; Di Bartolomeo, Francesca; Mårtensson, Christoph U.; Daum, Günther; Becker, Thomas (2016): Phosphatidylcholine Affects Inner Membrane Protein Translocases of Mitochondria. In: The Journal of biological chemistry 291 (36), S. 18718–18729. DOI: 10.1074/jbc.M116.722694.

Schwalie, Petra C.; Dong, Hua; Zachara, Magda; Russeil, Julie; Alpern, Daniel; Akchiche, Nassila et al. (2018): A stromal cell population that inhibits adipogenesis in mammalian fat depots. In: Nature 559 (7712), S. 103–108. DOI: 10.1038/s41586-018-0226-8.

Schweizer, Sabine; Liebisch, Gerhard; Oeckl, Josef; Hoering, Marcus; Seeliger, Claudine; Schiebel, Carolin et al. (2019): The lipidome of primary murine white, brite, and brown adipocytes-Impact of beta-adrenergic stimulation. In: PLoS biology 17 (8), e3000412. DOI: 10.1371/journal.pbio.3000412.

Scorrano, Luca; Ashiya, Mona; Buttle, Karolyn; Weiler, Solly; Oakes, Scott A.; Mannella, Carmen A.; Korsmeyer, Stanley J. (2002): A distinct pathway remodels mitochondrial cristae and mobilizes cytochrome c during apoptosis. In: Developmental cell 2 (1), S. 55–67. DOI: 10.1016/s1534-5807(01)00116-2.

Seki T, Yang Y, Sun X, Lim S, Xie S, Guo Z, Xiong W, Kuroda M, Sakaue H, Hosaka K, Jing X, Yoshihara M, Qu L, Li X, Chen Y, Cao Y, 2022. Brown-fat-mediated tumour suppression by cold-altered global metabolism. Nature, 608 (7922), 421–428.

Shabalina, Irina G.; Jacobsson, Anders; Cannon, Barbara; Nedergaard, Jan (2004): Native UCP1 displays simple competitive kinetics between the regulators purine nucleotides and fatty acids. In: The Journal of biological chemistry 279 (37), S. 38236–38248. DOI: 10.1074/jbc.M402375200.

Shabalina, Irina G.; Ost, Mario; Petrovic, Natasa; Vrbacky, Marek; Nedergaard, Jan; Cannon, Barbara (2010): Uncoupling protein-1 is not leaky. In: Biochimica et biophysica acta 1797 (6-7), S. 773–784. DOI: 10.1016/j.bbabio.2010.04.007.

Shen, Hong; Jiang, Lin; Lin, Jiandie D.; Omary, M. Bishr; Rui, Liangyou (2019): Brown fat activation mitigates alcohol-induced liver steatosis and injury in mice. In: The Journal of clinical investigation 129 (6), S. 2305–2317. DOI: 10.1172/JCI124376.

Shiao, Y. J.; Lupo, G.; Vance, J. E. (1995): Evidence that phosphatidylserine is imported into mitochondria via a mitochondria-associated membrane and that the majority of mitochondrial phosphatidylethanolamine is derived from decarboxylation of phosphatidylserine. In: The Journal of biological chemistry 270 (19), S. 11190–11198. DOI: 10.1074/jbc.270.19.11190.

Shimizu, Y.; Kielar, D.; Minokoshi, Y.; Shimazu, T. (1996): Noradrenaline increases glucose transport into brown adipocytes in culture by a mechanism different from that of insulin. In: The Biochemical journal 314 (Pt 2) (Pt 2), S. 485–490. DOI: 10.1042/bj3140485.

Shin, Hyunsu; Ma, Yinyan; Chanturiya, Tatyana; Cao, Qiang; Wang, Youlin; Kadegowda, Anil K. G. et al. (2017): Lipolysis in Brown Adipocytes Is Not Essential for Cold-Induced Thermogenesis in Mice. In: Cell metabolism 26 (5), 764-777.e5. DOI: 10.1016/j.cmet.2017.09.002.

Shoshan-Barmatz, Varda; Nahon-Crystal, Edna; Shteinfer-Kuzmine, Anna; Gupta, Rajeev (2018): VDAC1, mitochondrial dysfunction, and Alzheimer's disease. In: Pharmacological research 131, S. 87–101. DOI: 10.1016/j.phrs.2018.03.010.

Shoshan-Barmatz, Varda; Pittala, Srinivas; Mizrachi, Dario (2019): VDAC1 and the TSPO: Expression, Interactions, and Associated Functions in Health and Disease States. In: International journal of molecular sciences 20 (13). DOI: 10.3390/ijms20133348.

Shoshan-Barmatz, Varda; Shteinfer-Kuzmine, Anna; Verma, Ankit (2020): VDAC1 at the Intersection of Cell Metabolism, Apoptosis, and Diseases. In: Biomolecules 10 (11). DOI: 10.3390/biom10111485.

Simonson, D. C.; DeFronzo, R. A. (1990): Indirect calorimetry: methodological and interpretative problems. In: The American journal of physiology 258 (3 Pt 1), E399-412. DOI: 10.1152/ajpendo.1990.258.3.E399.

Singer, S. J.; Nicolson, G. L. (1972): The fluid mosaic model of the structure of cell membranes. In: Science (New York, N.Y.) 175 (4023), S. 720–731. DOI: 10.1126/science.175.4023.720.

Singh, Abhishek K.; Aryal, Binod; Chaube, Balkrishna; Rotllan, Noemi; Varela, Luis; Horvath, Tamas L. et al. (2018): Brown adipose tissue derived ANGPTL4 controls glucose and lipid metabolism and regulates thermogenesis. In: Molecular metabolism 11, S. 59–69. DOI: 10.1016/j.molmet.2018.03.011.

Solsona-Vilarrasa, Estel; Fucho, Raquel; Torres, Sandra; Nuñez, Susana; Nuño-Lámbarri, Natalia; Enrich, Carlos et al. (2019): Cholesterol enrichment in liver mitochondria impairs oxidative phosphorylation and disrupts the assembly of respiratory supercomplexes. In: Redox biology 24, S. 101214. DOI: 10.1016/j.redox.2019.101214.

Song, Anying; Dai, Wenting; Jang, Min Jee; Medrano, Leonard; Li, Zhuo; Zhao, Hu et al. (2020): Low- and high-thermogenic brown adipocyte subpopulations coexist in murine adipose tissue. In: The Journal of clinical investigation 130 (1), S. 247–257. DOI: 10.1172/JCI129167.

Sontheimer, Erik J. (2005): Assembly and function of RNA silencing complexes. In: Nature reviews. Molecular cell biology 6 (2), S. 127–138. DOI: 10.1038/nrm1568.

Sperka-Gottlieb, C. D.; Hermetter, A.; Paltauf, F.; Daum, G. (1988): Lipid topology and physical properties of the outer mitochondrial membrane of the yeast, Saccharomyces cerevisiae. In: Biochimica et biophysica acta 946 (2), S. 227–234. DOI: 10.1016/0005-2736(88)90397-5.

Ståhl, Ulf; Stålberg, Kjell; Stymne, Sten; Ronne, Hans (2008): A family of eukaryotic lysophospholipid acyltransferases with broad specificity. In: FEBS letters 582 (2), S. 305–309. DOI: 10.1016/j.febslet.2007.12.020.

Stanford, Kristin I.; Middelbeek, Roeland J. W.; Goodyear, Laurie J. (2015): Exercise Effects on White Adipose Tissue: Beiging and Metabolic Adaptations. In: Diabetes 64 (7), S. 2361–2368. DOI: 10.2337/db15-0227.

Stanford, Kristin I.; Middelbeek, Roeland J. W.; Townsend, Kristy L.; An, Ding; Nygaard, Eva B.; Hitchcox, Kristen M. et al. (2013): Brown adipose tissue regulates glucose homeostasis and insulin sensitivity. In: The Journal of clinical investigation 123 (1), S. 215–223. DOI: 10.1172/JCI62308.

Steenbergen, Rineke; Nanowski, Terry S.; Beigneux, Anne; Kulinski, Agnes; Young, Stephen G.; Vance, Jean E. (2005): Disruption of the phosphatidylserine decarboxylase gene in mice causes embryonic lethality and mitochondrial defects. In: The Journal of biological chemistry 280 (48), S. 40032–40040. DOI: 10.1074/jbc.M506510200.

Strålfors, P.; Björgell, P.; Belfrage, P. (1984): Hormonal regulation of hormone-sensitive lipase in intact adipocytes: identification of phosphorylated sites and effects on the phosphorylation by lipolytic hormones and insulin. In: Proceedings of the National Academy of Sciences of the United States of America 81 (11), S. 3317–3321. DOI: 10.1073/pnas.81.11.3317.

Sugawara, Sho; Kanamaru, Yusuke; Sekine, Shiori; Maekawa, Lila; Takahashi, Akinori; Yamamoto, Tadashi et al. (2020): The mitochondrial protein PGAM5 suppresses energy consumption in brown adipocytes by repressing expression of uncoupling protein 1. In: The Journal of biological chemistry 295 (17), S. 5588–5601. DOI: 10.1074/jbc.RA119.011508.

Sun, Lijuan; Yan, Jianhua; Goh, Hui Jen; Govindharajulu, Priya; Verma, Sanjay; Michael, Navin et al. (2020): Fibroblast Growth Factor-21, Leptin, and Adiponectin Responses to Acute Cold-Induced Brown Adipose Tissue Activation. In: The Journal of clinical endocrinology and metabolism 105 (3), e520-31. DOI: 10.1210/clinem/dgaa005.

Suresh, Pavana; London, Erwin (2022): Using cyclodextrin-induced lipid substitution to study membrane lipid and ordered membrane domain (raft) function in cells. In: Biochimica et biophysica acta. Biomembranes 1864 (1), S. 183774. DOI: 10.1016/j.bbamem.2021.183774.

Sustarsic, Elahu G.; Ma, Tao; Lynes, Matthew D.; Larsen, Michael; Karavaeva, Iuliia; Havelund, Jesper F. et al. (2018): Cardiolipin Synthesis in Brown and Beige Fat Mitochondria Is Essential for Systemic Energy Homeostasis. In: Cell metabolism 28 (1), 159-174.e11. DOI: 10.1016/j.cmet.2018.05.003.

Symonds, Michael E.; Farhat, Grace; Aldiss, Peter; Pope, Mark; Budge, Helen (2019): Brown adipose tissue and glucose homeostasis - the link between climate change and the global rise in obesity and diabetes. In: Adipocyte 8 (1), S. 46–50. DOI: 10.1080/21623945.2018.1551689.

Sztalryd, Carole; Kimmel, Alan R. (2014): Perilipins: lipid droplet coat proteins adapted for tissue-specific energy storage and utilization, and lipid cytoprotection. In: Biochimie 96, S. 96–101. DOI: 10.1016/j.biochi.2013.08.026.

Szymański, Jędrzej; Janikiewicz, Justyna; Michalska, Bernadeta; Patalas-Krawczyk, Paulina; Perrone, Mariasole; Ziółkowski, Wiesław et al. (2017): Interaction of Mitochondria with the Endoplasmic Reticulum and Plasma Membrane in Calcium Homeostasis, Lipid Trafficking and Mitochondrial Structure. In: International journal of molecular sciences 18 (7). DOI: 10.3390/ijms18071576.

Tait, Stephen W. G.; Green, Douglas R. (2012): Mitochondria and cell signalling. In: Journal of cell science 125 (Pt 4), S. 807–815. DOI: 10.1242/jcs.099234.

Tamura, Yasushi; Kawano, Shin; Endo, Toshiya (2020): Lipid homeostasis in mitochondria. In: Biological chemistry 401 (6-7), S. 821–833. DOI: 10.1515/hsz-2020-0121.

Tamura, Yasushi; Onguka, Ouma; Itoh, Kie; Endo, Toshiya; Iijima, Miho; Claypool, Steven M.; Sesaki, Hiromi (2012): Phosphatidylethanolamine biosynthesis in mitochondria: phosphatidylserine (PS) trafficking is independent of a PS decarboxylase and intermembrane space proteins UPS1P and UPS2P. In: The Journal of biological chemistry 287 (52), S. 43961–43971. DOI: 10.1074/jbc.M112.390997.

Tamura, Yasushi; Sesaki, Hiromi; Endo, Toshiya (2014): Phospholipid transport via mitochondria. In: Traffic (Copenhagen, Denmark) 15 (9), S. 933–945. DOI: 10.1111/tra.12188.

Tasseva, Guergana; Bai, Helin Daniel; Davidescu, Magdalena; Haromy, Alois; Michelakis, Evangelos; Vance, Jean E. (2013): Phosphatidylethanolamine deficiency in Mammalian mitochondria impairs oxidative phosphorylation and alters mitochondrial morphology. In: The Journal of biological chemistry 288 (6), S. 4158–4173. DOI: 10.1074/jbc.M112.434183.

Tatsuta, Takashi; Scharwey, Melanie; Langer, Thomas (2014): Mitochondrial lipid trafficking. In: Trends in cell biology 24 (1), S. 44–52. DOI: 10.1016/j.tcb.2013.07.011.

Tokubuchi, Ichiro; Tajiri, Yuji; Iwata, Shimpei; Hara, Kento; Wada, Nobuhiko; Hashinaga, Toshihiko et al. (2017): Beneficial effects of metformin on energy metabolism and visceral fat volume through a possible mechanism of fatty acid oxidation in human subjects and rats. In: PloS one 12 (2), e0171293. DOI: 10.1371/journal.pone.0171293.

Trayhurn, P.; Duncan, J. S.; Rayner, D. V. (1995): Acute cold-induced suppression of ob (obese) gene expression in white adipose tissue of mice: mediation by the sympathetic system. In: The Biochemical journal 311 (Pt 3) (Pt 3), S. 729–733. DOI: 10.1042/bj3110729.

Trayhurn, Paul (2022): Brown Adipose Tissue: A Short Historical Perspective. In: Methods in molecular biology (Clifton, N.J.) 2448, S. 1–18. DOI: 10.1007/978-1-0716-2087-8_1.

Trotter, P. J.; Pedretti, J.; Voelker, D. R. (1993): Phosphatidylserine decarboxylase from Saccharomyces cerevisiae. Isolation of mutants, cloning of the gene, and creation of a null allele. In: The Journal of biological chemistry 268 (28), S. 21416–21424.

Tyanova, Stefka; Temu, Tikira; Sinitcyn, Pavel; Carlson, Arthur; Hein, Marco Y.; Geiger, Tamar et al. (2016): The Perseus computational platform for comprehensive analysis of (prote)omics data. In: Nature methods 13 (9), S. 731–740. DOI: 10.1038/nmeth.3901.

Vallerand, A. L.; Jacobs, I. (1989): Rates of energy substrates utilization during human cold exposure. In: European journal of applied physiology and occupational physiology 58 (8), S. 873–878. DOI: 10.1007/BF02332221.

van Baak, Marleen A.; Hul, Gabby B. J.; Toubro, Søren; Astrup, Arne; Gottesdiener, Keith M.; DeSmet, Marina; Saris, Wim H. M. (2002): Acute effect of L-796568, a novel beta 3-adrenergic receptor agonist, on energy expenditure in obese men. In: Clinical pharmacology and therapeutics 71 (4), S. 272–279. DOI: 10.1067/mcp.2002.122527.

van der Veen, Jelske N.; Kennelly, John P.; Wan, Sereana; Vance, Jean E.; Vance, Dennis E.; Jacobs, René L. (2017): The critical role of phosphatidylcholine and phosphatidylethanolamine metabolism in health and disease. In: Biochimica et biophysica acta. Biomembranes 1859 (9 Pt B), S. 1558–1572. DOI: 10.1016/j.bbamem.2017.04.006.

van Marken Lichtenbelt, Wouter D.; Vanhommerig, Joost W.; Smulders, Nanda M.; Drossaerts, Jamie M. A. F. L.; Kemerink, Gerrit J.; Bouvy, Nicole D. et al. (2009): Cold-activated brown adipose tissue in healthy men. In: The New England journal of medicine 360 (15), S. 1500–1508. DOI: 10.1056/NEJMoa0808718.

van Meer, Gerrit; Voelker, Dennis R.; Feigenson, Gerald W. (2008): Membrane lipids: where they are and how they behave. In: Nature reviews. Molecular cell biology 9 (2), S. 112–124. DOI: 10.1038/nrm2330.

Vance, Dennis E. (2014): Phospholipid methylation in mammals: from biochemistry to physiological function. In: Biochimica et biophysica acta 1838 (6), S. 1477–1487. DOI: 10.1016/j.bbamem.2013.10.018.

Vance, J. E. (1990): Phospholipid synthesis in a membrane fraction associated with mitochondria. In: The Journal of biological chemistry 265 (13), S. 7248–7256.

Vance, Jean E. (2015): Phospholipid synthesis and transport in mammalian cells. In: Traffic (Copenhagen, Denmark) 16 (1), S. 1–18. DOI: 10.1111/tra.12230.

Vance, Jean E.; Tasseva, Guergana (2013): Formation and function of phosphatidylserine and phosphatidylethanolamine in mammalian cells. In: Biochimica et biophysica acta 1831 (3), S. 543–554. DOI: 10.1016/j.bbalip.2012.08.016.

Vander Heiden, M. G.; Chandel, N. S.; Li, X. X.; Schumacker, P. T.; Colombini, M.; Thompson, C. B. (2000): Outer mitochondrial membrane permeability can regulate coupled respiration and cell survival. In: Proceedings of the National Academy of Sciences of the United States of America 97 (9), S. 4666–4671. DOI: 10.1073/pnas.090082297.

Villanueva-Carmona, Teresa; Cedó, Lídia; Madeira, Ana; Ceperuelo-Mallafré, Victòria; Rodríguez-Peña, M-Mar; Núñez-Roa, Catalina et al. (2023): SUCNR1 signaling in adipocytes controls energy metabolism by modulating circadian clock and leptin expression. In: Cell metabolism 35 (4), 601-619.e10. DOI: 10.1016/j.cmet.2023.03.004.

Virtanen, Kirsi A.; Lidell, Martin E.; Orava, Janne; Heglind, Mikael; Westergren, Rickard; Niemi, Tarja et al. (2009): Functional brown adipose tissue in healthy adults. In: The New England journal of medicine 360 (15), S. 1518–1525. DOI: 10.1056/NEJMoa0808949.

Vishvanath, Lavanya; Gupta, Rana K. (2019): Contribution of adipogenesis to healthy adipose tissue expansion in obesity. In: The Journal of clinical investigation 129 (10), S. 4022–4031. DOI: 10.1172/JCI129191.

Vizcaíno, Juan Antonio; Côté, Richard G.; Csordas, Attila; Dianes, José A.; Fabregat, Antonio; Foster, Joseph M. et al. (2013): The PRoteomics IDEntifications (PRIDE) database and associated tools: status in 2013. In: Nucleic acids research 41 (Database issue), D1063-9. DOI: 10.1093/nar/gks1262.

Voelker, D. R. (1984): Phosphatidylserine functions as the major precursor of phosphatidylethanolamine in cultured BHK-21 cells. In: Proceedings of the National Academy of Sciences of the United States of America 81 (9), S. 2669–2673. DOI: 10.1073/pnas.81.9.2669.

Voelker, D. R. (1997): Phosphatidylserine decarboxylase. In: Biochimica et biophysica acta 1348 (1-2), S. 236–244. DOI: 10.1016/s0005-2760(97)00101-x.

Voilquin, Laetitia; Lodi, Massimo; Di Mattia, Thomas; Chenard, Marie-Pierre; Mathelin, Carole; Alpy, Fabien; Tomasetto, Catherine (2019): STARD3: A Swiss Army Knife for Intracellular Cholesterol Transport. In: Contact 2, 251525641985673. DOI: 10.1177/2515256419856730.

Wang, Guo-Xiao; Zhao, Xu-Yun; Meng, Zhuo-Xian; Kern, Matthias; Dietrich, Arne; Chen, Zhimin et al. (2014): The brown fat-enriched secreted factor Nrg4 preserves metabolic homeostasis through attenuation of hepatic lipogenesis. In: Nature medicine 20 (12), S. 1436–1443. DOI: 10.1038/nm.3713.

Wieckowski, Mariusz R.; Giorgi, Carlotta; Lebiedzinska, Magdalena; Duszynski, Jerzy; Pinton, Paolo (2009): Isolation of mitochondria-associated membranes and mitochondria from animal tissues and cells. In: Nature protocols 4 (11), S. 1582–1590. DOI: 10.1038/nprot.2009.151.

Wu, Jun; Boström, Pontus; Sparks, Lauren M.; Ye, Li; Choi, Jang Hyun; Giang, An-Hoa et al. (2012): Beige adipocytes are a distinct type of thermogenic fat cell in mouse and human. In: Cell 150 (2), S. 366–376. DOI: 10.1016/j.cell.2012.05.016.

Wu, Jun; Cohen, Paul; Spiegelman, Bruce M. (2013): Adaptive thermogenesis in adipocytes: is beige the new brown? In: Genes & development 27 (3), S. 234–250. DOI: 10.1101/gad.211649.112.

Xiang, Chunchen; Wang, Yujia; Zhang, Han; Han, Fang (2017): The role of endoplasmic reticulum stress in neurodegenerative disease. In: Apoptosis : an international journal on programmed cell death 22 (1), S. 1–26. DOI: 10.1007/s10495-016-1296-4.

Xiao, Fei; Jiang, Haizhou; Li, Zi; Jiang, Xiaoxue; Chen, Shanghai; Niu, Yuguo et al. (2023): Reduced hepatic bradykinin degradation accounts for cold-induced BAT thermogenesis and WAT browning in male mice. In: Nature communications 14 (1), S. 2523. DOI: 10.1038/s41467-023-38141-0.

Xu, Yibin; Xue, Ding; Bankhead, Armand; Neamati, Nouri (2020): Why All the Fuss about Oxidative Phosphorylation (OXPHOS)? In: Journal of medicinal chemistry 63 (23), S. 14276–14307. DOI: 10.1021/acs.jmedchem.0c01013.

Yaffe, M. P.; Kennedy, E. P. (1983): Intracellular phospholipid movement and the role of phospholipid transfer proteins in animal cells. In: Biochemistry 22 (6), S. 1497–1507. DOI: 10.1021/bi00275a026.

Yang, Felix T.; Stanford, Kristin I. (2022): Batokines: Mediators of Inter-Tissue Communication (a Mini-Review). In: Current obesity reports 11 (1), S. 1–9. DOI: 10.1007/s13679-021-00465-7.

Yang, Li; Na, Cheng-Lun; Luo, Shiyu; Wu, David; Hogan, Simon; Huang, Taosheng; Weaver, Timothy E. (2017): The Phosphatidylcholine Transfer Protein Stard7 is Required for Mitochondrial and Epithelial Cell Homeostasis. In: Scientific reports 7, S. 46416. DOI: 10.1038/srep46416.

Yang, Ziyun; Wang, Liang; Yang, Cheng; Pu, Shiming; Guo, Ziqi; Wu, Qiong et al. (2021): Mitochondrial Membrane Remodeling. In: Frontiers in bioengineering and biotechnology 9, S. 786806. DOI: 10.3389/fbioe.2021.786806.

Yao, Lu; Cui, Xiaona; Chen, Qi; Yang, Xiaoying; Fang, Fude; Zhang, Jun et al. (2017): Cold-Inducible SIRT6 Regulates Thermogenesis of Brown and Beige Fat. In: Cell reports 20 (3), S. 641–654. DOI: 10.1016/j.celrep.2017.06.069.

Yasukawa, Kai; Oshiumi, Hiroyuki; Takeda, Makoto; Ishihara, Naotada; Yanagi, Yusuke; Seya, Tsukasa et al. (2009): Mitofusin 2 inhibits mitochondrial antiviral signaling. In: Science signaling 2 (84), ra47. DOI: 10.1126/scisignal.2000287.

Yu, Peng; Petzoldt, Svenja; Wilhelm, Mathias; Zolg, Daniel Paul; Zheng, Runsheng; Sun, Xuefei et al. (2017): Trimodal Mixed Mode Chromatography That Enables Efficient Offline Two-Dimensional Peptide Fractionation for Proteome Analysis. In: Analytical chemistry 89 (17), S. 8884–8891. DOI: 10.1021/acs.analchem.7b01356.

Zborowski, J.; Dygas, A.; Wojtczak, L. (1983): Phosphatidylserine decarboxylase is located on the external side of the inner mitochondrial membrane. In: FEBS letters 157 (1), S. 179–182. DOI: 10.1016/0014-5793(83)81141-7.

Zecha, Jana; Satpathy, Shankha; Kanashova, Tamara; Avanessian, Shayan C.; Kane, M. Harry; Clauser, Karl R. et al. (2019): TMT Labeling for the Masses: A Robust and Cost-efficient, In-solution Labeling Approach. In: Molecular & cellular proteomics: MCP 18 (7), S. 1468–1478. DOI: 10.1074/mcp.TIR119.001385.

Zemski Berry, Karin A.; Murphy, Robert C. (2004): Electrospray ionization tandem mass spectrometry of glycerophosphoethanolamine plasmalogen phospholipids. In: Journal of the American Society for Mass Spectrometry 15 (10), S. 1499–1508. DOI: 10.1016/j.jasms.2004.07.009.

Zhang, Enming; Mohammed Al-Amily, Israa; Mohammed, Sarheed; Luan, Cheng; Asplund, Olof; Ahmed, Meftun et al. (2019): Preserving Insulin Secretion in Diabetes by Inhibiting VDAC1 Overexpression and Surface Translocation in β Cells. In: Cell metabolism 29 (1), 64-77.e6. DOI: 10.1016/j.cmet.2018.09.008.

Zhao, Haifang; Wang, Tao (2020): PE homeostasis rebalanced through mitochondria-ER lipid exchange prevents retinal degeneration in Drosophila. In: PLoS genetics 16 (10), e1009070. DOI: 10.1371/journal.pgen.1009070.

Zhao, J.; Unelius, L.; Bengtsson, T.; Cannon, B.; Nedergaard, J. (1994): Coexisting beta-adrenoceptor subtypes: significance for thermogenic process in brown fat cells. In: The American journal of physiology 267 (4 Pt 1), C969-79. DOI: 10.1152/ajpcell.1994.267.4.C969.

Zhao, Tian; Goedhart, Caitlin M.; Sam, Pingdewinde N.; Sabouny, Rasha; Lingrell, Susanne; Cornish, Adam J. et al. (2019): PISD is a mitochondrial disease gene causing skeletal dysplasia, cataracts, and white matter changes. In: Life science alliance 2 (2). DOI: 10.26508/lsa.201900353.

Zinser, E.; Sperka-Gottlieb, C. D.; Fasch, E. V.; Kohlwein, S. D.; Paltauf, F.; Daum, G. (1991): Phospholipid synthesis and lipid composition of subcellular membranes in the unicellular eukaryote Saccharomyces cerevisiae. In: Journal of bacteriology 173 (6), S. 2026–2034. DOI: 10.1128/jb.173.6.2026-2034.1991.

Zwaal, R. F.; Schroit, A. J. (1997): Pathophysiologic implications of membrane phospholipid asymmetry in blood cells. In: Blood 89 (4), S. 1121–1132.

7 APPENDIX

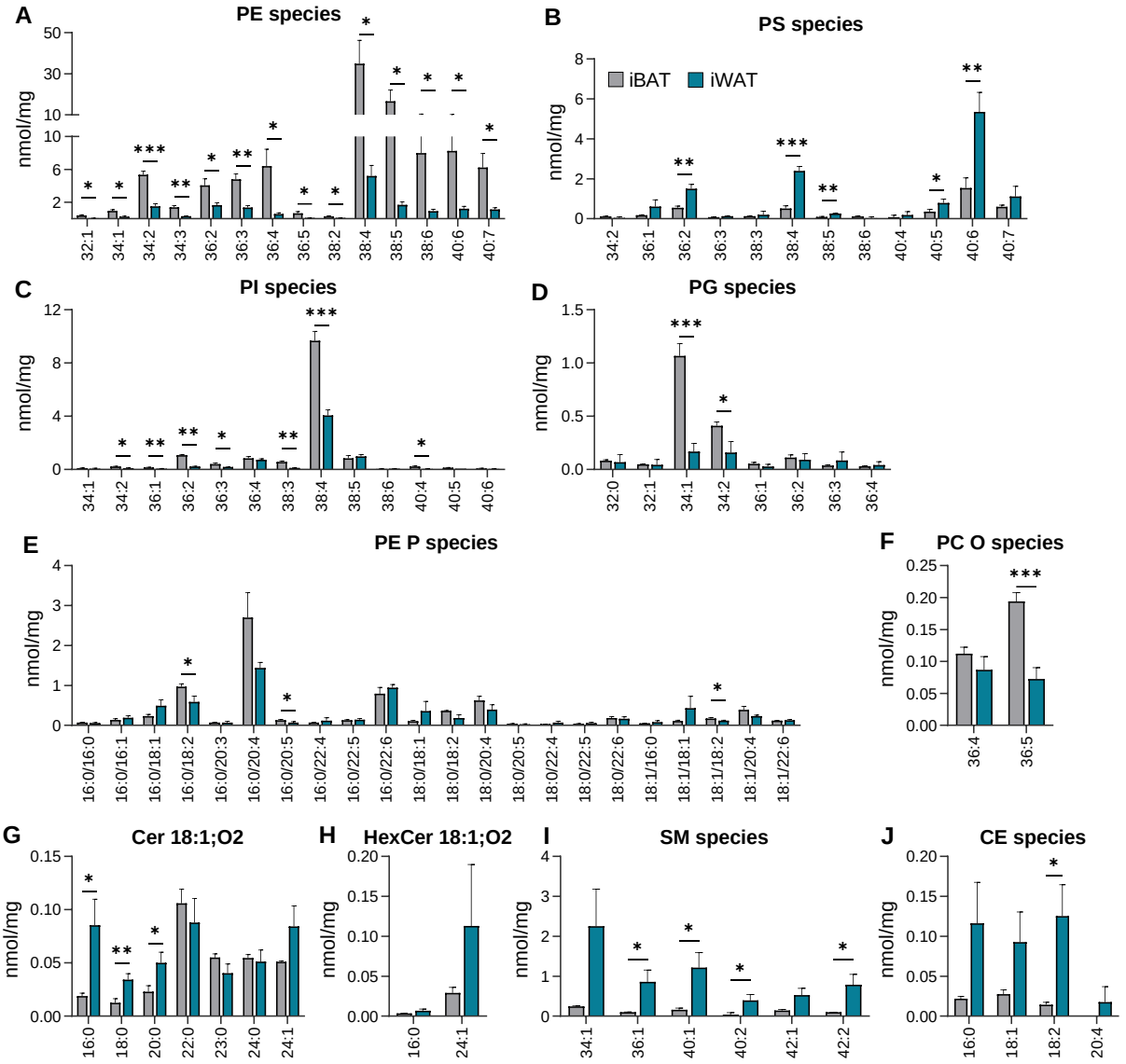

Supplementary Figure 1: Mitochondrial lipid species profile of iBAT mitochondria significantly differ to those of iWAT. *(A-J) Lipid species composition of mitochondria from iBAT (n= 3) vs. iWAT (n= 3). (A) PE, (B) PS, (C) PI, (D) PG, (E) PE P, (F) PC O, (G) Cer 18:1; O2, (H) HexCer 18:1; O2, (I) SM and (J) CE species; lipids were analysed using mass spectrometry. Shown are means +SD; *p<0.05, **p<0.01 and ***p<0.001 indicate significant differences to control determined with student's two-tailed t-test with Welch's correction. Each mitochondrial sample was pooled from tissue pooled of n= 5-10 mice.*

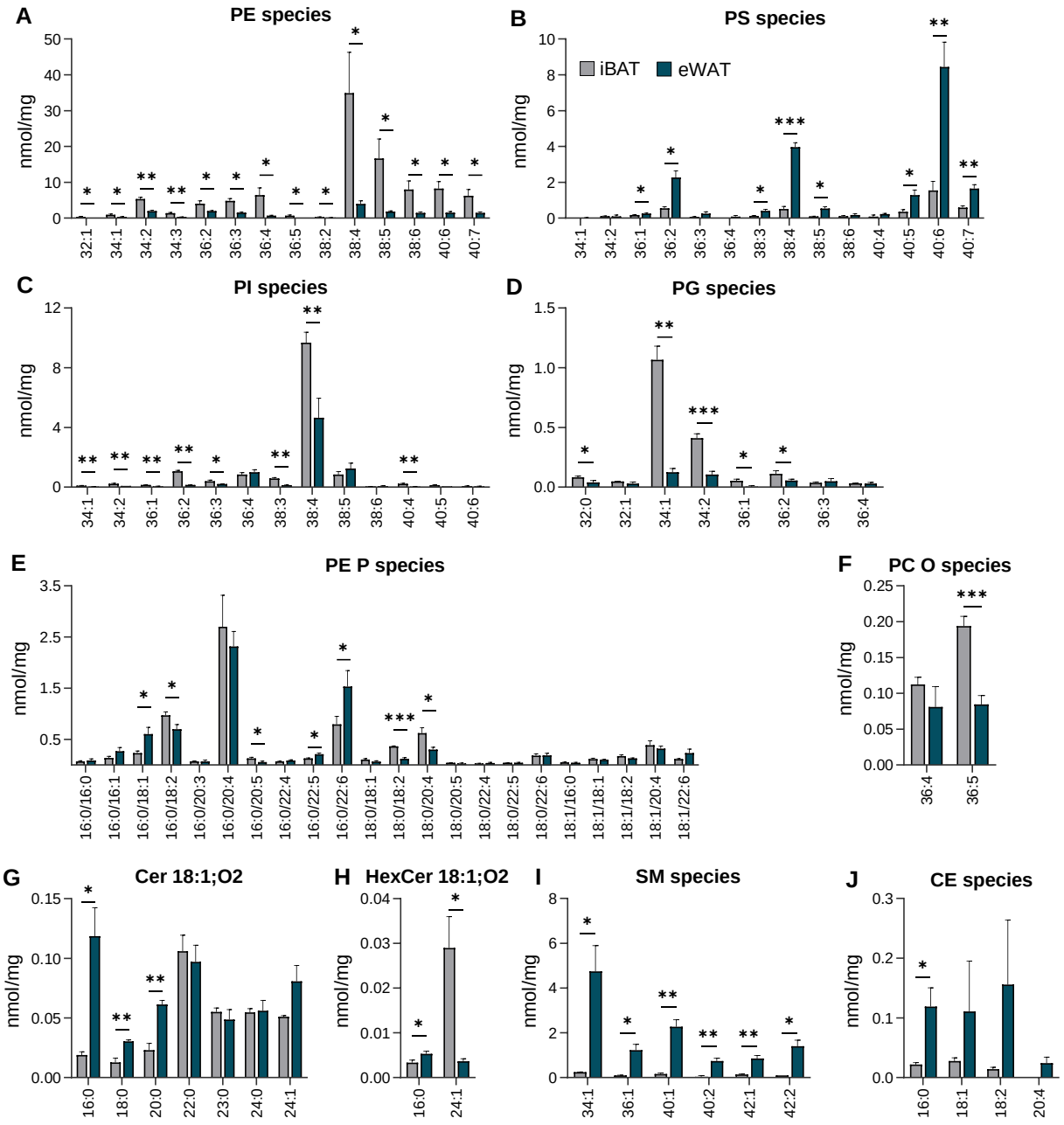

Supplementary Figure 2: Mitochondrial lipid species profiles of iBAT mitochondria significantly differ to those of eWAT. *(A-J) Lipid species composition of mitochondria from iBAT (n= 3) vs. eWAT (n= 3). (A) PE, (B) PS, (C) PI, (D) PG, (E) PE P, (F) PC O, (G) Cer 18:1; O2, (H) HexCer 18:1; O2, (I) SM and (J) CE species; lipids were analyzed using mass spectrometry. Shown are means +SD; *p<0.05, **p<0.01 and ***p<0.001 indicate significant differences to control determined with student's two-tailed t-test with Welch's correction. Each mitochondrial sample was pooled from tissue pooled of n= 5-10 mice.*

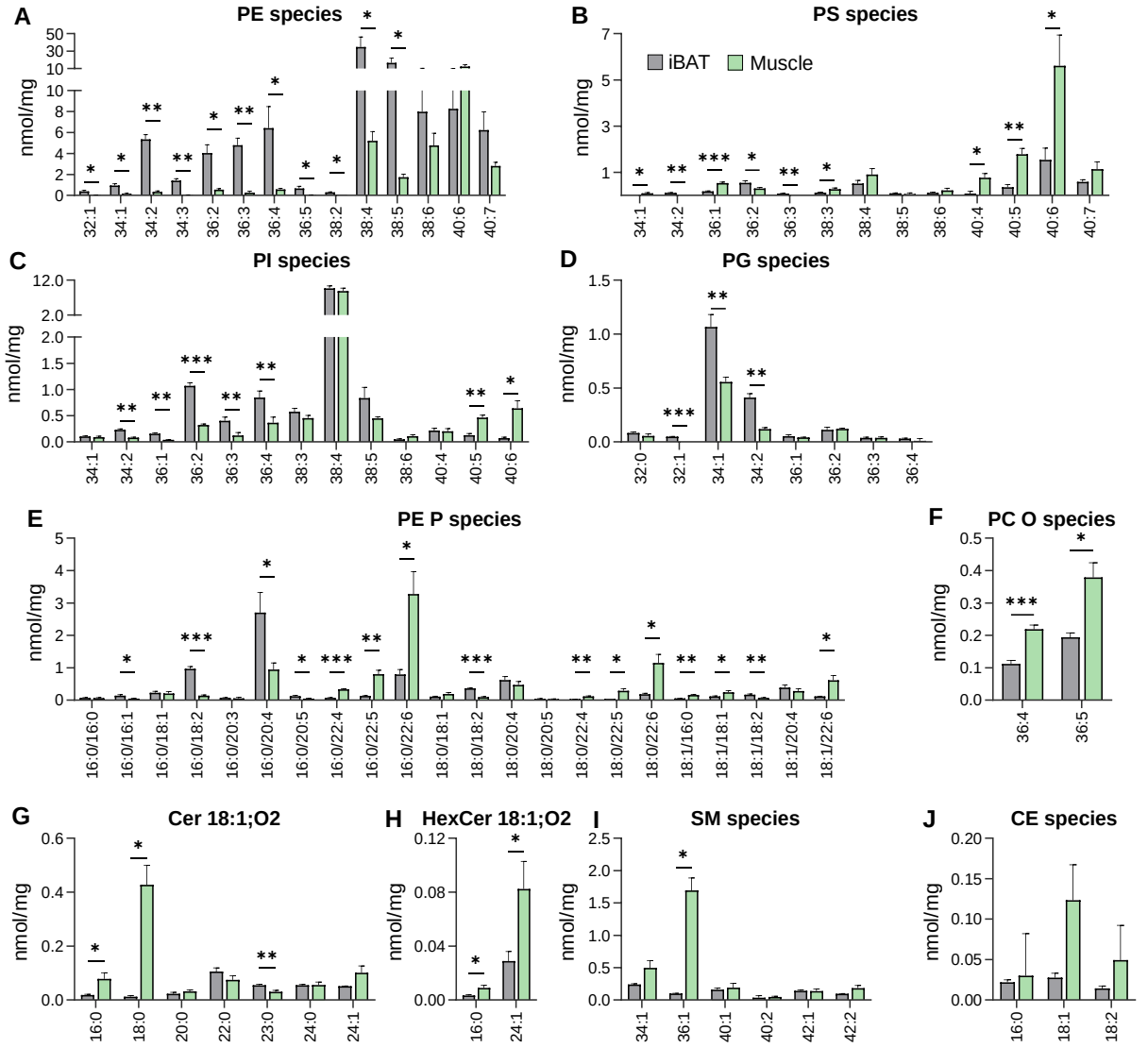

Supplementary Figure 3: Mitochondrial lipid species profiles of iBAT mitochondria significantly differ to those of muscle. *(A-J) Lipid species composition of mitochondria from iBAT (n= 3) vs. muscle (n= 3). (A) PE, (B) PS, (C) PI, (D) PG, (E) PE P, (F) PC O, (G) Cer 18:1; O2, (H) HexCer 18:1; O2, (I) SM and (J) CE species; lipids were analyzed using mass spectrometry. Shown are means +SD; *p<0.05, **p<0.01 and ***p<0.001 indicate significant differences to control determined with student's two-tailed t-test with Welch's correction. Each mitochondrial sample was pooled from tissue pooled of n= 5 mice.*

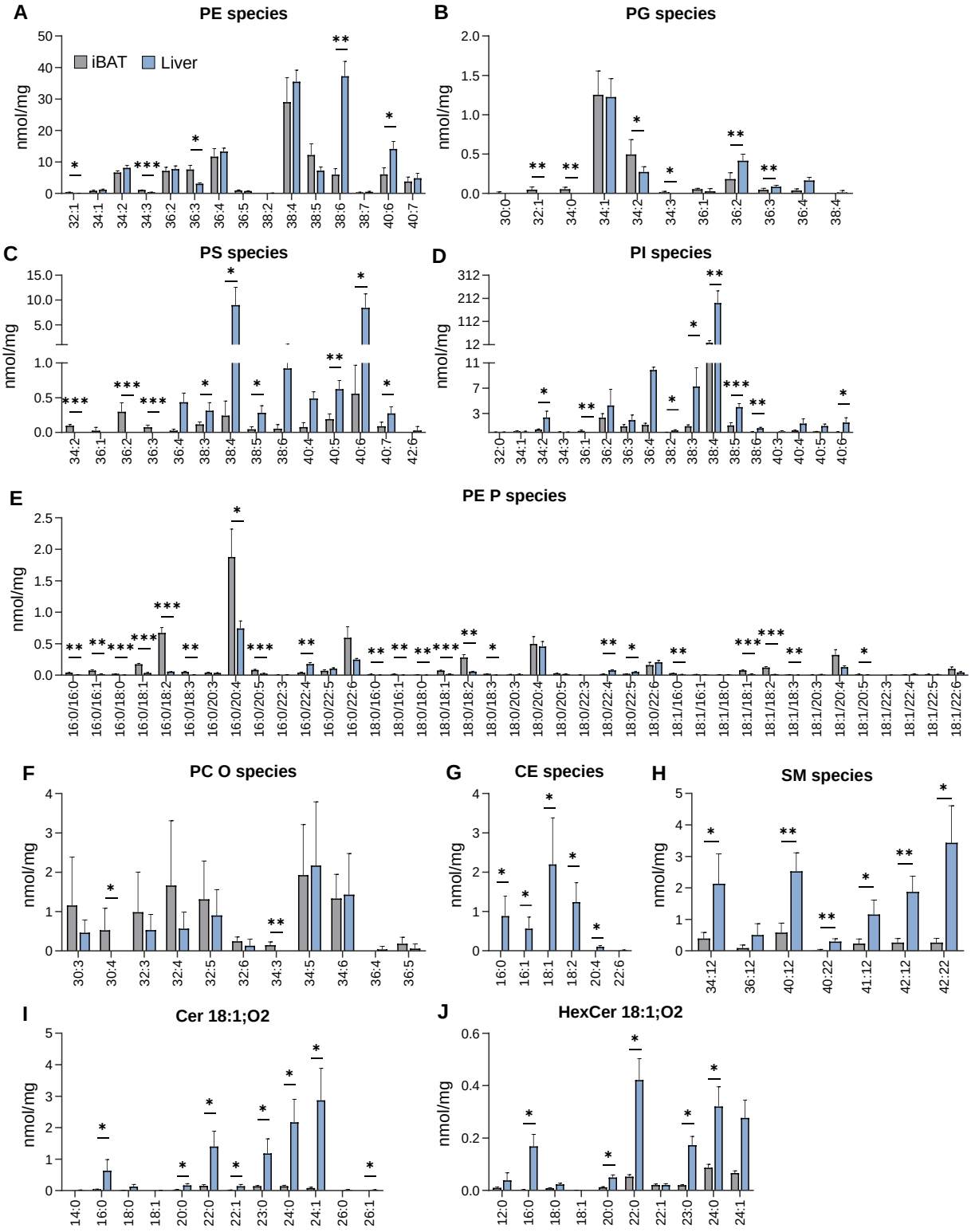

Supplementary Figure 4: Mitochondrial lipid species profiles of iBAT mitochondria significantly differ to those of liver. (A-J) Lipid species composition of mitochondria from iBAT (n= 4) vs. liver (n= 7). (A) PE, (B) PG, (C) PS, (D) PI, (E) PE P, (F) PC O, (G) CE, (H) SM, (I) Cer 18:1; O2 and (J) HexCer 18:1; O2 species; lipids were analyzed using mass spectrometry. Shown are means +SD; *p<0.05, **p<0.01 and ***p<0.001 indicate significant differences to control determined with student's two-tailed t-test with Welch's correction. Each mitochondrial sample was pooled from tissue pooled of n= 2-5 mice.

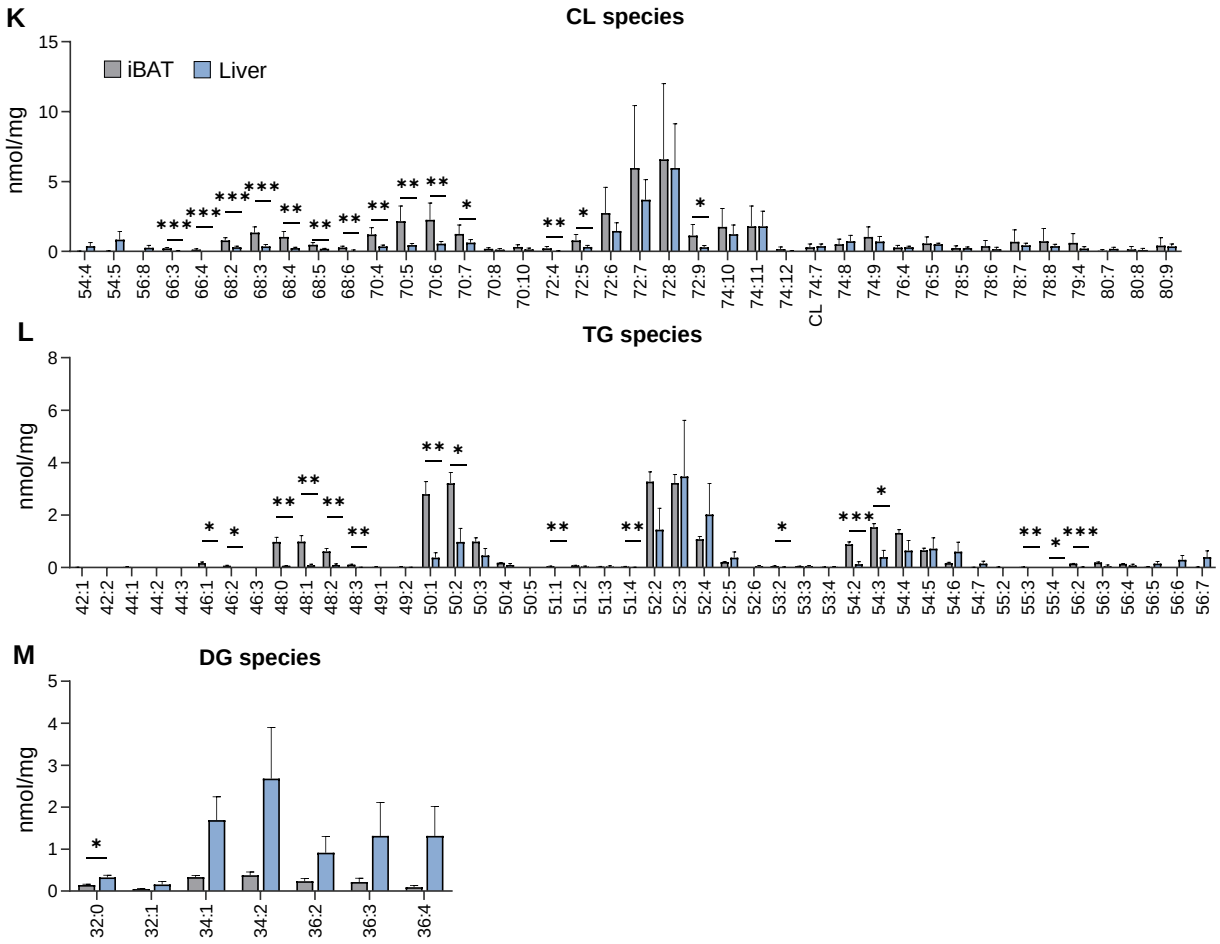

Supplementary Figure 5: Mitochondrial lipid species profiles of iBAT mitochondria significantly differ to those of liver. *(K-M) Lipid species composition of mitochondria from iBAT (n= 4) vs. liver (n= 7). (K) CL, (L) TG and (M) DG species; lipids were analysed using mass spectrometry. Shown are means +SD; *p<0.05, **p<0.01 and ***p<0.001 indicate significant differences to control determined with student's two-tailed t-test with Welch's correction. Each mitochondrial sample was pooled from tissue pooled of n= 2-5 mice.*

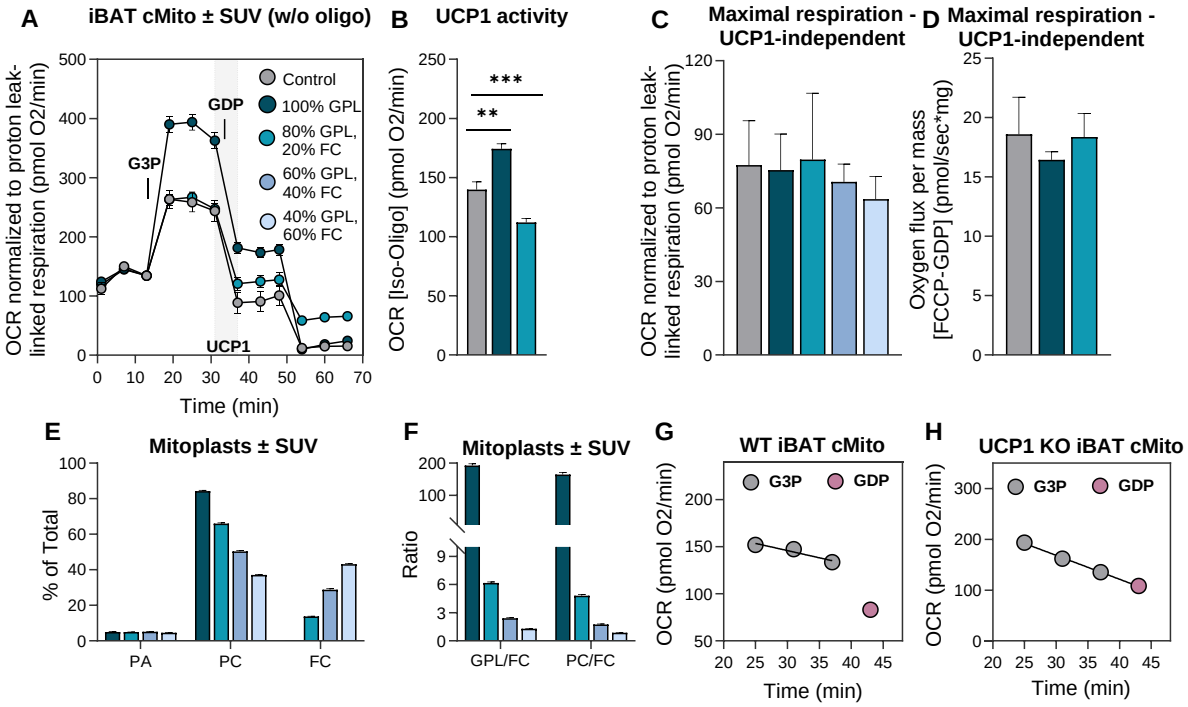

Supplementary Figure 6: GPL/FC influences UCP1 activity in mitochondria isolated from BAT of WT mice, independently of oligomycin application prior to G3P injection. Basal respiration and maximal respiratory capacity unrelated to UCP1 are not affected. GDP reduces UCP1 dependent O_2 consumption in mitochondria isolated of WT iBAT, but not UCP1 KO iBAT. *(A) Microplate-based respirometry applied to profile UCP1 activity in mitochondria isolated from iBAT of mice housed at 23°C. The oxygen consumption rate (OCR) was measured at basal conditions, after injections of G3P (to fuel electron transport chain and UCP1 activity), GDP (to inhibit UCP1 activity) and antimycin A (to block electron transport chain, equals non-mitochondrial respiration). Mitochondria were loaded without or with SUVs containing 100% GPL or 80% GPL+ 20% FC. Shown are data normalized to the OCR determined before G3P injection (19.0 min). (B) UCP1 activity calculated by subtraction of the OCR after GDP injection from G3P-mediated respiration determined in A. (C) FCCP-induced maximal respiratory capacity determined with microplate-based respirometry of BAT WT mitochondria loaded without or with SUVs containing 100% GPL, 80% GPL+20% FC, 60% GPL+40% FC or 40% GPL+60% FC. (D) FCCP-induced maximal respiratory capacity determined with high resolution respirometry of BAT WT mitochondria loaded without or with SUVs containing 100% GPL or 80% GPL+20% FC. (E) PA, PC and FC concentrations, (F) GPL/FC and PC/FC ratios of mitoplasts prepared of mitochondria previously treated with SUVs containing 100% GPL, 80% GPL+20% FC, 60% GPL+40% FC or 40% GPL+60% FC. Shown are means +SD; *p<0.05, **p<0.01 and ***p<0.001 indicate a significant difference for the comparisons control vs. 100% GPL and 100% GPL vs. 80% GPL-20% FC; determined using a two-sided Student's t test. (G) Oxygen consumption rate (OCR) after G3P (25-31-37 min) and GDP injection (43 min) in control mitochondria (not incubated with donor vesicles) isolated from BAT of WT mice. Shown are means of n= 8. OCRs at 25-31-37 min were related by linear regression. (H) Oxygen consumption rate (OCR) after G3P (25-31-37 min) and GDP injection (43 min) in control mitochondria (not incubated with donor vesicles) isolated from BAT of UCP1 KO mice. Shown are means of n= 4. OCRs at 25-31-37-43 min were related by linear regression. Analyzed with the microplate-based respirometry assay shown in* ***section 3.1****.*

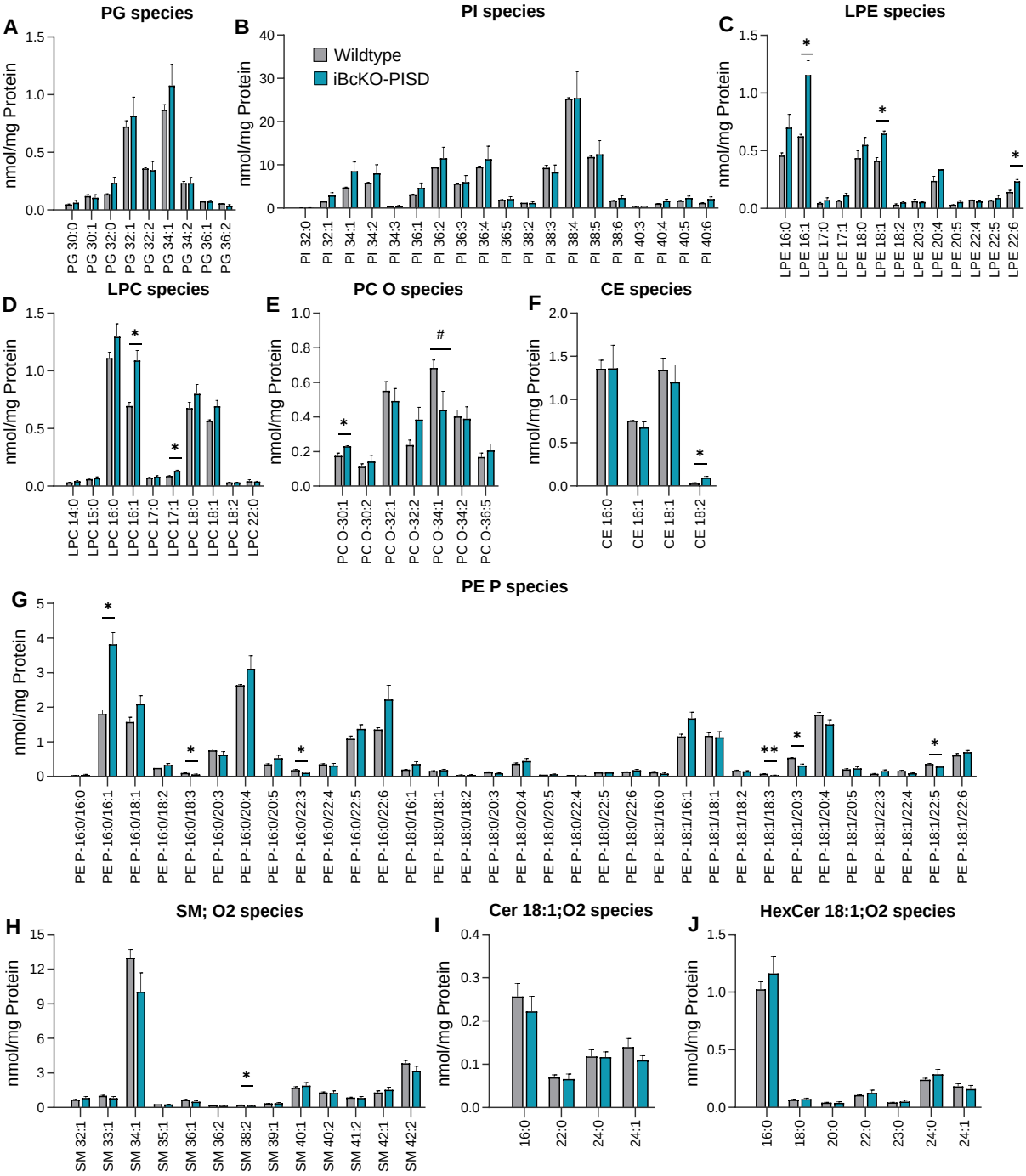

Supplementary Figure 7: The mitochondrial lipid species profile is differentially distributed between mPBAC mitochondria of iBcKO-PISD and WT mice. *(A) PG, (B) PI, (C) LPE, (D) LPC, (E) PC O, (F) CE species (G) PE P, (H) SM;O2, (I) Cer 18:1; O2 and (J) HexCer 18:1; O2 species in mitochondria isolated of mPBAC which were previously treated with 2 µM tamoxifen for 48 hours to induce PISD cKO; lipids were analyzed using mass spectrometry. Shown are means +SD of n= 2 per group; #p<0.1, *p<0.05 and **p<0.01 indicate significant differences to control determined with student's two-tailed t-test with Welch's correction. Each mitochondrial sample was pooled from adipocytes originating from n= 3 mice.*

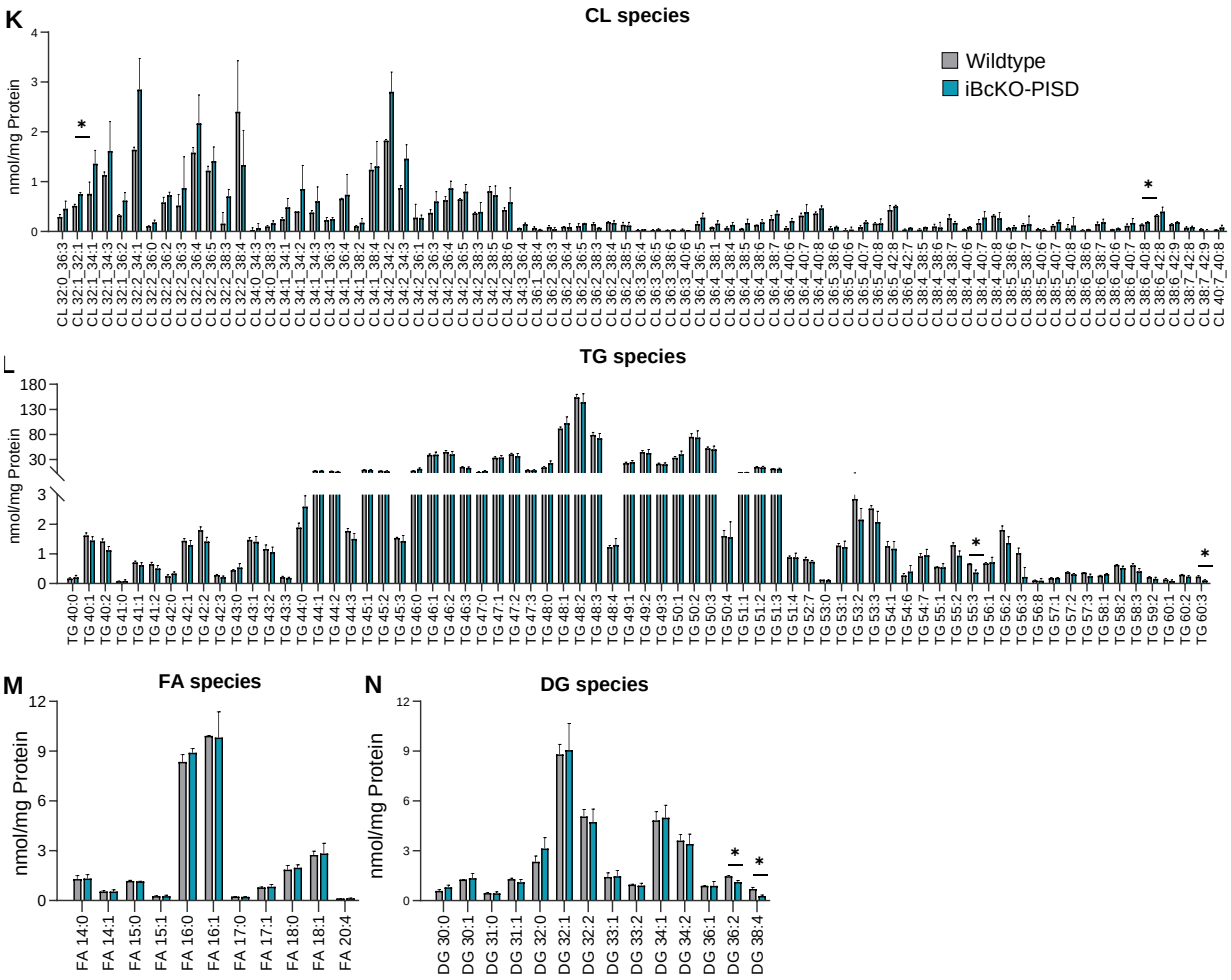

Supplementary Figure 8: The mitochondrial lipid species profile is differentially distributed between mPBAC mitochondria of iBcKO-PISD and WT mice. *(K) CL, (L) TG, (M) FA, (N) DG species in mitochondria isolated of mPBAC which were previously treated with 2 µM tamoxifen for 48 hours to induce PISD cKO; lipids were analyzed using mass spectrometry. Shown are means +SD of n= 2 per group; *p<0.05 indicate significant differences to control determined with student's two-tailed t-test with Welch's correction. Each mitochondrial sample was pooled from adipocytes originating from n= 3 mice.*

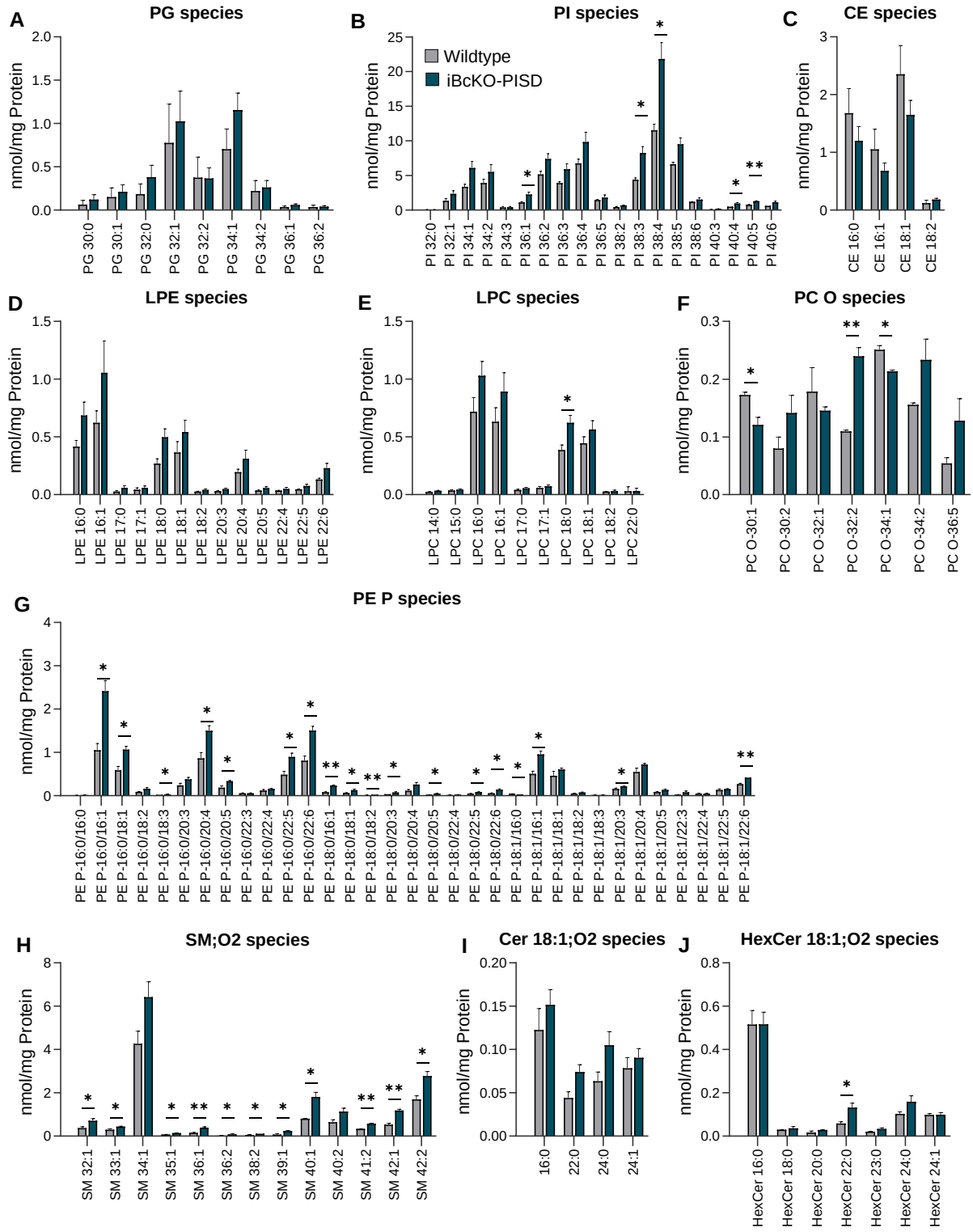

Supplementary Figure 9: The mitochondrial lipid species profile is differentially distributed between mPWAC mitochondria of iBcKO-PISD and WT mice. *(A) PG, (B) PI, (C) CE, (D) LPE, (E) LPC, (F) PC O (G) PE P, (H) SM;O2, (I) Cer 18:1; O2 and (J) HexCer 18:1; O2 species in mitochondria isolated of mPWAC which were previously treated with 2 µM tamoxifen for 48 hours to induce PISD cKO; lipids were analyzed using mass spectrometry. Shown are means +SD of n= 2 per group; *p<0.05 and **p<0.01 indicate significant differences to control determined with student's two-tailed t-test with Welch's correction. Each mitochondrial sample was pooled from adipocytes originating from n= 3 mice.*

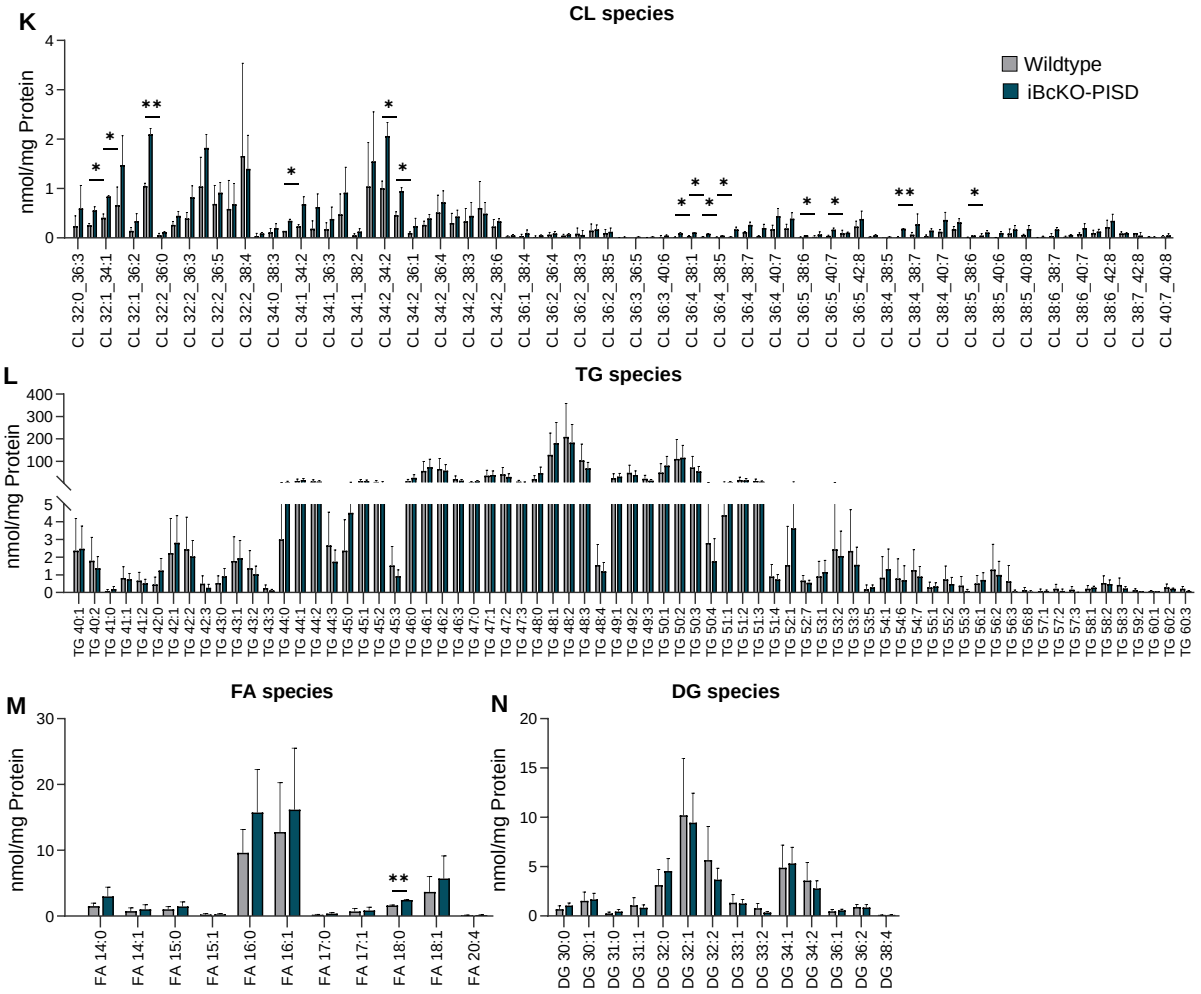

Supplementary Figure 10: The mitochondrial lipid species profile is differentially distributed between mPWAC mitochondria of iBcKO-PISD and WT mice. *(K) CL, (L) TG, (M) FA, (N) DG species in mitochondria isolated of mPWAC which were previously treated with 2 µM tamoxifen for 48 hours to induce PISD cKO; lipids were analyzed using mass spectrometry. Shown are means +SD of n= 2 per group; *p<0.05 and **p<0.01 indicate significant differences to control determined with student's two-tailed t-test with Welch's correction. Each mitochondrial sample was pooled from adipocytes originating from n= 3 mice.*

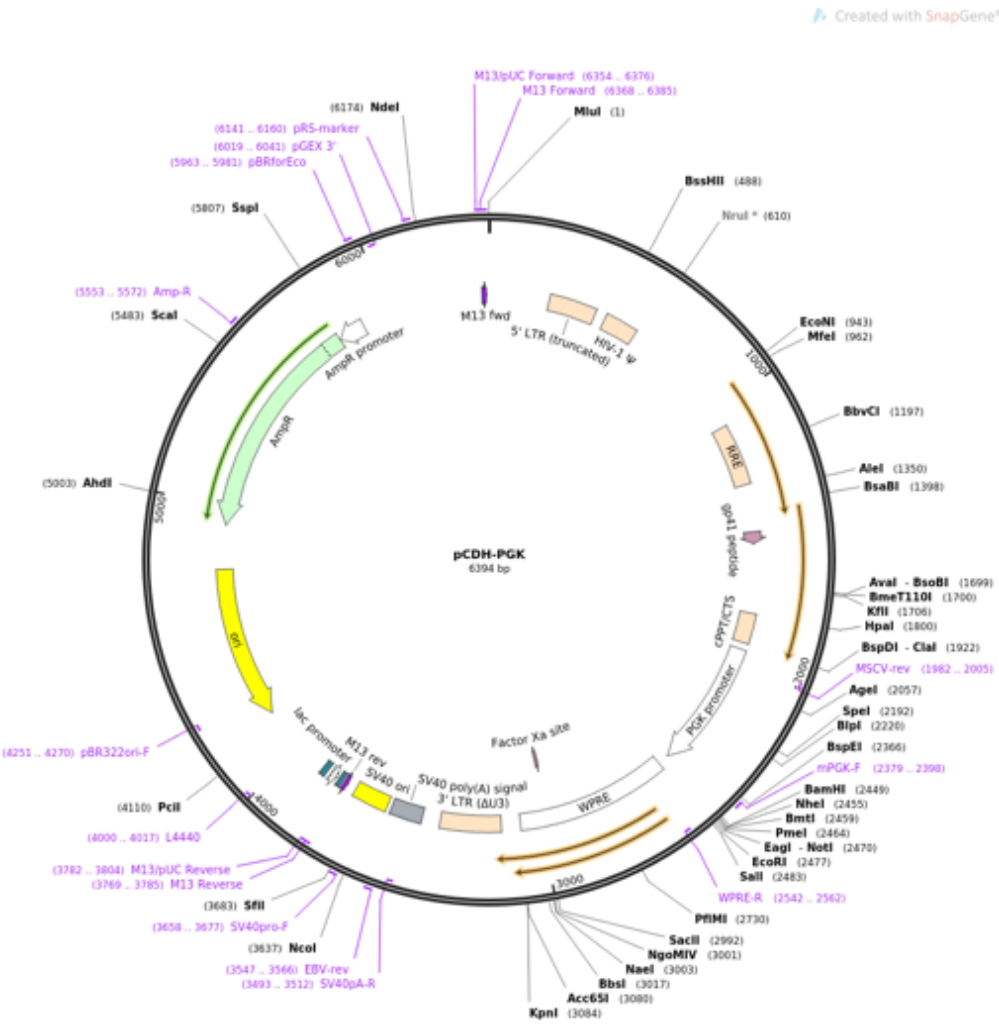

Supplementary Figure 11: *Vector map of pCDH-PGK backbone used for lentiviral overexpression of STARD3.*

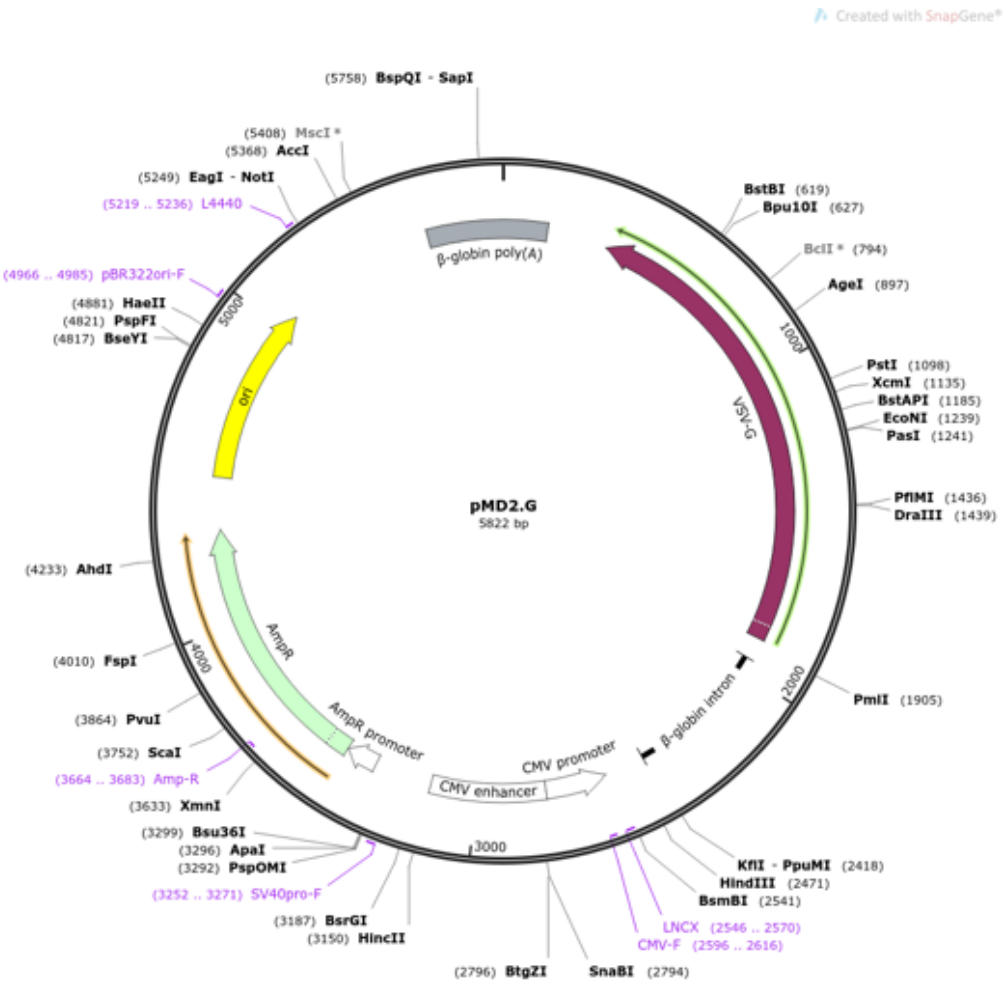

Supplementary Figure 12: *Vector map of pMD2.G envelope plasmid used for overexpression of STARD3.*

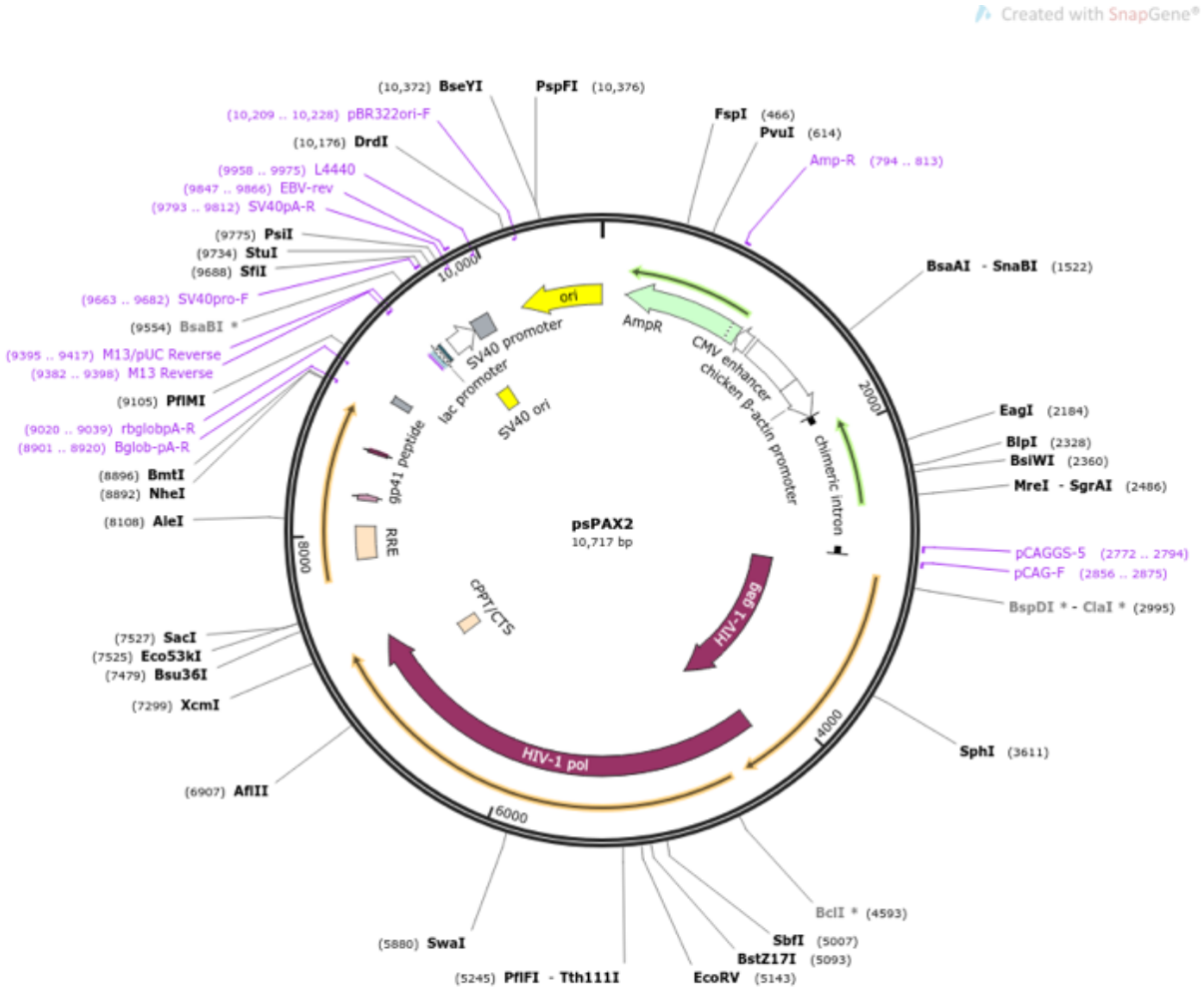

Supplementary Figure 13: *Vector map of psPAX2 packaging plasmid used for overexpression of STARD3.*

Supplementary Table 1: Known GPL/FC and FC contents of mammalian organelles.

Organelle	GPL/FC	FC (%)	Reference
Plasma Membrane	1.0-1.3	43.5-50.0	*(van Meer et al. 2008; Vance 2015)*
ER	6.7-14.3	6.5-13.0	*(van Meer et al. 2008; Vance 2015)*
Golgi	5.0-6.7 1	3.0-16.7	(van Meer et al. 2008; Vance 2015)
Lysosome	2.0-2.6	27.5-32.9	(Schoer et al. 2000; Vance 2015)
Peroxisome	12.5	7.4	(Khan et al. 2000)
Nucleus	4.5	18.0	(Ramjiawan et al. 1996)
MAM	Not available	Not available	-

Supplementary Table 2: Composition of Control and HFD

Ingredients	Control (S5745-E906)	Chow (3800, Kiba)	HFD (S5745-E920)
Casein (%)	24.000	-	24.000
L-Cysteine (%)	0.200	-	0.200
Corn starch (%)	47.800	-	27.800
Maltodextrin (%)	5.600	-	5.600
Sucrose (%)	5.000	-	5.000
Inulin (%) [1)]	2.500	-	2.500
Oat fiber (%) [2)]	2.500	-	2.500
Vitamin premix (%)	1.200	-	1.200
Mineral premix (%)	6.000	-	6.000
Choline Cl (%)	0.200	-	0.200
Palm oil (%)	-	-	20.000
Soybean oil (%)	5.000	-	5.000
Proximate contents			
Crude protein (%)	21.1	24.0	21.1
Crude fat (%)	5.1	4.9	25.1
Crude fiber (%) [1), 2)]	4.8	4.7	4.8
NDF (%) [1), 2)]	2.3	-	2.3
Soluble fiber (%)[1), 2)]	2.1	-	2.1
Total dietary fiber (%) [1), 2)]	4.5	-	4.5
Crude ash (%)	5.4	7.0	5.4
Starch (%)	45.9	47.5	26.7
Dextrin (%)	5.5	-	5.5
Sugar (%)	6.2	-	6.2
Energy (Atwater) MJ/kg [3)]	15.4	16.5	19.7
Protein kcal (%)	23	-	18
Fat kcal (%)	13	-	48
Carbohydrate (%)	64	-	34

[1)] Calculated with 94 % crude fiber, 90 % total dietary fiber and 85 % soluble fiber 92

[2)] Calculated with 96 % crude fiber, 90 % total dietary fiber and 89 % insoluble fiber 93

[3)] Physiological fuel value

8 ACKNOWLEDGEMENTS

This work would not have been possible without the support of many people, both scientifically and personally. Therefore, I would like to express my great appreciation. Thank you all!

First and foremost, I want to thank my doctoral advisor, Prof. Dr. Josef Ecker, for giving me the opportunity to work on this project. He has always provided me with help and inspiring ideas over the past years. His way of encouraging me when things got difficult was essential for this thesis. I particularly want to emphasize his part in going through such a nerve-wracking publication process.

Equally, I want to thank all the members of our research group - Claudine, Johannes, Maria, Sven and Adolfo. Their scientific and personal advice, assistance with various experiments, as well as the group effort when it came to tasks such as moving the labs really made a huge difference. I particularly want to mention Maria. We have really gone through all sorts of emotions over the last few years and there is no way, I could have done it without her friendship.

I would like to thank Prof. Dr. Martin Klingenspor for supporting me in this project. He provided me with novel ideas to improve experiments and concepts, as well as hypotheses to think about. Furthermore, this project would not have been possible without giving me the opportunity to work in his laboratories and to use all kinds of equipment. Additionally, a big thank you to all members of Martin's group and others of the ZIEL Institute, especially Anni, Josef, Sabine, Tobi, Eva, Johanna, Akim, Kathi, Manu, Daniela, Ronny, and Maren. I also want to thank Nico, who was always there to help with problems, even with very unusual things such as catching a bird in our office.

Next, I want to thank all the new colleagues in Regensburg (UKR), especially Marcus and Gerhard, for their great advice and support in everything related to lipidomics. Also, for their company at several conferences, which was always fun!

The collaboration with the lab of Christian Wolfrum (ETH) has greatly improved this work. Therefore, I would like to thank Lucy, Manu, Alex and Matthias for their hospitality during all my visits to Zurich, as well as for their efforts in generating/breeding the mouse line and supporting the experiments.

I want to acknowledge the (always extremely quick) help of Piero (TUM) with proteomics measurements and analyses, the assistance of Natalia (Helmholtz) during many exhausting days of mitochondrial seahorse measurements, as well as Klaus-Peter (MRI TUM) for his mentorship and helpful advice.

Last but not least, I would like to thank everyone outside of the laboratory, including family and friends, for always having my back and open ears for my whining throughout the PhD. The biggest thank you goes to my husband Manu. It was (and still is) very unique and helpful to go through the whole academic experience at the same time, and yet, in such different ways. He pushed me and kept me going every single day, but also held me back when it was time to do so. I am forever grateful for his love, support, patience and understanding.

Without each and every one of you, this journey would not have been the same.

Thank you!